

*coatings*

Special Issue Reprint

---

# Multifunctional Coatings on Medical Devices

---

Edited by  
Margareta Gabriela Ciobanu

[mdpi.com/journal/coatings](https://mdpi.com/journal/coatings)



# **Multifunctional Coatings on Medical Devices**



# Multifunctional Coatings on Medical Devices

Guest Editor

**Margareta Gabriela Ciobanu**



Basel • Beijing • Wuhan • Barcelona • Belgrade • Novi Sad • Cluj • Manchester

*Guest Editor*

Margareta Gabriela Ciobanu  
Department of Organic,  
Biochemical and Food  
Engineering  
“Gheorghe Asachi” Technical  
University of Iasi  
Iasi  
Romania

*Editorial Office*

MDPI AG  
Grosspeteranlage 5  
4052 Basel, Switzerland

This is a reprint of the Special Issue, published open access by the journal *Coatings* (ISSN 2079-6412), freely accessible at: [https://www.mdpi.com/journal/coatings/special\\_issues/medical\\_devices](https://www.mdpi.com/journal/coatings/special_issues/medical_devices).

For citation purposes, cite each article independently as indicated on the article page online and as indicated below:

Lastname, A.A.; Lastname, B.B. Article Title. <i>Journal Name</i> <b>Year</b> , <i>Volume Number</i> , Page Range.
--

**ISBN 978-3-7258-4631-3 (Hbk)**

**ISBN 978-3-7258-4632-0 (PDF)**

**<https://doi.org/10.3390/books978-3-7258-4632-0>**

© 2025 by the authors. Articles in this book are Open Access and distributed under the Creative Commons Attribution (CC BY) license. The book as a whole is distributed by MDPI under the terms and conditions of the Creative Commons Attribution-NonCommercial-NoDerivs (CC BY-NC-ND) license (<https://creativecommons.org/licenses/by-nc-nd/4.0/>).

# Contents

<b>About the Editor</b> . . . . .	<b>vii</b>
<b>Florian Priese, Dimitri Wiegel, Caterina Funaro, Giusi Mondelli and Bertram Wolf</b> Comparison of Mini-Tablets and Pellets as Multiparticulate Drug Delivery Systems for Controlled Drug Release Reprinted from: <i>Coatings</i> <b>2023</b> , <i>13</i> , 1891, <a href="https://doi.org/10.3390/coatings13111891">https://doi.org/10.3390/coatings13111891</a> . . . . .	<b>1</b>
<b>Sara Knigge, Marc Mueller, Lara Fricke, Tobias Schilling and Birgit Glasmacher</b> In Vitro Investigation of Corrosion Control of Magnesium with Degradable Polycaprolactone Coatings for Cardiovascular Grafts Reprinted from: <i>Coatings</i> <b>2023</b> , <i>13</i> , 94, <a href="https://doi.org/10.3390/coatings13010094">https://doi.org/10.3390/coatings13010094</a> . . . . .	<b>15</b>
<b>Shusen Hou, Tingting Yang, Yue Li, Liming Lian, Weixin Yu and Lin Yang</b> Topography Control of Micro-Nanosized Anatase Coating on Magnesium Alloy Reprinted from: <i>Coatings</i> <b>2022</b> , <i>12</i> , 1063, <a href="https://doi.org/10.3390/coatings12081063">https://doi.org/10.3390/coatings12081063</a> . . . . .	<b>31</b>
<b>Harumi Tsutsumi, Yusuke Tsutsumi, Masaya Shimabukuro, Tomoyo Manaka, Peng Chen, Maki Ashida, et al.</b> Investigation of the Long-Term Antibacterial Properties of Titanium by Two-Step Micro-Arc Oxidation Treatment Reprinted from: <i>Coatings</i> <b>2021</b> , <i>11</i> , 798, <a href="https://doi.org/10.3390/coatings11070798">https://doi.org/10.3390/coatings11070798</a> . . . . .	<b>42</b>
<b>Julietta V. Rau, Angela De Bonis, Mariangela Curcio, Katharina Schuhladen, Katia Barbaro, Giovanni De Bellis, et al.</b> Borate and Silicate Bioactive Glass Coatings Prepared by Nanosecond Pulsed Laser Deposition Reprinted from: <i>Coatings</i> <b>2020</b> , <i>10</i> , 1105, <a href="https://doi.org/10.3390/coatings10111105">https://doi.org/10.3390/coatings10111105</a> . . . . .	<b>53</b>
<b>Hannah Kranebitter, Bernd Wallner, Andreas Klinger, Markus Isser, Franz J. Wiedermann and Wolfgang Lederer</b> Rescue Blankets-Transmission and Reflectivity of Electromagnetic Radiation Reprinted from: <i>Coatings</i> <b>2020</b> , <i>10</i> , 375, <a href="https://doi.org/10.3390/coatings10040375">https://doi.org/10.3390/coatings10040375</a> . . . . .	<b>66</b>
<b>Xingda Wu, Cuijuan Liu, Hongpeng Chen, Yanfang Zhang, Lin Li and Nan Tang</b> Layer-by-Layer Deposition of Hyaluronan and Quercetin-Loaded Chitosan Nanoparticles onto Titanium for Improving Blood Compatibility Reprinted from: <i>Coatings</i> <b>2020</b> , <i>10</i> , 256, <a href="https://doi.org/10.3390/coatings10030256">https://doi.org/10.3390/coatings10030256</a> . . . . .	<b>75</b>
<b>Michał Bartmański, Łukasz Pawłowski, Andrzej Zieliński, Aleksandra Mielewczyk-Gryń, Gabriel Strugała and Bartłomiej Cieślik</b> Electrophoretic Deposition and Characteristics of Chitosan–Nanosilver Composite Coatings on a Nanotubular TiO <sub>2</sub> Layer Reprinted from: <i>Coatings</i> <b>2020</b> , <i>10</i> , 245, <a href="https://doi.org/10.3390/coatings10030245">https://doi.org/10.3390/coatings10030245</a> . . . . .	<b>87</b>
<b>Xinwei Ming, Yan Wu, Ziyue Zhang and Yan Li</b> Micro-Arc Oxidation in Titanium and Its Alloys: Development and Potential of Implants Reprinted from: <i>Coatings</i> <b>2023</b> , <i>13</i> , 2064, <a href="https://doi.org/10.3390/coatings13122064">https://doi.org/10.3390/coatings13122064</a> . . . . .	<b>103</b>



## About the Editor

### **Margareta Gabriela Ciobanu**

Margareta Gabriela Ciobanu is a full-time professor in the Department of Organic, Biochemical and Food Engineering at the Faculty of Chemical Engineering and Environmental Protection “Cristofor Simionescu”, the “Gheorghe Asachi” Technical University of Iași, Romania. Her scientific activity is mainly focused on conducting theoretical and experimental studies in the field of micro- and nanostructured biomaterials and porous membranes with applications in medicine and environmental protection. The results of her own didactic and scientific research have been published in 71 scientific articles in ISI national/international journals, 3 patents, and 11 books. She has also participated in over 200 national/international symposia and been the recipient of 26 national/international grants/research contracts. Furthermore, she serves as an article reviewer for various international ISI journals, as well as being a member of multiple other national/international professional associations. In Web of Science, her “h index” is 21 and she has received 1188 citations (excluding self-citations).



# Comparison of Mini-Tablets and Pellets as Multiparticulate Drug Delivery Systems for Controlled Drug Release

Florian Priese <sup>1,\*</sup>, Dimitri Wiegel <sup>1</sup>, Caterina Funaro <sup>2</sup>, Giusi Mondelli <sup>2</sup> and Bertram Wolf <sup>1</sup>

<sup>1</sup> Department of Applied Biosciences and Process Engineering, Anhalt University of Applied Sciences, Strenzfelder Allee 28, 06406 Bernburg, Germany; bertram.wolf@hs-anhalt.de (B.W.)

<sup>2</sup> IMA S.p.A.—ACTIVE Division, Via 1 Maggio 14-16, 40064 Ozzano dell'Emilia, BO, Italy; caterina.funaro@ima.it (C.F.); giusi.mondelli@ima.it (G.M.)

\* Correspondence: florian.priese@hs-anhalt.de; Tel.: +49-15209542416

**Abstract:** Mini-tablets made into hard capsules or administered using special dosing units, as well as pellets in hard capsules or compressed into tablets, offer the advantages of multiparticulate drug delivery systems and are suitable for controlled drug release using polymer coatings. Four different kinds of solid drug preparations were manufactured and investigated concerning drug release. Inert pellets were coated with the model drug sodium benzoate and, in a second step, with the insoluble polymer ethylcellulose. The coated pellets were compressed into mini-tablets and into normal tablets. Another kind of mini-tablet was compressed from a sodium benzoate compression mixture and finally coated with ethylcellulose. The coating of the tablets was performed using fluidized bed technology. The sodium benzoate release plots of the coated pellets show a lag time and retarded release according to first-order kinetics. The mini-tablets and normal tablets compressed from pellets release sodium benzoate according to first-order kinetics as well, but without the lag time due to distinct ethylcellulose layer destruction during tableting. The release is retarded with increasing ethylcellulose layer thickness on directly compressed mini-tablets. The different formulations of coated pellets, mini-tablets, and normal tablets offer a broad choice for variable drug release kinetics depending on the biopharmaceutical and pharmacological requirements.

**Keywords:** pellets; mini-tablets; controlled drug release

## 1. Introduction

In contrast to classical single-drug units like tablets, hard and soft gelatine capsules, and single powder or granule doses in sachets and stick packs, mini-tablets and pellets are small, solid drug units providing several distinct advantages, i.e., dose definition through the combination of single units, and homogeneous spreading after administration in the stomach and small intestine, therefore increasing the adsorption area and improving bioavailability.

Tablets developed in a solid drug dosage form for human use are in the range of 4–15 mm in diameter, whereas mini-tablets range from 1 to 4 mm, making them suitable for the manufacture of multiparticulate drug delivery systems. Mini-tablets may be filled, hard gelatine capsules or compressed into tablets as the final drug formulation. There has been an increasing interest in mini-tablets over the last 20 years. Until now, the investigation of mini-tablets has focused on their compression behavior and properties. Mini-tablets are compressed using lower compression force than classical tablets and exhibit lower tensile strength, but also exhibit sufficiently low friability depending on the formulation components. The capping tendency is reduced in some cases compared to large tablets [1], and doses of up to 90% of some critical drug substances may be successfully compressed [2]. The content uniformity of mini-tablets depends on the component particle size, particle size distribution, the high level of interactive blending of the components [3], compression blend flow properties [4], and the drug substance's physical behavior [5].

Controlled drug release is one of the most important aims of mini-tablet manufacturing. In analogy to large tablets with slow and sustained release, matrix mini-tablets were investigated that consisted of insoluble, but slowly swellable ethylcellulose [6] and high-molecular hydroxypropylmethylcellulose [7–9], polyvinylacetate/polyvinylpyrrolidone [10], and pH-value-sensitive acrylate polymers [11].

Similar insoluble acrylate polymers [12,13], copolymer vinylpyrrolidone–vinylacetate [14], ethylcellulose [15], and hydroxypropylmethylcellulose acetate succinate [9] were used as coating materials for mini-tablets with sustained drug release, distinct lag time, and enteric coating properties. Mini-tablets were developed with different application and indication aims. Mucoadhesive mini-tablets for ocular medication consist of high-molecular polyacrylic acid or waxy maize starch [16,17]. After administration into the saccus conjunctivae, the mini-tablets swell, forming a gel that sticks to the mucosa and releases the drug over a long time period. For the prolongation of the gastric emptying time, the mini-tablets were compressed into large tablets with effervescent substances for gas generation and a larger content of high-molecular hydroxypropylmethylcellulose, leading to a prolonged residence time in the stomach and sustained drug release [18–20]. The absorption of peptides after oral administration was improved and delayed by using N-trimethyl chitosan chloride as the main component of mini-tablets [21]. Drug release was optimized through drug complexation with  $\beta$ -cyclodextrin [22]. Mini-tablets have also received increasing interest in terms of dose-controlled use for children. The taste of sodium benzoate was successfully improved by the use of hard fat in mini-tablets [23], and the suitability of powdered milk for the production of paracetamol mini-tablets was investigated [24].

Compared to mini-tablets, pellets and coated pellets are used for a longer time as the drug-containing components of multiparticulate drug delivery systems. Research and development in the field of pharmaceutical pellets include processing, i.e., extrusion/spheronization [25], fluidized bed rotor agglomeration [26], and layering and coating with enteric [27,28] and retarding polymers like ethylcellulose [29–33]. Drug substances may be incorporated into the pellets, layered onto the surface of the pellets, or both for the initial and maintenance dosage [34,35].

Mini-tablets and pellets are comparable so far, but differ in size, with drug-loaded pellets for pharmaceutical use being in the range of 100–800  $\mu\text{m}$ . The contents of mini-tablets and drug pellets are filled into hard capsules or compressed into tablets. Consequently, some authors compare the suitability and the properties of pellets and mini-tablets with the same drug substance and similar formulations, indicating the advantages and disadvantages of both dosage forms. Drug release depends on the kind of coating polymer and layer thickness, the wetting and water absorption of the neutral cores, and formulation changes induced by matrix formers [36]. The release of easily soluble drug substances from ethylcellulose-coated pellets according to the manufacturing method, kind of binder used in the wet granulation, and layer thickness increased in comparison to mini-tablets due to their significantly higher specific surface area [37]. For prolonged release, pellets require a much thicker coating layer compared to mini-tablets. The coating layer thickness of similarly formulated mini-tablets and pellets was successfully measured using dynamic image analysis [38]. The use of mini-tablets competes with new development dosage forms and modifications for sustained release [39,40].

The aim of the present paper was to examine the development of coated pellets and mini-tablets and to compare the different solid dosage forms on the release kinetics of easily soluble sodium benzoate as a model drug substance. Therefore, three different solid dosage forms were manufactured.

Inert microcrystalline cellulose pellets were used as starter cores. In a first step, the pellets were coated with sodium benzoate, and in a second step, with the ethylcellulose as an insoluble retarding polymer (EC pellets). The coated pellets were compressed into mini-tablets type 1 (MT1) and normal tablets (NT). Furthermore, mini-tablets type 2 (MT2) were manufactured through the direct compression of sodium benzoate and excipients (filling agent, disintegration agent, lubricant) and were then coated with ethylcellulose

(Figure 1). The coating was performed using fluidized bed technology. The influence of the process parameters and formulation parameters on the coating was evaluated, as well as the impact of the compression procedures on the product properties and sodium benzoate release. Finally, the products were compared regarding the product parameters and benefits for industrial manufacturing.

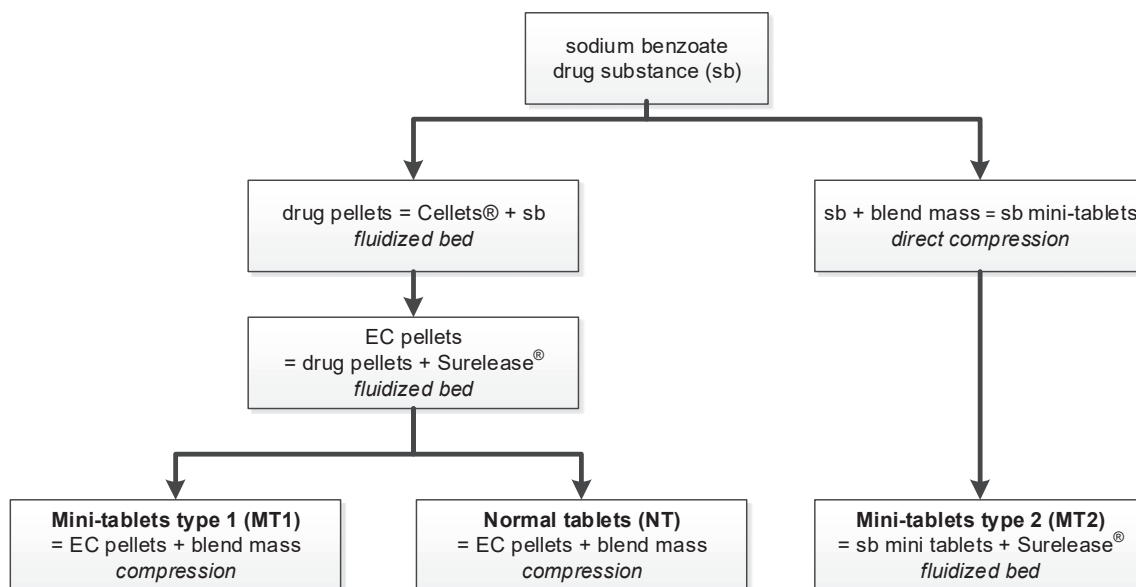


**Figure 1.** Overview of three different solid dosage forms for sustained release.

## 2. Materials and Methods

### 2.1. Materials

All excipients were used as received. The quality of all substances refers to pharmacopoeia [Ph. Eur. 2020]. Inert microcrystalline cellulose pellets (Cellets®200, IPC, Dresden, Germany), sodium benzoate (Chemie Vertrieb, Magdeburg, Germany), polyvinylpyrrolidone (PVP, Kollidon 30®, BASF, Ludwigshafen, Germany), talcum (Chemie Vertrieb, Magdeburg, Germany), ethylcellulose (Surelease®, Colorcon, Dartford, UK), microcrystalline cellulose (MCC, VIVAPUR®102, JRS Pharma, Rosenberg, Germany), lactose monohydrate (Meggler, Wasserburg, Germany), high-dispersed silicon dioxide (Aerosil®200, Evonik Industries, Germany), carboxymethylcellulose, sodium salt, magnesium stearate, and zinc stearate (all substances from Merck, Darmstadt, Germany) were used.

The formulation of the sodium-benzoate-layered and ethylcellulose-coated pellets is summarized in Table 1, and the formulations of the mini-tablets MT1 and MT2 and normal tablets (NT) are presented in Table 2.

**Table 1.** Formulation of the final pellets coated with sodium benzoate and ethylcellulose.

Components of Pellet Lot	Content (%)
Microcrystalline cellulose (Cellets®200)	23.2
Sodium benzoate	30.2
Polyvinylpyrrolidone	1.6
Talcum	0.6
Ethylcellulose	44.4
Total	100.0

**Table 2.** Formulation mini-tablets MT1 and MT2 and normal tablets NT.

Components of (Mini) Tablets	MT1/NT Content (%)	MT2 Content (%)
Microcrystalline cellulose	36.6	38.8
Sodium benzoate	15.1	15.5
Polyvinylpyrrolidone	0.8	
Talcum	0.3	
Ethylcellulose	22.2	20.0
Lactose monohydrate	18.5	19.0
Carboxymethylcellulose, sodium salt	5.0	5.2
Magnesium stearate	1.0	1.0
High dispersed silicon dioxide	0.5	0.5
Total	100.0	100.0

In the case of the mini-tablets MT1, polyvinylpyrrolidone was added to the sodium benzoate layering fluid to increase the plasticity and mechanical stability of the sodium benzoate layer, and talcum was added to prevent the pellets from sticking during the process (Table 2). Surelease<sup>®</sup> is a ready-to-use aqueous coating dispersion made of ethylcellulose and the addition of further excipients is not necessary. Polyvinylpyrrolidone and talcum were not included in the MT2 mini-tablet lot due to the direct compression of all components. Lactose monohydrate serves as a filling agent, sodium carboxymethylcellulose as a disintegrant, magnesium stearate as a lubricant, and high-dispersed silicon dioxide as a flow promotor in the compression powder mixture in order to obtain successful compression and final tablets of high quality.

## 2.2. Methods

### 2.2.1. Sodium Benzoate Layering of Pellets and Ethylcellulose Coating in the Fluidized Bed

The fluidized bed layering of the inert pellets with sodium benzoate and the coating of the sodium benzoate pellets and mini-tablets with the ethylcellulose was performed using a lab-scale fluidized bed coater (Mylab, IMA S.p.A., Bologna, Italy) equipped with the central partition and the bottom spray setup. The fluidized bed coating process parameters are reported in Table 3. The direct-compressed mini-tablets MT2 were coated with ethylcellulose using an increased process air rate of 200 m<sup>3</sup>/h compared to the sodium benzoate layering and the ethylcellulose coating of pellets (125 m<sup>3</sup>/h, Table 3). Therefore, the water evaporation rate was increased and the product temperature was raised to 55 °C compared to 42 °C for MT1 and NT. The spray rate was lower in all cases of ethylcellulose coating compared to sodium benzoate layering to prevent the pellets and mini-tablets from sticking and to stop the fluidized bed from over-wetting and breaking down.

**Table 3.** Fluidized bed process parameters, sodium benzoate layering, and ethylcellulose coating of pellets and mini-tablets.

Process Parameters	Sodium Benzoate Layering	EC Pellets Ethylcellulose Coating	MT2 Ethylcellulose Coating
Batch size (kg)	3.0	1.6	2.0
Process air rate (m <sup>3</sup> /h)	125	125	200
Process air temperature (°C)	70	60	70
Product temperature (°C)	43	41	55
Spray pressure (bar)	2.0	2.0	2.0
Spray rate (g/min)	30	15	10
Spray nozzle diameter (mm)	1	1	1

### 2.2.2. Tableting

The PREXIMA 80 (IMA, Bologna, Italy) rotary tablet press was used for the mini-tablet compression (MT1 and MT2). It was equipped with a mixed turret Eu-B and Euro-D, suitable for laboratory trials, consisting of Euro-D dies and Euro-D biconvex round multi-tip punches of 2 mm in diameter (24 tips per punch). The normal biplane tablets (NT) of a 6 mm diameter round shape were compressed using the same press and tablet press configuration. Two levels of compression forces were used for the mini-tablets (6 and 11 kN) and normal tablets (11 and 31 kN) with the aim of assessing the release profile of the solid oral dosage forms. The thickness of the mini-tablets was 3 mm and that of the normal tablets was 4 mm.

### 2.2.3. In Vitro Release of Sodium Benzoate

An in vitro release investigation was carried out using a dissolution tester (PTW II, Pharma Test, Hainburg, Germany) equipped with 6 vessels and paddle at a temperature of 37 °C and a rotation rate of 50 rpm in purified water (1000 mL), according to the pharmacopoeia method [Ph. Eur. 2020]. A suitable measure of EC pellets (33 mg) or number of mini-tablets (10 and 12 for MT1 and MT2, respectively), amounting to approximately 10 mg sodium benzoate, was placed into each vessel. The samples of the release fluid (10 mL) were withdrawn at predetermined time intervals over at least 120 min and were filtered using a membrane filter of pore size 0.22 µm. The sodium benzoate content of the filtrate was directly measured using UV spectroscopy.

The sodium benzoate content of the EC pellets and mini-tablets was measured using UV spectroscopy (Spekol 1300, Analytik Jena, Jena, Germany) at 220 nm wavelength and 10 mm quartzite cuvette length, compared to blind purified water. Therefore, a defined measure of EC pellets or mini-tablets amounting to 10–12 mg sodium benzoate was dispersed in purified water, agitated for 30 min, and filtered, and then the filtrate was transferred to a 1 L volumetric flask and filled up to the measurement line.

### 2.2.4. Scanning Electron Microscopy (SEM)

The morphology of the pellet and the mini-tablet surfaces was examined using SEM (Type PWB6703/SEM 515, Philips Corp., Eindhoven, The Netherlands). Accordingly, the samples were coated with gold–palladium plasm for 230 s under an argon atmosphere (SCD 040, Balzers Union, Liechtenstein).

### 2.2.5. Powder Characterization

The particle size, size distribution, and sphericity of the pellet products were measured using dynamic image analysis (Camsizer<sup>®</sup> P4, Retsch, Haan, Germany). The bulk density of the pellet products (100 g) was measured using an SVM 102 tap volumeter (Erweka, Heusenstamm, Germany) with a 250 mL graduated cylinder.

The tablet friability was investigated using a TA 10 friabilator (Erweka, Heusenstamm, Germany). In this process, a 6.5 g weight of the tablets is exposed to friction and fall forces over 4 min using a rotating wheel 30 cm in diameter with a baffle. The tablets are inspected for the percentage mass lost through chipping. The Ph. Eur. Specification allows maximum of 1% mass to be lost [Ph. Eur. 2020].

### 2.2.6. Linearization of Release Curves

The evaluation of the release curves was performed according to different models of release kinetics used by several authors [41–44]. In the first step of release evaluation, the amount of a cumulatively released substance is plotted compared to time. Linear curves arise in the case of zero-order kinetics, i.e., equal drug amounts are released at equal time intervals (Equation (1)). This behavior is typical for long-acting drug delivery systems with pronounced retarded release like implants, oral therapeutic systems in the sense of an osmotic pump, ocular therapeutic systems, and special kinds of microparticles

and nanoparticles with biodegradable polymers, and is not typical in the case of pellets and tablets.

$$M_t = M_0 - k_0 \times t \quad (1)$$

First-order release kinetics is typical for slightly soluble drugs in solid preparations like tablets, pellets, and granules dominated by slow dissolution and diffusion control. The dissolution, or the release rate, is highest at the beginning according to the large concentration gradient—as the most important factor in Fick's first law for transport flow density by diffusion (Equation (2))—and diminishes with process time.

$$1/A \times dn/dt = -D \times dc/dx \quad (2)$$

The released drug amount at moment  $t$  is calculated using Equation (3), and linearization gives the Sigma Minus function (Equation (4)).

$$M_t = M_0 \times \exp(-k_1 \times t) \quad (3)$$

$$\ln(M_0 - M_t) = \ln(M_0) - k_1 \times t \quad (4)$$

Another approach to the first-order kinetics evaluation of release processes includes the RRSB function (Equation (5)) and linearized form (Equation (6)).

$$M_t = M_0 \times (1 - \exp(-t^b/a)) \quad (5)$$

$$\ln(-\ln(1 - M_t/M_0)) = b \times \ln(t) - \ln(a) \quad (6)$$

The square root function (Equation (7)) is preferred in cases of the diffusive transport processes of non-disintegrating matrices and semisolid systems like ointments and gels.

$$M_t = k_q \times \sqrt{t} \quad (7)$$

The difference factor describes the relative error between two release profiles calculated from the cumulative released amounts  $R_i$  and  $T_i$  at distinct moments for reference and test formulation ( $f_1$ , Equation (8)). The similarity factor is based on the sum of the deviation squares of the released drug amounts ( $f_2$ , Equation (9)) of the reference and test formulation, and takes a value of 100 in the case of identical release profiles and values between 50 and 100 for similar release profiles. Both factors are used for the comparison of generics and standard drug product release rates. In this study, the factors are used to evaluate the similarity (or difference) of the sodium benzoate release from mini-tablets, normal tablets, and EC pellets.

$$f_1 = \frac{\sum_{i=1}^n R_i - T_i}{\sum_{i=1}^n R_i} \times 100 \quad (8)$$

$$f_2 = 50 \times \log \left\{ \left[ 1 + \frac{1}{n} \times \sum_{i=1}^n (R_i \times T_i)^2 \right]^{-0.5} \times 100 \right\} \quad (9)$$

### 3. Results and Discussion

#### 3.1. Manufacturing of Coated Pellets and Tableting and Coating of Tablets

The process of consecutive Cellets<sup>®</sup> 200 layering with sodium benzoate and ethylcellulose coating in the fluidized bed was performed according to earlier investigations [34]. The ethylcellulose coating of MT2 was accompanied by agglomeration due to the greater contact area of the mini-tablets in comparison to the pellets. Successful agglomeration mitigation was achieved by increasing the process air rate and reducing the spray rate from 15 to 10 g/min (Table 3). During the ethylcellulose coating of MT2, the samples

of intermediate product were taken at 10% and 20% ethylcellulose content in order to investigate the sodium benzoate release.

### 3.2. Product Properties

#### 3.2.1. EC Pellets

The ethylcellulose-coated sodium benzoate pellets provide the advantage of a multiparticulate drug delivery system with a median  $x_{50.3}$  of 574  $\mu\text{m}$ . The bulk density of 0.74 g/mL hints to the slight densification and physical stability of the pellets. The surface is smooth and homogeneous with only low roughness (Figure 2). The inner microcrystalline cellulose pellet is surrounded by layers of sodium benzoate and ethylcellulose and the pellets indicate high sphericity at 0.96.

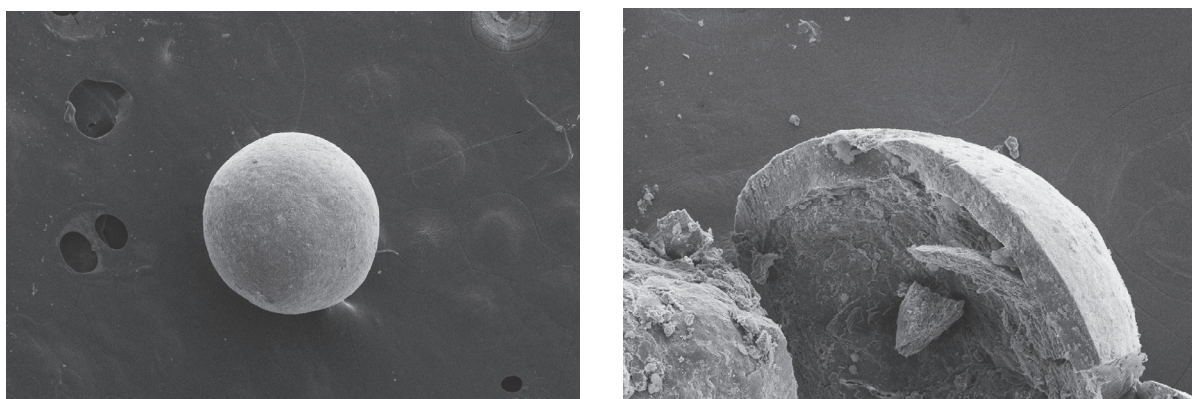


**Figure 2.** SEM of Cellets<sup>®</sup>200 layered with sodium benzoate and ethylcellulose: complete pellet (**left**) and section with core and coating layer (**right**).

#### 3.2.2. Mini-Tablets and Normal Tablets

The mini-tablets MT1 and MT2 (before ethylcellulose coating) show relatively high thickness (3 mm, Table 4) compared to diameter (2 mm). MT1 contains 50% *w/w* EC pellets and MT2 is compressed from a powder mixture lacking in polyvinylpyrrolidone and talcum and, finally, coated with ethylcellulose. The increased average weight of MT1 (8.46 mg) compared to MT2 (7.36 mg) results from the high density of the EC pellets in MT1. The sufficient hardness and mechanical stability of all three kinds of tablets are evidenced by their low friability (Table 4).

**Table 4.** Properties of mini-tablets MT1 and MT2 with ethylcellulose layer and normal tablets NT.

Samples	Avg. Weight (mg)	Weight Uniformity (%)	Diameter (mm)	Thickness (mm)	Friability (%)
MT1	8.46	4	2	3	0.5
MT2	7.36	4	2	3	0.0
NT	151.8	1	6	3	0.1

The SEM microphotographs of MT1 compressed from EC pellets show the three-dimensional dispersion of the pellets (Figure 3). The interparticulate space between the pellets is filled with the mixture of powder excipients (Table 2). The pellets are visible not only through SEM imaging, but also using stereo light microscopy.

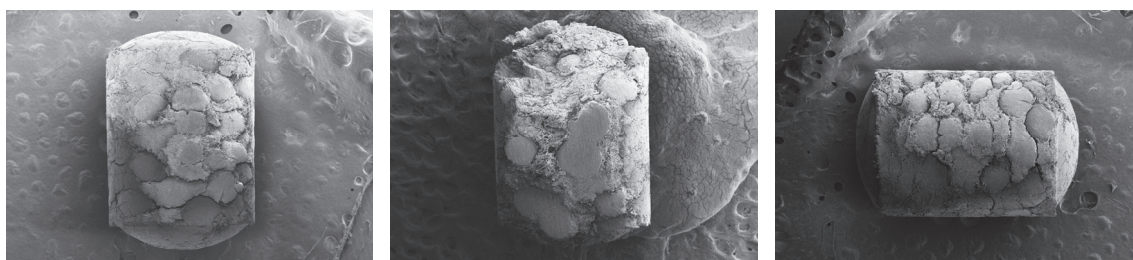


**Figure 3.** SEM of mini-tablets MT1 compressed from EC pellets and excipients: complete mini-tablet (left,middle) and section (right).

The ethylcellulose-coated MT2 mini-tablets manufactured from the powder mixture and not from the pellets show a smooth surface (Figure 4). The section indicates the mini-tablet's core of compressed powder components surrounded by ethylcellulose film.

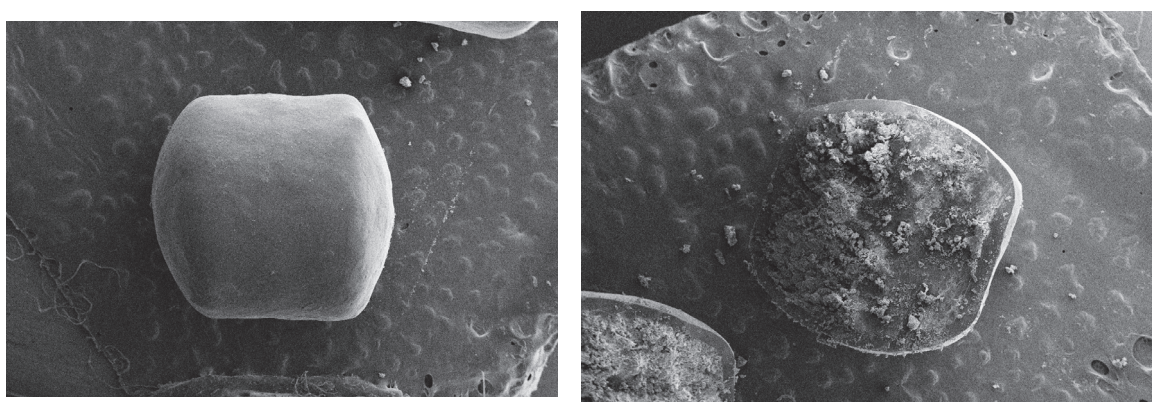


**Figure 4.** SEM of mini-tablets MT2 compressed from powder mixture of sodium benzoate and excipients and coated with ethylcellulose: complete (left) and section (right).

### 3.3. Sodium Benzoate Release from EC Pellets, Mini-Tablets MT1, and Normal Tablets NT

#### 3.3.1. Release versus Time, Zero-Order Kinetics

The ascents of the MT1, 11 kN and NT, 31 kN release plots are similar, but the plot of the pellets is increased (Figure 5, double linear plot). The sodium benzoate is released at a high rate after a lag time and there is obvious sufficient wetting and swelling of the ethylcellulose film. The ethylcellulose-coated pellets release the sodium benzoate with a lag time of 10 min due to the delayed wetting of the homogeneous surface consisting of insoluble ethylcellulose and the slow swelling of the polymer (Figure 5). After a lag time of 10 min, the release is somewhat increased (steeper ascent) compared to the mini-tablets and normal tablets, resulting in similar release plots after 60 min. In all cases, the sodium benzoate release reaches 90% after 90 min.

The mini-tablets MT1 and normal tablets NT compressed from the same EC pellets do not show a lag time. In contact with water, the tablets undergo disintegration and the liberation of the pellets, and the sodium benzoate release starts immediately, contrary to the pellets. The diminishing release rate (Figure 5) in the case of the tablets may derive from both the delayed tablet disintegration and the wetting of the pellets in the inner tablet volume or in the fragments. In addition, the compression of the EC pellets into tablets is connected with the pressure onto the pellets, and, therefore, onto the ethylcellulose layer. This is accompanied by mechanical friction, generating partial layer cracking and leading to increased release and lack of lag time. Release plots at different compression forces indicate the impact factor on the drug release. With MT1 as well as with NT, the release rate is increased under high compression force (11 kN MT1 and 31 kN NT, Figure 5). A high compression force leads to stronger destruction of the ethylcellulose layer and the pellets themselves, and to faster release. The overlapping and interaction of the

simultaneous ongoing processes lead to the present release behavior. The compression of the ethylcellulose-coated pellets into mini-tablets MT1 does not pose any advantages in comparison to compression into normal tablets NT regarding the sustained sodium benzoate release (Figure 5). The variation in the release from mini-tablets is increased compared to EC pellets and normal tablets compressed from pellets.

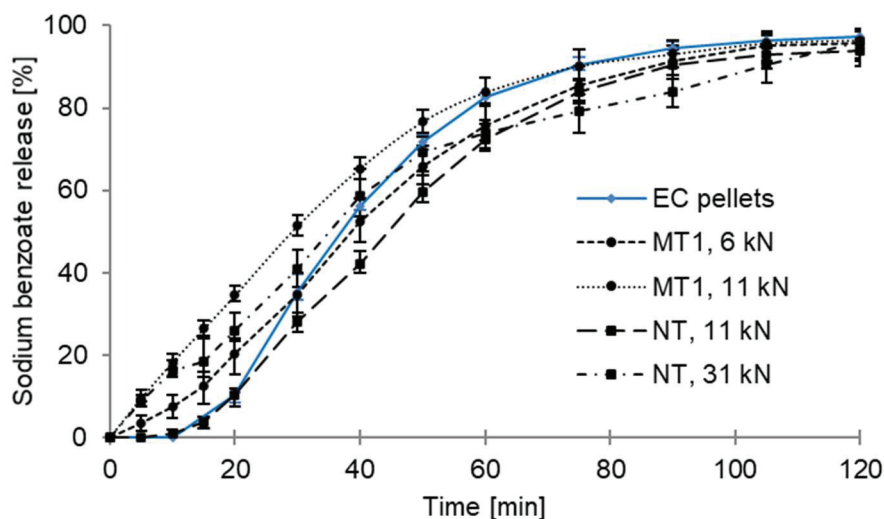


**Figure 5.** Sodium benzoate release from EC pellets (blue line), mini-tablets MT1 compressed with compression force 6 and 11 kN, and normal tablets NT compressed with 11 and 31 kN (black lines) versus time.

Normal tablets produced under a low compression force (NT, 11 kN) show the most similar release profile to the reference profile of pellets. As expected, the results obtained for both NT and MT1 show that the main retardation effect on the drug release profile depends more on the decrease in the compression force in comparison to the disintegration rate of the tablets. This can be explained by the preferred ethylcellulose layer breakage of the coated pellets on the external side of the cores due to the compression force of the tablet stamps.

### 3.3.2. Linearization of the Sodium Benzoate Release Plots of MT1, MT2, and EC Pellets

The first-order kinetics of the sodium benzoate release is most obvious for MT1 compressed with a force of 11 kN and NT with a force of 31 kN, with a coefficient of determination (CoD) of 0.99 (Table 5). The initial phase of the wetting and swelling of the ethylcellulose film is short, lag time does not occur, and the dissolution and the release rate are high at the beginning and decelerate in the terminal phase. The CoD in the case of the pellets amounts to only 0.95 due to the pronounced lag time at the beginning resulting from the wetting and swelling of the comparably thick and homogeneous ethylcellulose layer. The zero-order kinetics and square root show a lower CoD, appearing less probable.

**Table 5.** Coefficient of determination of sodium benzoate release from MT1, NT, and EC pellets.

Coefficient of Determination $R^2$	MT1 (11 kN)	NT (31 kN)	Pellets
Zero-Order	0.87	0.91	0.90
Square Root	0.95	0.96	0.88
Sigma Minus Plot (First-Order)	0.99	0.99	0.95
RRSB (First-Order)	0.99	0.98	0.95

The Sigma Minus Plots show only little deviation of the ascents (Table 6). The form parameter  $b > 1$  (RRSB plot) hints to biphasic release with a slow rate in the initial phase. The scale parameter  $1/a$ , corresponding to the release rate, is diminished for pellets (0.10) compared to tablets (0.22 and 0.23) regarding the complete release curve resulting from the lag time. Slow release corresponds to a higher time parameter ( $t_{63.2\%}$ , 60 min for EC pellets versus MT1 35 min and NT 46 min, Table 6).

**Table 6.** Ascent first-order release and parameters of RRSB plot: MT1, NT, and EC pellets.

Parameter	MT1 (11 kN)	NT (31 kN)	Pellets
Ascent Sigma Minus	0.04	0.03	0.04
RRSB: $1/a$ (scale)	0.22	0.23	0.10
RRSB: $b$ (form)	1.27	1.15	2.47
RRSB: $t_{63.2\%}$ (time in min)	35	46	60

### 3.3.3. Difference Factor and Similarity Factor of Sodium Benzoate Release from MT1, NT, and EC Pellets

The sodium benzoate release profiles from MT1, 11 kN and NT, 31 kN are similar (difference factor 11, Table 7). The tablets are compressed from the same coated EC pellets. Otherwise, difference factors above 15 (MT1/EC pellets 32 and NT/EC pellets 21) indicate no similarity. The reasons are the lag time and the more homogeneous ethylcellulose film in the case of the pellets compared to the tablets.

**Table 7.** Difference factor and similarity factor for comparison of release from MT1, NT, and EC pellets.

Parameter	Evaluation	MT1/NT	MT1/ EC Pellets	NT/ EC Pellets
Difference Factor	"similar" 0–15	11	32	21
Similarity Factor	"similar" 50–100	77	68	73

All three similarity factors are in the range of 50–100, hinting to similarity. The similarity factor is calculated based on deviation squares, and is not as sensitive as the difference factor. In this case, the influence of lag time is not as strong as in the case of the difference factor (Table 7).

### 3.3.4. Results for MT2 with Different Ethylcellulose Coatings

The cores without an ethylcellulose coating (0% ethylcellulose, Figure 6) release the sodium benzoate immediately due to the absence of a diffusion polymer and the high solubility of sodium benzoate. A distinct retarded release is observed for MT2 with a 10% ethylcellulose coating, but without a certain lag time. The release from MT2 with a 20% ethylcellulose coating is similar to the EC pellets with a high ethylcellulose content at 44.4% (Figure 6). One should expect a lower release rate for MT2 due to a somewhat thicker ethylcellulose layer as a result of the lower surface area compared to EC pellets. The reason for the similar release is explained by the thinner coating layer at the edges of the mini-tablets. This is a critical point compared to the nearly ideal spherical pellets. In the case of a comparable thin ethylcellulose layer, the film will erupt preferentially at the edges in contact with water. In order to avoid burst effects, it is essential to exceed the critical thickness of the ethyl cellulose film, especially at the edges of the MT2 tablets. For MT1, the critical EC layer thickness was not achieved; thus, no lag time and only a limited sustained release were obtained.

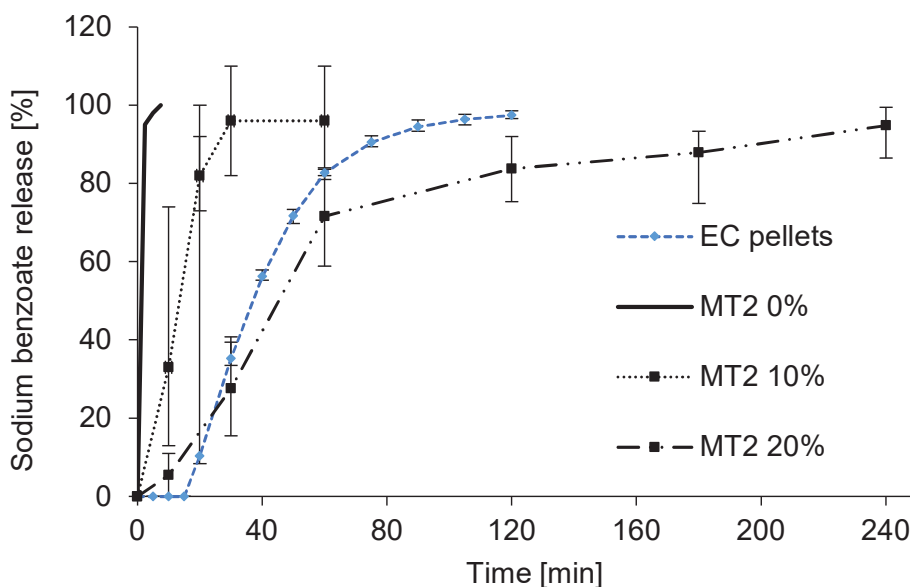


**Figure 6.** Sodium benzoate release from EC pellets (blue line), from uncoated mini-tablets MT2 (solid line), and from MT2 with increasing amounts of ethylcellulose (10%, dotted line and 20%, dashed line) versus time.

Difference factors distinctly above 15 (Table 8) indicate no similarity in the sodium benzoate release from MT2 10%, MT2 20%, and pellets. The different thickness and the condition of the ethylcellulose layers result in significant deviations in the release plots. Otherwise, the similarity factors meet the acceptable range of 50–100, hinting to the weaker evaluation of this parameter. The high coating level of EC pellets (44.4%) with a high specific surface area corresponds more obviously to the higher-coated MT2 20% (similarity factor 68) than to MT2 10% (similarity factor of 58).

**Table 8.** Difference factor and similarity factor for comparison of release from MT2 10%, MT2 20%, and EC pellets.

Parameter	Evaluation	MT2 10%/20%	MT2 10%/EC Pellets	MT2 20%/EC Pellets
Difference Factor	“similar” 0–15	64	56	23
Similarity Factor	“similar” 50–100	57	58	68

### 3.3.5. Linearization of the Release Plots for MT2 10% and MT2 20% in Comparison with EC Pellets

The similarity of the release from the MT2 20% and EC pellets is obvious when comparing the first-order kinetics CoD values of 0.92 and 0.95, respectively (Table 9). The lower-coated lot MT2 10% neither refers to zero-order kinetics nor to square root kinetics, but rather to first-order kinetics with CoD values in the range of 0.79 to 0.81. The interaction of the mini-tablet disintegration with the ethylcellulose swelling, sodium benzoate dissolution, and diffusion out of the pellets presumably leads to first-order kinetics, as in the case of EC pellets with a CoD of 0.95 (Table 9).

**Table 9.** Coefficient of determination of sodium benzoate release from MT2 10%, MT2 20%, and EC pellets with 44.4% ethylcellulose coating.

Coefficient of Determination R <sup>2</sup>	MT2 10%	MT2 20%	EC Pellets
Zero-Order	0.47	0.73	0.90
Square Root	0.75	0.85	0.88
Sigma Minus Plot (First-Order)	0.79	0.92	0.95
RRSB (First-Order)	0.81	0.92	0.95

#### 4. Conclusions

Drug- and polymer-coated pellets may be compressed into mini-tablets as well as into normal tablets. Pellets and mini-tablets compressed into tablets as a multiparticulate drug delivery system offer the advantage of being widely spread in the small intestine for improved drug absorption and increased bioavailability compared to normal tablets. With both tablet types (normal and mini), the sodium benzoate release is delayed depending on the thickness and properties of the ethylcellulose film on the pellets.

Ethylcellulose-coated mini-tablets obtained through the direct compression of sodium benzoate and excipients are an alternative method for multiparticulate drug delivery system preparation. The product is characterized by a slow release rate depending on the ethylcellulose film thickness that may be suitable when prolonged release is required. The variation in release is increased compared to pellets and normal multiple-unit tablets with pellets. Sodium benzoate layering on pellets in the fluidized bed and the subsequent tableting process are feasible for both mini-tablets and normal tablets, representing an interesting option when a variation in the final pharmaceutical form is required for marketing/patenting reasons.

**Author Contributions:** Conceptualization, F.P., B.W. and C.F.; methodology, F.P. and C.F.; software, F.P.; validation, B.W. and C.F.; formal analysis, F.P.; investigation, F.P., D.W. and G.M.; resources, F.P.; data curation, F.P.; writing—original draft preparation, F.P.; writing—review and editing, B.W.; visualization, F.P.; supervision, C.F.; project administration, F.P.; funding acquisition, F.P. All authors have read and agreed to the published version of the manuscript.

**Funding:** This research was funded by The German Research Foundation (Deutsche Forschungsgemeinschaft DFG)—project number 491460386, and the Open Access Publishing Fund of Anhalt University of Applied Sciences.

**Institutional Review Board Statement:** Not applicable.

**Informed Consent Statement:** Not applicable.

**Data Availability Statement:** All relevant data are available in the article.

**Conflicts of Interest:** The authors declare no conflict of interest.

#### Abbreviations

MT1	mini-tablets compressed from coated pellets and excipients
MT2	10%, 20% <i>w/w</i> mini-tablets compressed from compression powder mixture of sodium benzoate and excipients and finally coated with 10% or 20% ethylcellulose
NT	normal tablets compressed from coated pellets and excipients

EC pellets	Cellets <sup>®</sup> 200 layered with sodium benzoate and finally coated with 44.4% <i>w/w</i> ethylcellulose	
RRSB	logarithmic distribution function of Rosin, Rammler, Sperling, and Bennet	
SEM	scanning electron microscopy	
UV	ultraviolet, visible	
<b>Notation</b>		
$M_0$	dose, drug content	(%)
$M_t$	released drug amount	(%)
T	moment of drug release	(min)
$k_0$	release rate constant, zero order release kinetics	(-)
$k_1$	release rate constant, first order release kinetics	(1/min)
$k_q$	release rate constant, square root release kinetics	(-)
$k_c$	release rate constant, cubic root release kinetics	(-)
A	form factor RRSB	(-)
B	scale factor RRSB	(-)
$x_{50.3}$	median of volume density distribution	( $\mu\text{m}$ )
$f_1$	difference factor	(-)
$f_2$	similarity factor	(-)

## References

- Lennartz, P.; Mielck, J.B. Minitabletting: Improving the compactability of paracetamol powder mixtures. *Int. J. Pharm.* **1998**, *173*, 75–85. [CrossRef]
- Tissen, C.; Woertz, K.; Breikreutz, J.; Kleinebudde, P. Development of mini-tablets with 1 mm and 2 mm diameter. *Int. J. Pharm.* **2011**, *416*, 164–170. [CrossRef] [PubMed]
- Hagen, E.; Sandberg Loeding, F.; Mattsson, S.; Tho, I. Use of interactive mixtures to obtain mini-tablets with high dose homogeneity for paediatric drug delivery. *J. Drug Del. Sci. Technol.* **2016**, *34*, 51–59. [CrossRef]
- Rumondor, A.C.F.; Harris, D.; Flanagan, F.; Biyyala, V.; Johnson, M.A.; Zhang, D.; Patel, S. Minitablets: Manufacturing, characterization methods, and future opportunities. *Am. Pharm. Rev.* **2016**, *19*, 5–13.
- Mitra, B.; Chang, J.; Wu, S.-J.; Wolfe, C.N.; Ternik, R.L.; Gunter, T.Z.; Victor, M.C. Feasibility of mini-tablets as a flexible drug delivery tool. *Int. J. Pharm.* **2017**, *525*, 149–159. [CrossRef]
- Czajkowska, M.; Kotlowska, H.; Madanecka, A.; Doniza, D.; Sosnowicz, A.; Sznitowska, M. Development of matrix type and coated prolonged release minitables with carbamazepine. *Int. J. Pharm.* **2016**, *511*, 1132.
- Lopes, C.M.; Sousa Lobo, J.M.; Pinto, J.F.; Costa, P. Compressed mini-tablets as a biphasic delivery system. *Int. J. Pharm.* **2006**, *323*, 93–100. [CrossRef]
- Venkateswara Rao, K.; Venkatchalam, V.V. Mucoadhesive biphasic minitables of cefuroxime axetil: Formulation development, characterization and in vivo bioavailability study. *J. Drug Del. Sci. Technol.* **2016**, *35*, 260–271.
- Sauer, A.; Schmalz, D. Modifying mini-tablet dissolution with cellulose ethers. *Pharm. Ind.* **2017**, *79*, 1556–1559.
- Aleksovski, A.; Luštrik, M.; Šibanc, R.; Dreu, R. Design and evaluation of a specific, bi-phase extended release system based on differently coated mini-tablets. *Eur. J. Pharm. Sci.* **2015**, *75*, 114–122. [CrossRef]
- Angyal, N.; Dávid, A.Z.; Ujhelyi, G.; Szabó, A.; Marosi, G.; Klebovich, I.; Antal, I. Combination of film coating and matrix forming effect of Eudragit<sup>®</sup> copolymers in controlled release minitables. *Eur. J. Pharm. Sci.* **2007**, *32*, 40. [CrossRef]
- Munday, D.L.; Fassihi, A.R. Controlled release delivery: Effect of coating composition on release characteristics of mini-tablets. *Int. J. Pharm.* **2017**, *52*, 109–114. [CrossRef]
- Hautala, J.; Heinämäki, J.; Hietala, S.; Juppo, A.M. Development of novel flavored Eudragit<sup>®</sup> E films for feline minitab coating. *J. Drug Del. Sci. Technol.* **2016**, *34*, 41–50. [CrossRef]
- Omari, D.M. Formulation and in vitro / in vivo evaluation of esomeprazole enteric coated minitables. *J. Drug Del. Sci. Technol.* **2017**, *39*, 156–165. [CrossRef]
- LaFountaine, J.S.; Kumari Prasad, L.; Miller, D.A.; McGinity, J.W.; William, R.O., III. Mucoadhesive amorphous solid dispersions for sustained release of poorly water soluble drugs. *Eur. J. Pharm. Biopharm.* **2017**, *113*, 157–167. [CrossRef]
- Ceulemans, J.; Vermeire, A.; Adriaens, E.; Remon, J.P.; Ludwig, A. Evaluation of a mucoadhesive tablet for ocular use. *J. Contr. Rel.* **2001**, *77*, 333–344. [CrossRef]
- Weyenberg, W.; Bozdog, S.; Foreman, P.; Remon, J.P.; Ludwig, A. Characterization and in vivo evaluation of ocular minitables prepared with different bioadhesive Carbopol-starch components. *Eur. J. Pharm. Biopharm.* **2006**, *62*, 202–209. [CrossRef]
- Goole, J.; Vanderbist, F.; Amighi, K. Development and evaluation of new multiple-unit levodopa sustained-release floating dosage forms. *Int. J. Pharm.* **2007**, *334*, 35–41. [CrossRef]
- Goole, J.; Deleuze, P.; Vanderbist, F.; Amighi, K. New levodopa sustained-release floating minitables coated with insoluble acrylic polymer. *Eur. J. Pharm. Biopharm.* **2008**, *68*, 310–318. [CrossRef]

20. Goole, J.; Vanderbist, F.; Amighi, K. In vitro evaluation of two concepts of sustained release floating minitables according to the model drug used. *J. Drug Del. Sci. Technol.* **2008**, *18*, 133–138. [CrossRef]
21. Van der Merwe, S.M.; Verhoef, J.C.; Kotzé, A.F.; Junginger, H.E. N-Trimethyl chitosan chloride as absorption enhancer in oral peptide drug delivery. Development and characterization of minitables and granule formulations. *Eur. J. Pharm. Biopharm.* **2004**, *57*, 85–91. [CrossRef] [PubMed]
22. Salústio, P.J.; Cabral-Marques, H.M.; Costa, P.C.; Pinto, J.F. Comparison of ibuprofen release from minitables and capsules containing ibuprofen:  $\beta$ -Cyclodextrin complex. *Eur. J. Pharm. Biopharm.* **2011**, *78*, 58–66. [CrossRef] [PubMed]
23. Eckert, C.; Pein, M.; Breitreutz, J. Lean production of taste improved lipidic sodium benzoate formulations. *Eur. J. Pharm. Biopharm.* **2014**, *88*, 455–461. [CrossRef] [PubMed]
24. Pinto, J.T.; Brachkova, M.I.; Fernandes, A.I.; Pinto, J.F. Evaluation of the ability of powdered milk to produce minitables containing paracetamol for paediatric population. *Chem. Eng. Res. Des.* **2016**, *110*, 171–182. [CrossRef]
25. Albanez, R.; Nitz, M.; Pereira Taranto, O. Influence of the type of enteric coating suspension, coating layer and process conditions on dissolution profile and stability of coated pellets of diclofenac sodium. *Powder Technol.* **2015**, *269*, 185–192. [CrossRef]
26. Bouffard, J.; Dumont, H.; Bertrand, F.; Legros, R. Optimization and scale-up of a fluid bed tangential spray rotogranulation process. *Int. J. Pharm.* **2007**, *335*, 54–62. [CrossRef]
27. Kovacevic, J.; Mladenovic, A.; Djuris, J.; Ibric, S. Evaluation of powder, solution and suspension layering for the preparation of enteric coated pellets. *Eur. J. Pharm. Sci.* **2016**, *85*, 84–93. [CrossRef]
28. Kuang, C.; Sun, Y.; Li, B.; Fan, R.; Zhang, J.; Yao, Y.; He, Z. Preparation and evaluation of duloxetine hydrochloride enteric-coated pellets with different enteric polymers. *Asian J. Pharm. Sci.* **2017**, *12*, 216–226. [CrossRef]
29. Yang, M.; Xie, S.; Li, Q.; Wang, Y.; Chang, X.; Shan, L.; Sun, L.; Huang, X.; Gao, C. Effects of polyvinylpyrrolidone both as binder and pore-former on the release of sparingly water-soluble topiramate from ethylcellulose coated pellets. *Int. J. Pharm.* **2014**, *465*, 187–196. [CrossRef]
30. Marucci, M.; Andersson, H.; Hjærtstam, J.; Stevenson, G.; Baderstedt, J.; Stading, M.; Larsson, A.; von Corswandt, C. New insight on how to adjust the release profile from coated pellets by varying the molecular weight of ethyl cellulose in coating films. *Int. J. Pharm.* **2013**, *458*, 218–223. [CrossRef]
31. Xu, M.; Heng, P.W.S.; Liew, C.V. Formulation and process strategies to minimize coat damage for compaction of coated pellets in a rotary tablet press: A mechanistic view. *Int. J. Pharm.* **2016**, *499*, 29–37. [CrossRef] [PubMed]
32. Kazlauske, J.; Cafaro, M.M.; Caccavo, D.; Marucci, M.; Lamberti, G.; Barba, A.A.; Larsson, A. Determination of the release mechanism of theophylline from pellets coated with Surelease<sup>®</sup>—A water dispersion of ethyl cellulose. *Int. J. Pharm.* **2017**, *528*, 345–353. [CrossRef] [PubMed]
33. Villar López, E.; Luzardo Alvarez, A.; Méndez, J.B.; Otero Espinar, F.J. Cellulose-polysaccharide film-coating of cyclodextrin based pellets for controlled drug release. *J. Drug Del. Sci. Technol.* **2017**, *42*, 273–283. [CrossRef]
34. Prieze, F.; Frisch, T.; Wolf, B. Comparison of film-coated retarded release pellets manufactured by layering technique or by bed rotor pelletization. *Pharm. Dev. Technol.* **2015**, *20*, 417–425. [CrossRef] [PubMed]
35. Prieze, F.; Wolf, B. Development of high drug loaded pellets by Design of Experiment and population balance model calculation. *Powder Technol.* **2013**, *241*, 149–157. [CrossRef]
36. Antal, I.; Kállai, N.; Angyal, N.; Balogh, E.; Dredán, J.; Dévay, A.; Klebovich, I. Development of modified release multiple unit dosage forms. *Eur. J. Pharm. Sci.* **2017**, *32*, S10. [CrossRef]
37. Gaber, D.M.; Nafee, N.; Abdallah, O.Y. Mini-tablets versus pellets as promising multiparticulate modified release delivery systems for highly soluble drugs. *Int. J. Pharm.* **2015**, *488*, 86–94. [CrossRef]
38. Czajkowska, M.; Sznitowska, M.; Kleinebudde, P. Determination of coating thickness of minitables and pellets by dynamic image analysis. *Int. J. Pharm.* **2015**, *495*, 347–353. [CrossRef]
39. Ganguly, S.; Das, P.; Margel, S. Containers for drug delivery. In *Micro-and Nano-Containers for Smart Applications*; Springer Nature: Singapore, 2022; pp. 127–153.
40. Patel, D.K.; Patil, T.V.; Ganguly, K.; Dutta, S.D.; Luthifikasari, R.; Lim, K.T. Polymer Nanohybrid-Based Smart Platforms for Controlled Delivery and Wound Management. In *Nanorobotics and Nanodiagnostics in Integrative Biology and Biomedicine*; Springer International Publishing: Cham, Switzerland, 2022; pp. 171–199.
41. Pereira de Almeida, L.; Simões, S.; Brito, P.; Portugal, A.; Figueiredo, M. Modeling dissolution of sparingly soluble multisized powders. *J. Pharm. Sci.* **1997**, *86*, 726–732. [CrossRef]
42. Javadzadeh, Y.; Monajjemzadeh, F.; Safaei, E.; Adibkia, K. Release kinetics of sodium diclofenac from controlled release device. *Pharm. Ind.* **2016**, *76*, 1786–1793.
43. Cascone, S. Modeling and comparison of release profiles: Effect of the dissolution method. *Eur. J. Pharm. Sci.* **2017**, *106*, 352–361. [CrossRef] [PubMed]
44. Krueger, C.; Thommes, M.; Kleinebudde, P. Influence of storage conditions on properties of MCC II-based pellets with theophylline-monohydrate. *Eur. J. Pharm. Biopharm.* **2014**, *88*, 483–491. [CrossRef] [PubMed]

**Disclaimer/Publisher’s Note:** The statements, opinions and data contained in all publications are solely those of the individual author(s) and contributor(s) and not of MDPI and/or the editor(s). MDPI and/or the editor(s) disclaim responsibility for any injury to people or property resulting from any ideas, methods, instructions or products referred to in the content.

Article

# In Vitro Investigation of Corrosion Control of Magnesium with Degradable Polycaprolactone Coatings for Cardiovascular Grafts

Sara Knigge <sup>1,\*</sup>, Marc Mueller <sup>2</sup>, Lara Fricke <sup>2</sup>, Tobias Schilling <sup>1</sup> and Birgit Glasmacher <sup>2</sup>

<sup>1</sup> Department of Cardiothoracic, Transplantation, and Vascular Surgery, Hannover Medical School, 30625 Hannover, Germany

<sup>2</sup> Institute for Multiphase Processes, Leibniz University Hannover, 30823 Garbsen, Germany

\* Correspondence: knigge.sara@mh-hannover.de

**Abstract:** Magnesium is a promising metal for resorbable cardiovascular implants due to its high biocompatibility, high corrosion tendency, and mechanical properties. However, adapting its corrosion rate to the physiological healing processes is required to ascertain a safe graft function. A protective polymeric layer is supposed to slow down the corrosion rate of magnesium. Additionally, coatings can improve the host's tissue interaction with the implant by implementing the local delivery of antibiotic drugs and growth or cell adhesion factors. However, little is known about the interaction of polymer-based coatings, their degradation, and magnesium corrosion. This study examines the corrosion mechanism of magnesium protected by spin coatings and electrospun fiber coatings under physiological conditions. Pure magnesium specimens were coated with polycaprolactone (PCL). The corrosion of the coated magnesium was evaluated using an immersion test in simulated body fluid. Spin coatings provided efficient protection against corrosive attacks and a significantly lower corrosion rate by 75% compared to uncoated magnesium. In contrast, fiber coatings did not provide relevant corrosion protection. On the other hand, magnesium corrosion caused the accelerated degradation of the PCL layer. A reliable and safe implant function is vital, especially in cardiovascular applications. Magnesium coating, therefore, should be carried out with spin coatings.

**Keywords:** magnesium degradation; polymeric coating; in vitro testing; degradable implants; electrospinning

## 1. Introduction

Magnesium serves as an ideal metallic substrate for different cardiovascular grafts. For instance, a well-known application is temporarily stenting stenosed coronary arteries [1–3]. In addition, patients with severe congestive heart failure can also benefit from novel magnesium grafts. Schilling et al. inaugurated the mechanical stabilization of delicate biological patch materials with degradable magnesium scaffolds [4–6] for patients with terminal heart failure requiring cardiac transplantation, left ventricular assist device (LVAD) implantation, or surgical reconstruction of the dysfunctional myocardium [7]. The known lack of donor organs and the significantly impaired quality of life after LVAD implantation still limit those therapies today. Thus, reconstructing the dysfunctional myocardium with regenerative biological grafts with the potential for in vivo physiological remodeling is a promising therapeutic approach. Unfortunately, biological grafts, such as small bowel or stomach tissue, display insufficient mechanical stability prior to physiological remodeling. Thus, those grafts have only been used in the low-pressure system of the heart to reconstruct atrial or right ventricular defects [8]. The high blood pressure in the left ventricle would cause life-threatening aneurysms or the rupture of biological grafts. The temporary mechanical stabilization of those grafts with degradable magnesium scaffolds could facilitate their application (see Figure 1). A controlled degradation rate of the magnesium scaffolds is mandatory to ensure a stabilization function that prevents catastrophic failure of the

initially delicate biological prosthesis until physiological remodeling leads to increased mechanical stability.

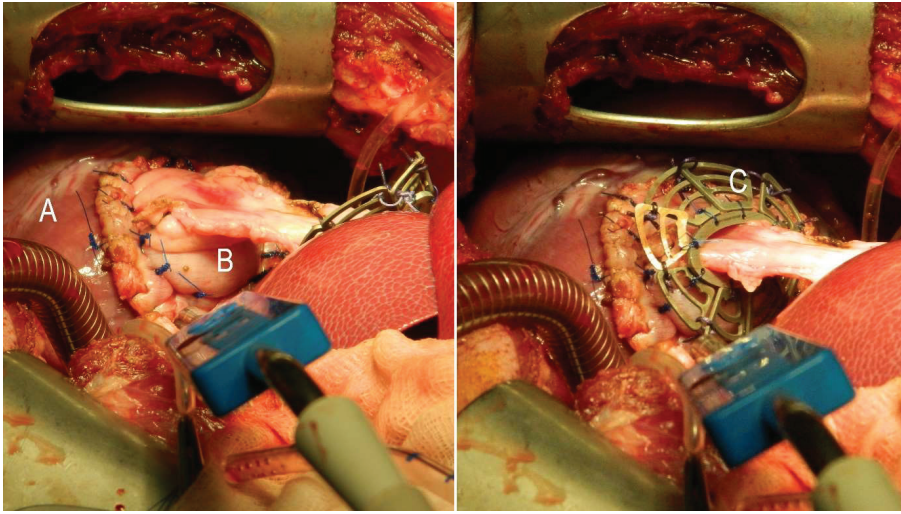


**Figure 1.** Operative situs. Autologous transplantation of a vascularized stomach segment (B) to reconstruct a complete wall defect of the left ventricle (A) in a porcine model. Stabilization of the delicate stomach tissue with a degradable magnesium alloy scaffold (C).

The discrepancy between the corrosion rate of magnesium implants and the physiological remodeling rate of biological grafts limits the widespread combination of these materials. The basic mechanism of Mg corrosion is the reaction of the metallic surface with water (Equation (1)) to form hydrogen, magnesium ions, and hydroxide ions. These ions form an oxide, which stabilizes at high pH values (Equation (2)):



In phosphate-containing (simulated) body fluids,  $\text{Mg}(\text{OH})_2$  transforms into a porous hydroxyapatite (HA)-like oxide layer, which covers the surface and serves as a protective layer for the graft [9]. Coatings are an effective way of controlling these corrosion reactions and adapting the corrosion rate to tissue regeneration.

Most frequently, ceramic coatings, such as hydroxyapatite (HA) [10,11] or silicates [12], have been investigated to improve the corrosion performance of magnesium. A few studies assessed alternative approaches based on polymer coatings [13,14]. In addition to controlling the corrosion reaction, these polymeric coatings offer further possibilities to improve implant performance. Drug delivery systems [14] or improving tissue ingrowth into the implant make polymeric coatings appealing for implant development [15,16].

The electrospinning of fibrous coatings is highly adjustable to those individual requirements [17–22]. Two alternatives to create dense polymeric coatings are dip and spin coatings. These methods produce a homogenous, non-porous, and dense layer on the bulk material [14,15], whereas the air-spraying [15] and electrospinning [13] of polymers form a fibrous coating. PCL and polylactic acid (PLA) are researched biomaterials for magnesium coating, which are approved for biomedical use by the FDA (Food and Drug Administration). There is evidence that dense and fibrous/porous polymeric coatings decrease the corrosion rate of magnesium. Xu et al. [16] and Wong et al. [15] showed that PCL coatings on magnesium improve cell attachment and tissue growth around the implant material, which is explained by the decreased magnesium corrosion rates.

Currently, polymer coating is often viewed only from the magnesium's perspective: how is the corrosion kinetic affected by its coating? The influences of the magnesium corrosion process or products on the coating are rarely considered. Questions such as how

long does the coating layer stay intact and how does the degradation change under the harsh conditions of magnesium corrosion (high local pH values and increased metal ion concentration) remain unanswered. The interaction of magnesium corrosion and polymer degradation has only been considered by Chen et al. [14], who reported that magnesium corrosion damaged PLA coatings. They hypothesize that the hydrolysis of the water-permeable PLA coating leads to a decreased pH value, which causes a dissolution of the  $Mg(OH)_2$  corrosion layer underneath the coating. This process results in the collapse of the coating and accelerated corrosion of the magnesium [14].

A detailed understanding of the mutual interactions of polymeric coatings, the degradation of the polymer layer, and magnesium corrosion could yield protocols for developing polymer-metallic implants with highly controllable degradation and corrosion rates. Reliable implants would suit various applications in cardiovascular surgery, such as bioresorbable stents or temporarily stabilizing scaffolds for biological grafts.

## 2. Materials and Methods

In this study, we aim to extend the picture of the influence of magnesium corrosion on polymer degradation. Therefore, we examine the unique characteristics of PCL fiber coating degradation compared to dense, homogenous PCL coatings. The materials were exposed to locally increased pH values caused by magnesium corrosion [14]. The pH value was adjusted to pH 13 assuming that near the magnesium surface the hydroxide ion concentration would be very high. For our experiments, we used high-purity magnesium to eliminate the influence of alloying elements on polymer degradation. Two kinds of experiments were performed. The magnesium corrosion behavior with two different coatings (PCL fiber and PCL spin coating) was studied in a corrosion experiment for 100 h. The behavior of the polymeric fiber material in a harsh environment was studied using immersion tests under high pH values for two weeks. Both experiments were carried out at body temperature (37 °C). This setup took account of the fact that magnesium corrosion proceeds much faster than polymer degradation.

### 2.1. Sample Preparation for the Mg Corrosion Experiment

For all experiments, cylindrical samples of high-purity magnesium (99.94% pure, Magnesium Elektron UK, Manchester, UK) with a diameter of 8 mm and a height of 2 mm were used. Before coating, the specimens were polished with 1000 grit and cleaned with 70% (*w/v*) ethanol to reduce the number of particles on the surface. The polymer coating solution and the solution for electrospun fiber mats consisted of 5% (*w/v*) PCL (molecular weight: 80,000, Sigma-Aldrich Chemistry Corporate, St. Louis, MS, USA) in 2,2,2-trifluoroethanol (TFE, 99.8%, abcr GmbH, Karlsruhe, Germany) in accordance with Degner et al. (2013) [23].

### 2.2. Polymeric Coating for the Mg Corrosion Experiment

The PCL spin coating was carried out using a spin-coating device (Rotationswerkzeug GRO 12V-35, Bosch, Gerlingen-Schillerhöhe, Germany) that allows a rotational speed of 5000 rpm. This value was evaluated by Xu et al. (2012), who investigated the spinning parameter for a polymeric spin coating on 8 mm cylindrical magnesium plates [16]. The PCL spin-coated specimens (denoted as MgSc) were made by dipping the magnesium specimens into the polymer solution. Subsequently, the rotation leads to spreading the polymer solution onto the specimens' surfaces. During this process time (30 s), the solvent successively evaporates. The specimens with an electrospun fiber coating (denoted as MgFc) were obtained using an electrospinning device with the same polymeric solution as used for spin coating. The polymeric solution was pumped with 3ml/h through a needle connected to a high voltage (HV) source (15 kV). The Mg specimens were connected to the HV source with a copper wire on the opposite side. The distance between the specimen and the needle tip was 15 cm; the electrospinning took 30 min.

### 2.3. Characterization of the Coating

The mass of the coating was determined by weighing the sample before and after the coating procedure. A cross-cut test characterized the adhesion of the coatings by cutting a right-angle pattern into the coating and classifying the coating appearance. The thickness of the electrospun and spin coatings was determined via scanning electron microscopy (SEM) (S-3400N, Hitachi High-Tech Analytical Science Ltd., Tubney Woods, Abington, UK) using detached coatings. For this purpose, the coatings could be removed. The detached coatings were frozen in paraffin wax (Tissue-Tek, Sakura Finetek Europe BV, Alphen aan den Rijn, The Netherlands) and cut with a cryotom (Tissue-Tek Cryo3, Sakura Finetek Europe BV, Alphen aan den Rijn, The Netherlands). The thickness was measured via SEM in the cross section. The fiber diameters were measured from SEM pictures using the software ImageJ<sup>®</sup> before and after the experiment. All fiber measurements were conducted after a drying period of 15 days. To analyze the influence of magnesium corrosion on the coating performance, the coatings were examined using SEM and light microscopy. Raman spectroscopy (Alpha 300 RA, WITec Wissenschaftliche Instrumente und Technologie GmbH, Ulm, Germany) was conducted to observe changes in the molecular structure of the PCL coatings. The wavelength of the Raman laser was 532 nm. The spectra were received using a CCD detector, with an integration time of 1 s and an accumulation of 100.

### 2.4. Magnesium Corrosion Experiment

The magnesium corrosion behavior was measured using an immersion test described by Knigge et al. [24]. The test setup (Figure 2) consists of a corrosion vessel connected to a coupled in- and outflow and a hydrogen measuring unit. The measuring unit consists of a measuring pipe (1ml, BRAND GMBH + CO KG, Wertheim, Germany) connected to the reaction vessel and a glass cylinder (1l, BRAND GMBH + CO KG, Wertheim, Germany) filled with vegetable oil. A continuous flow rate of the testing fluid (1 mL/h) provides constant experimental conditions by exchanging the immersion fluid continuously to avoid the accumulation of hydroxide ions. The syringes hold a volume of 24 mL, so they have to be refilled (inflow) or emptied (outflow) after 24 h. In this step, the pH value of the test fluid was measured in outflow to ensure that the experiment had taken place at a physiological pH value (pH 7.4–7.5).

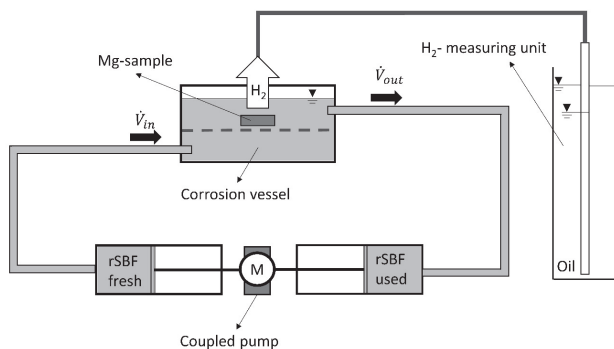


**Figure 2.** Experimental setup for measuring magnesium corrosion. The sample was placed in the corrosion vessel perfused with a continuous fluid flow. A coupled pump provided the fluid flow, transporting equal volumes of fluid in and out. The amount of hydrogen is determined using the H<sub>2</sub> measuring unit. The level difference between the outer glass cylinder filled with oil and the inner glass pipette filled with the H<sub>2</sub> gas was documented.

The magnesium mass loss was calculated from the collected hydrogen using the ideal gas equation (Equation (3)):

$$n_H = \frac{RT}{pV} \quad (3)$$

The pressure  $p$  was documented using a barometer (Feingerätebau K. Fischer GmbH, Drebach, Germany). The temperature was controlled using a thermal oven (Mettmert

GmbH + Co. KG, Schwabach, Germany) at 37 °C.  $R$  is the ideal gas constant,  $V$  is the measured volume of hydrogen, and  $n_H$  is the amount of emitted hydrogen in mol. The mass loss of magnesium can be calculated from the amount of hydrogen using Equation (1), which says that 1 mol of magnesium causes 1 mol of hydrogen. The mass loss of magnesium  $\Delta m$  can be calculated using Equation (4):

$$\Delta m_{Mg} = n_H \times 24,305 \text{ g/mol} \tag{4}$$

All experiments were conducted at 37 °C and in revised simulated body fluid (rSBF), in accordance with Oyane et al. [25], to simulate a physiological environment (Table 1). The syringes hold a test fluid volume of 24 mL, resulting in the replacement of the syringes after 24 h. A storage-related pH change in the rSBF (in accordance with Oyane et al. (2003) [25]) could thus be prevented.

**Table 1.** Composition of the fluids used for the magnesium corrosion and polymer degradation experiments.

Ion	Concentration in mM			
	rSBF	mSBF	0.1 M NaOH	H <sub>2</sub> O Dest.
Na <sup>+</sup>	142.0	142.0	100	-
K <sup>+</sup>	5.0	5.0	-	-
Mg <sup>2+</sup>	1.5	1.5	-	-
Ca <sup>2+</sup>	2.5	2.5	-	-
Cl <sup>-</sup>	103.0	103.0	-	-
HCO <sub>2</sub> <sup>-</sup>	27.0	10.0	-	-
HPO <sub>4</sub> <sup>2-</sup>	1.0	1.0	-	-
SO <sub>4</sub> <sup>2-</sup>	0.5	0.5	-	-
pH	7.4	7.4	13	7

The following Equation (5) can define the instantaneous corrosion rate (CR):

$$CR = \frac{\Delta m}{A(t)\Delta t} \tag{5}$$

$\Delta m$  represents the mass loss in mg,  $A(t)$  the corroding surface area in mm<sup>2</sup> at the time  $t$ , and  $\Delta t$  the immersion time in h. Usually,  $A(t)$  is equal to the initial surface area. As  $A(t)$  is estimated as a constant, the corrosion rates were determined from the  $\Delta m/\Delta t$ -curve. First, the initial phase in the mass loss curve was identified, characterized by an intense mass loss at the beginning of the immersion. The initial phase was followed by the linear phase, corresponding to a constant corrosion rate. The corrosion rate can be calculated from the interception value of the linear curve, as suggested by Nidadavolu et al. (2016) [26]. Figure 3 shows an exemplary procedure for calculating the corrosion rate.

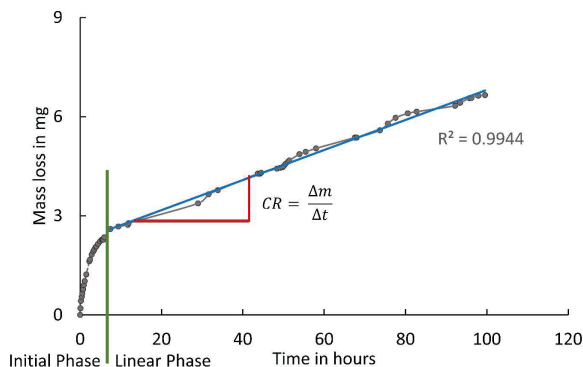


**Figure 3.** An exemplary procedure for calculating the corrosion rate according to Nidadavolu et al. [26]. The linear phase of the curve is identified (start of the linear phase at the green line). The linear part of the curve is approximated with a linear regression (blue). The interception value/corrosion rate can be extracted.

The immersion time for the coated samples (MgSc and MgFc) was limited to nine days to minimize the influence of the changing surface  $A(t)$ . The uncoated control (MgUc) was immersed for four days because pure magnesium corrodes very fast.

### 2.5. PCL Fiber Degradation

It is impossible to measure the magnesium corrosion and fiber degradation in one experiment because the mass loss is connected to both processes. In order to gain a more precise understanding of the degradation mechanism of the PCL fibers in contact with magnesium, an immersion experiment was carried out with fiber mats (denoted as efPCL). The efPCL specimens were cut into squares of 4 cm<sup>2</sup>, and the mass was measured using a microscale (Cubis, Sartorius AG, Göttingen, Germany). The mats were soaked in 70% (*w/v*) ethanol for several minutes to clean them and increase their wettability. Afterward, the mats were either immersed into 3 mL modified simulated body fluid (mSBF), or 3 mL NaOH solution with an adjusted pH value of 13, or 3 mL distilled water (control) (Table 1). The surface-to-test-fluid-volume ratio of 2 cm<sup>2</sup>/mL was adjusted to recommended values according to the DIN 10993-13 guideline [27]. The fiber mats are very sensitive and prone to damage if the test fluid is changed frequently. Therefore, the number of fluid exchanges had to be reduced by choosing a stable SBF. The mSBF was used to determine the influence of electrolytic components on PCL degradation. The hydrogen carbonate content of mSBF is lower than in rSBF (see Table 1). mSBF is suitable for long-term experiments without changing its pH value and without precipitating, according to Oyane et al. [25]. NaOH solution simulates the high pH value in proximity to the corroding magnesium surface. PCL degrades slower than magnesium. The PCL degradation experiment took place at 37 °C. For this reason, a longer immersion time is necessary to detect PCL degradation [28]. After two weeks of immersion, the samples were taken out and dried in a vacuum desiccator (Duran Borosilicate Glass 3.3 Complete Vacuum Desiccator, Fisher Scientific, Leicestershire, UK) for 12 h. The mass loss was measured using a microscale. After the experiment, the immersion fluid pH value was measured using a pH meter (SevenMulti pH Meter, Mettler Toledo, Columbus, OH, USA). Table 2 provides an overview of the experimental setup and surface characterization.

**Table 2.** Overview of experimental setups and analysis (MgUc: uncoated magnesium, MgSc: spin-coated magnesium, MgFc: electrospun fiber-coated magnesium, efPCL: electrospun fiber mats).

Experiment Sample	Magnesium Corrosion			Electrospun Fiber Degradation efPCL		
	MgUc	MgSc	MgFc			
Test fluid		rSBF		mSBF	in 0.1M NaOH (pH 13)	H <sub>2</sub> O dist.
Determination of mass loss		H <sub>2</sub> -measuring			Mass loss	
Coating characterization	-	Adhesion test			-	
Coating/fiber morphology	-	SEM			SEM	
Surface characterization		Optical			-	
Molecular structure of fiber/ coating	-	Raman spectroscopy			Raman spectroscopy and DSC	

### 2.6. Characterization of the Fiber Mats

Dynamic differential calorimetry (DSC) was carried out (DSC 204 F1 Phoenix, Netzsch-Gerätebau GmbH, Selb, Germany) to measure the change in crystallinity due to the degradation processes. First, 5–12 mg of the sample material was placed into an aluminum pan with a pierced lid. In accordance with Fricke et al. [29], each sample was scanned twice in a temperature range of 50 °C below the glass transition temperature and 50 °C above the melting temperature. The measurements were taken at a constant heating rate of 10 K/min and a nitrogen flow of 20 mL/min. The efPCL samples were measured from 110 to 110 °C. The temperature curves were evaluated using the software Proteus Analysis by Netzsch. In addition to DSC, Raman spectroscopy was used to visualize changes in the chemical

structure of PCL. The Raman spectroscopy was performed in the same way as described in Section 2.2. In addition, SEM images were taken to investigate the fiber morphology before and after the experiment. The fibers were examined after a drying period of 15 days.

### 2.7. Statistical Analysis

The immersion tests, the corrosion of coated and uncoated magnesium, as well as the degradation of the fibers under different conditions were carried out using four samples in independent experiments. All data, hydrogen volume, and mass loss were statistically analyzed. Error bars show 95% confidence intervals (CI). Normality distribution checks were performed using the D'Agostino and Pearson omnibus tests. The Student's *t*-test was used to compute the level of significance. Statistical significance levels are expressed as "ns"—not significant, \*  $p < 0.05$ , \*\*  $p < 0.01$ , \*\*\*  $p < 0.001$ , and \*\*\*\*  $p < 0.0001$ . The fiber diameter of the electrospun coating and mats and the thickness of the coatings were expressed as means  $\pm$  standard deviation (SD).

## 3. Results

### 3.1. Characterization of the Coating

The coating of MgSc had a thickness of  $38 \pm 5 \mu\text{m}$  ( $n = 16$ ). The mass of the coating was  $8 \pm 2 \text{ mg}$  ( $n = 4$ ). The cross-cut test for evaluating the adhesion ability shows B1 classification, which refers to a very weak adhesion. The thickness of the fiber coating on the MgFc was approximately  $40 \mu\text{m}$ . The cross-cut test revealed classification B0, referring to no adhesion. The dry electrospun fiber coating mass on each specimen was  $16 \pm 3 \text{ mg}$  for all samples. The mean fiber diameter was  $2 \mu\text{m}$ . The appearance of the uncoated, spin-coated, and electrospun-coated magnesium is depicted in Figure 4. The transparent spin coating covers the magnesium specimen homogeneously (Figure 4c). In contrast, the electrospun coating shows curling at the edges of the sample (Figure 4e).

### 3.2. Magnesium Corrosion Experiment

The corrosion of MgSc and MgFc strongly decreased the initial corrosion rate compared to the uncoated control (Figure 5a,b). The mass loss during the initial phase is reduced by 70% in the MgSc group and 88% in the MgFc group. After the initial phase, all mass loss curves change into a linear curve. No sudden changes in curve characteristics can be observed. The regression ( $0.9824 \leq R^2 \leq 0.9944$ ) indicates linearity for the entire observation period of nine days. Figure 5c shows the normalized mass loss rates (Equation (4)) obtained from the linear part of the curves in Figure 5. The mass loss rate of MgSc ( $0.00095 \text{ mg/h cm}^2$  ( $0.047 \text{ mm/y}$ )) is four times lower than the uncoated control ( $0.0038 \text{ mg/h cm}^2$  ( $0.19 \text{ mm/y}$ )) which results from strongly inhibited corrosion in the MgSc group. No corrosion rate can be given for MgFc because a gas bubble formed under the coating during corrosion (Figure 5b). The bubble blocked the fluid contact. Subsequently, extended and nonquantifiable areas of the sample were protected from corrosion. Therefore, no normalized mass loss rate for the fiber coating can be depicted.

There are clear differences between the coated samples and control group, as shown using light microscopy (Figure 4a–d). The uncoated control has an oxide layer covering the entire surface (Figure 4b). In contrast, the MgSc samples show uncorroded surface areas (Figure 4d). In some areas, however, the coating is delaminated and has exposed large parts of the magnesium sample to the rSBF. In these exposed areas, an oxide layer has formed similar to the oxide layer of the uncoated control (Figure 4f). The fiber coating was removed after immersion for a better view of the magnesium surface. The MgFc samples show corroded and uncorroded areas similar to the MgSc samples. The corroded areas are mainly located at the edges of the samples, whereas the central areas remain uncorroded. The PCL fibers on magnesium before the corrosion experiment have a smooth, regular morphology (Figure 6a) with an average fiber diameter of  $2.1 \pm 0.3 \mu\text{m}$  ( $n = 50$ ). After the immersion test of nine days (Figure 6b), the fibers appeared cracked, and some precipitation occurred. The fiber diameter increased up to  $2.7 \pm 0.5 \mu\text{m}$  ( $n = 50$ ). A similar picture of damage emerged

with the spin coating on magnesium. Before the immersion test (Figure 4c), the coating presents a dense morphology. After the immersion, the coating became brittle, and some areas showed holes and delamination (Figure 4d).

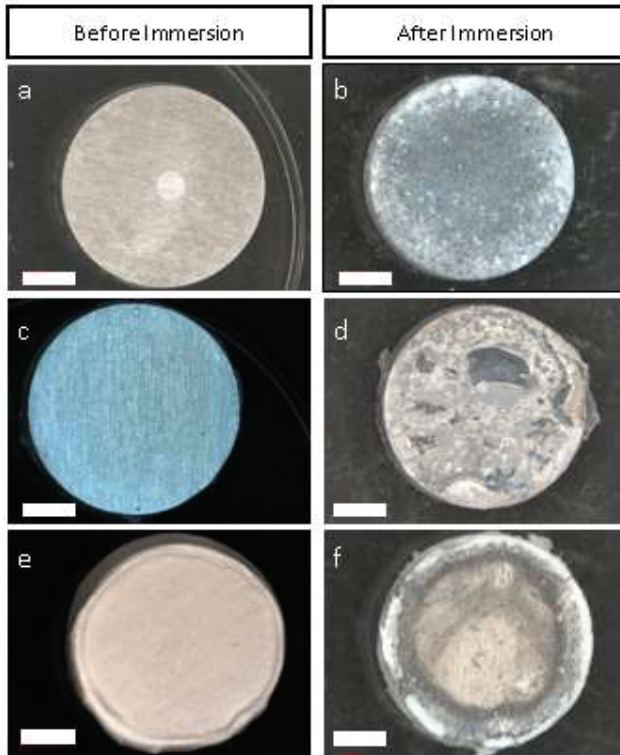


**Figure 4.** Light microscopy pictures of the surface of the samples before and after immersion in rSBF: (a) uncoated (MgUc) before immersion; (b) uncoated (MgUc) after immersion; (c) spin-coated magnesium (MgSc) before immersion; (d) spin-coated magnesium (MgSc) after immersion; (e) surface appearance of electrospun fiber-coated magnesium (MgFc) before immersion; (f) and after immersion (removed fiber coating) (white scale bar = 2 mm).

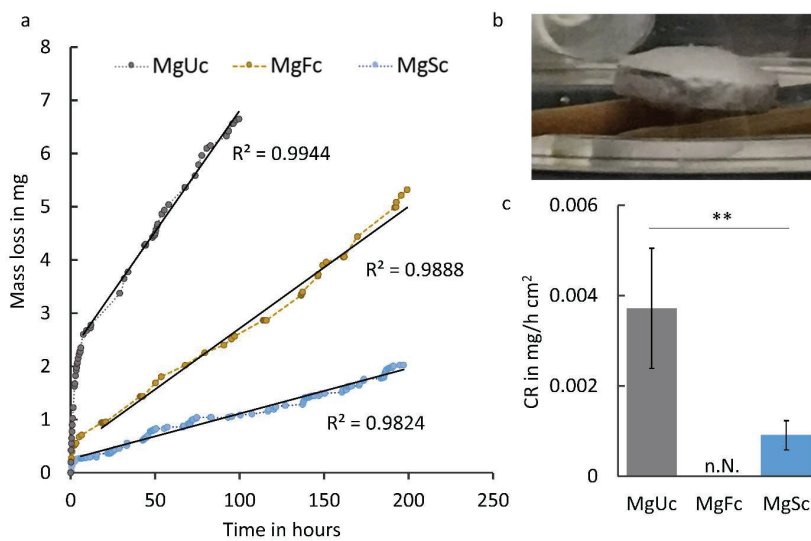


**Figure 5.** Corrosion behavior of uncoated (MgUc), spin-coated (MgSc), and electrospun fiber-coated magnesium (MgFc): (a) representative mass loss curves with linear regression (black lines) after the initial phase; (b) bubble formation underneath the fiber coating during corrosion; (c) normalized corrosion rate calculated from the linear regression (n.N.—not named) (\*\*  $p < 0.01$ ) ( $n = 4$ ).

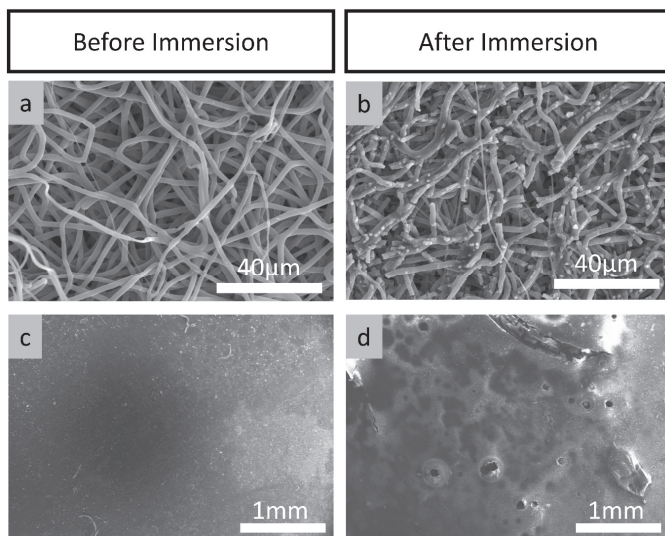


**Figure 6.** SEM pictures of the coatings before and after immersion in rSBF for nine days: (a) electro-spun fiber coating (MgFc) before; (b) and after immersion; (c) spin coating (MgSc) before; (d) and after immersion.

The SEM in Figure 6a–d shows that the PCL fibers on magnesium before the corrosion experiment have a smooth, regular morphology (Figure 6a) with an average fiber diameter of  $2.1 \pm 0.3 \mu\text{m}$  ( $n = 50$ ). After the immersion test of nine days (Figure 6b), the fibers appeared cracked, and some precipitation occurred. The fiber diameter increased to  $2.7 \pm 0.5 \mu\text{m}$  ( $n = 50$ ). A similar picture of damage emerged with the spin coating on magnesium. Before the immersion test (Figure 6c), the coating presents a dense morphology. After the immersion, the coating became brittle, and some areas showed holes and delamination (Figure 6d).

The Raman spectra show the typical peaks for PCL (Figure 7). The peaks at  $1725 \text{ cm}^{-1}$  ( $\nu\text{C=O}$ ) and  $1110 \text{ cm}^{-1}$  ( $\nu\text{COC}$ , skeletal stretching) characterize the crystalline phase of PCL. Despite the heavy damage (Figure 6b,d), no change in chemical structure can be detected using Raman spectroscopy. There is no change in the spectra after immersion. The more substantial noise of the spectra of the fiber coatings compared to the spin coating may be due to the fibers' cylindrical geometry, resulting in focus inaccuracies. The sharp peak at  $1725 \text{ cm}^{-1}$  indicates PCL's predominantly crystalline molecular structure. The presence of a broad peak at  $1735 \text{ cm}^{-1}$  would designate the amorphous phase of PCL [30].

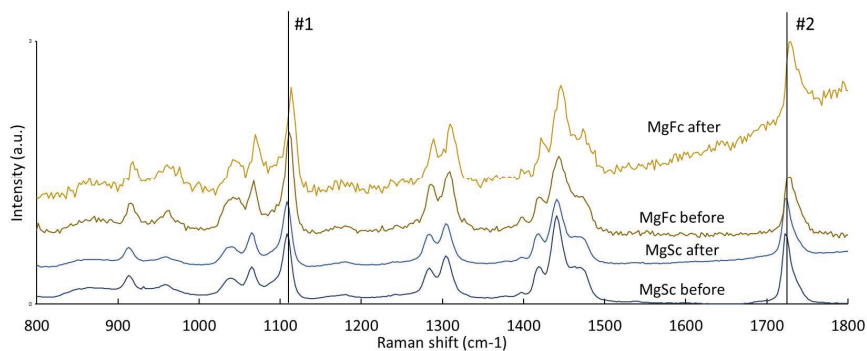


**Figure 7.** Raman spectra of the polymeric coatings on magnesium before and after immersion in rSBF for 9 days. Peaks for PCL are the C-COO stretch at  $913 \text{ cm}^{-1}$  and  $958 \text{ cm}^{-1}$ ; the C-C stretch at  $1034 \text{ cm}^{-1}$ ,  $1064 \text{ cm}^{-1}$ , and  $1110 \text{ cm}^{-1}$ ; the  $\text{CH}_2$ -twist at  $1284 \text{ cm}^{-1}$  and  $1304 \text{ cm}^{-1}$ ; and the  $\text{CH}_2$ -bend at  $1418 \text{ cm}^{-1}$  and  $1441 \text{ cm}^{-1}$ . Peaks in the spectra that indicate the crystallinity of the PCL are marked by #1 ( $1110 \text{ cm}^{-1}$ ) and the C=O stretch at  $1725 \text{ cm}^{-1}$  (#2).

### 3.3. Fiber Degradation Experiment

The fiber mats show no mass loss in the mSBF solution and dist. water (Figure 8). However, two weeks of immersion in the NaOH solution (pH 13) caused a mass loss of up to 7 wt.%. The pH value of the solutions (see Table 1) were constant during the experimental time.

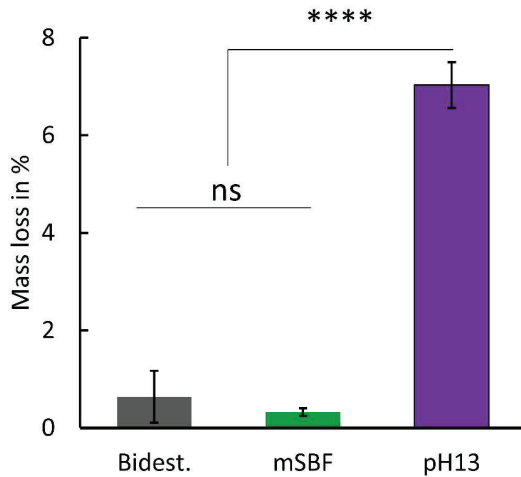


**Figure 8.** Mass loss of the PCL fibers after immersion in dist. water, mSBF, and NaOH solution (pH 13) for two weeks. (“ns”—not significant, \*\*\*\* $p < 0.0001$ ) ( $n = 4$ ).

The fiber morphology is depicted in Figure 9a,b for the fibers degraded in the mSBF and NaOH solutions. The fibers degraded in water show no differences from those degraded in mSBF. Compared to the fiber degradation experiment with a high pH value (Figure 9a), the fibers immersed in mSBF at pH 7.4 show no changes (Figure 9b). The fibers immersed in the NaOH solution (pH 13) suffered similar damages to those observed for the fiber coating (MgFc) (Figure 6b). The Raman spectra of the efPCL degraded in either 0.1M NaOH (pH 13) or mSBF reveal no change in the molecular structure. These findings are consistent with the Raman spectra of MgSc and MgFc (Figure 7).

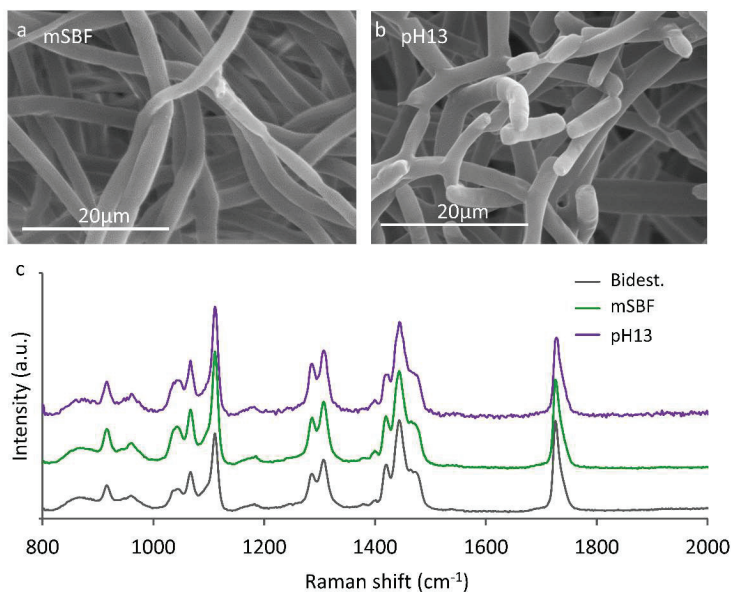


**Figure 9.** SEM pictures of PCL fiber mats: (a) after immersion in mSBF; (b) and NaOH-solution. (c) Raman spectra of PCL electrospun fiber mats after immersion in dist. water, mSBF, or NaOH-solution (pH 13).

The increase in the melting enthalpy  $\Delta H_m$  is closely associated with the crystallinity of the polymer [31]. The crystallinity was calculated based on the formula presented in the study of De Cassan et al. [32]. The crystallinity is slightly increased for the ePCL immersed in the NaOH solution (Table 3).

**Table 3.** Glass transition ( $T_g$ ), melting temperature ( $T_m$ ), melting enthalpy ( $\Delta H_m$ ), and the calculated crystallinity ( $x_c$ ) of the fiber mats ePCL after two weeks immersion in dist. H<sub>2</sub>O, mSBF, and NaOH solution (pH 13) ( $n = 3$ ).

Parameter	$T_g$ in °C	$T_m$ in °C	$\Delta H_m$ in J/g	$x_c$ in %
Dist. water	−61.2	60.8	80.2	58
mSBF	−60.8	60.2	79.9	57.3
NaOH solution	−61	61	84.7	60.8

#### 4. Discussion

A controlled corrosion rate of magnesium grafts would open new options for cardiovascular surgery because of magnesium's excellent biocompatibility and its temporary in vivo function due to its degradation kinetics. The transient stabilization of biological grafts with limited mechanical properties, such as the cholecyst-derived extracellular matrix [33], small bowel [8], stomach [34], bladder [35], or pericardium [36], would facilitate the reconstruction of left ventricular myocardial damage. There is evidence that autologous, vascularized segments of the small bowel or stomach have the potential for the functional replacement of lesioned myocardium after approximately 3 to 6 months of in vivo remodeling [6,8]. This concept of guided tissue engineering would be an ideal therapeutic approach for patients with terminal congestive heart failure that still require the implantation of ventricular assist devices or cardiac transplantation. However, the biological grafts require mechanical support in the phase of their in vivo remodeling, lasting up to 6 months [6], albeit the magnesium alloy support scaffolds are susceptible to a faster corrosion rate even though Schilling et al. employed magnesium fluoride (MgF) coating (chemical conversion) to decelerate the corrosion process [5]. An additional coating could further enhance the stabilizing support of the scaffold's function until the physiological remodeling of the biological graft provides sufficient mechanical stability, as concluded by Gray et al. [37].

Moreover, polymer coatings not only slow down the corrosion of the metallic structure but also provide better cytocompatibility [38,39]. Applying polymer coatings to metallic substrates includes dip coating, spraying, powder coating, painting, or spin coating [37,38]. Dip coating and fibrous coating are the predominant procedures for biomedical applications. Hence, on the one hand, this study was to determine the influence of dense and fibrous coatings on magnesium corrosion and, on the other hand, the effects of the corrosion process on the polymer layer.

##### 4.1. Corrosion Protection of Magnesium by the Dense Coating

The results of the magnesium immersion test demonstrate that a homogenous, dense coating significantly decelerates magnesium corrosion. Our findings align with the results of Xu et al. who used biodegradable PLLA and PCL films to improve early corrosion resistance and graft cytocompatibility [39]. The authors found that osteosarcoma cells adhered well to the polymer-coated magnesium. They also found a reduced corrosion rate of their magnesium samples, indicated by pH measurement and a reduced volume of released Mg<sup>2+</sup> ions. The main underlying mechanism of corrosion protection by coating is a polymer barrier that inhibits the mass transport on the magnesium surface.

Nevertheless, there are two ways to overcome this barrier (Figure 10, Stage I). First, defects in the coating enable convective fluid transport to the magnesium surface, and second, diffusion through the PCL coating [14]. The mass transport through the PCL layer by diffusion is slow and can only cause low corrosion rates underneath the coating. At the same time, defects in the protective coating allow contact of the bare magnesium

surface with the corrosive medium, causing corrosion at a higher rate. One product of magnesium corrosion is hydrogen gas (Equation (1)), which enlarges the defect by forming tiny bubbles underneath the coating (Figure 10, Stage II). These bubbles lead to the delamination of the polymer layer. With increasing gas pressure, the probability of a “break open” of the coating rises (Figure 10, Stage III). Subsequently, more fluid can reach the magnesium surface involving larger areas in the corrosion process. The coating prevents the mass transport of degradation products ( $Mg^{2+}$  and  $OH^-$ ), leading to its accumulation underneath the coating. Hence, passivation of the magnesium surface with  $Mg(OH)_2$  and calcium phosphates occurs. Eventually, the formed oxide layer provides efficient corrosion protection (Figure 10, Stage IV).

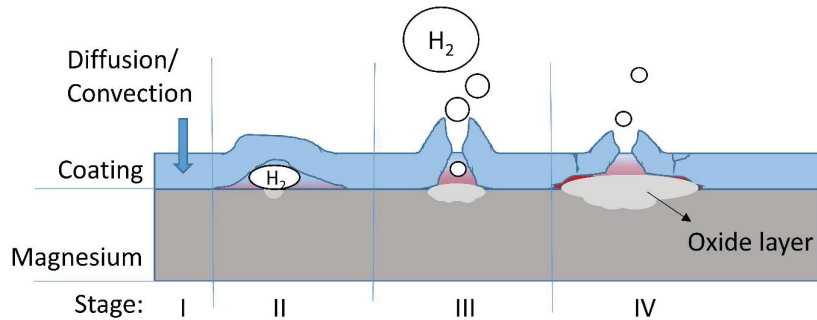


**Figure 10.** Schematic representation of the interaction of dense coating with magnesium corrosion. The fluid reaches the magnesium surface (Stage I), a hydrogen bubble forms due to magnesium reacting with the fluid (Stage II), the coating breaks open (Stage III), and accumulation leads to oxide layer formation and passivation (Stage IV).

Wong et al. [15] and Abdal-hey et al. [13] reported that the degradation rate of uncoated and coated magnesium after the initial phase converges during the experiment. In contrast, the results in the present study suggest that even a poor coating provides corrosion protection. The control of the pH value significantly impacts the corrosion rate of magnesium. In static conditions, the magnesium corrosion products accumulate in the fluid, and the pH value increases up to a critical pH where a passivating oxide layer is formed [24]. Uncoated and coated magnesium cause different alterations in the pH value of the test fluid because there is a positive correlation between the increase in pH and the corrosion rate. Finally, uncoated and coated magnesium reach a point of passivation if the experimental conditions allow for the accumulation of the degradation products. The inhibition of corrosion by OH accumulation in the control group can lead to an underestimation of the efficiency of the coating. If the experiments of Wong et al. [15] had not taken place in an environment with accumulated degradation products, the effect of the coating in comparison to uncoated magnesium certainly would have been prolonged and clearer.

#### 4.2. Corrosion Protection of Magnesium by Fibrous Coating

In contrast to the spin coating (MgSc), the fiber coating (MgFc) does not provide efficient, reproducible corrosion protection. The highly porous mesh of the fibers does not form an efficient barrier against the convection of rSBF to the magnesium surface (Figure 11, Stage I). The specific surface of electrospun fibers, in combination with the hydrophobic properties of PCL (with the contact angle of water on the PCL of  $115^\circ$  [40]), inhibit the gas from permeating the fibrous coating after contact with rSBF. Moreover, the weak adhesion of the coating to the magnesium surface supports spacious delamination. Consequently, a big hydrogen gas bubble in the delamination space between the magnesium surface and the fibrous PCL layer prevents the fluid from reaching the magnesium surface. So, no degradation occurs in these areas (Figure 11, Stage II).

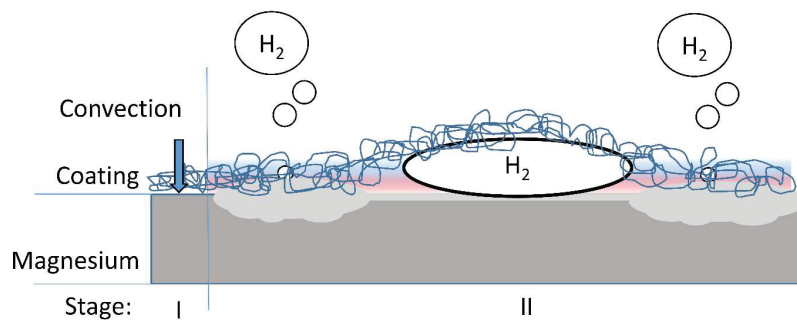


**Figure 11.** Schematic representation of the interaction of fiber coating with magnesium corrosion. The fluid reaches the magnesium surface (Stage I), and a hydrogen bubble forms due to magnesium reacting with water. The bubble is trapped underneath the coating and hinders water from reaching the surface (Stage II).

In contrast with these gas-covered areas, the areas with fluid contact show severe degradation. In vivo, e.g., in a blood vessel, big gas bubbles present an unbearable risk of gas embolism for patients.

The magnesium mass loss experiments do not consider the negative difference effect. This results in a little more hydrogen than indicated by the reaction equation (Equation (1)) [41]. Considering leakages and the low but present gas solubility in rSBF, this effect is neglected in this study.

#### 4.3. The Effects of Magnesium Corrosion on the Degradation of PCL Coatings

This study's second aim was to clarify the influence of magnesium corrosion on PCL coatings. The electrospun fiber degradation experiment demonstrates that the PCL degrades without measurable mass loss in mSBF, which aligns with the results from Taylor et al. [42]. In their study, the degradation experiment shows only a 0.7 wt.% mass loss of PCL in buffered solution after 16 weeks of exposure. The mass loss in high pH values (pH 13) is significant, and the PCL shows accelerated degradation when immersed in a harsh environment. However, the slight damage to the fiber structure, as seen in the PCL fiber experiment compared with the heavy damage in the coating immersion experiment (cracks, precipitation, and increased fiber diameter due to the uptake of water), suggests that the impact of magnesium corrosion on PCL degradation is not fully gauged. The depicted damages of the polymeric coating follow the results of Chen et al. [14] for PLA-coated magnesium, which documented similar damages. The spin coating in their study also suffered from embrittlement and precipitation [14]. The degradation of PCL is detectable by quantifying the increased crystallinity of the material because the amorphous areas in the polymeric structure suffer from degradation first [43]. The Raman spectra should change from a broader peak at around  $1736\text{ cm}^{-1}$  to a sharp peak at  $1726\text{ cm}^{-1}$  with increasing crystallinity [30]. As the crystallinity of the polymer was very high from the beginning, which caused a very sharp peak at  $1726\text{ cm}^{-1}$  before immersion, no change in crystallinity could be detected in the Raman spectra.

DSC offers information regarding the thermodynamic properties. The results of the DSC measurements show increasing crystallinity for electrospun fibers exposed to high pH values that indicates the degradation of the amorphous regions of the PCL material. The increased pH value and metallic cations ( $\text{Mg}^{2+}$ ) may cause a catalytical effect. Stokes et al. [44,45] described the catalytical effect of metal ions in the context of polyurethane degradation. Further research should be undertaken to investigate the influence of metal ions on PCL degradation.

Overall, dense polymer coatings for magnesium-based implants can provide corrosion protection. Despite the possible complicated coating process of complex geometry that may lead to coating defects, the autoinhibiting corrosion process of magnesium can compensate for these defects and inhomogeneities to a certain degree. Electrospun fiber coatings do not

provide efficient corrosion protection but should be considered an enhancement for cell interaction or drug delivery. Cardiovascular tissue brings special demands to implants. On the one hand, there are high demands on the mechanical strength, which make the choice of a metallic material appropriate; on the other hand, there is the particularly sensitive tissue, which should be as free as possible from scar tissue [46]. A combination of mechanical strength and the stimulation of healing by functionalized polymers makes polymer-coated magnesium an interesting approach. PCL can be functionalized with cell-binding peptides or cardiac ECM mimicking laminin-1 that support the healing process [47,48] or surfaces treated with laminin that enable stem cell therapy.

## 5. Conclusions

- Spin coating can decrease the initial strong corrosion reaction;
- A dense coating has a prolonged decelerating effect on corrosion because of the diffusion barrier and autoinhibition of the corrosion process;
- Fiber coatings do not provide efficient protection against corrosive attacks in the conducted experimental conditions;
- The degradation of the polymer is accelerated in the presence of magnesium corrosion.

**Author Contributions:** Conceptualization, S.K., M.M., and L.F.; methodology, S.K., M.M. and L.F.; formal analysis, S.K. and L.F.; investigation, S.K. and L.F.; writing—original draft preparation, S.K. and T.S.; writing—review and editing, B.G.; visualization, S.K.; supervision, B.G.; project administration, S.K., M.M. and B.G.; funding acquisition, S.K., T.S., and B.G. All authors have read and agreed to the published version of the manuscript.

**Funding:** This work was partially supported by the Dr. Jürgen und Irmgard Ulderup Stiftung and Caroline Herschel Program (Equal Opportunities Office) of Leibniz University Hannover.

**Institutional Review Board Statement:** Not applicable.

**Informed Consent Statement:** Not applicable.

**Data Availability Statement:** Not applicable.

**Acknowledgments:** We are grateful to Hans Jürgen Maier from the Institute of Material Science, Leibniz Universität Hannover, who enabled the sample manufacturing. We also thank Svea Doescher for her excellent technical support.

**Conflicts of Interest:** The authors declare no conflict of interest.

## References

1. Zhu, J.; Zhang, X.; Niu, J.; Shi, Y.; Zhu, Z.; Dai, D.; Chen, C.; Pei, J.; Yuan, G.; Zhang, R. Biosafety and efficacy evaluation of a biodegradable magnesium-based drug-eluting stent in porcine coronary artery. *Sci. Rep.* **2021**, *11*, 7330. [CrossRef] [PubMed]
2. Toušek, P.; Lazarák, T.; Varvařovský, I.; Nováčková, M.; Neuberger, M.; Kočka, V. Comparison of a Bioresorbable, Magnesium-Based Sirolimus-Eluting Stent with a Permanent, Everolimus-Eluting Metallic Stent for Treating Patients with Acute Coronary Syndrome: The PRAGUE-22 Study. *Cardiovasc. Drugs Ther.* **2022**, *36*, 1129–1136. [CrossRef] [PubMed]
3. Rukshin, V.; Santos, R.; Gheorghiu, M.; Shah, P.K.; Kar, S.; Padmanabhan, S.; Azarbal, B.; Tsang, V.T.; Makkar, R.; Samuels, B.; et al. A prospective, nonrandomized, open-labeled pilot study investigating the use of magnesium in patients undergoing nonacute percutaneous coronary intervention with stent implantation. *J. Cardiovasc. Pharmacol. Ther.* **2003**, *8*, 193–200. [CrossRef] [PubMed]
4. Schilling, T.; Bauer, M.; Biskup, C.; Haverich, A.; Hassel, T. Engineering of biodegradable magnesium alloy scaffolds to stabilize biological myocardial grafts. *Biomed. Tech.* **2017**, *62*, 493–504. [CrossRef] [PubMed]
5. Schilling, T.; Brandes, G.; Tudorache, I.; Cebotari, S.; Hilfiker, A.; Meyer, T.; Biskup, C.; Bauer, M.; Waldmann, K.-H.; Bach, F.-W.; et al. In vivo degradation of magnesium alloy LA63 scaffolds for temporary stabilization of biological myocardial grafts in a swine model. *Biomed. Tech.* **2013**, *58*, 407–416. [CrossRef]
6. Schilling, T.; Meyer, T.; Brandes, G.; Hartung, D.; Tudorache, I.; Nolte, I.; Wacker, F.; Hilfiker, A.; Hoeffler, K.; Haverich, A.; et al. Left Ventricular Wall Reconstruction with Autologous Vascularized Gastric Graft in a Porcine Pilot Model. *Eur. Surg. Res.* **2022**.
7. Dor, V.; Saab, M.; Coste, P.; Kornaszewska, M.; Montiglio, F. Left ventricular aneurysm: A new surgical approach. *Thorac. Cardiovasc. Surg.* **1989**, *37*, 11–19. [CrossRef]
8. Tudorache, I.; Kostin, S.; Meyer, T.; Teebken, O.; Bara, C.; Hilfiker, A.; Haverich, A.; Cebotari, S. Viable vascularized autologous patch for transmural myocardial reconstruction. *Eur. J. Cardiothorac. Surg.* **2009**, *36*, 306–311; discussion 311. [CrossRef]

9. Willumeit, R.; Fischer, J.; Feyerabend, F.; Hort, N.; Bismayer, U.; Heidrich, S.; Mihailova, B. Chemical surface alteration of biodegradable magnesium exposed to corrosion media. *Acta Biomater.* **2011**, *7*, 2704–2715. [CrossRef]
10. Song, Y.W.; Shan, D.Y.; Han, E.H. Electrodeposition of hydroxyapatite coating on AZ91D magnesium alloy for biomaterial application. *Mater. Lett.* **2008**, *62*, 3276–3279. [CrossRef]
11. Imwinkelried, T.; Beck, S.; Iizuka, T.; Schaller, B. Effect of a plasmaelectrolytic coating on the strength retention of in vivo and in vitro degraded magnesium implants. *Acta Biomater.* **2013**, *9*, 8643–8649. [CrossRef]
12. Lin, X.; Tan, L.; Wang, Q.; Zhang, G.; Zhang, B.; Yang, K. In vivo degradation and tissue compatibility of ZK60 magnesium alloy with micro-arc oxidation coating in a transcortical model. *Mater. Sci. Eng. C Mater. Biol. Appl.* **2013**, *33*, 3881–3888. [CrossRef] [PubMed]
13. Abdal-hay, A.; Barakat, N.A.; Lim, J.K. Influence of electrospinning and dip-coating techniques on the degradation and cytocompatibility of Mg-based alloy. *Colloids Surf. A Physicochem. Eng. Asp.* **2013**, *420*, 37–45. [CrossRef]
14. Chen, Y.; Song, Y.; Zhang, S.; Li, J.; Zhao, C.; Zhang, X. Interaction between a high purity magnesium surface and PCL and PLA coatings during dynamic degradation. *Biomed. Mater.* **2011**, *6*, 25005. [CrossRef] [PubMed]
15. Wong, H.M.; Yeung, K.W.K.; Lam, K.O.; Tam, V.; Chu, P.K.; Luk, K.D.K.; Cheung, K.M.C. A biodegradable polymer-based coating to control the performance of magnesium alloy orthopaedic implants. *Biomaterials* **2010**, *31*, 2084–2096. [CrossRef]
16. Xu, L.; Yamamoto, A. Characteristics and cytocompatibility of biodegradable polymer film on magnesium by spin coating. *Colloids Surf. B Biointerfaces* **2012**, *93*, 67–74. [CrossRef]
17. Repanas, A.; Glasmacher, B. Dipyrindamole embedded in Polycaprolactone fibers prepared by coaxial electrospinning as a novel drug delivery system. *J. Drug Deliv. Sci. Technol.* **2015**, *29*, 132–142. [CrossRef]
18. Yoshimoto, H.; Shin, Y.M.; Terai, H.; Vacanti, J.P. A biodegradable nanofiber scaffold by electrospinning and its potential for bone tissue engineering. *Biomaterials* **2003**, *24*, 2077–2082. [CrossRef]
19. Blakeney, B.A.; Tambralli, A.; Anderson, J.M.; Andukuri, A.; Lim, D.-J.; Dean, D.R.; Jun, H.-W. Cell infiltration and growth in a low density, uncompressed three-dimensional electrospun nanofibrous scaffold. *Biomaterials* **2011**, *32*, 1583–1590. [CrossRef]
20. Szentivanyi, A.; Chakradeo, T.; Zernetsch, H.; Glasmacher, B. Electrospun cellular microenvironments: Understanding controlled release and scaffold structure. *Adv. Drug Deliv. Rev.* **2011**, *63*, 209–220. [CrossRef]
21. Bode, M.; Mueller, M.; Zernetsch, H.; Glasmacher, B. Electrospun vascular grafts with anti-kinking properties. *Curr. Dir. Biomed. Eng.* **2015**, *1*, 459. [CrossRef]
22. Suresh, S.; Gryshkov, O.; Glasmacher, B. Impact of setup orientation on blend electrospinning of poly- $\epsilon$ -caprolactone-gelatin scaffolds for vascular tissue engineering. *Int. J. Artif. Organs* **2018**, *41*, 801–810. [CrossRef] [PubMed]
23. Degner, J.; Singer, F.; Cordero, L.; Boccaccini, A.R.; Virtanen, S. Electrochemical investigations of magnesium in DMEM with biodegradable polycaprolactone coating as corrosion barrier. *Appl. Surf. Sci.* **2013**, *282*, 264–270. [CrossRef]
24. Knigge, S.R.; Glasmacher, B. Comparison between three in vitro methods to measure magnesium degradation and their suitability for predicting in vivo degradation. *Int. J. Artif. Organs* **2018**, *41*, 772–778. [CrossRef]
25. Oyane, A.; Kim, H.-M.; Furuya, T.; Kokubo, T.; Miyazaki, T.; Nakamura, T. Preparation and assessment of revised simulated body fluids. *J. Biomed. Mater. Res. A* **2003**, *65*, 188–195. [CrossRef]
26. Nidadavolu, E.P.S.; Feyerabend, F.; Ebel, T.; Willumeit-Römer, R.; Dahms, M. On the Determination of Magnesium Degradation Rates under Physiological Conditions. *Materials* **2016**, *9*, 627. [CrossRef]
27. *DIN EN ISO 10993-1:2017-04; Biologische Beurteilung von Medizinprodukten—Teil 1: Beurteilung und Prüfungen im Rahmen eines Risikomanagementsystems.* Beuth Verlag GmbH: Berlin, Germany, 2017.
28. Poh, P.S.P.; Hege, C.; Chhaya, M.P.; Balmayor, E.R.; Foehr, P.; Burgkart, R.H.; Schantz, J.-T.; Schiller, S.M.; Schilling, A.F.; Hutmacher, D.W. Evaluation of polycaprolactone—poly-D,L-lactide copolymer as biomaterial for breast tissue engineering. *Polym. Int.* **2017**, *66*, 77–84. [CrossRef]
29. Fricke, D.; Becker, A.; Jütte, L.; Bode, M.; de Cassan, D.; Wollweber, M.; Glasmacher, B.; Roth, B. Mueller Matrix Measurement of Electrospun Fiber Scaffolds for Tissue Engineering. *Polymers* **2019**, *11*, 2062. [CrossRef]
30. Weselucha-Birczyńska, A.; Swiętek, M.; Sołtysiak, E.; Galiński, P.; Płachta, Ł.; Piekara, K.; Błażewicz, M. Raman spectroscopy and the material study of nanocomposite membranes from poly( $\epsilon$ -caprolactone) with biocompatibility testing in osteoblast-like cells. *Analyst* **2015**, *140*, 2311–2320. [CrossRef]
31. Kong, Y.; Hay, J.N. The measurement of the crystallinity of polymers by DSC. *Polymer* **2002**, *43*, 3873–3878. [CrossRef]
32. Cassan, D.; Becker, A.; Glasmacher, B.; Roger, Y.; Hoffmann, A.; Gengenbach, T.R.; Easton, C.D.; Hänsch, R.; Menzel, H. Blending chitosan-g-poly(caprolactone) with poly(caprolactone) by electrospinning to produce functional fiber mats for tissue engineering applications. *J. Appl. Polym. Sci.* **2020**, *137*, 48650. [CrossRef]
33. Burugapalli, K.; Pandit, A. Characterization of tissue response and in vivo degradation of cholecyst-derived extracellular matrix. *Biomacromolecules* **2007**, *8*, 3439–3451. [CrossRef] [PubMed]
34. Ruel, M.A.; Sellke, F.W.; Bianchi, C.; Khan, T.A.; Faro, R.; Zhang, J.-P.; Cohn, W.E. Endogenous myocardial angiogenesis and revascularization using a gastric submucosal patch. *Ann. Thorac. Surg.* **2003**, *75*, 1443–1449. [CrossRef] [PubMed]
35. Badylak, S.F.; Kochupura, P.V.; Cohen, I.S.; Doronin, S.V.; Saltman, A.E.; Gilbert, T.W.; Kelly, D.J.; Ignatz, R.A.; Gaudette, G.R. The use of extracellular matrix as an inductive scaffold for the partial replacement of functional myocardium. *Cell Transplant.* **2006**, *15* (Suppl. 1), S29–S40. [CrossRef]

36. Chang, Y.; Chen, S.-C.; Wei, H.-J.; Wu, T.-J.; Liang, H.-C.; Lai, P.-H.; Yang, H.-H.; Sung, H.-W. Tissue regeneration observed in a porous acellular bovine pericardium used to repair a myocardial defect in the right ventricle of a rat model. *J. Thorac. Cardiovasc. Surg.* **2005**, *130*, 705–711. [CrossRef]
37. Gray, J.E.; Luan, B. Protective coatings on magnesium and its alloys—a critical review. *J. Alloy. Compd.* **2002**, *336*, 88–113. [CrossRef]
38. Ostrowski, N.; Lee, B.; Enick, N.; Carlson, B.; Kunjukunju, S.; Roy, A.; Kumta, P.N. Corrosion protection and improved cytocompatibility of biodegradable polymeric layer-by-layer coatings on AZ31 magnesium alloys. *Acta Biomater.* **2013**, *9*, 8704–8713. [CrossRef]
39. Hornberger, H.; Virtanen, S.; Boccaccini, A.R. Biomedical coatings on magnesium alloys—a review. *Acta Biomater.* **2012**, *8*, 2442–2455. [CrossRef]
40. Intranuovo, F.; Gristina, R.; Brun, F.; Mohammadi, S.; Ceccone, G.; Sardella, E.; Rossi, F.; Tromba, G.; Favia, P. Plasma Modification of PCL Porous Scaffolds Fabricated by Solvent-Casting/Particulate-Leaching for Tissue Engineering. *Plasma Process. Polym.* **2014**, *11*, 184–195. [CrossRef]
41. Hatami, M.; Yeganeh, M.; Keyvani, A.; Saremi, M.; Naderi, R. Electrochemical behavior of polypyrrole-coated AZ31 alloy modified by fluoride anions. *J. Solid State Electrochem.* **2017**, *21*, 777–785. [CrossRef]
42. Taylor, M.S.; Daniels, A.U.; Andriano, K.P.; Heller, J. Six bioabsorbable polymers: In vitro acute toxicity of accumulated degradation products. *J. Appl. Biomater.* **1994**, *5*, 151–157. [CrossRef] [PubMed]
43. Kotula, A.P.; Snyder, C.R.; Migler, K.B. Determining conformational order and crystallinity in polycaprolactone via Raman spectroscopy. *Polymer* **2017**, *117*, 1–10. [CrossRef] [PubMed]
44. Stokes, K.; McVenes, R.; Anderson, J.M. Polyurethane elastomer biostability. *J. Biomater. Appl.* **1995**, *9*, 321–354. [CrossRef] [PubMed]
45. Stokes, K.; Coury, A.; Urbanski, P. Autooxidative Degradation of Implanted Polyether Polyurethane Devices. *J. Biomater. Appl.* **1986**, *1*, 411–448. [CrossRef] [PubMed]
46. Jawad, H.; Ali, N.N.; Lyon, A.; Chen, Q.Z.; Harding, S.E.; Boccaccini, A.R. Myocardial tissue engineering: A review. *J. Tissue Eng. Regen. Med* **2007**, *1*, 327–342. [CrossRef]
47. Stevens, J.S.; de Luca, A.C.; Downes, S.; Terenghi, G.; Schroeder, S.L.M. Immobilisation of cell-binding peptides on poly- $\epsilon$ -caprolactone (PCL) films: A comparative XPS study of two chemical surface functionalisation methods. *Surf. Interface Anal.* **2014**, *10–11*, 673–678. [CrossRef]
48. Boffito, M.; Di Meglio, F.; Mozetic, P.; Giannitelli, S.M.; Carmagnola, I.; Castaldo, C.; Nurzynska, D.; Sacco, A.M.; Miraglia, R.; Montagnani, S.; et al. Surface functionalization of polyurethane scaffolds mimicking the myocardial microenvironment to support cardiac primitive cells. *PLoS ONE* **2018**, *13*, e0199896. [CrossRef]

**Disclaimer/Publisher’s Note:** The statements, opinions and data contained in all publications are solely those of the individual author(s) and contributor(s) and not of MDPI and/or the editor(s). MDPI and/or the editor(s) disclaim responsibility for any injury to people or property resulting from any ideas, methods, instructions or products referred to in the content.

Article

# Topography Control of Micro-Nanosized Anatase Coating on Magnesium Alloy

Shusen Hou <sup>1,2,\*</sup>, Tingting Yang <sup>2</sup>, Yue Li <sup>2,\*</sup>, Liming Lian <sup>2</sup>, Weixin Yu <sup>2</sup> and Lin Yang <sup>1</sup>

<sup>1</sup> School of Chemistry and Chemical Engineering, Henan Normal University, Xinxiang 453007, China; yanglin1819@163.com

<sup>2</sup> School of Mechanical and Electrical Engineering, Xinxiang University, Xinxiang 453003, China; yangtingting@xxu.edu.cn (T.Y.); lianliming@xxu.edu.cn (L.L.); yuweixin@xxu.edu.cn (W.Y.)

\* Correspondence: shusenh@163.com (S.H.); liyue@xxu.edu.cn (Y.L.)

**Abstract:** Constructing surface topographies in the micro- or nanometer range is an effective way to improve the biocompatibility of biomaterials. For the present work, anatase coatings with controllable micro/nanoscale characteristics were successfully prepared on an MgZn alloy surface via solvothermal route, and their formation mechanisms are discussed. The features of the as-prepared coatings were characterized using a scanning electron microscope (SEM), a transmission electron microscope (TEM), an atomic force microscope (AFM), X-ray diffraction (XRD), and a contact angle goniometer. The corrosion behavior of the coatings was also evaluated by testing the open circuit potential (OCP) in SBF (Simulated Body Fluid). The results show that a gradual variation of the anatase coating morphologies was obtained through adjusting the solvothermal reaction conditions. With the increase of NH<sub>4</sub>F concentration in the solution, the cross-combined anatase nanosheets became more dispersed. The micro/nanostructured anatase coatings provide the MgZn alloy with good corrosion resistance, which increased with the density of anatase nanosheets in the coatings. In addition, the coatings exhibit the inhibition of platelet aggregation, and the micro/nano structures can also adsorb endothelial cells.

**Keywords:** topography; micro/nanostructure; anatase; coating; magnesium alloy

## 1. Introduction

### 1.1. Background

Biomedical metal, such as stainless steel, titanium alloy, and cobalt-based alloy, have been widely used in orthopedic, cardiovascular, and dental fields because of their high strength and corrosion resistance [1,2]. However, these metal materials are chemically stable in the human physiological environment. Sometimes they need to be removed by secondary surgery, which undoubtedly increases the pain and medical expenses of patients. As an implant material, biomedical magnesium alloy has good biocompatibility, and is easily corroded and destroyed in the physiological environment until it disappears completely. Its degradation products can be metabolized and absorbed by the human body, and thus secondary surgery can be avoided. Therefore, magnesium alloys, as biodegradable and absorbable biomedical materials, have attracted much attention in bone tissue repair and cardiovascular therapy, and have become a hot issue in the field of biomaterials [3,4].

Studies have shown that magnesium alloys corrode too fast in the physiological environment, which leads to a sharp decline in the stability of their structure and properties. In this case, stable support could not be provided in the process of tissue repair, since it may lead to the premature failure of implants. Proper surface modification of the magnesium alloy could control the degradation rate and improve biocompatibility [5–7]. The most common surface modification method is to produce protective coatings on magnesium alloys, which mainly include some inorganic coatings and degradable polymer coatings [8].

For example, in bone fixation implants field, hydroxyapatite (HA), one of the primary constituents of bone, has been extensively prepared onto magnesium alloy substrates by different methods. In many cases, HA coatings could slow down the corrosion rate and improve the biocompatibility or osseointegration of magnesium alloy implants [9,10].

In the field of magnesium alloy cardiovascular stents, some organic-based coatings have been employed as corrosion protection layers, or more importantly, as drug delivery carriers to prevent in-stent restenosis (ISR) [11–13]. On the other hand, as an inorganic material, titanium dioxide was gradually used to prepare the protective coating of magnesium alloy stents, aiming to provide increased corrosion resistance and improved biocompatibility of magnesium alloys [14–16].

It is generally believed that the optimal surface of cardiovascular implants should be blood compatible, and moreover, promote the adhesion and growth of endothelial cells (ECs), while suppressing the adhesion and proliferation of smooth muscle cells (SMCs). Building a monolayer of endothelial cells on the stents is considered to be the most efficient approach to reducing the risk of clot formation and restenosis, because an anticoagulant surface can be offered by the endothelial layer [17,18]. So, it is vital for stents to enhance the adherence, migration, and proliferation of ECs, resulting in rapid re-endothelialization after cardiac interventional therapy.

### 1.2. The Purpose of the Research

As is well known, the surface topography of biomaterial with micro- or nano- characteristics could play a critical role in cell adhesion and proliferation [17,19,20]. Hence, it is possible to fabricate specific surface microstructures on magnesium alloy stents to enhance the re-endothelialization, thus preventing the formation of ISR [21,22]. In our early research, anatase titanium dioxide coatings with flower-like and sheet-like structures were prepared on MgZn alloys for vascular stent application, since the titanium oxide films have excellent blood compatibility [23,24]. We believe that an intensive study is necessary to precisely control the structures and topographies of anatase coatings in micro/nanometer range. In this paper, gradually varying surface topographies provided by anatase coatings were constructed on MgZn alloy substrates by adjusting the solvothermal reaction conditions. The formation mechanism and properties of the coatings are discussed below.

## 2. Materials and Methods

### 2.1. Coating Preparation

In this study, anatase coatings were fabricated on an MgZn alloy (composition: 2.0 wt.% Zn, 0.5 wt.% Nd, 0.46 wt.% Y, and balance Mg), developed by Zhengzhou University, Zhengzhou, China [25]. Samples with dimensions of  $15 \times 10 \times 3 \text{ mm}^3$  were cut from the as-cast ingots by wire-electrode machining, mechanically polished, and sonicated in ethanol. Then, they were stored in ethanol before being solvothermal-treated in a Teflon vessel.

Solvothermal treatment was carried out in Teflon-lined stainless-steel autoclave, in which 18 mL absolute alcohol and 140  $\mu\text{L}$  titanium butoxide (TBOT) were employed as solvent and reactant, respectively. To obtain micro/nano anatase coatings on the MgZn samples, 70  $\mu\text{L}$  hydrofluoric acid (HF, 40 wt.%) and 140  $\mu\text{L}$   $\text{NH}_4\text{F}$  aqueous solution (0.1–0.3 M) were successively added into the former solution. After being stirred for 10 min, the Teflon vessel containing the mixed solution and upright samples was sealed and fixed in the autoclave, then treated at 170 °C for 12 h. Subsequently, the autoclave was cooled, and the samples were taken out from the Teflon vessel, cleaned ultrasonically in deionized water, then dried. In this study, for simplicity, abbreviations for the samples with different coatings are listed in Table 1.

## 2.2. Coating Characterization

The surface characteristics were observed by a scanning electron microscope (SEM, SU8000, Hitachi, Tokyo, Japan), an atomic force microscope (TEM, Talos F200X, FEI, Hillsboro, OR, USA), and an atomic force microscope (AFM, MultiMode8, Bruker, Billerica, MA, USA). To obtain the cross-section image, the coating was slightly scratched with a sharp blade, and the coating was partially damaged and broken away from the substrate, in order to find the cross-section morphology under a scanning electron microscope. For TEM analysis, a small number of powders was carefully scraped from the coatings and dispersed in ethanol, and the dispersion was dropped on carbon-copper grids and dried. The crystal structure of the coatings was determined through X-ray diffraction (XRD, X'Pert3 Powder, PANalytical, Malvern, UK) with Cu K $\alpha$  radiation at 45 kV and 40 mA. The water contact angle (CA,  $n = 3$ ) was measured with 10  $\mu$ L droplets of deionized water employing a contact angle meter.

**Table 1.** List of the abbreviations used in this paper.

No.	Abbreviation	Sample Description
1	MgZn	Bare MgZn substrate
2	MgZn-0.1 F	MgZn substrate with anatase coating, prepared in solution containing 140 $\mu$ L of 0.1 M-NH <sub>4</sub> F aqueous solution
3	MgZn-0.2 F	MgZn substrate with anatase coating, prepared in solution containing 140 $\mu$ L of 0.2 M-NH <sub>4</sub> F aqueous solution
4	MgZn-0.3 F	MgZn substrate with anatase coating, prepared in solution containing 140 $\mu$ L of 0.3 M-NH <sub>4</sub> F aqueous solution

## 2.3. Corrosion Resistance Tests

The corrosion resistance tests of the bare and coated MgZn samples were conducted on an electrochemical station (CS2350, Wuhan Corrtest Instrument Co., Ltd. Wuhan, China) with a three-electrode cell in which the sample, platinum electrode, and saturated calomel electrode were the working, counter, and reference electrodes, respectively. Electrochemical measurements were performed at 37 °C in simulated body fluid (SBF), based on Ref. [26].

## 2.4. Biocompatibility Evaluation

In this paper, biocompatibility was evaluated including the platelets and endothelial cells adhesion. For the platelets adhesion test, fresh human anticoagulant blood was centrifuged at 1500 rpm for 15 min, then the upper yellow liquid was separated to obtain platelet-rich plasma (PRP). An amount of 0.5 mL of PRP was dropped into 24-well culture plates containing samples, and incubated at 37 °C for 1 h. Then, the samples were rinsed with normal saline and fixed with glutaraldehyde. After that, samples were dehydrated in increasing concentrations of ethanol, successively. Human umbilical vein endothelial cells (HUVECs, Ea.hy926) were used to observe the cells adhesion to the samples. Firstly, the sterilized samples were put into 24-well culture plates, then the endothelial cells were seeded on the samples under a concentration of  $2 \times 10^4$  cells/mL. After a 24 h incubation period, the samples were washed with PBS buffer then treated by PBS buffer containing 2.5% glutaraldehyde for 12 h, and dehydrated with 50%, 75%, 90%, and 100% ethanol. The samples were dried, then the platelets and cells were observed by SEM.

## 3. Results and Discussion

### 3.1. Coating Characteristics

The surface morphologies of the MgZn-0.1 F, MgZn-0.2 F and MgZn-0.3 F are presented in Figure 1. All samples were prepared by solvothermal treatment at 170 °C for 12 h in the mixed solution of alcohol, TBOT, HF, and NH<sub>4</sub>F. The only different parameter is the NH<sub>4</sub>F concentration, varying from 0.1–0.3 M as described in the Experimental section. Figure 2 indicates the XRD patterns of the samples. Clearly, in each sample there were two phases detected: the MgZn phase as the substrate and the anatase phase (PDF#21-1271) as the surface coating. Figure 1 shows that the surface of every sample was composed of anatase sheets. However, the coatings were significantly different in topographies, reflected in the crystal size, density, as well as conglomeration state of the anatase microstructures.

At a lower  $\text{NH}_4\text{F}$  concentration (i.e., 0.1 M), the coating was very dense due to the high degree of aggregation of the layer-by-layer anatase sheets. These aggregates were crossed and interconnected with each other. There was hardly any porosity in this coating, as shown in Figure 1a,d. With the increase of  $\text{NH}_4\text{F}$  concentration, the number and size of anatase sheets in the aggregates decreased notably. Moreover, porous morphologies appeared in the coatings because the sheet-like aggregates were dispersing gradually, as shown in Figure 1b,c,e,f.

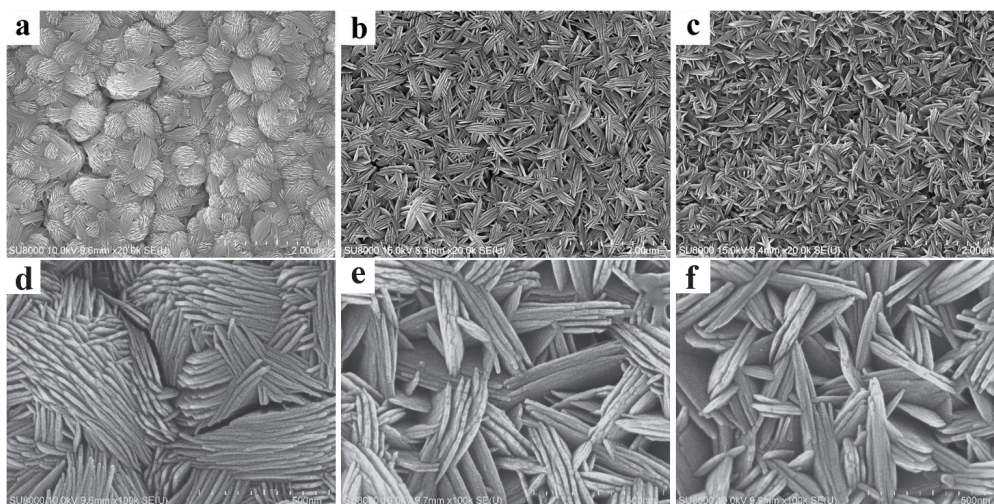


Figure 1. SEM surface morphologies of anatase coatings: (a,d) MgZn-0.1 F; (b,e) MgZn-0.2 F; (c,f) MgZn-0.3 F.

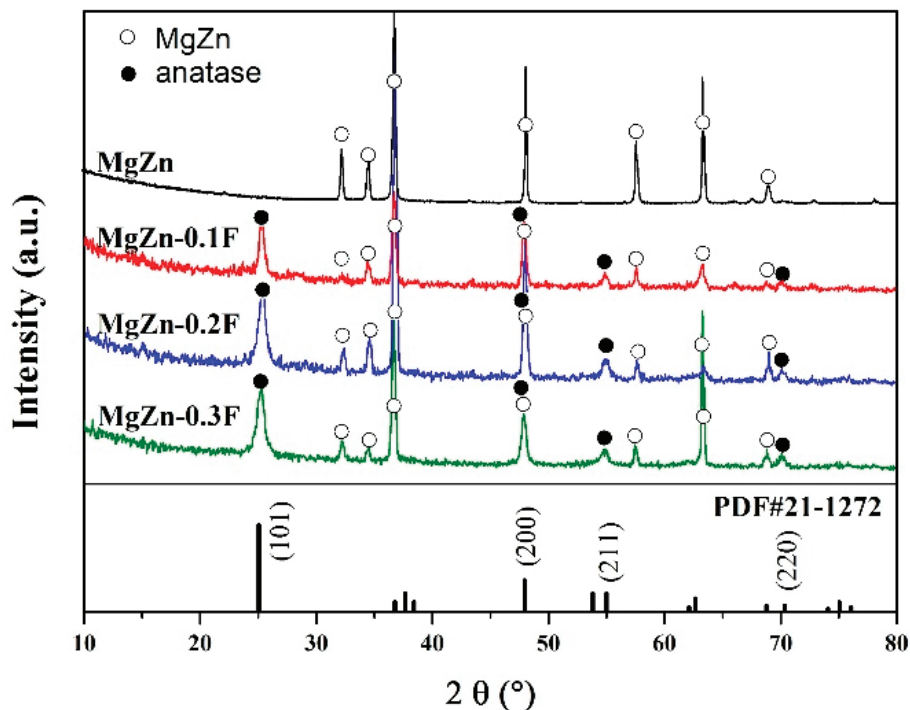
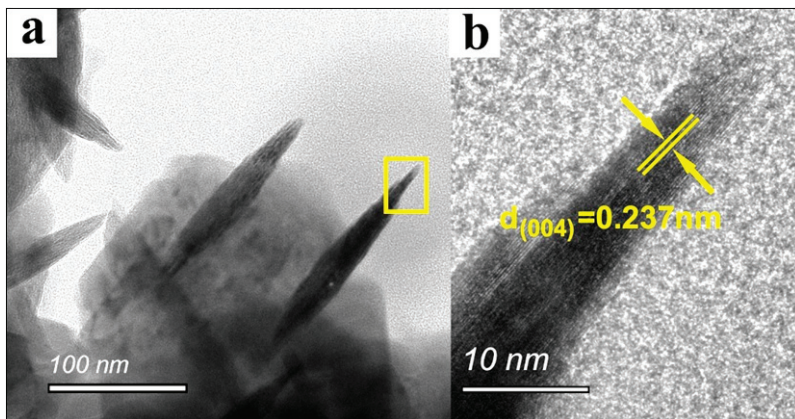


Figure 2. XRD patterns of the as-prepared anatase coatings.

Figure 3a shows the TEM image of a broken anatase aggregate partially scraped from the surface of the MgZn-0.3 F sample. It confirms that the aggregates were assembled from anatase nanosheets with a thickness of 10–20 nm. These nanosheets were parallel or crossed with each other during the growth process. As seen in Figure 1c,f, the aggregates of these

nanosheets were significantly larger than 100 nm, close to micron scale. So, we defined the coating as a micro/nano-scale structure coating. In Figure 3b, the High-resolution TEM image shows the (004) planes of anatase with a crystal plain spacing of 0.237 nm, which indicates that the top and bottom surfaces of the anatase sheets are (001) planes.



**Figure 3.** (a) TEM image of the of the anatase sheets; (b) high-resolution TEM image of the edge of a single anatase sheet selected in the rectangle region in (a).

### 3.2. Formation Mechanism of the Coatings

The above results demonstrate that the different morphologies of the as-prepared anatase coatings are strongly dependent on the  $\text{NH}_4\text{F}$  concentration in the solvothermal solution. After a 12 h solvothermal treatment, we can obtain a complete coating with a final thickness of 750 nm (Figure 4). In order to reveal the underlying causes of the difference in topographies, two samples were prepared by solvothermal treatment at 170 °C for 6 h in solutions containing 0.1 M- $\text{NH}_4\text{F}$  and 0.2 M- $\text{NH}_4\text{F}$ , separately. This is because after a shorter time of 6 h, some evolving information of the coating can emerge. In Figure 5, it can be seen that both coatings present a layered characteristic, i.e., the anatase sheets or their aggregates in the upper layer, and lots of blocks in the bottom layer. The nano-scale thin sheets were parallel or cross-combined, and developed into the aggregates. On the basis of the XRD results in Figure 2, we conclude that the blocks were also anatase crystals, the same as the nano-thin sheets. However, there as an obvious difference in the surface morphologies of the two samples. For the MgZn-0.2 F sample, the anatase blocks are bigger in size and have more regular shapes, and the number of the sheet aggregates is less than that of the MgZn-0.1 F sample.

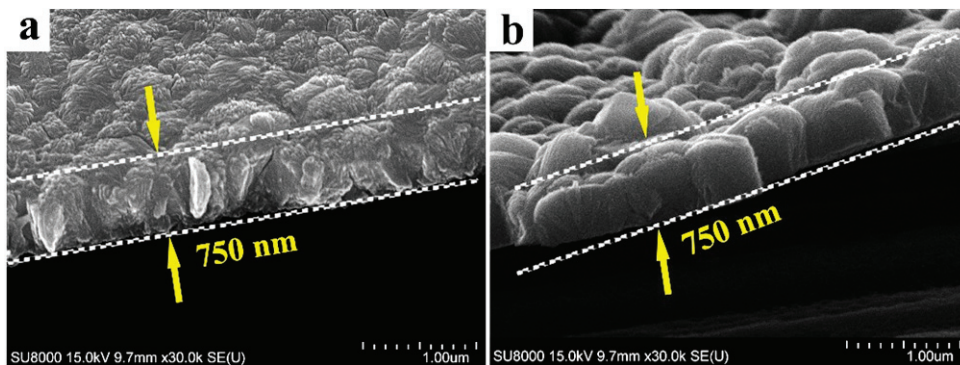


**Figure 4.** Cross-section morphologies of anatase coatings grown at 170 °C for 12 h in solutions containing: (a) 18 mL alcohol, 140  $\mu\text{L}$  TBOT, 70  $\mu\text{L}$  HF, 140  $\mu\text{L}$   $\text{NH}_4\text{F}$  (0.1 M); (b) 18 mL alcohol, 140  $\mu\text{L}$  TBOT, 70  $\mu\text{L}$  HF, 140  $\mu\text{L}$   $\text{NH}_4\text{F}$  (0.2 M).

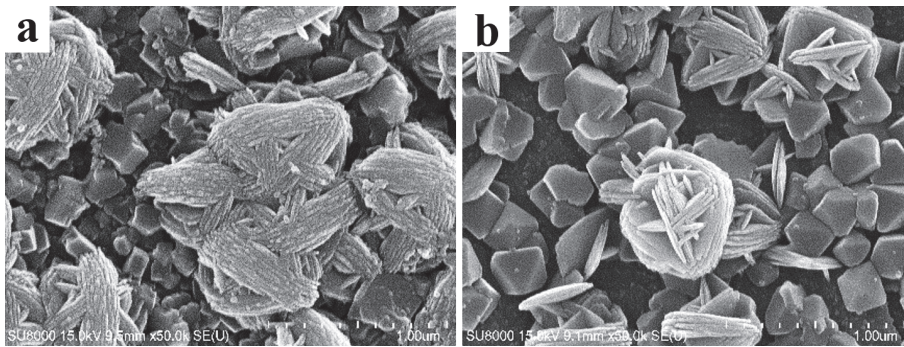


**Figure 5.** SEM morphologies of anatase coatings grown at 170 °C for 6 h in solutions containing: (a) 18 mL alcohol, 140  $\mu$ L TBOT, 70  $\mu$ L HF, 140  $\mu$ L  $\text{NH}_4\text{F}$  (0.1 M); (b) 18 mL alcohol, 140  $\mu$ L TBOT, 70  $\mu$ L HF, 140  $\mu$ L  $\text{NH}_4\text{F}$  (0.2 M).

From the cross-section morphologies in Figure 4, it is found that both the MgZn–0.1 F and MgZn–0.2 F coatings have the same thickness of about 750 nm after a 12 h hydrothermal reaction. However, the former coating has a rougher cross-section than the latter, and no blocks can be found within the whole cross-section of the former coating. Hence, we infer that the anatase blocks were almost entirely converted into anatase sheets from 6 h to 12 h during the hydrothermal reaction. For the latter coating, some anatase blocks, less than that of the same one prepared after a 6 h hydrothermal reaction, can still be seen in the cross-section (see Figures 4b and 5b). It could be concluded that during the anatase coating formation process, the anatase crystals were evolved from block-like to sheet-like, and the conversion process was slower when the hydrothermal reaction was conducted in solution with the higher  $\text{NH}_4\text{F}$  concentration.

Generally, anatase crystals are dominated by the {101} planes, causing them to exhibit the double-pyramidal appearance [27]. In Figure 5b, it can be seen that the anatase crystals at the bottom have a pyramidal shape, which are consistent with other studies. In fact, in this paper,  $\text{NH}_4\text{F}$  has important effects on the crystal growth of anatase crystals. Firstly, adequate fluorine ions ( $\text{F}^-$ ) were supplied by the hydrolysis of  $\text{NH}_4\text{F}$ , and these fluorine ions can be absorbed onto the surfaces of the anatase planes, markedly reducing the surface energy of the {001} planes to a level lower than that of the {101} planes, making the {001} planes more stable than the {101} planes [28]. So, the anatase crystal with exposed {001} planes can be achieved during its growth process, which led to the plate-like appearance. Secondly, it is found that the anatase crystals have a slower growth rate under a higher  $\text{NH}_4\text{F}$  concentration. In our previous research, it has been confirmed that the growth of anatase crystals would slow down when the HF amount was increased, because low pH would suppress the hydrolysis of TBOT [23]. However, in this current study the HF content is constant (70  $\mu$ L) for all the solvothermal treatment conditions. So, we think the slower growth rate of the anatase crystals (or the formation of the anatase coating) may be attributed to the slight adjustment of pH by the hydrolysis of  $\text{NH}_4\text{F}$ . This is because the aqueous solution of  $\text{NH}_4\text{F}$  is weakly acidic.

### 3.3. Properties of the Coatings

The surface roughness and wettability of biomaterials have an important influence on cell adhesion and growth [29]. Herein, atomic force microscopy (AFM) was used to measure the roughness of the anatase coatings, as well as to observe their surface topographies in detail. The AFM images of MgZn–0.1 F, MgZn–0.2 F, and MgZn–0.3 F are shown in Figure 6a–c. The AFM micrographs agreed well with the SEM results in Figure 1, and indicated a rougher surface for the MgZn–0.3 F sample with a roughness ( $R_a$ ) of 90.1 nm. On the other hand, both the MgZn–0.1 F and MgZn–0.2 F samples showed a smoother surface with  $R_a$  values of 49.7 and 53.8 nm, respectively. The results showed that the surface roughness of the coatings increased with the concentration of the  $\text{NH}_4\text{F}$ . In addition,

lower density of the anatase nanosheets were clearly observed in the surface of MgZn–0.2 F and MgZn–0.3 F samples. Furthermore, the contact angle of the sample surface with deionized water was tested to assess the surface wettability. The contact angles of the MgZn substrate [14], MgZn–0.1 F, MgZn–0.2 F, and MgZn–0.3 F were  $8.4^\circ$ ,  $13.02^\circ$ ,  $17.14^\circ$ , and  $16.73^\circ$ , as shown in Figure 6d–f. The results indicated that the anatase-coated samples were hydrophilic, and there was no significant difference in wettability between the anatase-coated samples.

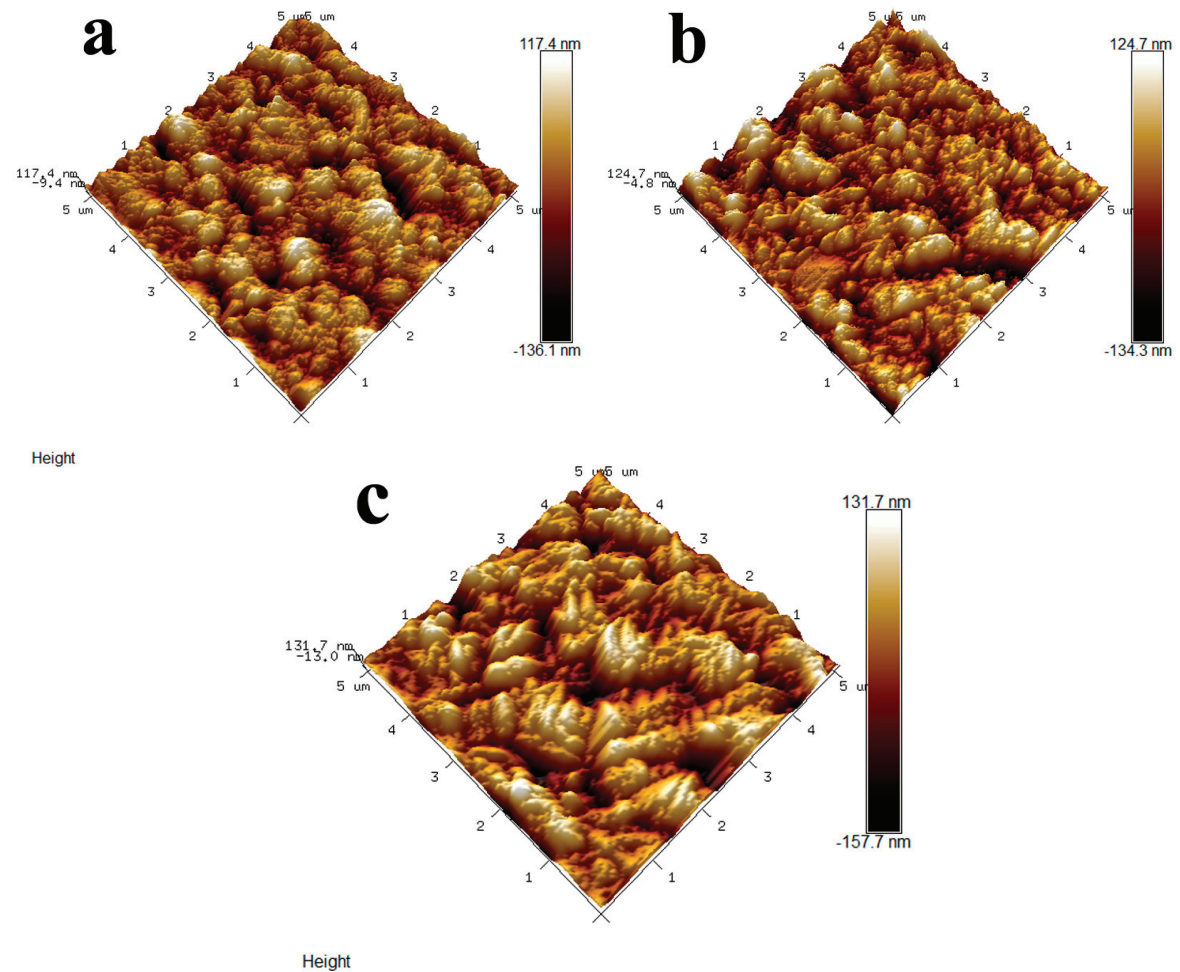


**Figure 6.** AFM micrographs and contact angles of the anatase coatings: (a,d) MgZn–0.1 F; (b,e) MgZn–0.2 F; (c,f) MgZn–0.3 F.

Open-circuit potential (OCP) was used to monitor the chemical stability and estimate the corrosion tendency of the samples. Figure 7 shows the OCP curves in SBF of the anatase-

coated and uncoated samples. For the uncoated MgZn substrate, the open-circuit potential increased continuously in the initial period, and then gradually decreased to a stable value of  $-1.756$  V during 20 min immersion. When the bare MgZn sample was immersed in the SBF, a film of corrosion products began to grow on its surface and acted as a protective layer to increase the potential. Then, the products damaged and broke away from the sample surface to decrease the potential. The damage of the previous products and the formation of the new products gradually reached a dynamic equilibrium. However, the OCP values of all anatase-coated MgZn samples were decreased at the beginning of immersion, until they reached a plateau stage. When the coated samples being immersed, the SBF would progressively permeate the coatings, and the potential of the samples decreased. The protection of the coatings delayed the corrosion process of the magnesium substrate, and led to a higher corrosion potential than that of the bare MgZn sample.

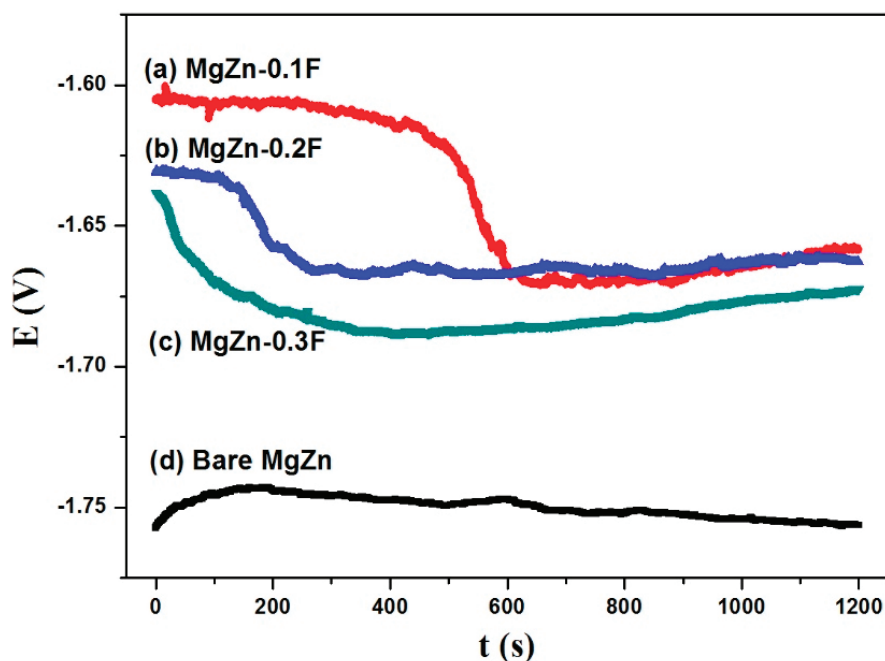


**Figure 7.** Open-circuit potential (OCP) curves of: (a) MgZn–0.1 F; (b) MgZn–0.2 F; (c) MgZn–0.3 F; (d) bare MgZn substrate.

It should be noted that the trend of the OCP curves was distinguishing between the anatase-coated samples. For the MgZn–0.1 F sample, due to the better protection by a compact coating, the OCP curve decreased more slowly than that of the MgZn–0.2 F and MgZn–0.3 F samples. We believe that the low permeability of the dense coating caused by the high densification of the anatase sheets is the major reason of the high level and the slow decrease of the OCP curve. Therefore, based on the above results and discussion, it can be inferred that the corrosion tendency of the samples is decreased with the densification of the coatings, at similar hydrophilicity as shown in Figure 6.

Figure 8a reveals the platelets adhesion to the bare MgZn alloy. The MgZn alloy was corroded by the plasma and the platelets were aggregated together on the surface of the sample. For the anatase-coated sample, the surface was not corroded due to the protection of the coating. A lower number of platelets were adhered on the surface of the MgZn–0.2 F sample, and the agglomeration of the adhered platelets did not exist. However, some platelets had been deformed and the parapodium had stretched out, which implied that the fixed platelets were activated (see in Figure 8b). Thus, it is hard to decide whether or not the coating has the effect of anti-thrombosis. At least the coatings exhibit the inhibition of platelet aggregation.

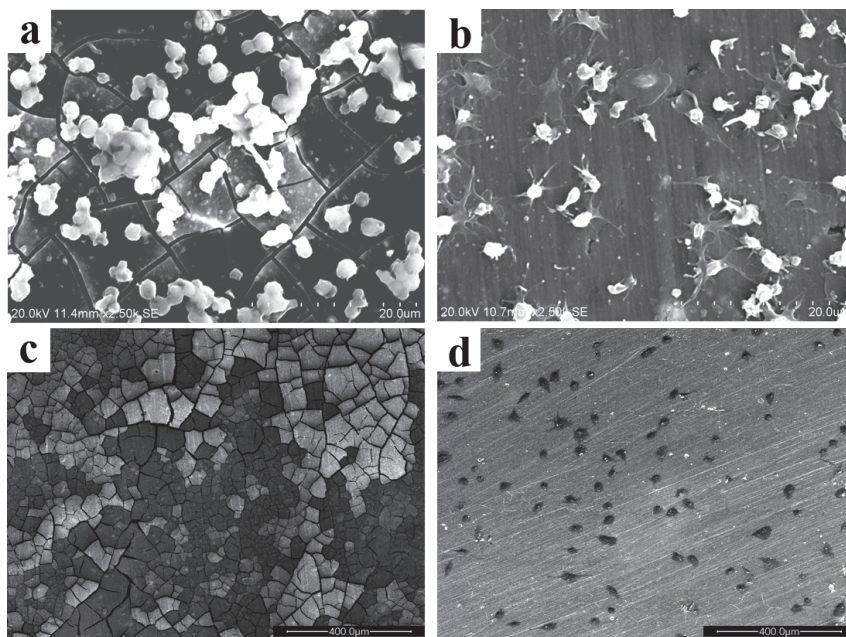


**Figure 8.** Morphology of adherent platelets on (a) MgZn substrate, (b) MgZn-0.2 F sample; and adherent Ea.hy926 cells on (c) MgZn substrate, (d) MgZn-0.2 F sample.

A layer of endothelial cells has been considered as an anticoagulant surface. For cardiovascular stents, if an endothelial cells layer forms quickly on the surface, the risk of clot formation and restenosis in stents could be significantly reduced. As is known, endothelialization can be influenced by the surface on which the endothelial cells attach. Figure 8c,d shows the morphologies of Ea.hy926 cells cultured on the samples for 1 day. On the bare MgZn surface, endothelial cells were not observed (see Figure 8c). However, for the coated sample, it is seen that many Ea.hy926 cells attached on the surface, and spread in a spindle shape, as presented in Figure 8d. The contact angles of the anatase-coated samples were lower than  $20^\circ$  (see Figure 6), and thus the as-prepared coatings can be considered as hydrophilic surfaces. Generally speaking, materials with a rough and hydrophilic surface are more conducive to cell adhesion. Moreover, due to the fact that the corrosion resistance of the MgZn substrate was improved greatly by the anatase coating, the coated sample was more stable in the Dulbecco's modified Eagle medium and more conducive to cell growth. The results suggest that the anatase coatings with micro/nano-characteristic could enhance the adhesion of endothelial cells and promote re-endothelialization, thus preventing the formation of ISR.

#### 4. Conclusions

The major conclusions of the present work are summarized as follows.

- (1) The surface topography of anatase coating could be controlled in the micro- and nanometer range by the solvothermal method. The anatase coatings were composed of anatase sheets with a thickness of 10–20 nm, and the anatase nanosheets were agglomerated with varying degrees of density. With the increase of  $\text{NH}_4\text{F}$  concentration in the solvothermal solution, the anatase nanosheets were more dispersed, and the surface roughness ( $R_a$ ) was increased from 49.7 to 90.1 nm. The contact angles of MgZn-0.1 F, MgZn-0.2 F, and MgZn-0.3 F samples were  $13.02^\circ$ ,  $17.14^\circ$ , and  $16.73^\circ$ , indicating good hydrophilicity of the anatase coatings.
- (2) After being coated with the anatase coatings, the corrosion resistance of the bare MgZn alloy substrate was improved. Additionally, the corrosion tendency was decreased with the increasing agglomeration density of the anatase nanosheets in the coatings.

- (3) The bare MgZn alloys caused serious platelet aggregation, yet the anatase-coated sample adsorbed a smaller number of platelets, and did not lead to the agglomeration of the adhered platelets. After being coated with anatase, the samples can adsorb endothelial cells on the surface, which maybe promote the re-endothelialization of stents.

**Author Contributions:** Conceptualization, S.H. and L.Y.; methodology, W.Y.; formal analysis, L.L. and S.H.; writing—original draft preparation, T.Y. and Y.L.; writing—review and editing, W.Y. and S.H. All authors have read and agreed to the published version of the manuscript.

**Funding:** This research was funded by Key Research and Development Specialized Project of Henan Province (Grant No. 182102210120, 222102230023) and Key Scientific Research Project of College and University of Henan Province (Grant No. 22A430035).

**Institutional Review Board Statement:** Not applicable.

**Informed Consent Statement:** Not applicable.

**Data Availability Statement:** Not applicable.

**Conflicts of Interest:** The authors declare no conflict of interest.

## References

1. Cho, Y.C.; Hung, W.C.; Lan, W.C.; Saito, T.; Huang, B.H.; Lee, C.H.; Tsai, H.Y.; Huang, M.S.; Ou, K.L. Anodized Biomedical Stainless-Steel Mini-Implant for Rapid Recovery in a Rabbit Model. *Metals* **2021**, *11*, 1575. [CrossRef]
2. Ho, M.Y.; Chen, C.C.; Wang, C.Y.; Chang, S.H.; Hsieh, M.J.; Lee, C.H.; Wu, V.; Hsieh, I.C. The Development of Coronary Artery Stents: From Bare-Metal to Bio-Resorbable Types. *Metals* **2016**, *6*, 168. [CrossRef]
3. Rout, P.K.; Roy, S.; Ganguly, S.; Rathore, D.K. A review on properties of magnesium-based alloys for biomedical applications. *Biomed. Phys. Eng. Express*. **2022**, *8*, 042002. [CrossRef] [PubMed]
4. Chagnon, M.; Guy, L.G.; Jackson, N. Evaluation of Magnesium-based Medical Devices in Preclinical Studies: Challenges and Points to Consider. *Toxicol. Pathol.* **2019**, *47*, 390–400. [CrossRef] [PubMed]
5. Zhang, D.; Liu, Y.; Liu, Z.; Wang, Q. Advances in Antibacterial Functionalized Coatings on Mg and Its Alloys for Medical Use—A Review. *Coatings* **2020**, *10*, 828. [CrossRef]
6. Soleymani, F.; Emadi, R.; Sadeghzade, S.; Tavangarian, F. Bioactivity Behavior Evaluation of PCL-Chitosan-Nanobaghdadite Coating on AZ91 Magnesium Alloy in Simulated Body Fluid. *Coatings* **2020**, *10*, 231. [CrossRef]
7. Gu, X.N.; Guo, H.M.; Wang, F.; Lu, Y.; Lin, W.T.; Li, J.; Zheng, Y.F.; Fan, Y.B. Degradation, hemolysis, and cytotoxicity of silane coatings on biodegradable magnesium alloy. *Mater. Lett.* **2017**, *193*, 266–269. [CrossRef]
8. Echeverry-Rendon, M.; Allain, J.P.; Robledo, S.M.; Echeverria, F.; Harmsen, M.C. Coatings for biodegradable magnesium-based supports for therapy of vascular disease: A general view. *Mater. Sci. Eng. C Mater.* **2019**, *102*, 150–163. [CrossRef]
9. Rourke, A.S.; Beard, M.C.; Jones, S.E.; Priddy, M.W.; Priddy, L.B. Hydroxyapatite coating promotes stable physicochemical properties of pure magnesium in a longitudinal degradation study. *J. Mater. Res.* **2022**, *37*, 1231–1245. [CrossRef]
10. Zhang, Q.; Zhang, L.; Yang, M.; Hong, Q.; Yang, Z.; Liu, S.; Xiong, Q.; Pan, C. Construction of Chi(Zn/BMP2)/HA composite coating on AZ31B magnesium alloy surface to improve the corrosion resistance and biocompatibility. *Nanotechnol. Rev.* **2021**, *10*, 870–882. [CrossRef]
11. Ben-Yehuda, O. Long-Term Outcomes with Drug-Eluting Stents: Beyond Stent Choice. *J. Am. Coll. Cardiol.* **2020**, *76*, 159–161. [CrossRef] [PubMed]
12. Dong, H.; Li, D.; Mao, D.; Bai, N.; Chen, Y.; Li, Q. Enhanced performance of magnesium alloy for drug-eluting vascular scaffold application. *Appl. Surf. Sci.* **2018**, *435*, 320–328. [CrossRef]
13. Liu, J.; Zheng, B.; Wang, P.; Wang, X.; Zhang, B.; Shi, Q.; Xi, T.; Chen, M.; Guan, S. Enhanced in Vitro and in Vivo Performance of Mg-Zn-Y-Nd Alloy Achieved with APTES Pretreatment for Drug-Eluting Vascular Stent Application. *ACS Appl. Mater. Interfaces* **2016**, *8*, 17842–17858. [CrossRef] [PubMed]
14. Hou, S.; Yu, W.; Yang, Z.; Li, Y.; Yang, L.; Lang, S. Properties of Titanium Oxide Coating on MgZn Alloy by Magnetron Sputtering for Stent Application. *Coatings* **2020**, *10*, 999. [CrossRef]
15. Ramos-Corella, K.J.; Sotelo-Lerma, M.; Gil-Salido, A.A.; Rubio-Pino, J.L.; Auciello, O.; Quevedo-López, M.A. Controlling crystalline phase of TiO<sub>2</sub> thin films to evaluate its biocompatibility. *Mater. Technol.* **2019**, *34*, 455–462. [CrossRef]
16. Hou, S.S.; Zhang, R.R.; Guan, S.K.; Ren, C.X.; Gao, J.H.; Lu, Q.B.; Cui, X.Z. In vitro corrosion behavior of Ti-O film deposited on fluoride-treated Mg-Zn-Y-Nd alloy. *Appl. Surf. Sci.* **2012**, *258*, 3571–3577. [CrossRef]
17. Liang, C.; Hu, Y.; Wang, H.; Xia, D.; Li, Q.; Zhang, J.; Yang, J.; Li, B.; Li, H.; Han, D.; et al. Biomimetic cardiovascular stents for in vivo re-endothelialization. *Biomaterials* **2016**, *103*, 170–182. [CrossRef]
18. Liu, T.; Liu, S.; Zhang, K.; Chen, J.; Huang, N. Endothelialization of implanted cardiovascular biomaterial surfaces: The development from in vitro to in vivo. *J. Biomed. Mater. Res. A* **2014**, *102*, 3754–3772. [CrossRef]

19. Guo, X.; Wang, X.; Li, X.; Jiang, Y.C.; Han, S.; Ma, L.; Guo, H.; Wang, Z.; Li, Q. Endothelial Cell Migration on Poly(epsilon-caprolactone) Nanofibers Coated with a Nanohybrid Shish-Kebab Structure Mimicking Collagen Fibrils. *Biomacromolecules* **2020**, *21*, 1202–1213. [CrossRef]
20. Cutiongco, M.F.A.; Goh, S.H.; Aid-Launais, R.; Le Visage, C.; Low, H.Y.; Yim, E.K.F. Planar and tubular patterning of micro and nano-topographies on poly(vinyl alcohol) hydrogel for improved endothelial cell responses. *Biomaterials* **2016**, *84*, 184–195. [CrossRef]
21. Bedair, T.M.; ElNaggar, M.A.; Joung, Y.K.; Han, D.K. Recent advances to accelerate re-endothelialization for vascular stents. *J. Tissue Eng.* **2017**, *8*. [CrossRef] [PubMed]
22. Jana, S. Endothelialization of cardiovascular devices. *Acta Biomater.* **2019**, *99*, 53–71. [CrossRef]
23. Hou, S.; Mi, L.; Wang, L.; Zhu, S.; Hu, J.; Ding, Q.; Guan, S. Corrosion protection of Mg-Zn-Y-Nd alloy by flower-like nanostructured TiO<sub>2</sub> film for vascular stent application. *J. Chem. Technol. Biot.* **2013**, *88*, 2062–2066. [CrossRef]
24. Hou, S. Solvothermal fabrication of TiO<sub>2</sub> nanosheet films on degradable Mg-Zn alloys. *Surf. Eng.* **2016**, *32*, 745–749. [CrossRef]
25. Wang, J.; Wang, L.; Guan, S.; Zhu, S.; Ren, C.; Hou, S. Microstructure and corrosion properties of as sub-rapid solidification Mg-Zn-Y-Nd alloy in dynamic simulated body fluid for vascular stent application. *J. Mater. Sci. Mater. Med.* **2010**, *21*, 2001–2008. [CrossRef]
26. Kokubo, T.; Takadama, H. How useful is SBF in predicting in vivo bone bioactivity? *Biomaterials* **2006**, *27*, 2907–2915. [CrossRef]
27. Lu, Y.; Wang, G.; Zhang, H.; Zhang, Y.; Kang, S.; Zhao, H. Photoelectrochemical manifestation of intrinsic photoelectron transport properties of vertically aligned {001} faceted single crystal TiO<sub>2</sub> nanosheet films. *RSC Adv.* **2015**, *5*, 55438–55444. [CrossRef]
28. Yang, H.G.; Sun, C.H.; Qiao, S.Z.; Zou, J.; Liu, G.; Smith, S.C.; Cheng, H.M.; Lu, G.Q. Anatase TiO<sub>2</sub> single crystals with a large percentage of reactive facets. *Nature* **2008**, *453*, 638–641. [CrossRef]
29. Hallab, N.J.; Bundy, K.J.; O'Connor, K.; Moses, R.L.; Joshua, J.; Jacobs, J.J. Evaluation of Metallic and Polymeric Biomaterial Surface Energy and Surface Roughness Characteristics for Directed Cell Adhesion. *Tissue Eng.* **2001**, *7*, 55–71. [CrossRef]

Article

# Investigation of the Long-Term Antibacterial Properties of Titanium by Two-Step Micro-Arc Oxidation Treatment

Harumi Tsutsumi<sup>1,\*</sup>, Yusuke Tsutsumi<sup>2,\*</sup>, Masaya Shimabukuro<sup>1,3</sup>, Tomoyo Manaka<sup>4</sup>, Peng Chen<sup>1</sup>, Maki Ashida<sup>1</sup>, Kunio Ishikawa<sup>3</sup>, Hideki Katayama<sup>2</sup> and Takao Hanawa<sup>1,5</sup>

<sup>1</sup> Institute of Biomaterials and Bioengineering, Tokyo Medical and Dental University (TMDU), 2-3-10 Kanda-Surugadai, Chiyoda, Tokyo 101-0062, Japan; shimabukuro@dent.kyushu-u.ac.jp (M.S.); chen.met@tmd.ac.jp (P.C.); ashida.met@tmd.ac.jp (M.A.); hanawa.met@tmd.ac.jp (T.H.)

<sup>2</sup> Research Center for Structural Materials, National Institute for Materials Science (NIMS), 1-2-1 Sengen, Ibaraki, Tsukuba 305-0047, Japan; KATAYAMA.Hideki@nims.go.jp

<sup>3</sup> Department of Biomaterials, Faculty of Dental Science, Kyushu University, 3-1-1 Maidashi, Higashi-ku, Fukuoka 812-8582, Japan; ishikawa@dent.kyushu-u.ac.jp

<sup>4</sup> Graduate School of Medical and Dental Sciences, Tokyo Medical and Dental University (TMDU), 1-5-45 Yushima, Bunkyo, Tokyo 113-8510, Japan; manaka.met@tmd.ac.jp

<sup>5</sup> Center for Advanced Medical Engineering Research and Development, Kobe University, 1-5-1 Minatojima-minamimachi, Chuoku, Hyogo, Kobe 650-0047, Japan

\* Correspondence: htsutsumi.met@tmd.ac.jp (H.T.); TSUTSUMI.Yusuke@nims.go.jp (Y.T.)

**Abstract:** Recently, biofilm formation caused by bacterial adhesion and colonization has been recognized as the major cause of failure in orthopedic and dental implant surgeries. In this study, a customized micro-arc oxidation (MAO) treatment technique was developed to obtain desirable antibacterial properties on Ti surfaces. The two-step MAO treatment was applied in the fabrication of specimens with Ag and with/without Zn in their surface oxide layer. In order to simulate practical usage, surface analyses and immersion tests were performed to evaluate the incorporation of Ag and Zn into the resulting oxide layer and ion release behavior, respectively. Additionally, the antibacterial properties of the specimens after long-term immersion in physiological saline were evaluated using Gram-negative facultative anaerobic bacteria. The MAO-treated specimens containing Ag and Zn exhibited excellent antibacterial properties against *Escherichia coli*, which were sustained even after 6 months of immersion in physiological saline to simulate practical usage. Moreover, the Ag ions released from the surface oxide indicate the antibacterial properties of the specimen in the early stage, while the release of the corrosion products of Zn demonstrates its antibacterial properties in the later stage.

**Keywords:** titanium; antibacterial property; micro-arc oxidation; *Escherichia coli*; silver; zinc

## 1. Introduction

Ti and its alloys are widely used in medical fields, such as orthopedics and dentistry, due to their excellent mechanical properties and biocompatibility. In implant devices, Ti has been associated with strong and accelerated adhesion between the implant surface and surrounding bone, achieving a shorter healing period and immediate loading [1–4]. However, in recent years, the major cause of failure in orthopedic and dental implant surgeries has been determined to be biofilm formation due to bacterial adhesion and subsequent colonization on biomaterials [5–9]. Once a biofilm is formed and firmly adhered to the implant, bacterial secretion plays a pestiferous role as a barrier against the defense mechanisms of the host, resulting in difficulty eliminating pathogens during biofilm formation from implanted devices. Further, in serious cases, the only way to prevent subsequent infections and other undesirable biological reactions is to remove contaminated devices from the patient.

The easiest strategy to prevent biofilm formation on metallic devices is polishing, as a rough surface promotes bacterial adhesion. In particular, the increase in surface area and formation of pockets increases bacterial presence [10,11]. However, for dental implants and orthodontic fixators in contact with bones, a rough surface is preferred to ensure hard-tissue compatibility; thus, surface polishing is not the most effective approach for this application. Another method to prevent biofilm formation is the application of antibacterial agents. Antibacterial properties are required for the biofunction of implant surfaces. Ag and Zn ions are known as reliable agents with superior antibacterial properties; thus, several studies have examined their effects against various bacteria [12–22]. Therefore, surface modification should enable the formation of a biofunctional layer that supports Ag and Zn ions to overcome problems associated with biofilms on metallic biomaterials.

Micro-arc oxidation (MAO) is a conventional wet-process surface treatment based on electrochemical reactions [23–26]. Under high voltage, anodic oxidation with microdischarges on the specimen surface forms a connective, porous oxide layer with elements incorporated from the electrolyte solution. For example, MAO using electrolytes comprising Ca and P ions improves the hard-tissue compatibility of Ti due to the spontaneous formation of calcium phosphate [27,28]. Therefore, MAO treatment can be utilized in incorporating the desired elements, which are dissolved in the electrolyte into the resulting oxide layer.

In our previous study, we reported the effectivity of Ag and Zn in inhibiting the proliferation of *Escherichia coli* (*E. coli*) and/or *Staphylococcus aureus* (*S. aureus*), respectively [29–32]. The results showed the different inhibition mechanisms and efficacies of the elements. Particularly, Ag exhibits a strong antibacterial effect during the initial period, and Zn exhibits a heightened antibacterial effect over time. Furthermore, we developed a two-step MAO treatment [33] that allows for the introduction of a high concentration of Ag into the Ti surface. The two-step MAO treatment also enabled the fabrication of a specimen containing both Ag and Zn in its surface oxide layer. After immersion for one month, the MAO-treated surfaces containing Ag with/without Zn maintained excellent antibacterial properties [33].

Implants, especially artificial joints, must exhibit a specific biofunction to ensure long-term antimicrobial resistance. Implants with long-term antibacterial activity are strongly desired to address the late-onset infection problems in artificial hip joints [34–36] that occur approximately three to eight weeks after surgery. Therefore, an ideal biomaterial surface should have an antibacterial activity that can prevent the initial stages of infection, such as bacterial adhesion, and inhibit bacterial growth at later stages.

The above-mentioned two-step MAO treatment that we proposed previously [33] has been demonstrated to be a promising tool for solving late-onset infection problems in implanted devices. However, it was not possible to clearly distinguish whether the strong antibacterial properties were derived from both Zn and Ag ions or from Ag ions alone. Furthermore, it is unclear for how long the antimicrobial activity will be maintained after a prolonged exposure of several months.

Therefore, the present study focused on incorporating antibacterial elements into a Ti surface through MAO treatment to develop novel antibacterial implants without harmful effects on osteogenic cells. Further, we analyzed the long-term behavior of Ag with/without a Zn-incorporated surface oxide layer produced by the two-step MAO treatment for preventing late-onset infections. Additionally, we investigated the time transient effect of the surface composition, metal-ion release and antibacterial activity of Ag and Zn. Changes in the antibacterial activity of the specimens before and after immersion for 2, 3, and 6 months in physiological saline were evaluated by using the standard method, with *E. coli* as the typical Gram-negative facultative anaerobic bacteria.

## 2. Materials and Methods

### 2.1. Specimen Preparation

Ti disks with diameters of 25 mm were fabricated by mechanically cutting rods of commercially pure grade 2 Ti. The surfaces of the disks were mechanically ground using #150, #320, #600, and #800 grit SiC abrasive papers and subsequently ultrasonicated using acetone and isopropanol. The disks were then kept in an auto-dry desiccator until further use. The Ti disk was fixed onto a polytetrafluoroethylene holder with an O-ring. The area in contact with the electrolyte was 398 mm<sup>2</sup> (22.5 mm in diameter). The details of the working electrode were adopted from a previous study [37]. A 304 stainless-steel plate was used as the counter electrode. For the MAO treatment, the base composition of the electrolyte was 100 mM calcium glycerophosphate and 150 mM calcium acetate. Silver nitrate (AgNO<sub>3</sub>) and zinc chloride (ZnCl<sub>2</sub>) were added to the base electrolyte. After pouring the electrolyte into the electrochemical cell, the electrodes were connected to a direct current (DC) power supply (PL-650-0.1, Matsusada Precision Inc., Shiga, Japan), and a positive voltage with a constant current density of 251 Am<sup>-2</sup> was applied for 10 min. The majority of the Ti disk was MAO-treated with an annular untreated area of 0.5 mm from the edge.

The two-step MAO treatment was conducted as follows: MAO treatment was performed in the first electrolyte until a voltage of 380 V was obtained, after which the current application was discontinued and the first electrolyte was immediately replaced with the second electrolyte. The current was reapplied with an upper limit of 400 V for a total treatment time of 10 min. The specimen prepared using the base electrolyte without Ag and Zn is referred to as “0AgZn.” The specimen prepared using the combination of the first and second electrolytes containing *i* mM Zn (*i* = 0 or 2) and/or *j* mM Ag (*j* = 0–10), respectively, is referred to as “*i*Zn–*j*Ag”.

### 2.2. Surface Characterization

Surface characterization was performed on the MAO-treated area of the specimens. A scanning electron microscope with an energy dispersive X-ray spectrometer (SEM/EDS, S-3400NX, Hitachi High-Tech Corp., Tokyo, Japan) was used to observe the surface morphology and perform the elemental analysis of the specimens.

### 2.3. Metal Ion Release Evaluation

Metal ion release measurements were recorded for the entire specimen. Inductively coupled plasma mass spectrometry (ICP-MS, ELEMENT XR, Thermo Fisher Scientific, Tokyo, Japan) was used to investigate the amounts of released Ag and Zn ions. The MAO-treated specimens in the electrolytes with/without Ag and Zn were incubated in 5 mL physiological saline (0.9% NaCl) under various treatment conditions. They were sealed in a polyethylene container to allow for the release of Ag and Zn ions from the surface of the specimen. Subsequently, they were maintained in a thermostatic chamber at 37 °C with moderate shaking (80–100 rpm). Every seventh day, the pooled solution was transferred into a fresh physiological saline. ICP-MS was used to measure the concentrations of Ag and Zn ions in the tested solutions collected at immersion periods of 2 months (53–60 days), 3 months (83–90 days), and 6 months (173–180 days). After the metal ion release evaluations of the specimens immersed for various durations, the specimens were used as aged specimens to compare their antibacterial properties with those of the as-prepared specimens.

### 2.4. Evaluation of Antibacterial Properties

Antibacterial property tests were conducted in accordance with the domestic [38] and international [39] standard methods JIS Z2801 [38] and ISO 22196:2007 [39], respectively. The proliferation of the anaerobic Gram-negative bacteria *E. coli* (NBRC3972, NITE, Tokyo, Japan) on the specimens was evaluated. *E. coli* is frequently utilized as one of the most standardized and convenient testing bacteria for evaluating the antibacterial properties of

biomaterials, although it is absent in the oral cavity environment. A suspension medium was prepared with the 500-fold dilution of the nutrient broth containing  $3 \text{ gL}^{-1}$  meat extract,  $10 \text{ gL}^{-1}$  peptone, and  $5 \text{ gL}^{-1}$  sodium chloride. The pH of each suspension medium was adjusted to 6.8 or 7.2 using sodium hydroxide or hydrochloric acid. The bacteria were added to the suspension mediums to obtain  $3.1 \times 10^6$  colony-forming units (CFU) per mL. The bacterial suspension (0.1 mL) was then dropped onto a specimen, and a cover film was immediately placed. The specimens and cover films were incubated at  $35 \text{ }^\circ\text{C}$  for 24 h. Thereafter, they were washed using 9.9 mL sterile physiological saline. The CFU of the living bacteria dispersed into the physiological saline was determined using the culture medium sheet for *E. coli* (JNC Corp., Tokyo, Japan).

### 3. Results and Discussion

Figure 1 shows the typical surface morphology of the untreated and MAO-treated as-prepared specimens observed using SEM. There are several interconnected pores on the MAO-treated specimens. In addition, there is no obvious difference in the pore size and number of pores among the specimens prepared under the various treatment conditions. Figure 2 shows the typical surface morphology of the untreated and MAO-treated specimens after immersion in physiological saline for 2 months. There are no changes in the surface morphology before and after immersion, confirming the non-existent or negligible dissolution of the porous oxide layer during immersion in physiological saline. Moreover, there are no remarkable differences in the pore size and quantity of the specimens before and after immersion.

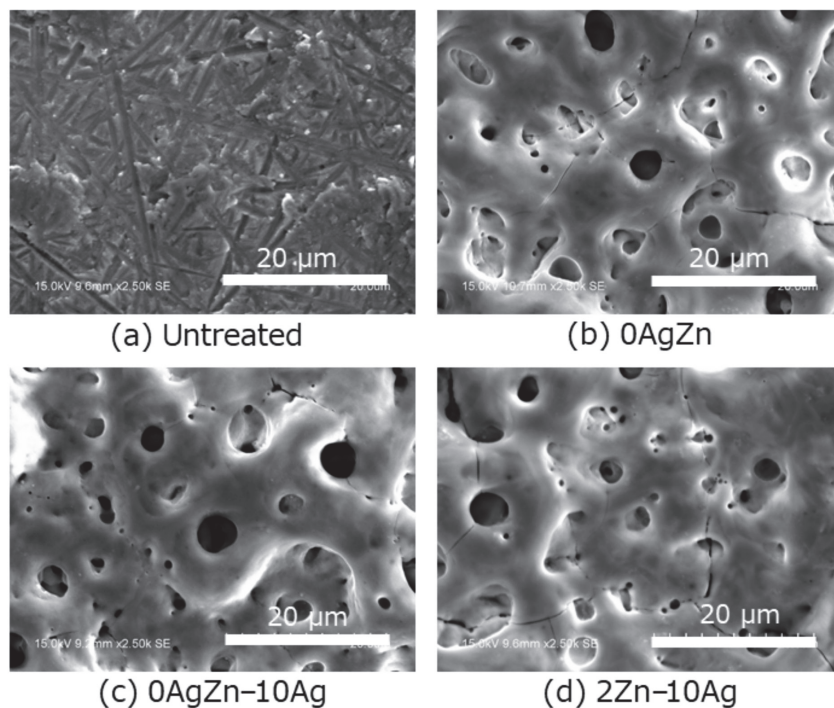


**Figure 1.** Typical surface morphology of the as-prepared specimens: (a) untreated, (b) 0AgZn, (c) 0AgZn–10Ag, and (d) 2Zn–10Ag.

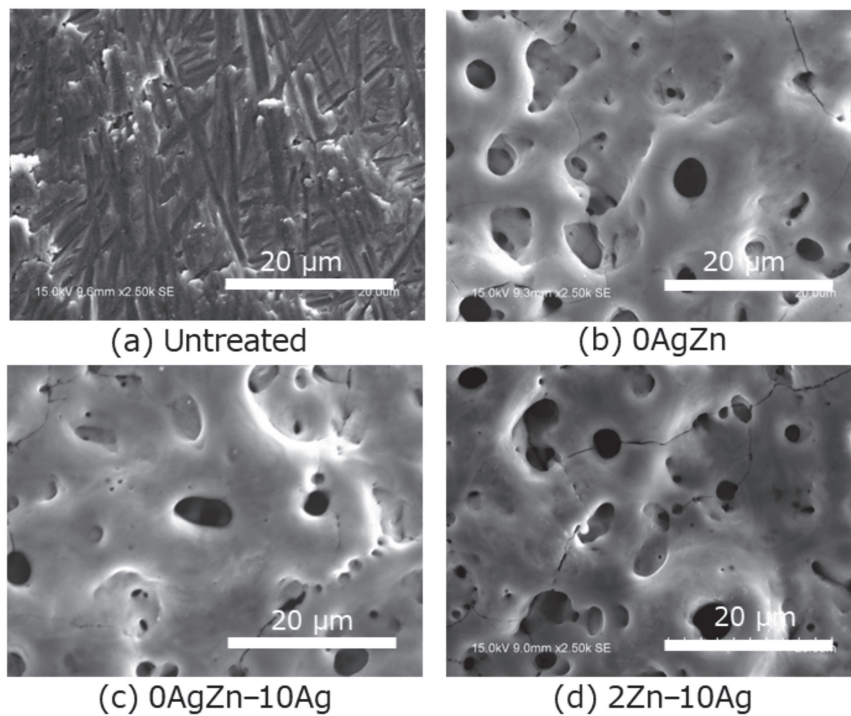
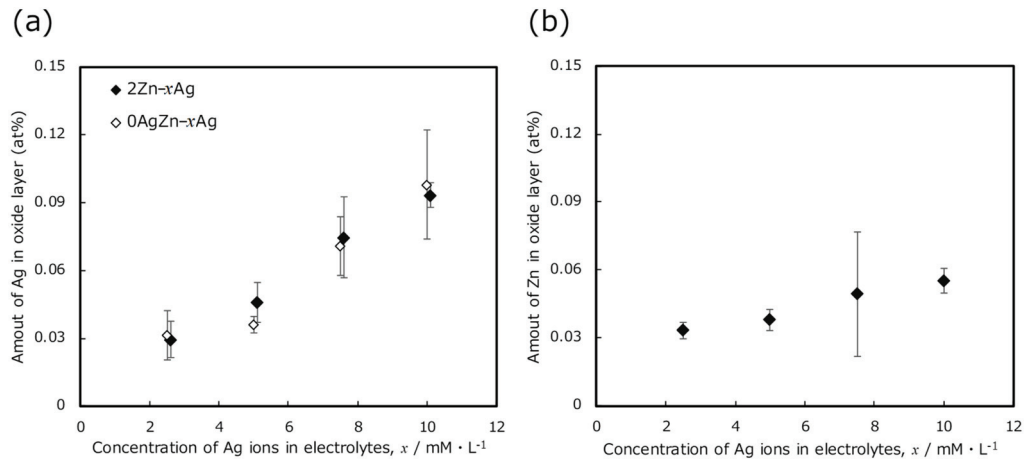


**Figure 2.** Typical surface morphology of the (a) untreated and MAO-treated (b) 0AgZn, (c) 0AgZn–10Ag, and (d) 2Zn–10Ag specimens after immersion in physiological saline for 2 months.

EDS measurements were performed to evaluate the amounts of Ag (treatment condition is 0AgZn– $x$ Ag) and Ag and Zn (treatment condition is 2Zn– $x$ Ag) incorporated into the oxide layers through the two-step MAO treatment. Regardless of the treatment conditions, the chemical compositions of the layers were approximately constant at 28 wt.% Ti, 47 wt.% O, 1 wt.% C, 13 wt.% Ca, and 11 wt.% P (12 at.% Ti, 57 at.% O, 3 at.% C, 9 at.% Ca, and 9 at.% P). Therefore, a surface titanium oxide layer containing relatively large amounts of Ca and P is formed after MAO treatment.

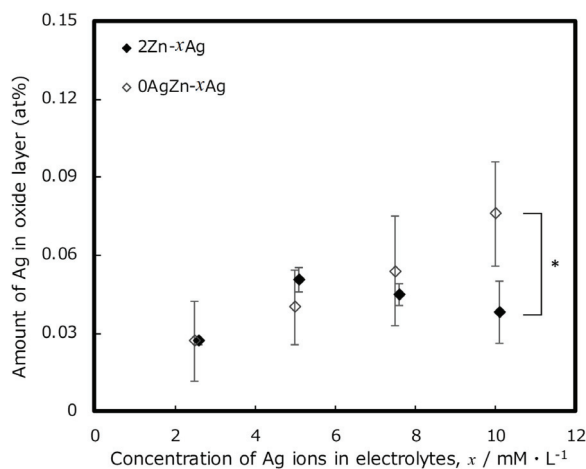
The relationship between the  $\text{AgNO}_3$  concentration in the treatment electrolyte for the two-step treatment and the amount of Ag incorporated into the resulting surface oxide layer is shown in Figure 3a. For 0AgZn– $x$ Ag, the amount of Ag in the oxide layer increased with an increase in the  $\text{AgNO}_3$  concentration in the second electrolyte. A similar trend was observed for 2Zn– $x$ Ag, in which the amount of Ag incorporated into the oxide layer increased with an increase in the  $\text{AgNO}_3$  concentration in the second electrolyte. Therefore, regardless of the presence of Zn, the amount of Ag increased with an increase in the Ag concentration in the electrolyte.

The two-step MAO treatment allowed for the use of solutions with high Ag content that exceeded the concentration limit for the single-step treatments (2.5–5 mM [29,33]). After the formation of the precursor oxide layer in the first step of the MAO treatment, the surface maintained a sufficiently high electrical resistance to maintain the MAO reaction. Figure 3b shows the relationship between the  $\text{AgNO}_3$  concentration in the electrolyte solution for the two-step treatment and the amount of Zn incorporated into the resulting surface oxide layer. With the  $\text{ZnCl}_2$  concentration of the electrolyte fixed to 2 mM, there was almost no difference in the amount of Zn incorporated into the surface oxide layer. Meanwhile, the  $\text{AgNO}_3$  concentration in the second electrolyte had a minimal effect on the amount of Zn incorporated into the surface oxide surface.



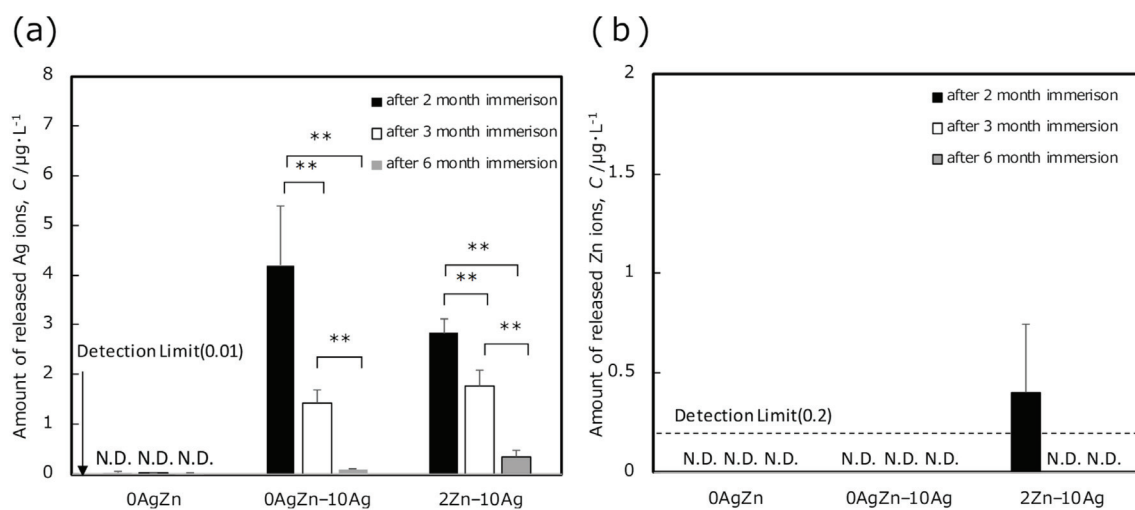
**Figure 3.** Relationship between the  $\text{AgNO}_3$  concentration in the second electrolyte and the amount of (a) Ag and (b) Zn incorporated into the resulting oxide layer.

Figure 4 shows the relationship between the  $\text{AgNO}_3$  concentration in the electrolyte and the amount of Ag in the oxide layer after immersion in physiological saline for 2 months. Comparing the specimens before (Figure 3a) and after (Figure 4) immersion in the saline solution, the amount of Ag in the oxide film decreased after immersion, especially in specimens with a higher Ag content. For  $0\text{AgZn}-x\text{Ag}$ , a relatively higher amount of Ag was maintained in the surface oxide layer, even after 2 months of immersion, showing a similar trend to that of  $0\text{AgZn}-x\text{Ag}$  before immersion. For the  $2\text{Zn}-x\text{Ag}$  specimens, although Ag was detected in the surface oxide layer after 2 months of immersion, the amount of residual Ag with respect to the Ag concentration in the electrolyte did not exhibit a linearly increasing trend. Particularly,  $2\text{Zn}-10\text{Ag}$  had a significantly lower Ag content than that of  $0\text{AgZn}-10\text{Ag}$ , which differed from the trend seen in  $2\text{Zn}-x\text{Ag}$  before immersion. In addition, after 2 months of immersion the amount of Zn in the surface oxide layer of all  $2\text{Zn}-x\text{Ag}$  specimens was under the detection limit of EDS. Moreover, the specific X-ray energy peak derived from Zn might overlap with that derived from Na. Nevertheless, it could be considered that the Zn incorporated into the oxide layer was consumed to some extent during the immersion period in physiological saline. However, it was suggested that the presence of Zn in the oxide layer affects the release of the Ag ions from the surface oxide during immersion in physiological saline.



**Figure 4.** Relationship between the  $\text{AgNO}_3$  concentration in the second electrolyte and the amount of Ag incorporated into the resulting oxide layer after 2 months of immersion in physiological saline. (\*: Statistically significant difference,  $p < 0.05$ ).

In order to elucidate the metal ion release behavior, long-term immersion tests were performed under specific specimen conditions following the same method as that described above. The amount of Ag ions released from the oxide layer into physiological saline, as determined by ICP-MS, is shown in Figure 5. The highest amount of Ag ions was released within the first 2 months of the measurement period, and the amount gradually decreased thereafter. Both 0AgZn–10Ag and 2Zn–10Ag demonstrated the suppressed release of Ag ions during the immersion period. After 2 months of immersion, the amount of Ag ions released from 2Zn–10Ag was slightly less than that released from 0AgZn–10Ag. After 3 and 6 months of immersion, both specimens exhibited the same amount of Ag ion release. In our previous study [33], the highest amount of released Ag ions was noted in the surface oxide layer of MAO-treated Ti containing Ag during the first week of immersion in physiological saline, and the amount gradually decreased after immersion for one month. The results of the present study are consistent with this trend, indicating that the release of Ag ions degrades after a long period of usage.



**Figure 5.** Amount of (a) Ag ions and (b) Zn ions released from the oxide layer into physiological saline. (N.D.: Not detected, \*\*: Statistically significant difference,  $p < 0.05$ ).

In our previous study [31,33], Zn ion release from specimens incorporated with Zn using MAO treatment could not be detected with ICP atomic emission spectroscopy. Therefore, ICP-MS, which has a 100–1000 times higher detection sensitivity, was employed to detect the trace amounts of released Zn; however, the volume of Zn ions released from the oxide layer was still below the detection limit for all tested specimens. This can be attributed to the strong adsorption of Zn ions followed by the formation of Zn products and complexes on the surface [31]. The Zn ions released from the oxidized layer were immediately consumed for the reaction that formed the Zn species; thus, only minimal amounts of Zn were released into the solution.

Antibacterial tests were performed to investigate the antibacterial effects of the Zn products that gradually formed on the specimen's surface after its long-term immersion in a simulated body fluid. Figure 6 shows the change in the antibacterial properties of the MAO-treated and untreated Ti specimens against *E. coli*. After 24 h of culturing, almost all bacteria survived on the surface of the reference specimens that lacked antibacterial agents (i.e., untreated Ti and 0AgZn). In contrast, 0AgZn–10Ag and 2Zn–10Ag exhibited strong antibacterial properties, as indicated by the complete absence of *E. coli* after 24 h of culturing. Further, this antimicrobial effect was maintained after specimens underwent 2 months of aging treatment by immersion in physiological saline solution. This superior antibacterial properties of the as-prepared fresh specimens against *E. coli* can be mainly attributed to the release of Ag ions, as shown in Figure 5a. In the case of 0AgZn–10Ag, the amount of Ag ions released continued to decrease during the immersion in physiological

saline, in which it decreased by a factor of approximately 3 after 3 months and a factor of approximately 40 after 6 months. Therefore, in practical usage, the antibacterial properties of MAO-treated specimens are expected to weaken because of the decreasing Ag ion release that occurs during long-term implantation.

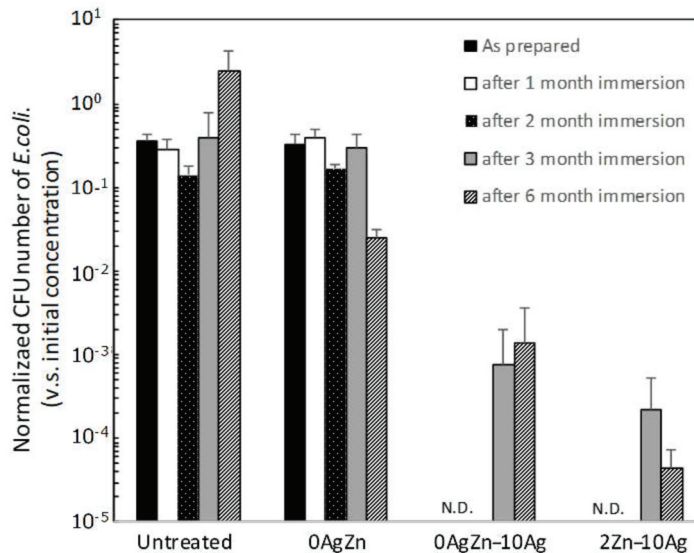


**Figure 6.** Changes in the antibacterial properties of the specimens against *E. coli* before and after immersion in physiological saline. (N.D.: Not detected).

As expected, antibacterial properties decreased as the immersion period increased from 2 to 6 months. This can be attributed to the depletion of the incorporated Ag ions and/or the formation of insoluble salts, such as AgCl, which covered the surface because the amount of leached Ag ions decreased with the increasing immersion time. For 2Zn–10Ag, the antibacterial effect decreased after 3 months of immersion and increased again after 6 months of immersion, which differs from ICP-MS measurement results, wherein the amount of released Ag ions decreased with the increasing immersion time. This suggests that the Zn products on the specimen surface gradually formed and matured during the immersion period [31]. Therefore, the prolonged antibacterial efficacy of the specimens could be attributed to the presence of Zn. The re-emergence of the antibacterial properties of 2Zn–10Ag after 6 months of aging corresponds with the delayed effect noted in the single-step MAO treatment proposed in our previous study [29,31], in which complex Zn products were detected by X-ray photoelectron spectroscopy (XPS). Therefore, the two-step MAO treatment that introduced Ag and Zn into the Ti surface enabled two independent antibacterial effects: an initial antibacterial property due to the release of Ag ions and a delayed antibacterial property due to the formation of Zn products. Moreover, the excellent antibacterial properties of the MAO-treated Ti surface were maintained after 6 months of practical usage.

Finally, the limitations of this study must be mentioned. Under the set experimental conditions, Zn could not be directly detected by EDS after immersion in physiological saline. Moreover, under most conditions, the trace amounts of Zn ions released during the immersion were almost undetectable even with high-resolution ICP-MS measurement. As a subject for future research, Zn can be detected by examining the chemical surface state of the specimen surface through XPS. In addition, we plan to optimize treatment conditions, such as the amount of incorporated Ag and Zn, because excess Ag ion release has a cytotoxic effect on osteogenic cells [40–45]. Realizing both antibacterial properties and hard-tissue compatibility is the ideal outcome of this study [29]. Another limitation of the present study is the lack of results on the effectiveness of the proposed method against various bacterial species. Although *E. coli* is used in standard tests, the effect of Ag and Zn on other bacteria remains unknown, even with the broad antibacterial

spectrum of Ag [13–15,46–49]. Particularly, Gram-positive facultative anaerobic bacteria, such as *S. aureus*, and primal bacteria play important roles in biofilm formation in practical environments; thus, they should be investigated in more detail.

#### 4. Conclusions

Ag and Zn were successfully incorporated onto Ti surfaces using the proposed two-step MAO treatment. The excellent antibacterial properties of the resulting surfaces were sustained even after 6 months of immersion in physiological saline, which simulated the behavior of the specimens in an implanted environment. During the 6-month immersion of the specimens, the release of Ag ions from the surface oxide demonstrates the antibacterial properties of the specimens in the early stage, while the formation of Zn products demonstrates the antibacterial properties of the specimens in the later stage. In the future, the treatment conditions for incorporating Ag and Zn should be investigated to realize the desirable long-term bactericidal properties of surfaces after implant surgery.

**Author Contributions:** Conceptualization, H.T., Y.T. and T.H.; methodology, Y.T. and M.S.; validation, H.T.; formal analysis, H.T.; investigation, H.T., M.S. and T.M.; resources, H.K. and T.H.; data curation, P.C. and M.A.; writing—original draft preparation, H.T.; writing—review and editing, Y.T.; visualization, H.T. and Y.T.; supervision, Y.T.; project administration, Y.T., K.I., H.K. and T.H.; funding acquisition, Y.T., K.I., H.K. and T.H. All authors have read and agreed to the published version of the manuscript.

**Funding:** This research was partially funded by the JSPS Research Fellowship under grant number JP201940065 and the Research Center for Biomedical Engineering.

**Institutional Review Board Statement:** Not applicable.

**Informed Consent Statement:** Not applicable.

**Data Availability Statement:** Not applicable.

**Conflicts of Interest:** The authors declare no conflict of interest. The funders had no role in the design of the study; in the collection, analyses, or interpretation of data; in the writing of the manuscript; or in the decision to publish the results.

#### References

- Zubery, Y.; Bichacho, N.; Moses, O.; Tal, H. Immediate loading of modular transitional implants: A histologic and histomorphometric study in dogs. *Int. J. Periodontics Restor. Dent.* **1999**, *19*, 343–353.
- Hui, E.; Chow, J.; Li, D.; Liu, J.; Wat, P.; Law, H. Immediate provisional for single-tooth implant replacement with Brånemark system: Preliminary report. *Clin. Implant Dent. Relat. Res.* **2001**, *3*, 79–86. [CrossRef]
- Cochran, D.L.; Buser, D.; Ten Bruggenkate, C.M.; Weingart, D.; Taylor, T.M.; Bernard, J.P.; Peters, F.; Simpson, J.M. The use of reduced healing times on ITI®implants with a sandblasted and acid-etched (SLA) surface: Early results from clinical trials on ITI®SLA implants. *Clin. Oral Implant. Res.* **2002**, *13*, 144–153. [CrossRef] [PubMed]
- Lorenzoni, M.; Pertl, C.; Zhang, K.; Wimmer, G.; Wegscheider, W.A. Immediate loading of single-tooth implants in the anterior maxilla. Preliminary results after one year. *Clin. Oral Implant. Res.* **2003**, *14*, 180–187. [CrossRef] [PubMed]
- Paquette, D.W.; Brodala, N.; Williams, R.C. Risk factors for endosseous dental implant failure. *Dent. Clin. N. Am.* **2006**, *50*, 361–374. [CrossRef]
- Dibart, S.; Warbington, M.; Su, M.F.; Skobe, Z. In vitro evaluation of the implant-abutment bacterial seal: The locking taper system. *Int. J. Oral Maxillofac. Implant.* **2005**, *20*, 732–737.
- Glauser, R.; Schupbach, P.; Gottlow, J.; Hammerle, C.H.F. Periimplant soft tissue barrier at experimental one-piece mini-implants with different surface topography in humans: A light-microscopic overview and histometric analysis. *Clin. Implant Dent. Relat. Res.* **2005**, *7*, s44–s51. [CrossRef] [PubMed]
- Tesmer, M.; Wallet, S.; Koutouzis, T.; Lundgren, T. Bacterial colonization of the dental implant fixture–abutment interface: An in vitro study. *J. Periodontol.* **2009**, *80*, 1991–1997. [CrossRef] [PubMed]
- MacKintosh, E.E.; Patel, J.D.; Marchant, R.E.; Anderson, J.M. Effects of biomaterial surface chemistry on the adhesion and biofilm formation of staphylococcus epidermidis in vitro. *J. Biomed. Mater. Res. A* **2006**, *78*, 836–842. [CrossRef] [PubMed]
- Ono, M.; Nikaido, T.; Ikeda, M.; Imai, S.; Hanada, N.; Tagami, J.; Matin, K. Surface properties of resin composite materials relative to biofilm formation. *Dent. Mater. J.* **2007**, *26*, 613–622. [CrossRef]

11. Meredith, D.O.; Eschbach, L.; Wood, M.A.; Riehle, M.O.; Curtis, A.S.G.; Richards, R.G. Human fibroblast reactions to standard and electropolished titanium and Ti-6Al-7Nb, and electropolished stainless steel. *J. Biomed. Mater. Res. A* **2005**, *75*, 541–555. [CrossRef]
12. Koerner, R.J.; Butterworth, L.A.; Mayer, I.V.; Dasbach, R.; Busscher, H.J. Bacterial adhesion to titanium-oxy-nitride (TiNO<sub>x</sub>) coatings with different resistivities: A novel approach for the development of biomaterials. *Biomaterials* **2002**, *23*, 2835–2840. [CrossRef]
13. Simonetti, N.; Simonetti, G.; Bougnol, F.; Scalzo, M. Electrochemical Ag<sup>+</sup> for preservative use. *Appl. Environ. Microbiol.* **1992**, *58*, 3834–3836. [CrossRef] [PubMed]
14. Wassall, M.A.; Santin, M.; Isalberti, C.; Cannas, M.; Denyer, S.P. Adhesion of bacteria to stainless steel and silver-coated orthopedic external fixation pins. *J. Biomed. Mater. Res.* **1997**, *36*, 325–330. [CrossRef]
15. Massè, A.; Bruno, A.; Bosetti, M.; Biasibetti, A.; Cannas, M.; Gallinaro, P. Prevention of pin track infection in external fixation with silver coated pins: Clinical and microbiological results. *J. Biomed. Mater. Res.* **2000**, *53*, 600–604. [CrossRef]
16. Samani, S.; Hossainipour, S.M.; Tamizifar, M.; Rezaie, H.R. In vitro antibacterial evaluation of sol-gel-derived Zn-, Ag-, and (Zn + Ag)-doped hydroxyapatite coatings against methicillin resistant *Staphylococcus aureus*. *J. Biomed. Mater. Res. A* **2013**, *101*, 222–230. [CrossRef] [PubMed]
17. Jin, G.; Qin, H.; Cao, H.; Qian, S.; Zhao, Y.; Peng, X.; Zhang, X.; Liu, X.; Chu, P.K. Synergistic effects of dual Zn/Ag ion implantation in osteogenic activity and antibacterial ability of titanium. *Biomaterials* **2014**, *35*, 7699–7713. [CrossRef]
18. Applerot, G.; Lipovsky, A.; Dror, R.; Perkas, N.; Nitzan, Y.; Lubart, R.; Gedanken, A. Enhanced antibacterial activity of nanocrystalline ZnO due to increased ROS-mediated cell injury. *Adv. Funct. Mater.* **2009**, *19*, 842–852. [CrossRef]
19. Storrie, H.; Stupp, S.I. Cellular response to zinc-containing organoapatite: An in vitro study of proliferation, alkaline phosphatase activity and biomineralization. *Biomaterials* **2005**, *26*, 5492–5499. [CrossRef]
20. Jones, N.; Ray, B.; Ranjit, K.T.; Manna, A.C. Antibacterial activity of ZnO nanoparticle suspensions on a broad spectrum of microorganisms. *FEMS Microbiol. Lett.* **2008**, *279*, 71–76. [CrossRef]
21. Dastjerdi, R.; Montazer, M. A review on the application of inorganic nano-structured materials in the modification of textiles: Focus on anti-microbial properties. *Colloids Surf B Biointerfaces* **2010**, *79*, 5–18. [CrossRef]
22. Raghupathi, K.R.; Koodali, R.T.; Manna, A.C. Size-dependent bacterial growth inhibition and mechanism of antibacterial activity of zinc oxide nanoparticles. *Langmuir* **2011**, *27*, 4020–4028. [CrossRef]
23. Suh, J.Y.; Jang, B.C.; Zhu, X.; Ong, J.L.; Kim, K. Effect of hydrothermally treated anodic oxide films on osteoblast attachment and proliferation. *Biomaterials* **2003**, *24*, 347–355. [CrossRef]
24. Son, W.W.; Zhu, X.; Shin, H.I.; Ong, J.L.; Kim, K.H. In vivo histological response to anodized and anodized/hydrothermally treated titanium implants. *J. Biomed. Mater. Res. B Appl. Biomater.* **2003**, *66*, 520–525. [CrossRef]
25. Kim, D.Y.; Kim, M.; Kim, H.E.; Koh, Y.H.; Kim, H.W.; Jang, J.H. Formation of hydroxyapatite within porous TiO<sub>2</sub> layer by micro-arc oxidation coupled with electrophoretic deposition. *Acta Biomater.* **2009**, *5*, 2196–2205. [CrossRef]
26. Li, Y.; Lee, I.S.; Cui, F.Z.; Choi, S.H. The biocompatibility of nanostructured calcium phosphate coated on micro-arc oxidized titanium. *Biomaterials* **2008**, *29*, 2025–2032. [CrossRef] [PubMed]
27. Ha, J.Y.; Tsutsumi, Y.; Doi, Y.; Nomura, N.; Kim, K.H.; Hanawa, T. Enhancement of calcium phosphate formation on zirconium by micro-arc oxidation and chemical treatments. *Surf. Coat. Technol.* **2011**, *205*, 4948–4955. [CrossRef]
28. Song, W.H.; Ryu, H.S.; Hong, S.H. Antibacterial properties of Ag (or Pt)-containing calcium phosphate coatings formed by micro-arc oxidation. *J. Biomed. Mater. Res. A* **2009**, *88*, 246–254. [CrossRef]
29. Shimabukuro, M.; Tsutsumi, Y.; Yamada, R.; Ashida, M.; Chen, P.; Doi, H.; Nozaki, K.; Nagai, A.; Hanawa, T. Investigation of realizing both antibacterial property and osteogenic cell compatibility on titanium surface by simple electrochemical treatment. *ACS Biomater. Sci. Eng.* **2019**, *5*, 5623–5630. [CrossRef] [PubMed]
30. Shimabukuro, M. Antibacterial property and biocompatibility of silver, copper, and zinc in titanium dioxide layers incorporated by one-step micro-arc oxidation: A review. *Antibiotics* **2020**, *9*, 716. [CrossRef] [PubMed]
31. Shimabukuro, M.; Tsutsumi, Y.; Nozaki, K.; Chen, P.; Yamada, R.; Ashida, M.; Doi, H.; Nagai, A.; Hanawa, T. Chemical and biological roles of zinc in a porous titanium dioxide layer formed by micro-arc oxidation. *Coatings* **2019**, *9*, 705. [CrossRef]
32. Shimabukuro, M.; Hiji, A.; Manaka, T.; Nozaki, K.; Chen, P.; Ashida, M.; Tsutsumi, Y.; Nagai, A.; Hanawa, T. Time-transient effects of silver and copper in the porous titanium dioxide layer on antibacterial properties. *J. Funct. Biomater.* **2020**, *11*, 44. [CrossRef]
33. Shimabukuro, M.; Tsutsumi, H.; Tsutsumi, Y.; Manaka, T.; Chen, P.; Ashida, M.; Ishikawa, K.; Katayama, H.; Hanawa, T. Enhancement of antibacterial property of titanium by two-step micro arc oxidation treatment. *Dent. Mater. J.* **2021**, *40*, 592–598.
34. Coventry, M.B. Treatment of infections occurring in total hip surgery. *Orthop. Clin. N. Am.* **1975**, *6*, 991–1003. [CrossRef]
35. Rees, R.T. Infections associated with dental procedures in total hip arthroplasty. *J. Bone Jt. Surg. Br.* **2000**, *82*, 307. [CrossRef]
36. Rubin, R.; Salvati, E.A.; Lewis, R. Infected total hip replacement after dental procedures. *Oral. Surg. Oral Med. Oral Pathol.* **1976**, *41*, 18–23. [CrossRef]
37. Tanaka, Y.; Kobayashi, E.; Hiromoto, S.; Asami, K.; Imai, H.; Hanawa, T. Calcium phosphate formation on titanium by low voltage electrolytic treatments. *J. Mater. Sci. Mater. Med.* **2007**, *18*, 797–806. [CrossRef] [PubMed]
38. JIS Z 2801:2012 Antimicrobial Products—Test for Antimicrobial Activity and Efficacy; Japanese Standards Association: Tokyo, Japan. 2012. Available online: <https://www.jisc.go.jp/eng/index.html> (accessed on 30 June 2021).

39. ISO 22196:2011 Plastics-Measurement of Antibacterial Activity on Plastics Surfaces; International Organization of Standardization: Geneva, Switzerland. 2011. Available online: <https://www.iso.org/standard/54431.html> (accessed on 30 June 2021).
40. Odnevall Wallinder, I.; Leygraf, C. A critical review on corrosion and runoff from zinc and zinc-based alloys in atmospheric environments. *Corrosion* **2017**, *73*, 1016–1077. [CrossRef]
41. Poon, V.K.M.; Burd, A. In vitro cytotoxicity of silver: Implication for clinical wound care. *Burns*. **2004**, *30*, 140–147. [CrossRef]
42. Wataha, J.C.; Lockwood, P.E.; Schedle, A. Effect of silver, copper, mercury, and nickel ions on cellular proliferation during extended, low-dose exposures. *J. Biomed. Mater. Res.* **2000**, *52*, 360–364. [CrossRef]
43. Yamamoto, A.; Honma, R.; Sumita, M. Cytotoxicity evaluation of 43 metal salts using murine fibroblasts and osteoblastic cells. *J. Biomed. Mater. Res.* **1998**, *39*, 331–340. [CrossRef]
44. AshaRani, P.V.; Mun, G.L.K.; Hande, M.P.; Valiyaveetil, S. Cytotoxicity and genotoxicity of silver nanoparticles in human cells. *ACS Nano*. **2009**, *3*, 279–290. [CrossRef]
45. Rosário, F.; Hoet, P.; Santos, C.; Oliveira, H. Death and cell cycle progression are differently conditioned by the AgNP size in osteoblast-like cells. *Toxicology* **2016**, *368–369*, 103–115. [CrossRef]
46. Contreras, R.G.; Vilchis, J.R.S.; Sakagami, H.; Nakamura, Y.; Nakamura, Y.; Hibino, Y.; Nakajima, H.; Shimada, J. Type of cell death induced by seven metals in cultured mouse osteoblastic cells. *In Vivo* **2010**, *24*, 507–512. [PubMed]
47. Shao, W.; Liu, X.; Min, H.; Dong, G.; Feng, Q.; Zuo, S. Preparation, characterization, and antibacterial activity of silver nanoparticle-decorated graphene oxide nanocomposite. *ACS Appl. Mater. Interfaces* **2015**, *7*, 6966–6973. [CrossRef]
48. Jia, Z.; Xiu, P.; Li, M.; Xu, X.; Shi, Y.; Cheng, Y.; Wei, S.; Zheng, Y.; Xi, T.; Cai, H.; et al. Bioinspired anchoring AgNPs onto micro-nanoporous TiO<sub>2</sub> orthopedic coatings: Trap-killing of bacteria, surface-regulated osteoblast functions and host responses. *Biomaterials* **2016**, *75*, 203–222. [CrossRef] [PubMed]
49. De Faria, A.F.; Perreault, F.; Shaulsky, E.; Arias Chavez, L.H.; Elimelech, M. Antimicrobial electrospun biopolymer nanofiber mats functionalized with graphene oxide-silver nanocomposites. *ACS Appl. Mater. Interfaces* **2015**, *7*, 12751–12759. [CrossRef] [PubMed]

Article

# Borate and Silicate Bioactive Glass Coatings Prepared by Nanosecond Pulsed Laser Deposition

Julietta V. Rau <sup>1,2,\*</sup>, Angela De Bonis <sup>3,\*</sup>, Mariangela Curcio <sup>3</sup>, Katharina Schuhladen <sup>4</sup>,  
Katia Barbaro <sup>5</sup>, Giovanni De Bellis <sup>6,7</sup>, Roberto Teghil <sup>3</sup> and Aldo R. Boccaccini <sup>4</sup>

<sup>1</sup> Istituto di Struttura della Materia, Consiglio Nazionale delle Ricerche (ISM-CNR),  
Via del Fosso del Cavaliere, 100-00133 Rome, Italy

<sup>2</sup> Department of Analytical, Physical and Colloid Chemistry, Institute of Pharmacy, Sechenov First Moscow  
State Medical University, Trubetskaya 8, build. 2, 119991 Moscow, Russia

<sup>3</sup> Dipartimento di Scienze, Università della Basilicata, Via dell'Ateneo Lucano, 10-85100 Potenza, Italy;  
mariangela.curcio@unibas.it (M.C.); roberto.teghil@unibas.it (R.T.)

<sup>4</sup> Department of Materials Science and Engineering, Institute of Biomaterials, University of  
Erlangen-Nuremberg, Cauerstr.6, 91058 Erlangen, Germany; katharina.ks.schuhladen@fau.de (K.S.);  
aldo.boccaccini@ww.uni-erlangen.de (A.R.B.)

<sup>5</sup> Istituto Zooprofilattico Sperimentale Lazio e Toscana "M. Aleandri", Via Appia Nuova,  
1411-00178 Rome, Italy; katia.barbaro@izslt.it

<sup>6</sup> DIAEE-Department of Astronautical, Electrical and Energy Engineering, Sapienza University of Rome,  
via Eudossiana 18, 00184 Rome, Italy; giovanni.debellis@uniroma1.it

<sup>7</sup> CNIS-Research Centre on Nanotechnology Applied to Engineering, P.le Aldo Moro 5, 00185 Rome, Italy

\* Correspondence: giulietta.rau@ism.cnr.it (J.V.R.); angela.debonis@unibas.it (A.D.B.)

Received: 26 October 2020; Accepted: 16 November 2020; Published: 18 November 2020

**Abstract:** Silicate (13-93) and borate (13-93-B3) bioactive glass coatings were successfully deposited on titanium using the nanosecond Pulsed Laser Deposition technique. The coatings' microstructural characteristics, compositions and morphologies were examined by a number of physico-chemical techniques. The deposited coatings retain the same functional groups of the targets, are a few microns thick, amorphous, compact and crack free. Their surface is characterized by the presence of micrometric and nanometric particles. The surface topography, investigated by Atomic Force Microscopy, is characterized by spherical or ellipsoidal particles of the 0.2–3  $\mu\text{m}$  size range for the 13-93 silicate bioactive glass film and of the 0.1–1  $\mu\text{m}$  range for the 13-93-B3 borate bioactive glass coating. Equine adipose tissue-derived mesenchymal stem cells (ADMSCs) were applied for biological tests and the osteogenic differentiation activity of cells on the deposited coatings was studied after ADMSCs growth in osteogenic medium and staining with Alizarin Red. Cytocompatibility and osteogenic differentiation tests have shown that thin films retain the biocompatibility properties of the target silicate and borate glass, respectively. On the other hand, no antibacterial activity of the borate glass films was observed, suggesting that ion doping is advisable to inhibit bacterial growth on the surface of borate glass thin films.

**Keywords:** borate bioactive glass coatings; silicate bioactive glass coatings; nanosecond pulsed laser deposition; equine adipose tissue-derived stem cells; cytocompatibility; antibacterial activity

## 1. Introduction

Biomedical researchers are increasingly paying attention to the development and application of bioactive materials. In particular, in the field of prosthetic dentistry, maxillofacial surgery and orthopaedics, bioactive glasses and ceramics are increasingly chosen with respect to bioinert materials. In the 1960s, the first generation of biomaterials was selected for biomedical use due to their suitable physico-chemical characteristics and inertness in biological environments [1]. From the

1980s, bioactive materials with a controlled interaction with the biological surroundings were preferred for clinical use [1,2]. Nowadays, bioactive materials belonging to the third generation are being developed with the aim to induce a desired therapeutic effect [1].

Among bioinert materials, titanium (Ti) is still widely used to manufacture hard-tissue implants, especially for load-bearing application (hip, knee and dental prosthesis), due to its optimal mechanical characteristics. It has been employed for orthopedic implants since the 1960s, when Brånemark and his co-workers [3] discovered a titanium cage strongly integrated in a rabbit bone a few months after its implantation. However, it is not osteogenic; therefore, the osteointegration takes place over a longer time, during which the eventual occurrence of shift movements between the implant and the host bone could lead to the formation of a fibrous capsule around the implant surface and its consequent failure may occur. In order to increase the chances of successful bone-related implant procedures, the modification of the Ti surface by coating it with a bioactive material is advisable [4–9]. In this way the optimal bulk mechanical properties are preserved, and the implant surface is more suitable to provide a better osteointegration.

After Hench's discovery of the 45S5 Bioglass® in 1971 [10], significant progress was made in bioactive glass composition, which aimed to design biomaterials possessing specific properties for bone reconstruction. The goal was to obtain materials whose components, dissolved in the extracellular matrix, are able to stimulate specific biological responses, influencing gene expression, osteogenic differentiation and cellular proliferation. In addition, the risk of infection incurrence after a surgery is always high and more probable in the case of implantation [11]. A way to prevent microbial colonization and the consequent implant failure is to impart antimicrobial properties to biomaterials.

Moreover, in order to overcome problems related to phase separation [10,12,13] and devitrification during heat treatment of early silicate glasses, other ions were added to their composition. In particular, the addition of components such as potassium, magnesium, and boron improved glass processability, making it easier to produce glass without crystallization and to use it in the form of coating, fibers, scaffolds, etc. [13]. For this purpose, Brink and co-workers carried out a systematic study on the *in vivo* bone-bonding behavior of several glass compositions [13,14]. Among these, the glass registered as 13-93 ( $\text{Na}_2\text{O}-\text{K}_2\text{O}-\text{MgO}-\text{CaO}-\text{P}_2\text{O}_5-\text{SiO}_2$ ) had bioactive properties and was approved by the Food and Drug Administration in the USA and Europe for *in vivo* use. However, similarly to 45S5, the 13-93 bioactive glass is characterized by a slow and incomplete conversion into hydroxyapatite (HA) once in contact with the body fluids. For this reason, silicate was substituted by different percentages of borate, observing a faster and a more complete transformation into HA in the absence of silica [15–19]. This is because when borate glass is placed in the biological environment, there is no formation of a silica-rich layer, typical of the interaction process of the silicate glasses. Therefore, the reaction rate is limited by the dissolution of ions in biological surroundings [15–18,20,21].

Furthermore, boron has a number of key functions inside the biological environment, especially in bone metabolism, thanks to its interaction with calcium, magnesium and vitamin D, and, therefore, its presence is even more crucial for bone preservation and osteoporosis limitation [22,23]. Some studies evidenced that boron influences osteogenic differentiation of mesenchymal stem cells [24,25], being also angiogenic [26]. Many studies report that ion doping enhances the antibacterial properties of borate based bioglass [27–30]. On the other hand, Fu and collaborators [31] observed no beneficial effect on cell proliferation during *in vitro* testing, supposing an overly fast boron release in culture medium, while no toxic effects were found during *in vivo* testing due to the more dynamic microenvironment of the organism, which allows a rapid metabolization of boron. All these advantages make borate glasses a valuable alternative to conventional silicate bioactive glasses.

The potential of bioactive glass to be used as coating materials for metallic or alloy implants is related to the possibility of obtaining coating films that are dense, without cracks and well adherent to the substrate. Many of the coatings' techniques require high temperature treatment in order to allow the glass to react with the substrate surface [32–34]. In this contest, borate glasses are advantageous

with respect to silicate ones since boron oxide reduces the coefficient of thermal expansion of glass, better matching the coefficient of thermal expansion of metal substrate [29].

Among several deposition techniques, pulsed laser deposition is a promising route to obtain thin films for biomedical applications. The use of pulsed laser deposition (PLD) has in fact several advantages: coatings usually retain the bulk target composition, strongly adhere to the substrate surface, their thickness and crystallinity can be controlled by monitoring deposition parameters and their morphologies are typically characterized by nanometric and micrometric features [4,6,8,35], which support the osteointegration process [8,36,37]. Moreover, no heating treatment is required to deposit amorphous films.

Recently, several bioactive glasses [9,38–40] have been successfully deposited by PLD. Ma et al. [38] obtained, by PLD, Magnesium-containing bioactive glass coatings on Ti–6Al–4V that demonstrated higher corrosion resistance with respect to the uncoated substrates and film bioactivity by *in vitro* assay. Sanz et al. [39] deposited Niobium-containing bioactive glass on Ti substrate by nanosecond PLD, obtaining typical compact and granular films, which preserved target stoichiometry and improved cell adhesion in comparison with non-coated Ti. Rau et al. [6] coated Ti substrate with Cu-releasing bioactive glasses by nanosecond-PLD, showing their good wettability, bioactivity and antibacterial properties upon *in vitro* assay. Shaikh et al. [40] laser deposited 45S5 glass on Ti-alloy surface, testing films' biocompatibility on U2OS human osteosarcoma cells. Wang et al. [41,42] obtained composite hydroxyapatite/bioglass films by depositing, with a pulsed laser, on Ti–6Al–4V titanium alloy and demonstrated their osteoconductivity after implantation in shin bone of a rabbit.

In the present work, for the first time, borate-based (13-93-B3) and silicate-based (13-93) bioactive glasses (BGs) were deposited on titanium surface by nanosecond PLD at room temperature. The amorphous deposited films are compact and without cracks. Their surface presents nanometric and micrometric features that make films suitable for interaction with the biological medium. The coatings' biological properties were tested on equine adipose tissue-derived mesenchymal stem cells (ADMSCs) and microbiological tests were carried out, showing that borate-based glasses can be used as alternative materials to silicate glasses for the coating of titanium implants.

## 2. Materials and Methods

Silicate (13-93) and borate glasses (13-93-B3) were used as target materials for the pulsed laser deposition procedure.

### 2.1. Glasses Preparation

Silicate 13-93 (5.5 Na<sub>2</sub>O, 11.1 K<sub>2</sub>O, 4.6 MgO, 18.5 CaO, 3.7 P<sub>2</sub>O<sub>5</sub>, 56.6 SiO<sub>2</sub>, all in wt.%) and borate 13-93-B3 (5.5 Na<sub>2</sub>O, 11.1 K<sub>2</sub>O, 4.6 MgO, 18.5 CaO, 3.7 P<sub>2</sub>O<sub>5</sub>, 56.6 B<sub>2</sub>O<sub>3</sub>, all in wt.%) glasses were prepared by a melt-quenching method, reported in [18]. Briefly, the synthesis was carried out in a platinum crucible using all analytical grade reagents (Na<sub>2</sub>CO<sub>3</sub>, K<sub>2</sub>CO<sub>3</sub>, MgO, CaCO<sub>3</sub>, CaHPO<sub>4</sub>·2H<sub>2</sub>O, H<sub>3</sub>BO<sub>3</sub>) from Sigma-Aldrich (Steinheim, Germany), while the silicate source was a Belgian quartz sand (obtained from Åbo Akademi, Finland). The mixtures were heated for 2 h at 1050 °C and for 3 h at 1360 °C to obtain 13-93-B3 and 13-93 glasses, respectively. Afterwards, the melts were cast, annealed and crushed. The melting process was repeated twice. Bioactive glass blocks were crushed using a jaw crusher and milled using a planetary mill (both made of zirconia, Retsch, Haan, Germany). The obtained bioactive glass powders (0.3 g per pellet, with a mean particle size of 5–20 µm) were pressed into pellets (diameter of 10 and 3 mm height) using a hydraulic press (PE-010, MautheMaschinenbau, Wesel, Germany) with a load of 1t. The pressed pellets were then sintered at 1050 °C for 2 h with a heating rate of 2 °C per min.

Prior to depositions, the target materials were characterized by X-ray diffraction (XRD), by means of a D5000 (Siemens AG, Munich, Germany) in a  $\theta$ – $2\theta$  configuration, and by Fourier-transform infrared (FT-IR) spectroscopy, with a JASCO 460 Plus (Tokyo, Japan).

## 2.2. Pulsed Laser Deposition

The 13-93 and 13-93-B3 bioactive glass films were deposited on Si (100) and Ti 1 cm × 1 cm (both from Goodfellows, Huntingdon, UK) substrates. Ti substrates were preliminarily sandblasted and polished with a HNO<sub>3</sub>/H<sub>2</sub>SO<sub>4</sub> solution (aqua regia). Film depositions were performed in a stainless steel vacuum chamber equipped with a rotating target holder, at a pressure of 10<sup>-4</sup> Pa. The Nd:YAG laser (Handy YAG, Quanta System, Samarate, Italy) with the following characteristics was used: λ = 532 nm, pulse duration = 7 ns, repetition rate = 10 Hz. It was directed on the target by quartz lens (45°, 350 mm focal plane). In each deposition, the target-substrate distance was kept at 2 cm, the deposition time was 5 h and the laser fluence was 12 J/cm<sup>2</sup>; such experimental conditions were optimized in our previous work [4].

## 2.3. Characterization

The composition of the films deposited onto Si substrates was characterized by FT-IR (JASCO 460 Plus), in transmittance mode in the range of 4000–400 cm<sup>-1</sup>, by collecting 100 scans with a resolution of 4 cm<sup>-1</sup>. This analysis was carried out on the films deposited onto Si (100) substrates since silicon shows very weak absorption in medium IR range. The crystalline or amorphous character of the films were investigated by XRD (D5000). The morphology was characterized by scanning electron microscopy (SEM) (PHILIPS-FEI XL30, North Billerica, MA, USA), while the roughness was evaluated by atomic force microscopy (AFM). AFM measurements were carried out by a Bruker Dimension Icon system (Billerica, MA, USA), equipped with a Nanoscope V controller (Bruker Corporation, Billerica, MA, USA). AFM micrographs were acquired in tapping mode, by using n-doped Si probes (Bruker RTESP300, Billerica, MA, USA) with a resonant frequency of roughly 300 kHz, at a scan rate between 0.3 and 1 Hz. Scanned areas ranged from 1 μm × 1 μm to 10 μm × 10 μm. At least three different regions were scanned for each sample. The roughness coefficients are presented as average values.

## 2.4. Biological Test

### 2.4.1. Equine Adipose Tissue-Derived Mesenchymal Stem Cell (ADMSC): Isolation and Culture

Adipose tissue was collected from a 2 year-old male horse. It was stored at 4 °C in a sterile container with phosphate buffer saline (PBS, from Sigma-Aldrich, Irvine, UK), supplemented with 5% *v/v* penicillin-streptomycin. After a quick transportation in laboratory, it was washed three times with PBS in order to remove red blood cells, dissected in small pieces and digested at 37 °C for 60 min with 0.1% collagenase Type IA (Sigma-Aldrich, Saint Louis, MO, USA). After that, cell suspension was centrifuged at 800 rpm for 10 min. The obtained pellet was re-suspended in the Dulbecco's Modified Eagle's Medium (DMEM) with 10% (*v/v*) fetal bovine serum (FBS, Gibco, Paisley, UK) and cultured in polystyrene flasks for cell cultures (Falcon, Durham, NC, USA). For this purpose, an incubator kept at 37 °C with a humidified atmosphere containing 5% of CO<sub>2</sub> was used. After 24 h culture medium, cellular debris were removed by washing with PBS. Culture medium (DMEM with 10% FBS) was added and then changed every two days until a cell confluence of 80% was reached. Subsequently, ADMSCs were trypsinized (with trypsin from Sigma-Aldrich, London, UK) and re-suspended in fresh culture medium.

### 2.4.2. Cell Viability

In order to investigate the effect of the 13-93 and 13-93-B3 coated Ti on the viability of the ADMSC cells, the 3-[4,5-dimethylthiazole-2-yl]-2,5-diphenyltetrazolium bromide (MTT) assay was performed. The MTT assay is a colorimetric test used to evaluate the cellular metabolic activity. It is based on the enzymatic reduction of MTT to water insoluble formazan blue salts, determinable spectrophotometrically. This reaction can occur only in viable cells due to the presence of mitochondrial succinate dehydrogenase (SDH).

ADMSCs with a concentration of 50,000 cells/mL in culture medium (DMEM with 10% FBS) were distributed in 24-well plate and incubated for 24 h at 37 °C. After that, the 13-93 and 13-93-B3 coated Ti samples were introduced and incubated under the same conditions. Before cell culture, the samples were washed with distilled water and sterilized in autoclave (121 °C, 20 min, pressure of 1.1 bar). The MTT assay was carried out after 24 and 48 h of incubation, when culture medium was substituted by the MTT solution (Sigma-Aldrich, London, UK) 0.5 mg/mL in the DMEM. After an incubation time of 3 h under cell culture conditions, the MTT solution was substituted with isopropanol (Sigma-Aldrich) and left for 30 min at room temperature, in order to dissolve formazan crystals, detected by measuring the optical density (OD) at 600 nm with a BioPhotometer (Eppendorf, Hamburg, Germany). All experiments were made in triplicate.

#### 2.4.3. Osteogenic Differentiation

ADMSCs (50,000 cells/mL) were seeded in a 12-well plate (Falcon) and incubated under cell culture conditions (37 °C, 5% CO<sub>2</sub>). After 24 h, the 13-93 and 13-93-B3 coated Ti and control samples without coatings were added, and the osteogenic differentiation was induced by changing the culture medium with an osteogenic one, composed of ascorbic acid 50 µg/mL (Sigma-Aldrich), β-glycerophosphate 10 mM (Sigma-Aldrich) and dexamethasone 10<sup>-7</sup>M (Sigma-Aldrich) in the DMEM plus 10% FBS, and incubated under cell culture conditions for three weeks, changing the culture medium every two days. ADMSCs in DMEM plus 10% FBS with and without osteogenic medium were positive and negative controls, respectively.

The osteogenic differentiation was evaluated by staining with Alizarin Red S (Sigma-Aldrich), which allows the detection of calcified extracellular matrix deposits, forming bright-red complexes with calcium. The images were taken by the means of an inverted optical microscope (Nikon, Eclipse TE 2000U, Tokyo, Japan).

#### 2.4.4. Antibacterial Studies

The antibacterial activity was evaluated against *Enterococcus faecalis* (*E. faecalis*), *Escherichia coli* (*E. coli*), *Pseudomonas aeruginosa* (*P. aeruginosa*) and *Staphylococcus aureus* (*S. aureus*). All the bacteria strains were grown in Brain Heart Infusion (BHI, DIFCO, Sparks, NV, USA) in the presence of the sterilized 13-93 and 13-93-B3 coated Ti for 24 h at 37 °C. Bacterial growth was evaluated by measuring the optical density (OD<sub>600 nm</sub>) by means of a BioPhotometer (EppendorfD30, Hamburg, Germany). Samples with OD values over the measurement range were appropriately diluted. All experiments were made in triplicate.

#### 2.5. Statistical Analysis

All the experiments were carried out in triplicate and the results are expressed as mean ± standard deviation (SD). Statistical analysis was performed using the Origin Pro 9.0 software (Originlab Corporation, Northampton, MA, USA) and one-way ANOVA (Analysis of Variance) was applied, followed by a post hoc Tukey test. Values of  $p < 0.05$  were considered statistically significant, indicated by an asterisk (\*).

### 3. Results and Discussion

#### 3.1. Physico-Chemical Characterization

Based on the results obtained by the FT-IR analysis of films deposited on the Si substrates, it is possible to conclude that the deposited coatings maintain the spectral figures of targets (Figure 1). The main absorption band of the 13-93 silicate glass target and film (Figure 1a) in the 1100–900 cm<sup>-1</sup> range is related to the Si–O–Si stretching mode. In particular, in the target it is possible to distinguish between the stretching mode Si–O–(with non-bridging oxygen), around 930 cm<sup>-1</sup>, and the symmetric stretching mode of Si–O–Si, around 1020 cm<sup>-1</sup>. Signals related to the bending and the asymmetric

stretching of Si–O–Si are also visible in the target and film spectra at 470 and 760  $\text{cm}^{-1}$ , respectively. In the FT-IR spectra of both the target and of the film (Figure 1b) of the 13-93-B3 borate glass, the bending vibration of borates is observable at 715  $\text{cm}^{-1}$ , whereas the bands centered at 1000 and 1400  $\text{cm}^{-1}$  are related to the B–O stretching mode of  $\text{BO}_4$  units (tetrahedral coordinated) and  $\text{BO}_3$  (trigonal coordinated) units, respectively. The presence of different structural units is due to the ability of boron to transform its coordination number with oxygen in a borate glass network due to the presence of metal oxides, as in this case, that promotes the change from 3-fold to 4-fold coordination [43].

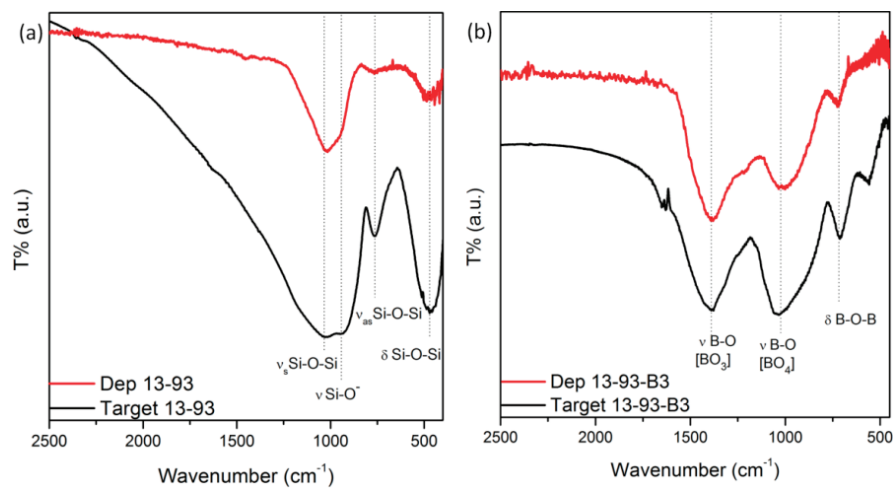


**Figure 1.** FT-IR spectra of target materials (black lines) and deposited films (red lines) of (a) 13-93 and (b) 13-93-B3 BGs.

It can be observed from the broad XRD patterns without any detectable peaks shown in Figure 2 that both of the target materials are amorphous with no measurable amount of crystalline phase [18]. The 13-93 glass spectrum presents a broad peak in the  $25^\circ$ – $30^\circ$  region that is typical for silicate glass [18]. In the 13-93-B3 spectrum, a broad peak appears, centered at about  $45^\circ$ , that can be related to the borate content of the glass. To obtain crystalline films, nanosecond PLD deposition is usually performed by the heating of the substrate or by using a buffer gas [41,44,45], so we can expect that also the deposited films are amorphous. We deposited the films at room temperature since it was demonstrated that amorphous materials show superior solubility in biological or simulated biological fluid media and are characterized by an increased bioactivity with respect to crystalline materials [8,9,29,46].

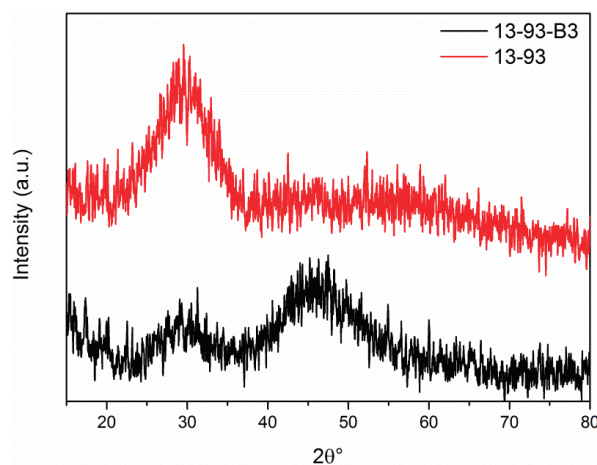


**Figure 2.** XRD patterns of 13-93 and 13-93-B3 BG targets material and deposited films.

The morphologies, registered by SEM (Figure 3), of films obtained by depositing silicate or borate targets are very similar. The films are uniform, dense, compact and without cracks. Micrometric particles homogeneously spread all over the surface and nanometric particles embedded in the dense background (Figure 3b,d) can be observed. Elongated and top flat microparticles are present on the surface of both films. The observed morphology is typical for ceramic films deposited by nanosecond PLD [4,6,8,35,39], where two different mechanisms of film growth are present: gas condensation and nano and micrometric droplets' coalescence. Gas condensation leads to the formation of the dense background covered by micrometric fused particles. Film surfaces, characterized by nanometric and micrometric features, may contribute to the implant's osteointegration [36,37].

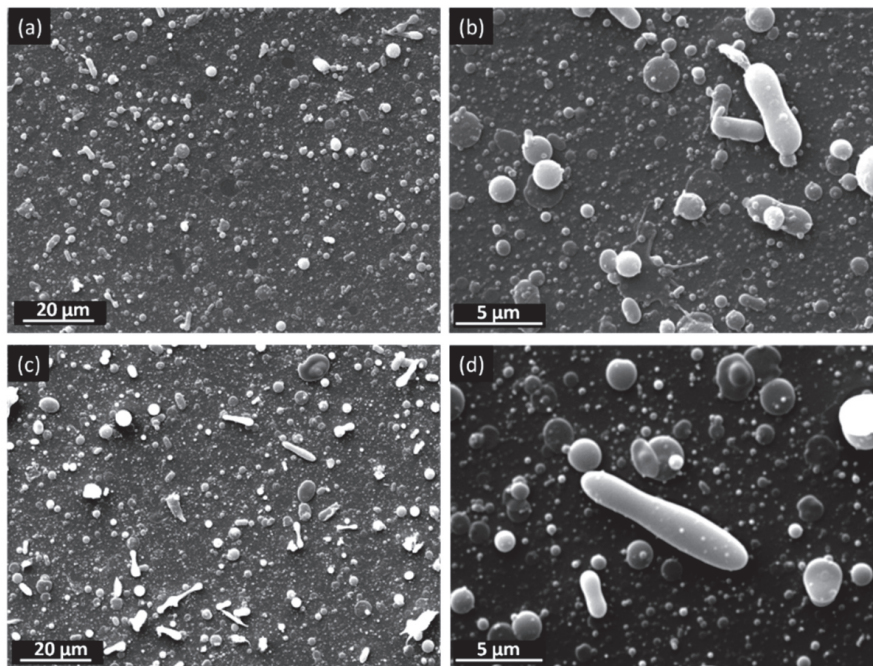


**Figure 3.** SEM images of (a,b) 13-93 and (c,d) 13-93-B3 BG coated Ti, registered at two different magnifications.

When a biomaterial is introduced into a living organism, the biochemical process responsible for osteointegration starts with the ion dissolution. During all the steps that lead to the formation of the apatite layer on the top of the implant, dynamic absorption and desorption of proteins and other moieties (e.g., sugars, phospholipids, amino acids) occur until equilibrium is reached. However, only certain proteins are able to bind selectively and irreversibly to the implant surface and this is influenced by ions released by bioactive glass, surface morphology, particle size and roughness, as well as protein composition and concentration. For this purpose, the presence of nanometric features on the implant surface may promote the adhesion of proteins involved in the regulation of osteoblast proliferation [36]. At the same time, microscale features stimulate the adhesion and differentiation of the same cells [47]. Therefore, glass-ceramics, with nanoscale crystal sizes and micro-/nanostructured surface topography, show superior bioactivity and promote adhesion, proliferation, osteogenic differentiation of stem cells and osteoblasts and, subsequently, stimulate bone growth [36,37].

Several studies have shown evidence of a strong correlation between substrates' surface morphology and cell adhesion [48], suggesting an enhancement of osteoblasts' adhesion for increasing surface roughness [49]. Therefore, AFM was employed to acquire information on the nanoscale features of the produced bioactive glasses. Figure 4a,b shows two typical  $10\ \mu\text{m} \times 10\ \mu\text{m}$  3D height maps of the 13-93 and 13-93-B3 coated Ti, respectively, highlighting marked differences on nanoscale surface features. In particular, while the 13-93 silicate glass film is characterized by spherical or ellipsoidal

particles of size ranging between 0.2 and 3  $\mu\text{m}$ , the 13-93-B3 borate glass coating shows a lower density of deposited particles, with sizes in the 0.1–1  $\mu\text{m}$  range. The surface roughness evaluated from 10  $\mu\text{m} \times 10 \mu\text{m}$  AFM images and expressed as RMS values ( $R_q$ ) has values of  $186 \pm 16$  and  $52 \pm 11$  nm for the silicate and borate glasses, respectively. However, these results are strongly affected by the Ti substrates' morphology. In order to highlight the nanometric roughness of the deposited films, 1  $\mu\text{m} \times 1 \mu\text{m}$  images were acquired (Figure 4c,d), resulting in very similar average  $R_q$  values for silicate and borate glass coatings ( $35 \pm 12$  and  $44 \pm 18$  nm, respectively).

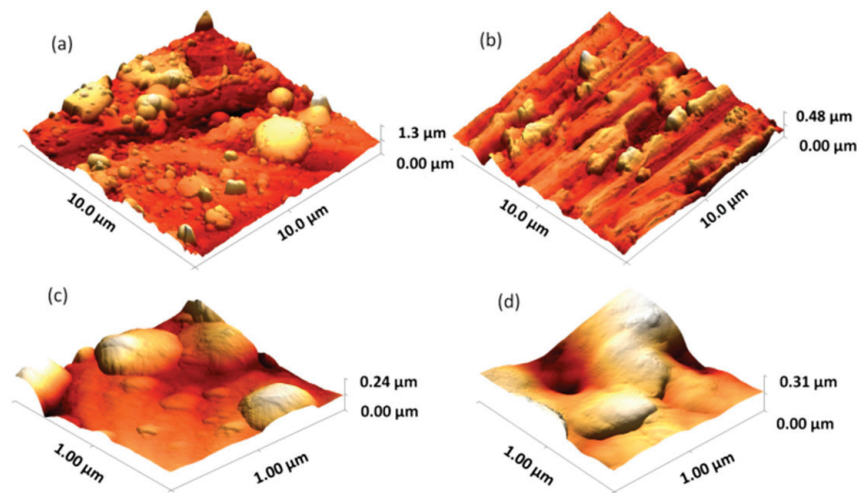


Figure 4. AFM images of (a,c) 13-93 and (b,d) 13-93-B3 BG coated Ti.

### 3.2. Biological Properties

ADMSCs were employed for the *in vitro* evaluation of cytotoxicity and osteogenic properties of the 13-93 and 13-93-B3 BG coated Ti. Adult adipose tissue of different species has a great potential as source of multipotent cells that are able to differentiate in different lineages [50]. The main advantage of choosing ADMSCs is their abundance and the easy and minimally invasive way to collect them by liposuction, making ADMSCs of great interest in the cell therapy field.

In order to study the cytotoxicity effect of the 13-93 and 13-93-B3 BG coated Ti samples, the MTT assay was performed. ADMSCs were incubated with and without (control sample) the two bioactive glass coatings and then treated with the MTT. The consequent formation of blue formazan crystals is possible only in the cells with metabolic activity. Therefore, the determination by the  $\text{OD}_{600 \text{ nm}}$  of formazan is related to the percentage of living cells. The measurements were executed in triplicate after 24 and 48 h of incubation time. The calculated averages are reported in Figure 5. It is possible to assert that both samples are not cytotoxic since no significant differences are noticeable between the samples incubated with 13-93 and 13-93-B3 BG coated Ti and the control sample both at 24 and 48 h of incubation time.

In Figure 6, it is possible to observe the extracellular calcium deposition detected by Alizarin Red stain in ADMSCs, a clear demonstration of the osteogenic differentiation, except for the negative control. No significant differences were detected for the 13-93 and 13-93-B3 coatings, while the percentage of red portion in Figure 6a,b and Figure 6c,d seems to be slightly more than in the positive control sample (Figure 6e,f).

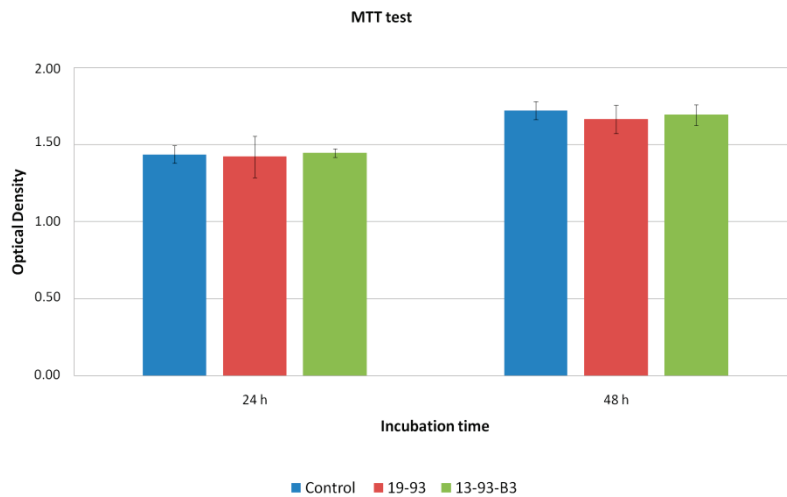


**Figure 5.** MTT results of 13-93 and 13-93-B3 BG coated Ti after 24 and 48 h of in vitro ADMSC culture, reported as optical density measured at 600 nm, expressed as mean values  $\pm$  standard deviation of 3 independent experiments. Statistical analysis was performed through ANOVA, followed by post hoc Tukey test.

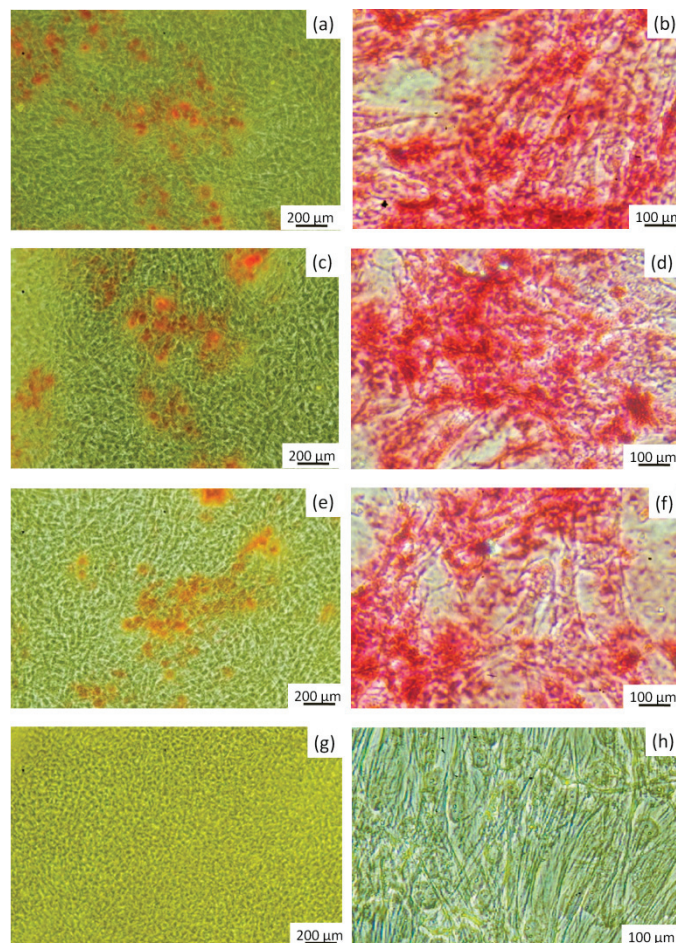


**Figure 6.** Optical microscopic images taken after staining with Alizarin Red S of ADMSCs cultured in the presence of (a,b) 13-93 BG coated Ti, (c,d) 13-93-B3 BG coated Ti in osteogenic medium, (e,f) positive control and (g,h) negative control (ADMSCs cultured with or without osteogenic medium, respectively) for three weeks. The magnification is 20 $\times$  (on the left) and 40 $\times$  (on the right).

The effect of the 13-93 and 13-93-B3 BG coated Ti on various microorganisms (*E. faecalis*, *E. coli*, *P. aeruginosa*, *S. aureus*) was evaluated after incubation at 37 °C for 24 h. The results of the OD<sub>600 nm</sub> measured with a BioPhotometer are shown in Figure 7, where the OD values are properly multiplied for the dilution factor. It is possible to note that even if borate glasses should have antibacterial properties, as follows from the literature [28–30], all microbiology tests show a rather high proliferation of all the four tested bacteria strains, comparative or higher than the control sample. In particular, for the Gram+ bacteria *E. faecalis* no significant differences can be noted with respect to the control sample; whereas slight differences can be observed for the Gram+ *S. aureus*. For the Gram– bacteria (*E. coli* and *P. aeruginosa*), their growth is favored by the presence of both the deposited coatings. No antibacterial effects can be expected for silicate glass films and, probably, the absence of these properties also for borate glass films can be imputed to the amount of boron released by the coatings, which could be too low to inhibit bacterial growth. Therefore, if the aim is to deposit thin bioactive films that also present antimicrobial effects, the addition of specific ions in the glass composition, such as Ag, Zn or Cu, is advisable [9,28,30,51].

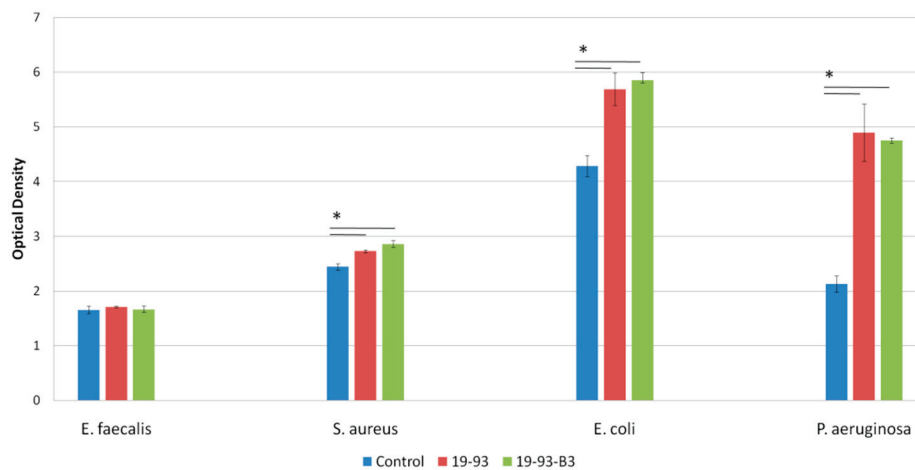


**Figure 7.** Antibacterial test carried out on 13-93 and 13-93-B3 BG coated Ti compared with the control sample, reported as optical density measured at 600 nm (obtained values are multiplied by the dilution factor), expressed as mean values  $\pm$  standard deviation of 3 independent experiments. Statistical analysis was performed through ANOVA, followed by post hoc Tukey test (\*  $p < 0.05$ ).

#### 4. Conclusions

Silicate (13-93) and borate (13-93-B3) bioactive glasses were successfully deposited on Ti substrate by ns-Pulsed Laser Deposition. The deposited films, characterized by SEM, AFM and XRD techniques, exhibit similar features: they are a few microns thick, amorphous, compact and crack free, and their morphologies are characterized by the presence of micrometric and nanometric particles. The cytocompatibility of coatings of both glass compositions was demonstrated by the MTT test and their osteogenic differentiation activity was studied after ADMSCs' growth in osteogenic medium and staining with Alizarin Red. Although it was reported that bulk 13-93-B3 can inhibit bacterial growth [28–30], no antibacterial effect of borate (13-93-B3) glass coatings on Ti was detected against the tested bacteria strains *E. faecalis*, *E. coli*, *P. aeruginosa* and *S. aureus*.

The results prove the potential use of the PLD technique to deposit dense, compact and crack-free silicate and borate coatings that retain the biological activity of the bulk materials. Further studies will be focused on the addition of other ions to the glass composition for imparting antibacterial properties to the implant coatings.

**Author Contributions:** Conceptualization, J.V.R. and A.R.B.; methodology, A.D.B. and R.T.; validation, J.V.R., A.D.B., K.B., R.T., and A.R.B.; investigation, M.C., K.S., K.B., and G.D.B.; resources, J.V.R., A.D.B., K.B., G.D.B., R.T., and A.R.B.; data curation, M.C., K.B., and G.D.B.; writing—original draft, J.V.R., M.C., A.D.B., and K.B.; writing—review and editing, J.V.R., M.C., A.D.B., and K.B. All authors have read and agreed to the published version of the manuscript.

**Funding:** This research was partially funded by the Italian Ministry of Health, Grant Nos. IZS LT 02/15 RC and IZS LT 01/17 RC.

**Acknowledgments:** The authors are grateful to Ettore Galvano for support in performing the cell tests. The technical assistance of Luca Imperatori, Massimo Di Menno Di Bucchianico and Marco Ortenzi is gratefully acknowledged. ÅboAkademi's Johan Gadolin Scholarship, and Leena Hupa, are gratefully acknowledged for a visiting fellowship for K.S.

**Conflicts of Interest:** The authors declare no conflict of interest.

## References

1. Hench, L.L.; Polak, J.M. Third-generation biomedical materials. *Science* **2002**, *295*, 1014–1017. [CrossRef] [PubMed]
2. Vallet-Regí, M. Evolution of bioceramics within the field of biomaterials. *C. R. Chim.* **2010**, *13*, 174–185. [CrossRef]
3. Brånemark, P.I.; Breine, U.; Johansson, B.; Roylance, P.J.; Röckert, H.; Yoffey, J.M. Regeneration of bone marrow. *Cell Tissue Organs* **1964**, *59*, 1–46. [CrossRef]
4. Rau, J.V.; Teghil, R.; Fosca, M.; De Bonis, A.; Cacciotti, I.; Bianco, A.; Rossi Albertini, V.; Caminiti, R.; Ravaglioli, A. Bioactive glass-ceramic coatings prepared by pulsed laser deposition from RKKP targets (sol-gel vs melt-processing route). *Mater. Res. Bull.* **2012**, *47*, 1130–1137. [CrossRef]
5. Rau, J.V.; Cacciotti, I.; Laureti, S.; Fosca, M.; Varvaro, G.; Latini, A. Bioactive, nanostructured Si-substituted hydroxyapatite coatings on titanium prepared by pulsed laser deposition. *J. Biomed. Mater. Res. Part B Appl. Biomater.* **2015**, *103 B*, 1621–1631. [CrossRef]
6. De Bonis, A.; Curcio, M.; Fosca, M.; Cacciotti, I.; Santagata, A.; Teghil, R.; Rau, J.V. RBP1 bioactive glass-ceramic films obtained by pulsed laser deposition. *Mater. Lett.* **2016**, *175*, 195–198. [CrossRef]
7. Ledda, M.; Fosca, M.; De Bonis, A.; Curcio, M.; Teghil, R.; Lolli, M.G.; De Stefanis, A.; Marchese, R.; Rau, J.V.; Lisi, A. Placenta derived mesenchymal stem cells hosted on RKKP glass-ceramic: A tissue engineering strategy for bone regenerative medicine applications. *BioMed Res. Int.* **2016**, *2016*, 3657906. [CrossRef]
8. Curcio, M.; De Stefanis, A.; De Bonis, A.; Teghil, R.; Rau, J.V. Pulsed laser deposited bioactive RKKP-Mn glass-ceramic coatings on titanium. *Surf. Coat. Technol.* **2019**, *357*, 122–128. [CrossRef]
9. Rau, J.V.; Curcio, M.; Raucci, M.G.; Barbaro, K.; Fasolino, I.; Teghil, R.; Ambrosio, L.; De Bonis, A.; Boccaccini, A.R. Cu-releasing bioactive glass coatings and their in vitro properties. *ACS Appl. Mater. Interfaces* **2019**, *11*, 5812–5820. [CrossRef]
10. Hench, L.L.; Splinter, R.J.; Allen, W.C.; Greenlee, T.K. Bonding mechanisms at the interface of ceramic prosthetic materials. *J. Biomed. Mater. Res. Symp.* **1971**, *2*, 117–141. [CrossRef]
11. Song, Z.; Borgwardt, L.; Høiby, N.; Wu, H.; Sørensen, T.S.; Borwardt, A. Prosthesis infections after orthopedic joint replacement: The possible role of bacterial biofilms. *Orthop. Rev.* **2013**, *5*, 65–71. [CrossRef] [PubMed]
12. Andersson, Ö.H. Glass transition temperatures of glasses in the SiO<sub>2</sub>-Na<sub>2</sub>O-CaO-P<sub>2</sub>O<sub>5</sub>-Al<sub>2</sub>O<sub>3</sub>-B<sub>2</sub>O<sub>3</sub> system. *J. Mater. Sci. Mater. Med.* **1992**, *3*, 326–328. [CrossRef]
13. Brink, M.; Turunen, T.; Happonen, R.P.; Yli-Urpo, A. Compositional dependence of bioactivity of glasses in the system Na<sub>2</sub>O-K<sub>2</sub>O-MgO-CaO-B<sub>2</sub>O<sub>3</sub>-P<sub>2</sub>O<sub>5</sub>-SiO<sub>2</sub>. *J. Biomed. Mater. Res.* **1997**, *37*, 114–121. [CrossRef]
14. Brink, M.; Karlsson, K.H.; Yli-Urpo, A. Novel Bioactive Glasses and Their Use. Patent No. WO 96/21628, 18 July 1996.
15. Yao, A.; Wang, D.; Huang, W.; Fu, Q.; Rahaman, M.N.; Day, D.E. In vitro bioactive characteristics of borate-based glasses with controllable degradation behaviour. *J. Am. Ceram. Soc.* **2007**, *90*, 303–306. [CrossRef]
16. Fu, Q.; Rahaman, M.N.; Fu, H.; Liu, X. Silicate, borosilicate, and borate bioactive glass scaffolds with controllable degradation rate for bone tissue engineering applications. I. Preparation and in vitro degradation. *J. Biomed. Mater. Res. A* **2010**, *95A*, 164–171. [CrossRef]

17. Balasubramanian, P.; Grünewald, A.; Detsch, R.; Hupa, L.; Jokic, B.; Tallia, F.; Solanki, A.K.; Jones, J.R.; Boccaccini, A.R. Ion release, hydroxyapatite conversion, and cytotoxicity of boron-containing bioactive glass scaffolds. *Int. J. Appl. Glass Sci.* **2016**, *7*, 206–215. [CrossRef]
18. Schuhladen, K.; Wang, X.; Hupa, L.; Boccaccini, A.R. Dissolution of borate and borosilicate bioactive glasses and the influence of ion (Zn, Cu) doping in different solutions. *J. Non-Cryst. Solids* **2018**, *502*, 22–34. [CrossRef]
19. Balasubramanian, P.; Büttner, T.; Miguez Pacheco, V.; Boccaccini, A.R. Boron-containing bioactive glasses in bone and soft tissue engineering. *J. Eur. Ceram. Soc.* **2018**, *38*, 855–869. [CrossRef]
20. Huang, W.; Day, D.E.; Kittiratanapiboon, K.; Rahaman, M.N. Kinetics and mechanisms of the conversion of silicate (45S5), borate, and borosilicate glasses to hydroxyapatite in dilute phosphate solution. *J. Mater. Sci. Mater. Med.* **2006**, *17*, 583–596. [CrossRef]
21. Liu, X.; Rahaman, M.N.; Day, D.E. Conversion of melt-derived microfibrinous borate (13-93B3) and silicate (45S5) bioactive glass in a simulated body fluid. *J. Mater. Sci.: Mater. Med.* **2013**, *24*, 583–595. [CrossRef]
22. Nielsen, F.H. Studies on the relationship between boron and magnesium which possibly affects the formation and maintenance of bones. *Magnes. Trace Elem.* **1990**, *9*, 61–69. [CrossRef] [PubMed]
23. Devirian, T.A.; Volpe, S.L. The physiological effects of dietary boron. *Crit. Rev. Food Sci. Nutr.* **2003**, *43*, 219–231. [CrossRef] [PubMed]
24. Marion, N.; Liang, W.; Reilly, G.; Day, D.E.; Rahaman, M.N.; Mao, J.J. Bioactive borate glass supports the osteogenic potential of human mesenchymal stem cells. *Mech. Adv. Mater. Struct.* **2005**, *12*, 239–246. [CrossRef]
25. Thyparambil, N.J.; Gutgesell, L.C.; Hurley, C.C.; Flowers, L.E.; Day, D.E.; Semon, J.A. Adult stem cell response to doped bioactive borate glass. *J. Mater. Sci. Mater. Med.* **2020**, *31*, 13. [CrossRef] [PubMed]
26. Haro Durand, L.A.; Vargas, G.E.; Romero, N.M.; Vera-Mesones, R.; Porto-López, J.M.; Boccaccini, A.R.; Zago, M.P.; Baldi, A.; Gorustovich, A. Angiogenic effects of ionic dissolution products released from a boron-doped 45S5 bioactive glass. *J. Mater. Chem. B* **2015**, *3*, 1142–1148. [CrossRef]
27. Kalmodia, S.; Molla, A.R.; Basu, B. In vitro cellular adhesion and antimicrobial property of SiO<sub>2</sub>-MgO-Al<sub>2</sub>O<sub>3</sub>-K<sub>2</sub>O-B<sub>2</sub>O<sub>3</sub>-F glass ceramic. *J. Mater. Sci. Mater. Med.* **2010**, *21*, 1297–1309. [CrossRef]
28. Ottomeyer, M.; Mohammadkhan, A.; Day, D.; Westenberg, D. Broad-spectrum antibacterial characteristics of four novel borate-based bioactive glasses. *Adv. Microbiol.* **2016**, *6*, 776–787. [CrossRef]
29. Rodriguez, O.; Ston, W.; Schemitsch, E.H.; Zalzal, P.; Waldman, S.; Papini, M.; Towler, M.R. Titanium addition influences antibacterial activity of bioactive glass coatings on metallic implants. *Heliyon* **2017**, *3*, e00420. [CrossRef]
30. Jung, S.; Day, T.; Boone, T.; Buziak, B.; Omar, A. Anti-biofilm activity of two novel, borate based, bioactive glass wound dressings. *Biomed. Glasses* **2019**, *5*, 67–75. [CrossRef]
31. Fu, Q.; Rahaman, M.N.; Sonny Bal, B.; Bonewald, L.F.; Kuroki, K.; Brown, R.F. Silicate, borosilicate, and borate bioactive glass scaffolds with controllable degradation rate for bone tissue engineering applications. II. In vitro and in vivo biological evaluation. *J. Biomed. Mater. Res. A* **2010**, *95A*, 1172–1179. [CrossRef]
32. Peddi, L.; Brow, R.K.; Brown, R.F. Bioactive borate glass coatings for titanium alloys. *J. Mater. Sci. Mater. Med.* **2008**, *19*, 3145–3152. [CrossRef] [PubMed]
33. Matinmanesh, A.; Li, Y.; Nouhi, A.; Zalzal, P.; Schemitsch, E.H.; Towler, M.R.; Papini, M. Evaluating the critical strain energy release rate of bioactive glass coatings on Ti<sub>6</sub>Al<sub>4</sub>V substrates after degradation. *J. Mech. Behav. Biomed. Mater.* **2018**, *78*, 273–281. [CrossRef] [PubMed]
34. Kargozar, S.; Montazerian, M.; Fiume, E.; Bano, F. Multiple and promising applications of strontium (Sr)-containing bioactive glasses in bone tissue engineering. *Front. Bioeng. Biotechnol.* **2019**, *7*, 161. [CrossRef] [PubMed]
35. Rau, J.V.; Antoniac, I.; Fosca, M.; De Bonis, A.; Blajan, A.I.; Cotrut, C.; Graziani, V.; Curcio, M.; Cricenti, A.; Niculescu, M.; et al. Glass-ceramic coated Mg-Ca alloys for biomedical implant applications. *Mater. Sci. Eng. C* **2016**, *64*, 362–369. [CrossRef]
36. Gittens, R.A.; Mclachlan, T.; Olivares-Navarrete, R.; Cai, Y.; Berner, S.; Tannenbaum, R.; Schwartz, Z.; Sandhage, K.H.; Boyan, B.D. Biomaterials the effects of combined micron-/submicron-scale surface roughness and nanoscale features on cell proliferation and differentiation. *Biomaterials* **2011**, *32*, 3395–3403. [CrossRef]
37. Im, B.J.; Lee, S.W.; Oh, N.; Lee, M.H.; Kang, J.H.; Leesungbok, R.; Lee, S.C.; Ahn, S.J.; Park, J.S. Texture direction of combined microgrooves and submicroscale topographies of titanium substrata influence adhesion, proliferation, and differentiation in human primary cells. *Arch. Oral Biol.* **2011**, *57*, 898–905. [CrossRef]

38. Ma, J.; Wang, C.Z.; Ban, C.L.; Chen, C.Z.; Zhang, H.M. Pulsed laser deposition of magnesium-containing bioactive glass film on porous Ti-6Al-4V substrate pretreated by micro-arc oxidation. *Vacuum* **2016**, *125*, 48–55. [CrossRef]
39. Sanz, C.K.; dos Santos, A.R.; da Silva, M.H.P.; Marçal, R.; Tute, E.M.; Meza, E.L.; Mello, A.; Borghi, F.F.; de Souza Camargo, S.A. Niobo-phosphate bioactive glass films produced by pulsed laser deposition on titanium surfaces for improved cell adhesion. *Ceram. Int.* **2019**, *45*, 18052–18058. [CrossRef]
40. Shaikh, S.; Shaikh, S.; Majumdar, A.G.; Subramanian, M.; Sucharita, S. 45S5 bioactive glass coating on Ti6Al4V alloy using pulsed laser deposition technique. *Mater. Res. Express* **2020**, *6*, 125428. [CrossRef]
41. Wang, D.G.; Zhang, W.L.; Li, H.J.; Zhang, J.H.; Chen, C.Z. HA/BG composite films deposited by pulse laser under O<sub>2</sub> atmosphere. *Ceram. Int.* **2017**, *43A*, 672–676. [CrossRef]
42. Wang, D.G.; Chen, C.Z.; Yang, X.X.; Ming, X.C.; Zhang, W.L. Effect of bioglass addition on the properties of HA/BG composite films fabricated by pulsed laser deposition. *Ceram. Int.* **2018**, *44*, 14528–14533. [CrossRef]
43. Abdelghany, A.M.; Elbatal, H.A.; Ezzeldin, F.M. Bone bonding ability behavior of some ternary borate glasses by immersion in sodium phosphate solution. *Ceram. Int.* **2012**, *38*, 1105–1113. [CrossRef]
44. Gyorgy, E.; Grigorescu, S.; Socol, G.; Mihailescu, I.N.; Janackovic, D.; Dindune, A.; Kanepe, Z.; Palcevskis, E.; Zdrentu, E.L.; Petrescu, S.M. Bioactive glass and hydroxyapatite thin films obtained by pulsed laser deposition. *Appl. Surf. Sci.* **2007**, *253*, 7981–7986. [CrossRef]
45. Liste, S.; Serra, J.; González, P.; Borrajo, J.P.; Chiussi, S.; León, B.; Pérez-Amor, M. The role of the reactive atmosphere in pulsed laser deposition of bioactive glass films. *Thin Solid Films* **2004**, *453–454*, 224–228. [CrossRef]
46. Lefebvre, L.; Chevalier, J.; Gremillard, L.; Zenati, R.; Thollet, G.; Bernache-Assolant, D.; Govin, A. Structural transformations of bioactive glass 45S5 with thermal treatments. *Acta Mater.* **2007**, *55*, 3305–3313. [CrossRef]
47. Begam, H.; Kundu, B.; Chanda, A.; Nandi, S. MG63 osteoblast cell response on Zn doped hydroxyapatite (HAp) with various surface features. *Ceram. Int.* **2017**, *43*, 3752–3760. [CrossRef]
48. Donoso, N.G.; Mendez-Vilas, A.; Bruque, J.M.; Gonzalez-Martin, M.L. On the relationship between common amplitude surface roughness parameters and surface area: Implications for the study of cell–material interactions. *Int. Biodeterior. Biodegrad.* **2007**, *59*, 245–251. [CrossRef]
49. Zareidoost, A.; Yousefpour, M.; Ghaseme, B.; Amanzadeh, A. The relationship of surface roughness and cell response of chemical surface modification of titanium. *J. Mater. Sci. Mater. Med.* **2012**, *23*, 1479–1488. [CrossRef]
50. Alipour, F.; Parham, A.; KazemiMehrerjerd, H.; Dehghani, H. Equine adipose-derived mesenchymal stem cells: Phenotype and growth characteristics, gene expression profile and differentiation potentials. *Cell J.* **2015**, *16*, 456–465.
51. Ciraldo, F.E.; Liverani, L.; Gritsch, L.; Goldmann, W.H.; Boccaccini, A.R. Synthesis and characterization of silver-doped mesoporous bioactive glass and its applications in conjunction with electrospinning. *Materials* **2018**, *11*, 692. [CrossRef]

**Publisher’s Note:** MDPI stays neutral with regard to jurisdictional claims in published maps and institutional affiliations.



© 2020 by the authors. Licensee MDPI, Basel, Switzerland. This article is an open access article distributed under the terms and conditions of the Creative Commons Attribution (CC BY) license (<http://creativecommons.org/licenses/by/4.0/>).

Article

# Rescue Blankets-Transmission and Reflectivity of Electromagnetic Radiation

Hannah Kranebitter <sup>1,2</sup>, Bernd Wallner <sup>3</sup>, Andreas Klinger <sup>2</sup>, Markus Isser <sup>2</sup>, Franz J. Wiedermann <sup>3</sup> and Wolfgang Lederer <sup>3,\*</sup>

<sup>1</sup> Hall County Hospital, Milserstr. 10, 6060 Hall, Austria; hannah.kranebitter@tirol-kliniken.at

<sup>2</sup> Medical Division, Austrian Mountain Rescue Service—Tyrol, Florianistr. 2, 6410 Telfs, Austria; andiklinger@yahoo.com (A.K.); m.isser@bergrettung.tirol (M.I.)

<sup>3</sup> Department of Anesthesiology and Critical Care Medicine, Medical University of Innsbruck, Anichstr. 35, 6020 Innsbruck, Austria; bernd.wallner@i-med.ac.at (B.W.); franz.wiedermann@i-med.ac.at (F.J.W.)

\* Correspondence: wolfgang.lederer@i-med.ac.at

Received: 19 March 2020; Accepted: 8 April 2020; Published: 10 April 2020

**Abstract:** Rescue blankets are medical devices made of a polyethylene terephthalate sheet coated with a thin aluminum layer. Blankets are used for protection against hypothermia in prehospital emergency medicine and outdoor sports, but totally different qualities are typical for these multi-functional tools. On the one hand, rescue sheets prevent hypothermia by reducing thermo-convection and diminishing heat loss from evaporation and thermal radiation. On the other hand, the sheets promote cooling by acting as a radiant barrier, by providing shade and even by increasing heat conduction when the sheet is in direct contact with the skin. As foils are watertight and windproof, they can function as vapor barriers and even as stopgap bivouac sacks. We evaluated three experimental studies, one on heat loss by rescue blankets according to surface color, one on transparency with ultraviolet radiation, high-energy visible light and visible light, and one on infrared radiation from rescue blankets. When evaluating the effects of different bands of the electromagnetic spectrum on rescue sheets, we focused on ultraviolet radiation (200–380 nm), high-energy visible light in the violet/blue band (380–450 nm), visible light (380–760 nm) and infrared radiation (7500–13,500 nm). Rescue sheets transmit between 1% and 8% of visible light and about 1% of ultraviolet B radiation (280–315 nm), providing sufficient transparency and adequate protection from snow blindness. Reflection of visible light increases detectability in search and rescue missions performed in good visibility conditions, while reflection of infrared radiation increases detectability in poor visibility conditions and provides protection against hypothermia.

**Keywords:** emergency medicine; far infrared; hypothermia; insulation; rescue work; rescue blanket; space blanket; survival blanket

## 1. Introduction

Rescue blankets are medical devices with a characteristic silver and gold surface on either side that are used for protection against hypothermia by emergency medical services (EMS) and by sportsmen in outdoor activities. Accidental hypothermia, defined as a core body temperature of less than 35 °C, is more frequently observed during the winter season, but it occurs throughout the year, even in geographic regions with hot climate [1]. There is a risk of hypothermia whenever the ability to control body temperature through the nervous system, metabolism, circulation and muscle activity is insufficient to compensate for heat loss due to the emission, conduction and convection of infrared (IR) radiation. Both clothing and absorption of infrared radiation reflected by the environment help balance heat loss. Beside acidosis and coagulopathy, hypothermia is one of three life-threatening conditions

that constitute a lethal triad in emergency patients [2]. The decrease in core temperature goes along with impaired organ function, clotting disorders and increased mortality.

Hypothermia prevention is important in prehospital treatments involving the external rewarming techniques employed by EMS [3]. When comparing different conventional blankets, e.g., space blankets, bubble wrap, blizzard blankets, ambulance blankets and ready heat blankets, Zasa et al. observed that all tested tools significantly reduced heat loss but could not completely compensate for the temperature deficit [4]. Contrarily, Leung et al. observed an increase in skin temperature of approximately 1 °C, when measured with a thermal camera aimed at a forearm wrapped in a rescue blanket [5]. Allen et al. performed an experimental study on a fluid torso model and observed diminished temperature loss when applying passive warming devices such as space blankets [6]. The authors reported that comparison of medical devices providing either active or passive rewarming did not find striking differences between the two methods [6]. Rescue blankets achieved a heat loss of less than 1 °C within 60 min and less than 2 °C within 120 min. An increase in body temperature was observed only in shivering patients with mild hypothermia. In fact, shivering heat production is crucial for thermoregulation during cold-exposure [7]. Haverkamp et al. confirmed that in the prehospital setting patients can be protected from excessive heat loss by rescue blankets, but cannot be rewarmed [8]. However, the fact that passive hypothermia-prevention devices function independently of electricity means they are especially suitable in remote areas [6]. Rescue blankets act as a vapor barrier and limit the need for shivering thermogenesis [8]. Protection from heat loss was especially efficient when the rescue blanket was arranged between two layers of woolen blankets [8]. In the prehospital setting, plastic bags used as vapor barriers were as effective as the removal of wet clothes [9]. In accident and emergency departments, rescue blankets proved their effectiveness in protecting against hypothermia [10], in particular when applied in combination with woolen blankets [11].

In this manuscript, we focused on experimental research dealing with the transmission and reflection of radiation by rescue blankets. The originality and novelty of this review are based in its investigations of the physical properties that affect the medical applicability of the tools used in emergency care.

## 2. Factors Influencing Electromagnetic Measurements with Rescue Sheets

### 2.1. Ultraviolet (UV) Radiation

When testing metallized rescue sheets for transmission of UV radiation, it must be remembered that the thickness and transparency of foils can differ between production series, and among the variety of available rescue sheet products [12]. This may have a direct impact on transparency. Furthermore, the metallized surface increases the sheet's ability to reflect radiation. The conservation of energy means the relation between transmissivity (T) and reflectivity (R) is complementary (1).

$$T = 1 - R \quad (1)$$

A considerable fraction of the electromagnetic spectrum contained in solar radiation is made up of UV radiation and visible light. Manifold environmental conditions influence accurate measurement of the intensity of solar radiation, including geographic location, altitude and reflected radiant energy from the ground [13,14]. Direct effects on eyes caused by UV radiation may be difficult to assess as intense solar radiation leads to pupillary constriction and squinting, which reduce ocular exposure [13,15]. The use of rescue sheets to protect the face from UV radiation entails the risk of rebreathing CO<sub>2</sub> when the rescue sheet is kept tight to the skin [12].

### 2.2. Infrared (IR) Radiation

All objects with a temperature greater than absolute zero (0 K) emit electromagnetic radiation arising from the thermal motion of particles. This results in energy losses via surface areas [16,17]. Human beings with a skin temperature of around 33 °C (306 K) emit infrared radiation at peak

wavelengths of 10  $\mu\text{m}$  [17]. The human body can control body temperature by means of the nervous system, metabolic system, circulation and muscle activity. In addition, clothing and absorption of infrared radiation reflected by the environment help balance heat loss. Spectral distribution of intensity depends on temperature [18]. The spectrum of hot objects shifts towards higher frequencies and shorter wavelengths. Thus, wavelengths of radiation reflected by objects are shorter than wavelengths of radiation emitted by objects. Ideally, a black body absorbs and emits radiation regardless of frequency ( $\nu$ ). The total intensity emitted by a black body is proportional to  $T^4$  according to the Stephan–Boltzmann law [16]. A real body will have both frequency-dependent emissivity ( $\nu$ ) and absorptivity ( $\nu$ ) (2).

$$e(\nu) = a(\nu) \quad (2)$$

Incident electromagnetic radiation on a surface can be absorbed (a), reflected (r) or transmitted (t). For a given radiant power  $\Phi$  (3) hitting a surface,  $a\Phi$  is absorbed,  $r\Phi$  is reflected and  $t\Phi$  is transmitted, with a, r and t being complementary (4) [16,17].

$$\Phi = dQ/dt \quad (3)$$

$$a + r + t = 1 \quad (4)$$

Emissivity (E), defined as the ability to emit radiation via the surface, depends on various factors such as surface morphology, viewing angle, material composition and temperature. The emissivity coefficient “ $\epsilon$ ” gives the radiation of heat from various materials as compared with the radiation of heat from an ideal black surface as  $\epsilon = 1$  [16]. The thermal radiative properties of films depend on the content, size and nature of aluminum particles [19]. For anodized aluminum,  $\epsilon = 0.55$  [20]. With increasing concentrations of aluminum, Sonnier et al. observed an increase in R, making it a suitable product for limiting thermal radiation from a body [19], whereas for a thin polyethylene terephthalate sheet  $T = 1.5$ , for an aluminum-coated foil T can be expected to be less than 1% [20,21]. E and R are complementary, as radiometric measurements mostly depend on surface E and R of radiation [20]. R is more relevant at short distances as both the heat sustained by the surface and the reflected temperature of the surrounding environment influence measurements [20].

### 2.3. Thermal Imaging

Accurate temperature measurements depend on many factors including, E and R from objects and T from the atmosphere [20]. Detection of IR radiation within the wavelength-range of 6000 to 15,000 nm (mid- to far IR), using thermal cameras, is based on emission, transmission and reflection. Temperatures between  $-10$  and  $200$   $^{\circ}\text{C}$  give off no radiation that is visible to the naked eye other than what is reflected. Glass does not allow transmission of radiation in the range of 8000 to 12,000 nm. As E from an aluminum layer is negligible, most of the radiation from a metallized rescue blanket will actually be reflected radiation from the environment. Radiometric measurements from distances exceeding 100 m are influenced by atmospheric radiation. Remote temperature sensing using thermal cameras relies on the ability to accurately compensate for surface characteristics, atmospheric interference and the imaging system [21]. Imaging systems provide further adjustments with digital detail enhancement, active contrast enhancement, and high-gain mode with increased sensitivity to temperature differences [20].

## 3. Materials and Methods

Rescue blankets are low-weight and low-bulk medical devices; Category 1, according to Directive 93/42/EEC [22]. Rescue blankets are metallized foils that reflect electromagnetic waves; they are robust, watertight and windproof [8,10,11,23]. We investigated two different brands of rescue blanket commonly used by ground emergency medical services (EMS) and helicopter EMS in Tyrol, Austria. Blankets were obtained from Austrian Red Cross (ARC Rescue Sheet, ÖRK, A-1230 Vienna, Austria), and from Mountain Rescue Tyrol (LEINA-WERKE GmbH, D-51570 Windeck, Germany) [12,24]. The

effects of radiation on rescue blankets from UV radiation in the spectral range between 200 and 380 nm, high-energy visible (HEV) light in the violet/blue band range between 380 and 450 nm, visible light in the range between 380 and 760 nm, and IR radiation in the range between 7500 and 13,500 nm, were all evaluated.

There are only a few scientific publications that focus on the T and R of electromagnetic radiation by rescue sheets used in emergency medicine (Figure 1) [25]. PubMed, Web of Science and Google were screened for the combined key words: “survival blanket and hypothermia” (31 in Web of Science, 38 in PubMed and 1,170,000 in Google.at); “space blanket and hypothermia” (14 in Web of Science, 13 in PubMed and 498,000 in Google.at); “rescue blanket and hypothermia” (18 in Web of Science, 10 in PubMed and 1,240,000 in Google.at). There were no findings for: “infrared radiation” and either “survival blanket”, “space blanket” or “rescue blanket” according to our query in PubMed. However, when searching for “radiation and space blanket” in Web of Science, five out of 75 papers dealt with the resistance of polymer films to atom oxygen erosion, vacuum UV stability and radiation resistance in low earth orbit. Six papers in Web of Science concerned “infrared radiation and space blanket” (4 astrophysical, 2 environmental), but were not directly related to the topic. After exclusion of papers that dealt with space-flight, therapeutic hypothermia, animal research and in-hospital research, one theoretical and two experimental studies remained that focused on “radiation and rescue blankets in emergency medicine” (Figure 1).

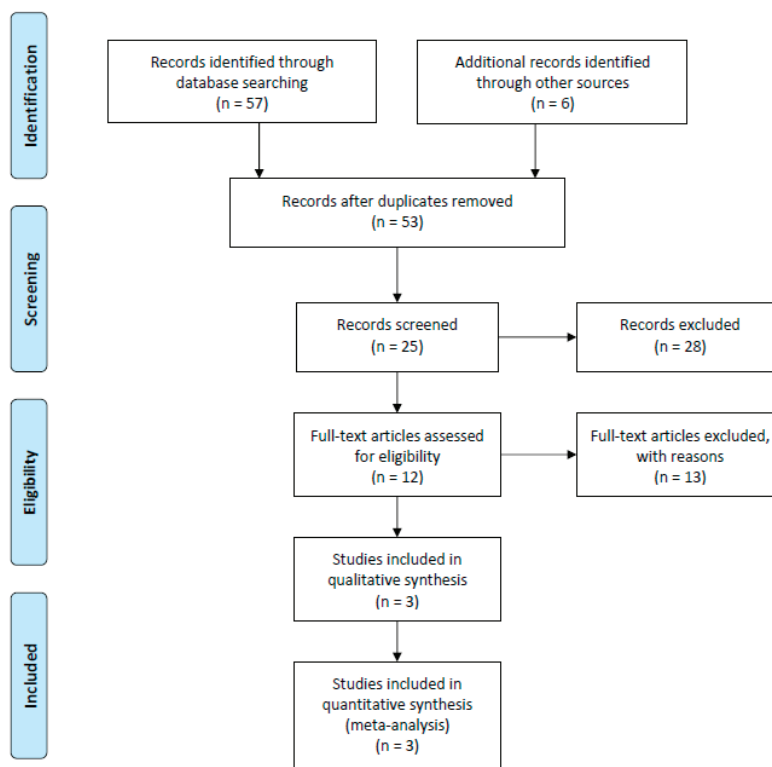


**Figure 1.** PRISMA Flow Diagram of literature research. The PRISMA Group (2009).

### 3.1. Measurement of Heat Loss by Rescue Blankets According to Surface Color

In order to find out which side of the rescue blanket should be up to protect against hypothermia, Viennot and Décamp applied a linear model in a theoretical experimental study [16]. The authors performed an experiment with 210 cm<sup>3</sup> of water in a plastic bowl wrapped in a rescue blanket, with either gold or silver outside. Starting at 38 °C, the bowl was kept in a freezer at −17 °C for one hour. The experiment was repeated four times and the gradients between initial temperature and accurate temperature after the cooling time were compared [16].

### 3.2. *Optometric Measurement of Transparency with UV Radiation, HEV Light and Visible Light*

The effects of radiation on rescue blankets from UV radiation, HEV light and visible light in the spectral range between 200 and 760 nm were measured optometrically using a lens analyzer (Humphrey Systems LA 360; Carl Zeiss Meditec Inc., Dublin, CA, USA). Measurements were performed with silver or gold side up [24].

### 3.3. *Thermographic Measurement of IR Radiation from Rescue Blankets*

For thermographic imaging, we used a radiometric thermal camera (DJI Zenmuse XT, Shenzhen, China; uncooled microbolometer, image resolution: 640 (H) × 512 (V); pixel pitch: 17 µm; lens model: 13 mm; digital zoom: 8×; sensitivity: <50 mK at f/1.0; accuracy of +10 °C; image optimization and digital detail enhancement; operating temperature: −10 to 40 °C at a relative humidity between 5% and 95%), mounted on a Zenmuse XT gimbal and remotely controlled [21,23]. The ability to spatially resolve detailed temperature measurements in a thermal image depends on pixel resolution, image focus, blur, and environmental conditions including distance, humidity, temperature, and atmospheric transmission [21]. In order to maintain at least a 10-pixel resolution in the thermal image, the distance between the camera and the object did not exceed 50 m in our study. To diminish reflection, we kept the view angle within 60° of straight-on and oblique measurements [23].

## 4. Results and Discussion

### 4.1. *Measurement of Heat Loss by Rescue Blankets According to Surface Color*

It is still not clear which side, silver or gold, should be up in order to protect sufficiently against cold [16,26]. Viennot and Décamp's discussion and analysis of the topic is restricted to the high reflective power of the silver side [16]. The authors concluded that in the case of hypothermia the common recommendation, with silver down in order to reflect IR radiation, is based on three hypotheses. Firstly, protection against hypothermia using rescue blankets is entirely a radiant process. Secondly, the continuing production of heat from metabolism and muscle activity of the victim is not considered. Thirdly, while interactions between the body and the rescue blanket are taken into account, reflected radiation and blocked absorption of environmental radiation are ignored [16]. When applying a linear model, as used in electricity and increased resistance to heat transfer, silver up is recommended for dry and calm weather, and silver down for rainy and windy weather [16]. Their recommendations were based on an experimental setting with 38 °C warm water in a plastic bowl wrapped in a bag made of an emergency blanket and kept in a freezer at −17 °C for one hour. In the calm and dry environment of the freezer, the authors observed less cooling with silver up [16].

### 4.2. *Optometric Measurement of Transparency with UV Radiation, HEV Light and Visible Light*

We optometrically investigated the properties of conventional rescue sheets subjected to the electromagnetic spectrum in the range between 200 and 780 nm using a lens analyzer [12]. Regarding protection from UV radiation, we particularly focused on the UVB fraction, as even short exposure to high doses of UVB rays reflected by snow or glaciers at high altitude can cause acute snow blindness. While UVC rays are blocked by the ozone layer of the atmosphere, UVB and most UVA rays penetrate the atmosphere [13]. We found that rescue blankets adequately protect against UV radiation and HEV light [12]. No differences were observed between silver and gold side up. T correlated negatively with the degree of protection from UV radiation. According to our investigation, even a single layer of a rescue blanket can significantly diminish UV light exposure. Single-layer transparency for visible light ranged between 1% and 8%. Transparency for UVB rays afforded by each tested rescue sheet brand was between 0% and 1% for the single layer. Double-layer rescue sheets blocked 100% of ultraviolet B radiation. As there is still sufficient transparency for visible light, a rescue sheet put over the mountaineer's head allows him to descend under his own power while being protected from UV radiation [12].

#### 4.3. Thermographic Measurement of IR Radiation from Rescue Blankets

Our study with optometrical measurements also showed that transmission of near-IR radiation in the IR–visible radiation boundary region is very low, regardless of whether gold or silver is up [12]. In a further experimental study, we measured thermoradiation in the spectrum 760–13,500 nm from probands in a snow-covered backcountry environment. Radiometric measurements were performed on a model in supine position on an insulating sheet covered with rescue blankets, either silver side up or gold side up (Figure 2).

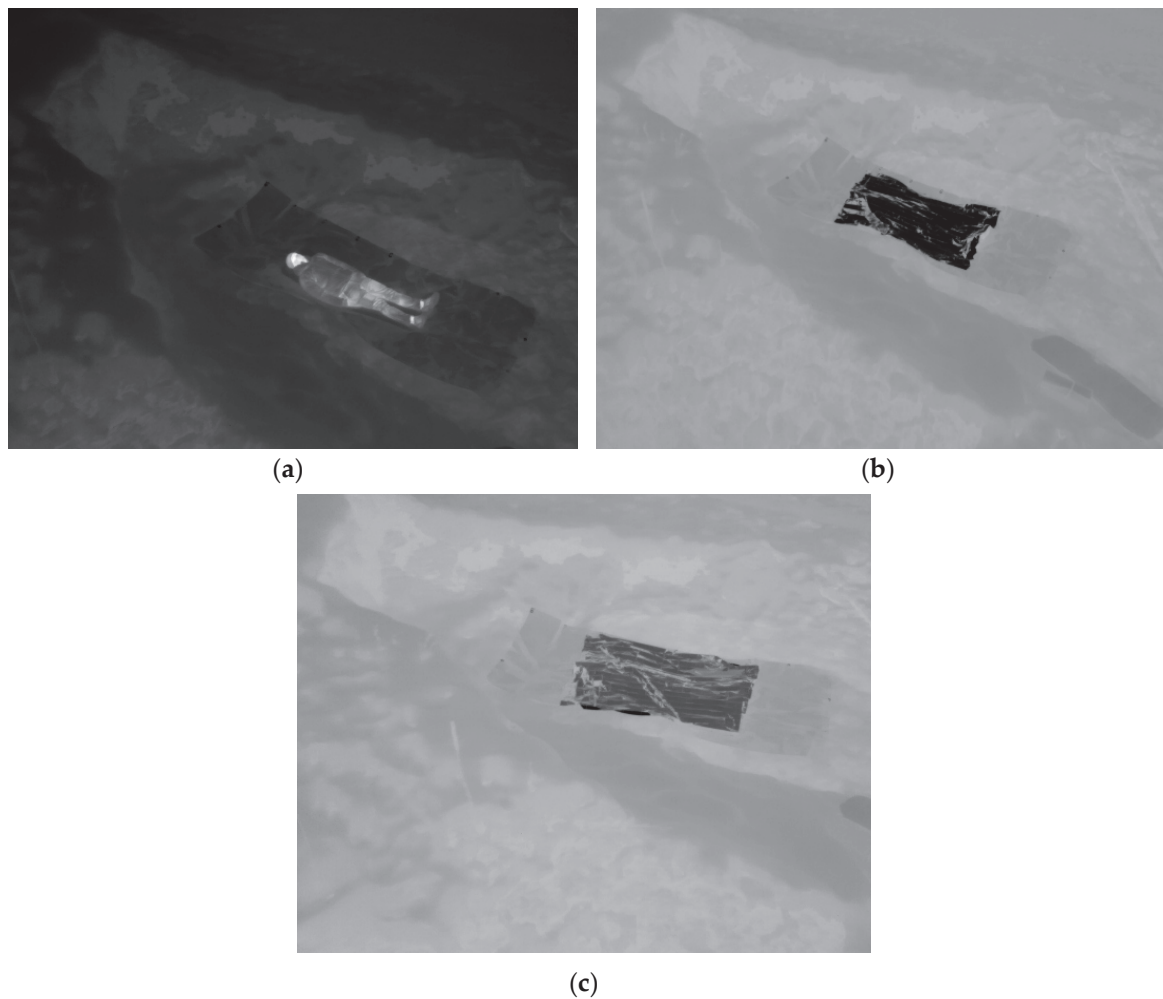


**Figure 2.** Thermal images in a snow-covered backcountry environment. (a) Model in supine position on an insulating sheet. (b) Model in supine position on an insulating sheet covered with a single-layer rescue blanket, silver side up. (c) Model in supine position on an insulating sheet covered with a single-layer rescue blanket, gold side up (air temperature:  $-6.2\text{ }^{\circ}\text{C}$ ; snow temperature:  $-7.6$  or  $-6.3\text{ }^{\circ}\text{C}$  when considering the emissivity coefficient  $\varepsilon = 0.83$  for snow).

Thermal imaging was performed with an IR camera lifted to altitudes of 5 and 50 m above ground with a gas-filled balloon. Thermal images of rescue blankets on a snow surface, exposing either their gold or silver side, indicated different surface temperatures. As compared to forehead temperature, IR radiation was diminished between 72.6% and 92.3%, depending on the number of covering garments. The median percentage of IR transmission blocked by a single-layer rescue blanket when the gold side was up was 82.1% [20]. With a single layer rescue blanket, body shape was completely hidden (Figure 2). With three layers of rescue blankets, up to 100% of transmission was blocked. Our findings

indicate that rescue blankets can effectively block infrared radiation. A single-layer rescue blanket is sufficient to render detection of a body shape impossible.

## 5. Implications

Rescue blankets have the potential to protect from solar radiation in the electromagnetic spectrum between UV radiation and far IR. A single-layer rescue sheet put over a person's head provides sufficient transparency with regard to visible light for one to walk under one's own power, with the eyes and skin being adequately protected from UVB radiation. Thus, rescue blankets have the potential to function as makeshift sun goggles against snow blindness during outdoor activities under high solar irradiation [12]. As transmission of radiation in the near, mid- and far IR region is very low, it does not matter whether the gold or silver is up when rescue blankets are used to protect against hypothermia in wilderness emergencies [12,24]. It is more important to arrange the blanket under the outer layer of clothing but without making direct contact with the skin. Viennot and Décamp discuss a potential advantage when keeping silver up during dry and calm weather, and silver down during rainy and windy weather [16]. In search and rescue (SAR) missions, the actual temperature measured with thermal cameras is of less importance than the gradients of IR radiation between objects and environment [16,24]. As victims covered with a rescue blanket are difficult to detect, the camera operator should not exclusively concentrate on human body shapes but additionally watch for objects of 1 to 2 m lengths with strikingly low temperatures [24]. In SAR missions where thermal imaging is used by unmanned aerial vehicles to search for victims, rescue blankets should be removed from the body to increase the chance of being sighted [24].

## 6. Conclusions

Summing up the scarce information, based on our own measurements and on literature research, we conclude that, with regard to protection against hypothermia, it does not matter whether silver is turned down or not. There are several factors to be considered, including convective and conductive effects, vapor barrier function, and distance and moisture between the body and the blanket, among others. In the case of windy and wet weather and whenever protection from sunlight is desired, silver should be up. However, for SAR missions in snow and ice, having the gold side up will facilitate detection of the missing person during daytime. In low-visibility conditions and during the night, victims should remove the blanket whenever they expect surveillance from rescue personnel, as indicated by engine noise from drones and quadricopters. Operators of thermal cameras should not only focus on body shapes, but also be on the lookout for objects with a size of 1 to 2 m. Giving consideration to the different physical properties of rescue blankets increases the scope of medical applicability. This review accentuates the multi-functional applicability of rescue blankets in emergency medicine.

**Author Contributions:** Conceptualization, M.I. and W.L.; methodology H.K., M.I. and W.L.; validation, H.K., B.W., F.J.W. and W.L.; formal analysis, A.K. and W.L.; literature research, H.K., B.W., A.K., and W.L.; writing—original draft preparation, H.K., B.W., A.K., and W.L.; writing—review and editing, F.J.W. and W.L.; visualization, M.I.; supervision, F.J.W.; project administration, M.I. All authors have read and agreed to the published version of the manuscript.

**Funding:** This research received no external funding.

**Acknowledgments:** The authors are thankful to Andreas Kofler and Erich Kuehn for their constructive support in experimental research.

**Conflicts of Interest:** The authors declare no conflict of interest.

## References

1. Mommsen, P.; Andruszkow, H.; Frömke, C.; Zeckey, C.; Wagner, U.; van Griensven, M.; Frink, M.; Krettek, C.; Hildebrand, F. Effects of accidental hypothermia on posttraumatic complications and outcome in multiple trauma patients. *Injury* **2013**, *44*, 86–90. [CrossRef]

2. Gerecht, R. The lethal triad. Hypothermia, acidosis & coagulopathy create a deadly cycle for trauma patients. *JEMS* **2014**, *39*, 56–60. [PubMed]
3. Brugger, H.; Putzer, G.; Paal, P. Accidental hypothermia. *Anaesthesist* **2013**, *62*, 624–631. [CrossRef] [PubMed]
4. Zasa, M.; Flowers, N.; Zideman, D.; Hodgetts, T.J.; Harris, T. A torso model comparison of temperature preservation devices for use in the prehospital environment. *Emerg. Med. J.* **2016**, *33*, 418–422. [CrossRef] [PubMed]
5. Leung, E.M.; Colorado Escobar, M.; Stiubianu, G.T.; Jim, S.R.; Vyatskikh, A.L.; Feng, Z.; Garner, N.; Patel, P.; Naughton, K.L.; Follador, M.; et al. A dynamic thermoregulatory material inspired by squid skin. *Nat. Commun.* **2019**, *10*, 1–10. [CrossRef] [PubMed]
6. Allen, P.B.; Salyer, S.W.; Dubick, M.A.; Holcomb, J.B.; Blackburn, L.H. Preventing hypothermia: Comparison of current devices used by the US Army in an in vitro warmed fluid model. *J. Trauma* **2010**, *69*, 154–161. [CrossRef]
7. Tikuisis, P.; Giesbrecht, G.G. Prediction of shivering heat production from core and mean skin temperatures. *Eur. J. Appl. Physiol. Occup. Physiol.* **1999**, *79*, 221–229. [CrossRef] [PubMed]
8. Haverkamp, F.J.C.; Giesbrecht, G.G.; Tan, E.C.T.H. The prehospital management of hypothermia—An up-to-date overview. *Injury* **2018**, *49*, 149–164. [CrossRef]
9. Henriksson, O.; Lundgren, P.J.; Kuklane, K.; Holmér, I.; Giesbrecht, G.G.; Naredi, P.; Bjornstig, U. Protection against cold in prehospital care: Wet clothing removal or addition of a vapor barrier. *Wilderness Environ. Med.* **2015**, *26*, 11–20. [CrossRef]
10. Chadwick, S.; Gibson, A. Hypothermia and the use of space blankets: A literature review. *Accid. Emerg. Nurs.* **1997**, *5*, 122–125. [CrossRef]
11. Henriksson, O.; Lundgren, J.P.; Kuklane, K.; Holmér, I.; Bjornstig, U. Protection against cold in prehospital care—thermal insulation properties of blankets and rescue bags in different wind conditions. *Prehosp. Disaster Med.* **2009**, *24*, 408–415. [CrossRef] [PubMed]
12. Isser, M.; Kranebitter, H.; Kühn, E.; Lederer, W. High-energy visible light transparency and ultraviolet ray transmission of metallized rescue sheets. *Sci. Rep.* **2019**, *9*, 1–6. [CrossRef]
13. International Commission on Non-Ionizing Radiation Protection. ICNIRP statement—Protection of workers against ultraviolet radiation. *Health Phys.* **2010**, *99*, 66–87. [CrossRef] [PubMed]
14. Izadi, M.; Jonaidi-Jafari, N.; Pourazizi, M.; Alemzadeh-Ansari, M.H.; Hoseinpourfard, M.J. Photokeratitis induced by ultraviolet radiation in travelers: A major health problem. *J. Postgrad. Med.* **2018**, *64*, 40–46. [PubMed]
15. Sliney, D.H. How light reaches the eye and its components. *Int. J. Toxicol.* **2002**, *21*, 501–509. [CrossRef] [PubMed]
16. Viennot, L.; Décamp, N. Which Side to Put the Survival Blanket? Analysis and Suggestions for Activities with Students. Published by the MUSE Group (More Understanding with Simple Experiments) in the Physics Education Division (PED) of the European Physical Society (EPS). Available online: [https://cdn.ymaws.com/www.eps.org/resource/collection/016775D4-8888-474D-887F-3E33AEA5E6D0/EPSPED\\_SurvivalBlanket.pdf](https://cdn.ymaws.com/www.eps.org/resource/collection/016775D4-8888-474D-887F-3E33AEA5E6D0/EPSPED_SurvivalBlanket.pdf) (accessed on 30 March 2020).
17. Besson, U. Paradoxes of thermal radiation. *Eur. J. Phys.* **2009**, *30*, 995–1007. [CrossRef]
18. Boyer, T.H. Thermodynamics of the harmonic oscillator: Wien’s displacement law and the Planck spectrum. *Am. J. Phys.* **2003**, *71*, 866–870. [CrossRef]
19. Sonnier, R.; Ferry, L.; Gallard, B.; Boudenne, A.; Lavaud, F. Controlled Emissivity Coatings to Delay Ignition of Polyethylene. *Materials* **2015**, *8*, 6935–6949. [CrossRef]
20. FLIR. Drone Education Lab for Thermal Applications. Available online: <https://www.flir.com/suas/delta/> (accessed on 12 February 2020).
21. Zenmuse, X.T. TECHN. DATEN User Manual. Available online: <http://www.dji.com/product/zenmuse-xt> (accessed on 12 February 2020).
22. Council Directive 93/42/EEC. Medical Devices. Available online: <https://cemarking.net/medical-devices-directive/> (accessed on 10 January 2019).
23. Isser, M.; Kranebitter, H.; Fink, H.; Wiedermann, F.J.; Lederer, W. High tensile strength increases multifunctional use of survival blankets in wilderness emergencies. *Wilderness Environ. Med.* **2020**, in press.

24. Isser, M.; Kranebitter, H.; Kofler, A.; Groemer, G.; Wiedermann, F.J.; Lederer, W. Rescue blankets hamper thermal imaging by infrared cameras. *Appl. Compos. Mater.* **2020**, in press.
25. Moher, D.; Liberati, A.; Tetzlaff, J.; Altman, D.G.; PRISMA Group. Reprint-preferred reporting items for systematic reviews and meta-analyses: The PRISMA statement. *Phys. Ther.* **2009**, *89*, 873–880. [CrossRef] [PubMed]
26. Renström, B. Space or rescue blanket—A bluff? *Arct. Med. Res.* **1992**, *51*, 212–213.



© 2020 by the authors. Licensee MDPI, Basel, Switzerland. This article is an open access article distributed under the terms and conditions of the Creative Commons Attribution (CC BY) license (<http://creativecommons.org/licenses/by/4.0/>).

Article

# Layer-by-Layer Deposition of Hyaluronan and Quercetin-Loaded Chitosan Nanoparticles onto Titanium for Improving Blood Compatibility

Xingda Wu <sup>1,†</sup>, Cuijuan Liu <sup>1,†</sup>, Hongpeng Chen <sup>1</sup>, Yanfang Zhang <sup>1</sup>, Lin Li <sup>2</sup> and Nan Tang <sup>1,\*</sup>

<sup>1</sup> School of Biomedical Engineering, School of Pharmacy, Guangdong Medical University, Dongguan 523808, China; shuradio@shu.edu.cn (X.W.); liu-cj@foxmail.com (C.L.); chenhpgdmc@foxmail.com (H.C.); zjzyf2006@163.com (Y.Z.)

<sup>2</sup> Guangdong Provincial Key Laboratory of New Drug Screening, Guangzhou Key Laboratory of Drug Research for Emerging Virus Prevention and Treatment, School of Pharmaceutical Sciences, Southern Medical University, Guangzhou 510515, China; li75lin@126.com

\* Correspondence: tn6559@foxmail.com

† These authors contributed equally to this work.

Received: 23 January 2020; Accepted: 29 February 2020; Published: 9 March 2020

**Abstract:** Surface modification is an effective way to improve the hemocompatibility of biomaterials. Quercetin has significant anticoagulation and antithrombotic effects, and thus it is a promising candidate agent for the surface modification of blood-contacting materials. In this study, quercetin was successfully encapsulated in tripolyphosphate–chitosan nanoparticles (TCs) based on the ionic gelation of chitosan with tripolyphosphate (TPP) anions. Then, hyaluronan acid (HA)/quercetin-loaded TPP–chitosan nanoparticle (QTCs) films, in addition to HA/TCs films, were prepared separately using an electrostatic layer-by-layer self-assembly technique. The encapsulation of quercetin in the chitosan nanoparticles was confirmed by UV spectra. The quercetin-loaded multilayer coatings were also successfully self-assembled, as confirmed by the UV spectra and contact angle measurements. Platelet adhesion experiments were carried out with platelet-enriched plasma so as to evaluate the blood compatibility of the different samples. There were many platelets on the surfaces of the glass and HA/TC-coated titanium, which were partially activated but not aggregated. Meanwhile, many more platelets were observed on the uncoated titanium surfaces, most of which developed pseudopodia. By contrast, the platelet adhesion and activation were reduced remarkably on the surface of the HA/QTC-coated titanium. These results showed that the multilayer coatings containing quercetin could act as potential biomaterials to improve the anticoagulation performance of blood-contacting materials.

**Keywords:** biomaterial; surface modification; self-assembly; multilayer; blood compatibility

## 1. Introduction

In the design of blood-contacting implants, such as artificial blood vessels and vascular stents, there are two major issues that should be considered, namely, antithrombosis and endothelialization [1]. Native endothelium plays a unique role in maintaining vascular homeostasis, which includes active antithrombosis, inhibiting the proliferation of smooth muscle cells, and reducing intimal hyperplasia [2,3]. Thus, the endothelialization of implant surfaces may provide fully blood-compatible interfaces. However, we know that it takes some time to complete the endothelialization of implant surfaces *in vivo*. Therefore, the blood compatibility of an implant is the first consideration, especially in the initial implantation.

Many approaches have been explored to improve the blood compatibility of blood-contacting medical implants. Surface modification enables the combination of a material's bulk properties with

the desired biological attributes, and it has become the most popular method for preventing blood clotting. Various anticoagulant molecules, including heparin [4,5], citric acid [6], hirudin [7], and some enzymes [8], have been used to develop clinical devices with anticoagulant properties. In addition, endothelial cell seeding has also been used in surface coatings [9]. Biomaterials functionalized with endothelial cell seeding may function in a similar way as the endothelial surface itself, but the poor adhesion and slow formation process limit its clinical application [10]. To date, there are no blood-contacting materials used in clinical settings that can meet all of the hemocompatibility requirements, whether short-term applied or long-term implanted [11]. Thus, the field of biomaterials modification, from the perspective of improving the blood compatibility, is still evolving. More innovative approaches and strategies need to be explored and developed.

The layer-by-layer (LbL) self-assembly technique is a simple and facile approach for the immobilization of biomolecules onto various surfaces, and it has already been extensively applied in the surface modification of biomaterials. Compared with the classic chemical immobilization, the LbL technique has the lowest demand for reactive chemical bonds and efficiently keeps the molecular activity. The LbL self-assembled multilayers produce a more stable coating than that prepared by physical adsorption because of the electrostatic attractions between the different layers. In many previous studies, the LbL technique was used to immobilize heparin onto various kinds of biomaterials. As an important anticoagulant in clinics, heparin was the most popular surface modifier. Li et al. constructed LbL-assembled heparin/fibronectin multilayers on titanium implants, and these multilayers displayed excellent antithrombotic properties [12]. Similarly, Su et al. developed a dual drug-eluting stent, with Duraflo heparin and sirolimus coated layer-by-layer onto a Multi-Link PIXEL stent, which showed prolonged resistance to thrombosis [13]. Chou et al. demonstrated that the anticoagulation performance of collagen/heparin multilayers on titanium surfaces was superior to that of an uncoated one [14]. Meng et al. designed a chitosan/heparin LbL-coated coronary stent and tested both in *in vitro* and *in vivo*. It was found that this self-assembly coating was safe and efficient in promoting re-endothelialization and intimal healing after stent implantation, in addition to having a good hemocompatibility [15]. The anticoagulation effect of heparin has been well recognized. However, extensive use of heparin may lead to bleeding and thrombocytopenia [16]. With this in mind, some researchers have turned to other anticoagulant molecules for developing blood compatible membranes, such as nattokinase and lumbrokinase [17].

Quercetin, a naturally occurring flavonoid, has also been shown to have effects of antithrombosis and anticoagulation similar to heparin. BijakM et al. reported that quercetin had an inhibitory effect on active factor X (FXa) activity, and that it might be a potential structural base for the design of new nature-based, safe, orally bioavailable, direct FXa inhibitors [18]. The coagulation assays conducted by Choi J H et al. also demonstrated that quercetin inhibits the enzymatic activity of thrombin and FXa, and suppresses fibrin clot formation and blood clotting [19]. Actually, the antithrombotic effects of quercetin, including the inhibition of the platelet activation and aggregation, *in vivo* thrombosis inhibition, and human interventional studies on cardiovascular diseases, have been widely reported [20–24]. Furthermore, quercetin has other pharmacological functions, such as antioxidation [25], anti-inflammation [26], and the inhibition of smooth muscle cell proliferation and migration [27]. Therefore, quercetin is also a promising candidate agent for the modification of vascular stents.

Quercetin has a poor aqueous solubility and is easily degradable, which limits its application in the pharmaceutical field. To solve this problem, some studies have focused on the preparation of chitosan nanoparticles loaded with quercetin. Chitosan is a natural, cationic polysaccharide. It is commonly used in drug delivery systems because of its biocompatibility and low toxicity [28,29]. It also plays a critical role in the attachment and growth of endothelial cells [15]. Encapsulation of quercetin into chitosan-based nanoparticles has been reported to efficiently overcome the shortcomings of quercetin and to improve its efficiency. Chitosan-based delivery systems are effective in controlling the release of quercetin, which has paved the way for a better bioavailability of quercetin [30].

In this work, we tried to immobilize quercetin onto titanium (Ti) surfaces so as to enhance blood compatibility. We encapsulated quercetin into chitosan nanoparticles based on the ionic interactions between chitosan and tripolyphosphate (TPP). TPP is a polyanion with negatively charged groups that can interact with the positively charged amino groups of chitosan. This ionic gelation process is convenient and mild, and thus it has attracted considerable attention as a way to prepare chitosan nanoparticles [30,31]. The surface charge of quercetin-loaded TPP–chitosan nanoparticles (QTCs) is positive because of the presence of amine groups on its surface [31,32]. Negatively charged hyaluronic acid (HA) and positively charged QTCs were deposited onto a Ti surface and formed a multilayer coating through the LbL technique. Finally, the hemocompatibility of these HA/QTCs multilayers was assessed by platelet-rich plasma contacting experiments. There have been many previous studies that have focused on the surface modification of implant metal via the LbL self-assembly technique [12–15], but, as far as we know, this is the first report of improving the blood compatibility of biomaterials by the surface immobilization of quercetin-loaded multilayer coatings. The results of this study will provide a design reference for the anticoagulant materials.

## 2. Materials and Methods

### 2.1. Preparation and Characterization of QTCs

TPP–chitosan nanoparticles (TCs) were fabricated based on the ionic interactions between the chitosan and TPP anions. Chitosan was dissolved into a 1 vol% aqueous acetic acid solution in order to form a polymer solution with a concentration of 1 mg/mL. The pH of the chitosan solution was adjusted to 5.2 using 1.25 M sodium hydroxide. Under magnetic stirring at room temperature, 0.5 mL of TPP solution, with a concentration of 2 mg/mL, was dropwise added into 5 mL of the chitosan solution. The QTCs were formed by dropwise adding 1 mL of quercetin–ethanol solution, with a concentration of 0.2 mg/mL, into 5 mL of the chitosan solution before adding the TPP.

The encapsulation efficiency (EE) of quercetin was conducted according to the method described in references [33,34]. The encapsulated and non-encapsulated portions of quercetin from the QTC suspensions were separated using a centrifugal device with centrifugation at 10,000 rpm for 30 min. The concentration of quercetin in the supernatant liquid was detected by UV–VIS spectrophotometry at 370 nm. The quercetin encapsulation efficiency was calculated according to the following formula:

$$EE (\%) = (W_{\text{total}} - W_{\text{free}}) \times 100 / W_{\text{total}}$$

where  $W_{\text{total}}$  is the total quercetin weight in the QTC suspensions and  $W_{\text{free}}$  is the weight of the non-encapsulated quercetin.

The particle size and zeta potential of the QTCs were assessed by a Nanotracer Wave II particle size analyzer (Microtrac INC., Florida, USA). The surface morphologies of the QTCs and TCs were observed by transmission electron microscope (TEM; JEOL-2100F, Tokyo, Japan). The UV absorption spectra of the native quercetin, chitosan, and QTCs were obtained in a UV–VIS spectrophotometer (UV-6000PC, Shanghai Metash Instruments Co., Ltd., Shanghai, China).

### 2.2. Substrate Preparation

Commercially pure titanium sheets (From Qinghe Hengzhong Metal Materials Co. Ltd., Xingtai, China) were used as the substrates for the HA/TC and HA/QTC multilayer films syntheses. The Ti plates were mechanically polished to a mirror-like status, then, were ultrasonically cleaned in acetone and ethanol, and finally in deionized (DI) water. The cleaning procedure lasted for 10 min in each fluid. The cleaned samples were activated in 1.25 M of NaOH solution at 80 °C for 24 h, and then thoroughly rinsed with DI water and blown dry. The NaOH-treated Ti samples are referred to from here on as TiOH.

### 2.3. Multilayer Coating Preparation

The polyethylenimine (PEI) solution was prepared at a concentration of 5 mg/mL by dissolving PEI (50 wt.% water solution, MW 70,000) in 0.14 M NaCl, and its pH was adjusted to 4.5 using diluted HCl. The TiOH substrates were immersed in the PEI solution for 20 min, thus obtaining a precursor layer with a stable positive charge to initiate the LbL self-assembly process. Figure 1 shows an illustration of the construction of the multilayer surfaces. The substrates were first immersed into the anionic HA solution (1 mg/mL in DI water, pH = 5.2) for 15 min (Step 1), and then rinsed with distilled water and dried with a nitrogen flow (Step 2). Afterwards, the substrates were immersed into the QTC or TC suspensions for 15 min (Step 3), and subsequently rinsed with distilled water and dried again with a nitrogen flow (Step 4). The pH of the rinsing water was 5.2. The above steps were repeated  $n$  times ( $n = 5$  and  $10$ ) in order to obtain the films that consisted of  $n$ -HA/QTC or  $n$ -HA/TC bilayers with the QTC or TC coatings on the top.

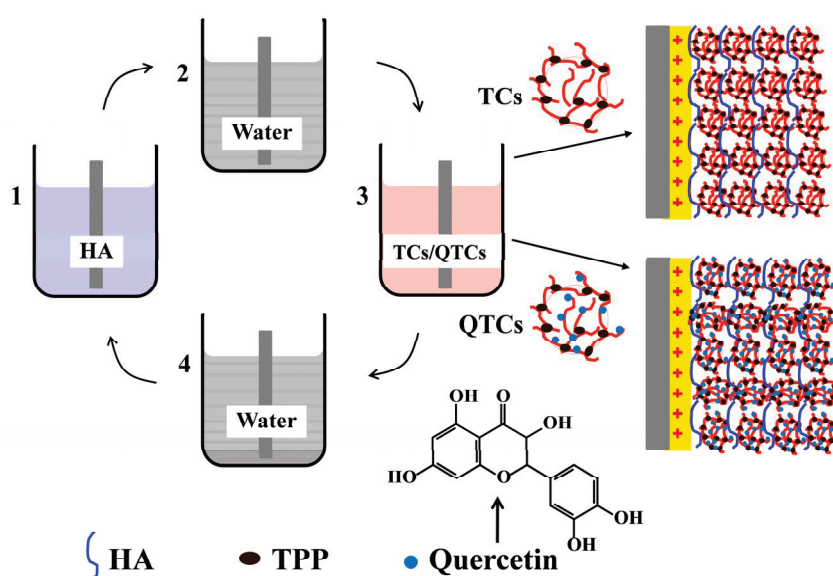


**Figure 1.** Schematic representation of the construction of hyaluronan acid (HA)/quercetin-loaded tripolyphosphate (TPP)–chitosan nanoparticle (QTCs) and HA/TPP–chitosan nanoparticle (TCs) multilayer thin films by layer-by-layer (LbL).

### 2.4. Multilayer Coating Characterization

The water contact angle of the TiOH, TiOH coated with the PEI pre-layer, and HA/QTC films after each alternating deposition were measured to monitor the LbL self-assembly process. All of the prepared coatings were dried with a nitrogen flow before performing the contact angle measurements. The static water contact angles were measured at room temperature using a video contact angle goniometer (SL2008 Powereach, Xiamen, China). The volume of the individual water droplet was 6  $\mu$ L, and the contact angle of each type of surface was obtained by averaging the three measurement results performed on the different regions.

To follow the multilayer coating assembly, Ti plates coated with 5 and 10 HA/QTCs bilayers were ultrasonically treated in 1 mL of anhydrous ethanol for 30 min, separately, after which ethanol solutions containing different concentrations of quercetin were obtained. A UV–VIS spectrophotometer was used to detect the absorption in the UV region of these ethanol solutions.

### 2.5. In Vitro Platelet Adhesion Experiments

In vitro platelet adhesion tests were conducted to evaluate the blood compatibility of all of the samples, including the glass, TiOH substrate, 5 and 10 (HA/TC) bilayer-coated TiOH substrates, and 5 and 10 (HA/QTC) bilayer-coated TiOH substrates. The entire blood of a healthy rabbit mixed with

3.2% sodium citrate (9:1) was centrifuged at 1000 rpm for 20 min in order to obtain a platelet-rich plasma (PRP). Each sample ( $1 \times 1 \text{ cm}^2$ ) was immersed in 1.5 mL PRP and incubated in a  $37^\circ \text{C}$  bath for 1 h. After rinsing three times with phosphate-buffered saline (PBS), the samples were fixed with a 4% paraformaldehyde solution for 1 h and then dehydrated in graded ethanol (30%, 50%, 70%, 90%, and 100%; 15 min each) sequentially, and critical point dried with  $\text{CO}_2$ . The quantity, morphology, aggregation, and pseudopodium of the adherent platelets were observed using a scanning electron microscope (SEM; VEGA3 LMH, Tescan, Brno, Czech Republic). Five random regions on each sample were chosen for the statistical analysis.

### 3. Results and Discussion

When the quercetin ethanol solution was dropwise added into the chitosan solution, a transparent light-yellow liquid formed, as shown in Figure 2a. Then, after the incorporation of the TPP solution, the liquid switched to a translucent state with a weak opalescence, and the yellowish color seemed to disappear, as shown in Figure 2b. The process of QTC formation was as follows: The quercetin first adhered to the chitosan based on the electrostatic attraction between the acidic phenolic OH groups of quercetin and the positively charged chitosan, and then formed nanospheres through TPP–CHI crosslinking under continuous stirring conditions [31,35]. The possible structure of the QTCs is shown in Figure 1. The encapsulation efficiency of quercetin was  $91.1\% \pm 1.2\%$ , indicating that most of the quercetin had been encapsulated in the nanoparticles, and therefore the yellowish color of the solution visually disappeared.

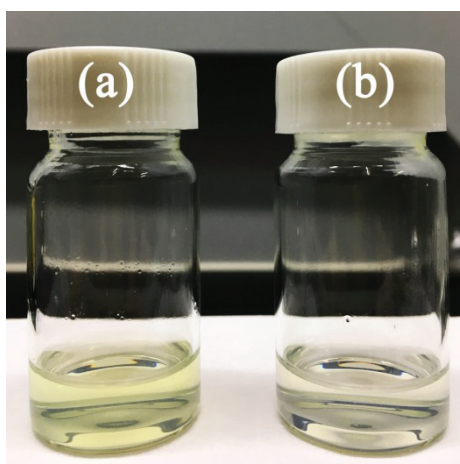


**Figure 2.** Visual observation of the quercetin–chitosan solution (a) before and (b) after adding the TPP solution.

The size and polydispersity index (PDI) are essential analyses for the characterization of nanoparticles. The dynamic light scattering (DLS) assay showed that the average size of the QTCs was about 279 nm, while the average TC size was 221 nm (slightly smaller than that of QTCs), as shown in Figure 3a. The polydispersity index of both the quercetin-loaded nanoparticles and the blank nanoparticles was less than 0.25, which featured a reasonably homogeneous suspension. Figure 3b,c shows the TEM images of the typical morphology of TCs and QTCs, respectively. The nanoparticles were nearly spherical in shape, with sizes ranging from 86 to 160 nm. The average particle size decreased when compared with the results of the DLS analysis, as the nanoparticles had shrunk during the drying procedure prior to the TEM observations. The Zeta potential is a measurement of the surface potential of suspended particles, which is an essential index in the stability of nanoparticles in suspension through the electrostatic repulsion among them. Both the TCs and QTCs had almost the same zeta potential, which was about 45 mV on average. This value is suitable for forming a

stable nanoparticle suspension, as particles can be dispersed stably when the absolute value of the zeta potential is above 30 mV [36].

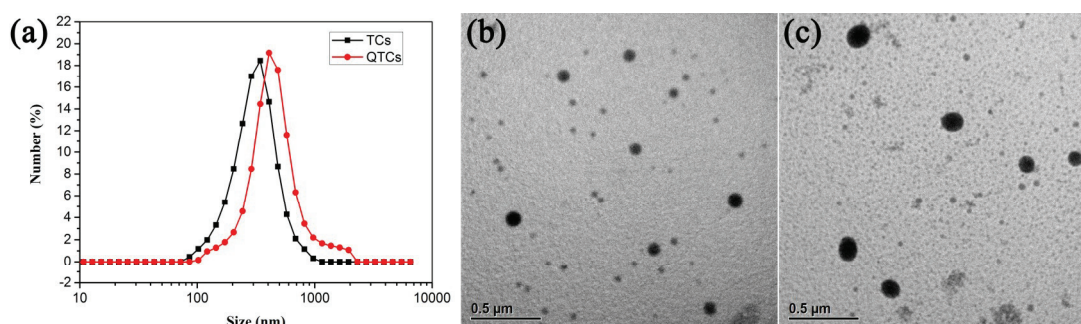


**Figure 3.** Characterization of TCs and QTCs. (a) Particle size distribution of TCs and QTCs measured by dynamic light scattering, transmission electron microscope (TEM) images of (b) TCs and (c) QTCs.

The UV spectra of the chitosan, QTCs, and native quercetin are presented in Figure 4 (curves a, b, and c, respectively). The native quercetin (dissolved in ethanol) showed two absorption bands at 255 and 370 nm (curve c), related to conjugations in the B-ring and A-ring, respectively. No apparent absorption peak in the chitosan solution was observed (curve a). In comparison, the spectrum of the QTCs (curve b) showed absorption bands at 255 and 370 nm, indicating the presence of quercetin in the nanoparticles. These results were similar to those of other studies on the encapsulation of quercetin into chitosan nanoparticles [33,34]. The HA/QTCs multilayer films were eluted from the Ti substrates by anhydrous ethanol under a supersonic effect. The obtained ethanol solutions contained different concentrations of quercetin, depending on the number of HA/QTC bilayers. Curves d and e in Figure 4 show the UV absorption spectra of the ethanol solutions obtained from the HA/QTC films with 5 and 10 bilayers, respectively. Two absorption bands at 255 and 370 nm were also found in each of the two curves, illustrating a successful incorporation of QTCs into the multilayer films. In addition, an increment of the absorbing intensity at 255 and 370 nm was seen as the number of bilayers increased from 5 to 10, indicating an increase in the amount of QTCs.

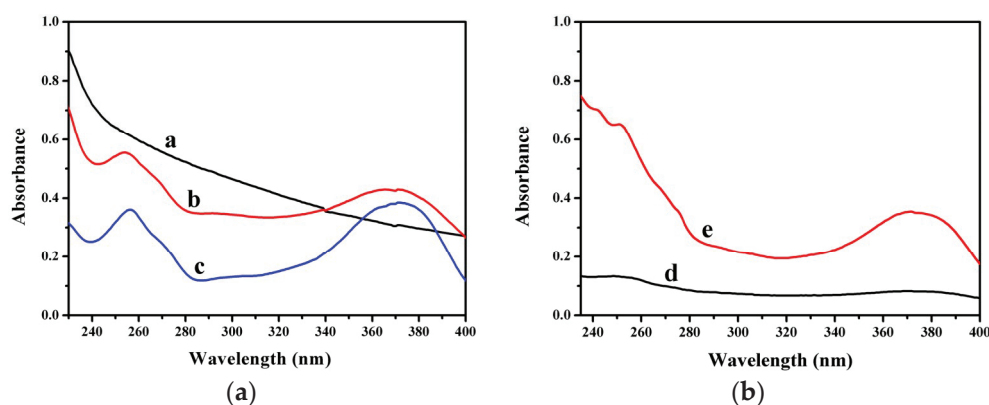


**Figure 4.** UV spectra of (a): three types of liquids, a: chitosan solution, b: quercetin-loaded nanoparticles suspension, c: quercetin–ethanol solution, and (b): ethanol solutions obtained from the HA/QTCs multilayer films with d: 5 and e: 10 bilayers.

The wettability of the HA and chitosan coatings had different values; it has been reported that the HA layers are more hydrophilic than the chitosan layers [37,38]. Hence, the LbL assembly of HA/QTCs can be monitored by measuring their respective water contact angles in each of the outermost layer. As seen in Figure 5, the TiOH sample, i.e., the alkali and heat-treated titanium, had a very hydrophilic surface of  $12.1^\circ \pm 0.1^\circ$ . The deposition of the PEI pre-layer on the TiOH changed its wettability from

$12.1^\circ \pm 0.1^\circ$  to  $61.8^\circ \pm 2.4^\circ$ . The later repeated coatings of the HA-QTC combinations exhibited a zig-zag effect. The HA layers were more hydrophilic than the QTCs layers, suggesting that alternated HA and QTCs surface layers were successfully achieved.

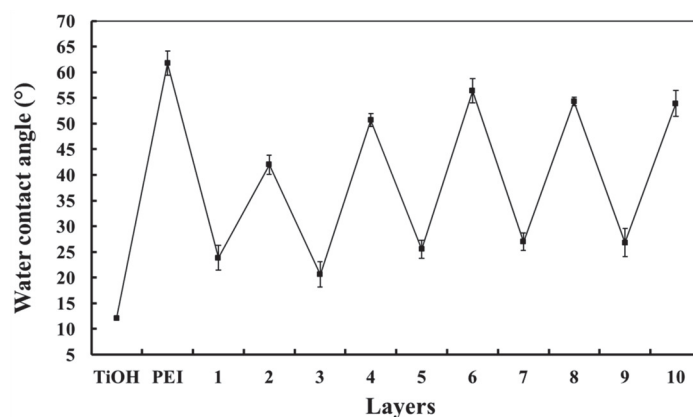


**Figure 5.** Water contact angles of the HA/QTC multilayer films. The odd numbers on the horizontal axis represent the film with HA as the outermost layer, and the even numbers represent the film with QTCs as the outermost layer.

Platelet adhesion and activation are important markers to evaluate the blood compatibility of blood-contacting materials. Typical SEM images of the adherent platelets on the glass, TiOH substrate, HA/TC-coated TiOH substrates with 5 and 10 bilayers, and HA/QTC-coated TiOH substrates with 5 and 10 bilayers are shown in Figure 6. Many platelets adhered to the smooth surface of the glass plate (Figure 6a). About half of them were round in shape, and the others had developed pseudopodia, which indicated that they had been partially activated. It could be seen that significantly more platelets adhered to the TiOH substrate (Figure 6b) than to the glass, and most of the adherent platelets developed pseudopodia. Platelet adhesion was significantly reduced in the case of the LbL-modified TiOH substrates with 5 and 10 HA/TCs bilayers (Figure 6c,d, respectively); most of them were isolated. It was easy to conclude that the existence of the HA/TCs LbL coating was efficient in the improvement of the hemocompatibility of the TiOH substrates. However, compared with the glass sample, the platelet adhesion and activation were slightly enhanced on the HA/TC-modified TiOH substrates. Compared with the four previously described substrates, the number of adherent platelets was strongly reduced. There were only a few platelets that could be observed on the surface of the substrate coated with 5 HA/QTCs bilayers, as shown in Figure 6e. Moreover, the platelet adhesion was reduced further when the number of HA/QTC bilayers increased to 10, as shown in Figure 6f. In addition, the platelets on the HA/QTC-modified samples appeared to be slightly smaller than those on the other four substrates, indicating a lower level of activation. These results suggested that the anticoagulation performance of the HA/QTC coatings was very obvious.

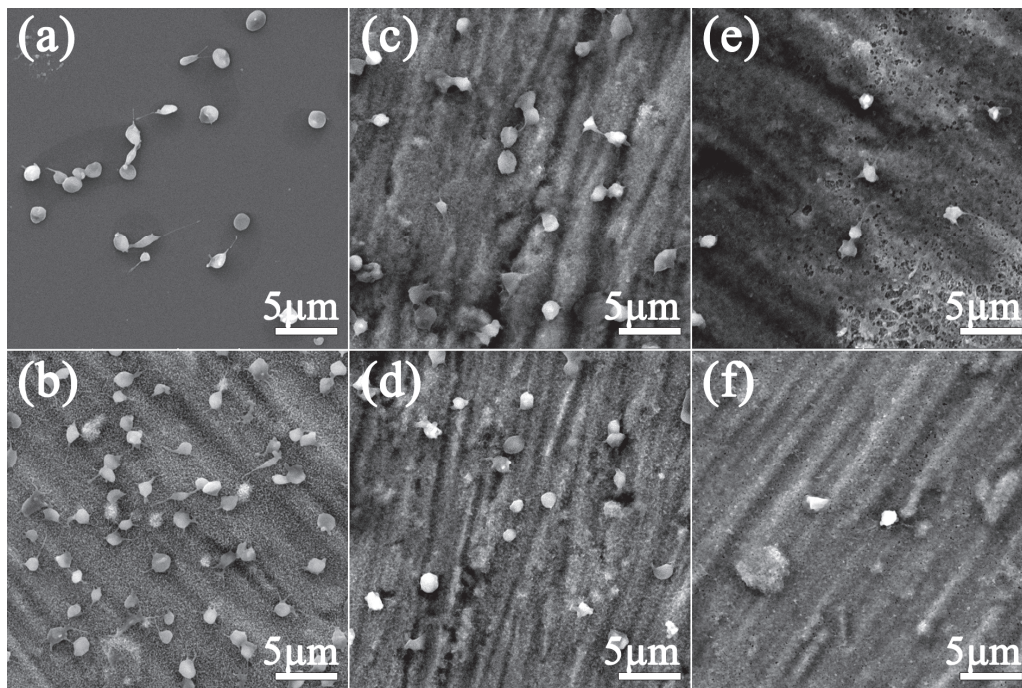


**Figure 6.** Typical SEM images of platelet adhesion on the surfaces of (a) glass, (b) TiOH substrate, HA/TC-coated Ti substrates with (c) 5 and (d) 10 bilayers, and HA/QTCs-coated Ti substrates with (e) 5 and (f) 10 bilayers.

The statistical number of platelets that adhered to different substrates is shown in Figure 7. The number of platelets that adhered to the surfaces of the glass and the HA/TC-coated TiOH substrates with 5 and 10 bilayers was  $15.8 \times 10^5$ ,  $19.3 \times 10^5$ , and  $17.6 \times 10^5$  per  $\text{cm}^2$ , respectively. There was no statistical difference in the number of platelets that adhered to these three substrates. For the TiOH substrate, the number of adherent platelets was  $65.4 \times 10^5$  per  $\text{cm}^2$ . While for the substrates coated with 5 and 10 HA/QTC layers, the numbers of adherent platelets dropped to  $1.9 \times 10^5$  and  $0.2 \times 10^5$  per  $\text{cm}^2$ , respectively, which were remarkably less than those on the HA/TC-coated substrates ( $p < 0.001$ ). The number of adherent platelets dropped sharply when the quercetin was incorporated into the modified coatings, which indicated an excellent anticoagulation effect of the quercetin.

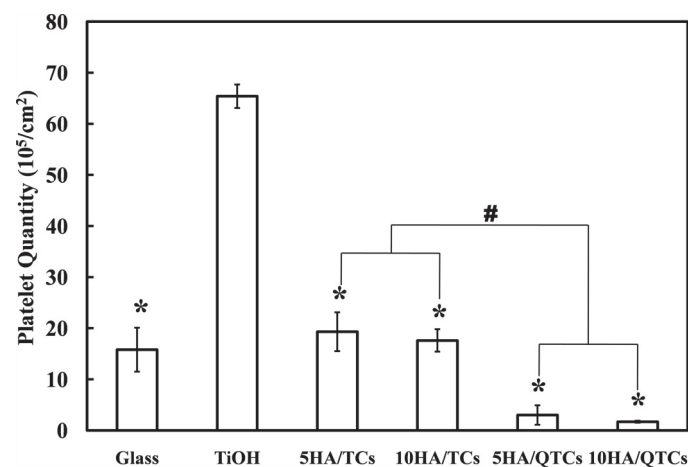


**Figure 7.** Quantitative analysis of the platelets adhered on the different substrates. \* indicates a significant difference ( $p < 0.001$ , one-way ANOVA) between the TiOH sample and the other five samples. # indicates a significant difference ( $p < 0.001$ , one-way ANOVA) between the HA/QTCs samples and the HA/TCs samples.

Chitosan is a weak base with amino groups, and has a pKa value of about 6.5. The drug-loaded chitosan nanoparticles exhibited a pH-sensitive behavior due to the existence of large quantities of amino groups on the chitosan. The drug release could be controlled by a change of pH [28,29]. The QTCs were formed at pH 5.2 and then deposited onto the TiOH substrates. The latter were incubated in platelet-rich plasma with a pH greater than 7. In this process, most of the amino groups on the chitosan were deprotonated, and thus significantly weakened the electrostatic interaction between the QTC and HA layers. Meanwhile, the QTCs became unstable, and quickly collapsed and precipitated, which allowed for a rapid release of quercetin.

Surface modification is a popular method used to improve the blood compatibility of biomaterials. A variety of anticoagulant molecules have been used to modify the surface of blood-contacting implants. Heparin, as an important anticoagulant in clinics, was the most popular surface modifier in earlier studies [4,5,12–15]. Subsequently, especially in recent years, other anticoagulant molecules were developed for surface modification, such as citric acid [6], hirudin [7], bovine serum albumin [11], nattokinase, and lumbrokinase [17]. However, to the best of our knowledge, there has been no report of improving the blood compatibility of biomaterials by the surface immobilization of quercetin. Quercetin is well known for its beneficial cardiovascular properties. It has been demonstrated to be effective in reducing or inhibiting platelet aggregation and activation in many studies, although the exact mechanism is not fully understood [20,21,39]. However, quercetin has a poor aqueous solubility, and cannot be directly immobilized onto the surface of biomaterials. This problem was efficiently solved in this work by encapsulating quercetin into the pH-sensitive chitosan nanoparticles and constructing multilayer coatings based on the LbL self-assembly of HA and QTC. Alkali and heat-treated titanium was chosen as the platform for the construction of the HA/QTC films. Platelet adhesion experiments demonstrated that the platelet adhesion and activation were reduced remarkably on the quercetin-loaded multilayer coatings. This approach has several advantages. Firstly, the amount of quercetin can be adjusted by simply varying the number of multilayers. Secondly, the alkali and heat-treated titanium has a negatively charged surface and a large number of nanoscale pores, and therefore provides a good platform for the LbL films. Thirdly, according to the reports in the literature [15], the LbL chitosan/heparin coating could significantly promote re-endothelialization, so we speculate that QTCs may also play a role in promoting rapid endothelialization, and further research is underway.

#### 4. Conclusions

Quercetin-loaded chitosan nanoparticles were fabricated based on the ionic interactions between chitosan and TPP anions. This study showed that QTCs are stable in suspension, with an average size of 279 nm and a zeta potential of 45 mV. Subsequently, the LbL self-assembly of QTCs and HA through electrostatic interaction was carried out, and the HA/QTC multilayer coatings were successfully constructed, which was confirmed by the UV spectra and water contact angle measurements. Platelet adhesion experiments were carried out with platelet-enriched plasma. Compared with glass, for the TiOH substrate and HA/TC-coated TiOH substrate, a marked reduction in platelet adhesion was observed on the surface of the HA/QTC-coated TiOH substrate, indicating an excellent anticoagulation performance for the quercetin-loaded multilayer coatings. This work provides a promising method to improving the anticoagulant and hemocompatibility of blood-contacting materials.

**Author Contributions:** Conceptualization, X.W. and H.C.; Methodology, X.W., H.C., and N.T.; Validation, C.L., X.W., and H.C.; Investigation, C.L.; Writing (Original Draft Preparation), X.W.; Writing (Review and Editing), C.L. and H.C.; Visualization, Y.Z.; Project Administration, L.L. and N.T. All authors have read and agreed to the published version of the manuscript.

**Funding:** This research was supported by “Group-type” Special Support Project for Education Talents in Universities (G619080438 and 4SG19045G), the Scientific Research Project of the Education Department of Guangdong Province (2017KTSCX079), Guangdong Medical Science and Research Foundation (A2018279 and A2019493), Science and Research Projects for Traditional Chinese Medicine of Guangdong (20172086 and 20191191),

Funds for PhD Researchers of Guangdong Medical University (B2017013), and the Research Fund of Guangdong Medical University (GDMUM201813).

**Conflicts of Interest:** The authors declare no conflict of interest.

## References

1. Lin, Q.; Yan, J.; Qiu, F.; Song, X.; Fu, G.; Jian, J. Heparin/collagen multilayer as a thromboresistant and endothelial favorable coating for intravascular stent. *J. Biomed. Mater. Res. A* **2011**, *96*, 132–141. [CrossRef] [PubMed]
2. Rogers, C.; Parikh, S.; Seifert, P.; Edelman, E.R. Endogenous cell seeding: Remnant endothelium after stenting enhances vascular repair. *Circulation* **1996**, *94*, 2909–2914. [CrossRef] [PubMed]
3. Kushwaha, M.; Anderson, J.M.; Bosworth, C.A.; Andukuri, A.; Minor, W.P.; Lancaster, J.R.; Anderson, P.G.; Brott, B.C.; Jun, H.-W. A nitric oxide releasing, self assembled peptide amphiphile matrix that mimics native endothelium for coating implantable cardiovascular devices. *Biomaterials* **2010**, *31*, 1502–1508. [CrossRef] [PubMed]
4. Yang, Y.; Qi, P.; Wen, F.; Li, X.; Xia, Q.; Maitz, M.F.; Yang, Z.; Shen, R.; Tu, Q.; Huang, N. Mussel-inspired one-step adherent coating rich in amine groups for covalent immobilization of heparin: Hemocompatibility, growth behaviors of vascular cells, and tissue response. *ACS Appl. Mater. Interfaces* **2014**, *6*, 14608–14620. [CrossRef]
5. Gao, A.; Liu, F.; Xue, L. Preparation and evaluation of heparin-immobilized poly (lactic acid) (PLA) membrane for hemodialysis. *J. Membr. Sci.* **2014**, *452*, 390–399. [CrossRef]
6. Xiang, T.; Wang, R.; Zhao, W.F.; Sun, S.D.; Zhao, C.S. Covalent deposition of zwitterionic polymer and citric acid by click chemistry-enabled layer-by-layer assembly for improving the blood compatibility of polysulfone membrane. *Langmuir* **2014**, *30*, 5115–5125. [CrossRef]
7. Li, J.; Liu, F.; Qin, Y.; He, J.; Xiong, Z.; Deng, G.; Li, Q. A novel natural hirudin facilitated anti-clotting polylactide membrane via hydrogen bonding interaction. *J. Membr. Sci.* **2017**, *523*, 505–514. [CrossRef]
8. Xue, T.; Peng, B.; Xue, M.; Zhong, X.; Chiu, C.Y.; Yang, S.; Qu, Y.; Ruan, L.; Jiang, S.; Dubin, S.; et al. Integration of molecular and enzymatic catalysts on graphene for biomimetic generation of antithrombotic species. *Nat. Commun.* **2014**, *5*, 3200. [CrossRef]
9. Wei, Y.; Ji, Y.; Xiao, L.; Lin, Q.; Xu, J.; Ren, K.; Ji, J. Surface engineering of cardiovascular stent with endothelial cell selectivity for in vivo re-endothelialisation. *Biomaterials* **2013**, *34*, 2588–2599. [CrossRef]
10. Su, Y.; Luo, C.; Zhang, Z.; Hermawan, H.; Zhu, D.; Huang, J.; Liang, Y.; Li, G.; Ren, L. Bioinspired surface functionalization of metallic biomaterials. *J. Mech. Behav. Biomed. Mater.* **2018**, *77*, 90–105. [CrossRef]
11. Lin, S.; Li, X.; Wang, K.; Shang, T.; Zhou, L.; Zhang, L.; Wang, J.; Huang, N. An albumin biopassive polyallylamine film with improved blood compatibility for metal devices. *Polymers* **2019**, *11*, 734. [CrossRef] [PubMed]
12. Li, G.; Yang, P.; Huang, N. Layer-by-layer construction of the heparin/fibronectin coatings on titanium surface: Stability and functionality. *Phys. Procedia* **2011**, *18*, 112–121. [CrossRef]
13. Su, L.C.; Chen, Y.H.; Chen, M.C. Dual drug-eluting stents coated with multilayers of hydrophobic heparin and sirolimus. *ACS Appl. Mater. Interfaces* **2013**, *5*, 12944–12953. [CrossRef] [PubMed]
14. Chou, C.C.; Zeng, H.J.; Yeh, C.H. Blood compatibility and adhesion of collagen/heparin multilayers coated on two titanium surfaces by a layer-by-layer technique. *Thin Solid Film.* **2013**, *549*, 117–122. [CrossRef]
15. Meng, S.; Liu, Z.; Shen, L.; Guo, Z.; Chou, L.L.; Zhong, W.; Du, Q.; Ge, J. The effect of a layer-by-layer chitosan-heparin coating on the endothelialization and coagulation properties of a coronary stent system. *Biomaterials* **2009**, *30*, 2276–2283. [CrossRef]
16. Brieger, D.B.; Mak, K.H.; Kottke-Marchant, K.; Topol, E.J. Heparin-induced thrombocytopenia. *J. Am. Coll. Cardiol.* **1998**, *31*, 1449–1459. [CrossRef]
17. Ji, M.; Chen, X.; Luo, J.; Wan, Y. Improved blood compatibility of polysulfone membrane by anticoagulant protein immobilization. *Colloids Surf. B Biointerfaces* **2019**, *175*, 586–595. [CrossRef]
18. Bijak, M.; Ponczek, M.B.; Nowak, P. Polyphenol compounds belonging to flavonoids inhibit activity of coagulation factor X. *Int. J. Biol. Macromol.* **2014**, *65*, 129–135. [CrossRef]

19. Choi, J.H.; Kim, K.J.; Kim, S. Comparative effect of quercetin and quercetin-3-O- $\beta$ -D-glucoside on fibrin polymers, blood clots, and in rodent models. *J. Biochem. Mol. Toxicol.* **2016**, *30*, 548–558. [CrossRef]
20. Mosawy, S.; Jackson, D.E.; Woodman, O.L.; Linden, M.D. The flavonols quercetin and 3', 4'-dihydroxyflavonol reduce platelet function and delay thrombus formation in a model of type 1 diabetes. *Diab. Vasc. Dis. Res.* **2014**, *11*, 174–181. [CrossRef]
21. Kaneider, N.C.; Mosheimer, B.; Reinisch, N.; Patsch, J.R.; Wiedermann, C.J. Inhibition of thrombin-induced signaling by resveratrol and quercetin: Effects on adenosine nucleotide metabolism in endothelial cells and platelet-neutrophil interactions. *Thromb. Res.* **2004**, *114*, 185–194. [CrossRef] [PubMed]
22. Lee, K.H.; Park, E.; Lee, H.J.; Kim, M.O.; Cha, Y.J.; Kim, J.M.; Lee, H.; Shin, M.J. Effects of daily quercetin-rich supplementation on cardiometabolic risks in male smokers. *Nutr. Res. Pract.* **2011**, *5*, 28–33. [CrossRef] [PubMed]
23. Egert, S.; Boesch-Saadatmandi, C.; Wolfram, S.; Rimbach, G.; Müller, M.J. Serum lipid and blood pressure responses to quercetin vary in overweight patients by apolipoprotein E genotype. *J. Nutr.* **2010**, *140*, 278–284. [CrossRef] [PubMed]
24. Yu, P.X.; Zhou, Q.J.; Zhu, W.W.; Wu, Y.H.; Wu, L.C.; Lin, X.; Chen, M.H.; Qiu, B.T. Effects of quercetin on LPS-induced disseminated intravascular coagulation (DIC) in rabbits. *Thromb. Res.* **2013**, *131*, e270–e273. [CrossRef] [PubMed]
25. Patel, R.V.; Mistry, B.M.; Shinde, S.K.; Syed, R.; Singh, V.; Shin, H.S. Therapeutic potential of quercetin as a cardiovascular agent. *Eur. J. Med. Chem.* **2018**, *155*, 889–904. [CrossRef]
26. Kleemann, R.; Verschuren, L.; Morrison, M.; Zadelaar, S.; van Erk, M.J.; Wielinga, P.Y.; Kooistra, T. Anti-inflammatory, anti-proliferative and anti-atherosclerotic effects of quercetin in human in vitro and in vivo models. *Atherosclerosis* **2011**, *218*, 44–52. [CrossRef]
27. Alcocer, F.; Whitley, D.; Salazar-Gonzalez, J.F.; Jordan, W.D.; Sellers, M.T.; Eckhoff, D.E.; Suzuki, K.; Macrae, C.; Bland, K.I. Quercetin inhibits human vascular smooth muscle cell proliferation and migration. *Surgery* **2002**, *131*, 198–204. [CrossRef]
28. Sivakumar, P.; Priyatharshni, S.; Nagashanmugam, K.B.; Thanigaivelan, A.; Kumar, K. Chitosan capped nanoscale Fe-MIL-88B-NH<sub>2</sub> metal-organic framework as drug carrier material for the pH responsive delivery of doxorubicin. *Mater. Res. Express* **2017**, *4*, 085023. [CrossRef]
29. Tıǧlı Aydın, R.S.; Pulat, M. 5-fluorouracil encapsulated chitosan nanoparticles for pH-stimulated drug delivery: Evaluation of controlled release kinetics. *J. Nanomater.* **2012**, *2012*, 313961. [CrossRef]
30. Zhang, Y.; Yang, Y.; Tang, K.; Hu, X.; Zou, G. Physicochemical characterization and antioxidant activity of quercetin-loaded chitosan nanoparticles. *J. Appl. Polym. Sci.* **2008**, *107*, 891–897. [CrossRef]
31. Nan, W.; Ding, L.; Chen, H.; Khan, F.U.; Yu, L.; Sui, X.; Shi, X. Topical use of quercetin-loaded chitosan nanoparticles against ultraviolet B radiation. *Front. Pharmacol.* **2018**, *9*, 826. [CrossRef] [PubMed]
32. Souza, M.P.; Vaz, A.F.M.; Costa, T.B.; Cerqueira, M.A.; De Castro, C.M.M.B.; Vicente, A.A.; Carneiro-da-Cunha, M.G. Construction of a biocompatible and antioxidant multilayer coating by layer-by-layer assembly of  $\kappa$ -carrageenan and quercetin nanoparticles. *Food Bioprocess Technol.* **2018**, *11*, 1–11. [CrossRef]
33. Hao, J.; Guo, B.; Yu, S.; Zhang, W.; Zhang, D.; Wang, J.; Wang, Y. Encapsulation of the flavonoid quercetin with chitosan-coated nanoliposomes. *LWT-Food Sci. Technol.* **2017**, *85*, 37–44.
34. Souza, M.P.; Vaz, A.F.M.; Correia, M.T.S.; Cerqueira, M.A.; Vicente, A.A.; Carneiro-da-Cunha, M.G. Quercetin-loaded lecithin/chitosan nanoparticles for functional food applications. *Food Bioprocess Technol.* **2014**, *7*, 1149–1159. [CrossRef]
35. Tan, Q.; Liu, W.; Guo, C.; Zhai, G. Preparation and evaluation of quercetin-loaded lecithin-chitosan nanoparticles for topical delivery. *Int. J. Nanomed.* **2011**, *6*, 1621.
36. Liu, J.; Gong, T.; Wang, C.; Zhong, Z.; Zhang, Z. Solid lipid nanoparticles loaded with insulin by sodium cholate-phosphatidylcholine-based mixed micelles: Preparation and characterization. *Int. J. Pharm.* **2007**, *340*, 153–162. [CrossRef]
37. Hernández-Montelongo, J.; Nascimento, V.F.; Murillo, D.; Taketa, T.B.; Sahoo, P.; de Souza, A.A.; Beppu, M.M.; Cotta, M.A. Nanofilms of hyaluronan/chitosan assembled layer-by-layer: An antibacterial surface for *Xylella fastidiosa*. *Carbohydr. Polym.* **2016**, *136*, 1–11. [CrossRef]

38. Nascimento, V.; Franca, C.; Hernández-Montelongo, J.; Machado, D.; Lancellotti, M.; Cotta, M.; Landers, R.; Beppu, M. Influence of pH and ionic strength on the antibacterial effect of hyaluronic acid/chitosan films assembled layer-by-layer. *Eur. Polym. J.* **2018**, *109*, 198–205. [CrossRef]
39. Mosawy, S. Effect of the flavonol quercetin on human platelet function: A review. *Food Public Health* **2015**, *5*, 1–9.



© 2020 by the authors. Licensee MDPI, Basel, Switzerland. This article is an open access article distributed under the terms and conditions of the Creative Commons Attribution (CC BY) license (<http://creativecommons.org/licenses/by/4.0/>).

Article

# Electrophoretic Deposition and Characteristics of Chitosan–Nanosilver Composite Coatings on a Nanotubular TiO<sub>2</sub> Layer

Michał Bartmański <sup>1,\*</sup>, Łukasz Pawłowski <sup>1</sup>, Andrzej Zieliński <sup>1</sup>, Aleksandra Mielewczyk-Gryń <sup>2</sup>, Gabriel Strugała <sup>1</sup> and Bartłomiej Cieślik <sup>3</sup>

<sup>1</sup> Department of Materials Engineering and Bonding, Gdańsk University of Technology, Narutowicza 11/12, 80-233 Gdansk, Poland; lukasz.pawlowski@pg.edu.pl (Ł.P.); andrzej.zielinski@pg.edu.pl (A.Z.); gabriel.strugala@pg.edu.pl (G.S.)

<sup>2</sup> Department of Solid State Physics, Gdańsk University of Technology, Narutowicza 11/12, 80-233 Gdansk, Poland; alegryn@pg.edu.pl

<sup>3</sup> Department of Analytical Chemistry, Gdańsk University of Technology, Narutowicza 11/12, 80-233 Gdansk, Poland; bartlomiej.cieslik@pg.edu.pl

\* Correspondence: michal.bartmanski@pg.edu.pl; Tel.: +48-500-034-220

Received: 28 January 2020; Accepted: 3 March 2020; Published: 6 March 2020

**Abstract:** The surface treatment of titanium implants has been applied mainly to increase surface bioactivity and, more recently, to introduce antibacterial properties. To this end, composite coatings have been investigated, particularly those based on hydroxyapatite. The present research was aimed at the development of another coating type, chitosan–nanosilver, deposited on a Ti13Zr13Nb alloy. The research comprised characterization of the coating’s microstructure and morphology, time-dependent nanosilver dissolution in simulated body fluid, and investigation of the nanomechanical properties of surface coatings composed of chitosan and nanosilver, with or without a surface-active substance, deposited at different voltages for 1 min on a nanotubular TiO<sub>2</sub> layer. The microstructure, morphology, topography, and phase composition were examined, and the silver dissolution rate in simulated body fluid, nanoscale mechanical properties, and water contact angle were measured. The voltage value significantly influenced surface roughness. All specimens possessed high biocompatibility. The highest and best adhesion of the coatings was observed in the absence of a surface-active substance. Silver dissolution caused the appearance of silver ions in solution at levels effective against bacteria and below the upper safe limit value.

**Keywords:** bioactive coatings; chitosan coatings; antibacterial coatings; silver release; nanomechanical properties; wettability

## 1. Introduction

Titanium and its alloys are the most promising biomaterials applied for long-term orthopedic, dental, and maxillofacial implants. Among the many titanium alloys, the Ti13Zr13Nb alloy seems to be the best choice compared to the widely used commercial Ti-6Al-4V and Ti-6Al-7Nb alloys, as it possesses Young’s modulus approaching that of a bone, and it contains no harmful elements such as Al or V [1].

The rejection of long-term implants observed during the primary and long-term fixation period has resulted in the development of a variety of antibacterial titanium surfaces for titanium implants, with the most popular including Ag, Cu, Zn, F, Y, Fe, N, Co, antibiotics, chitosan, and peptides [2,3]. Silver is used in medical applications as pure metallic silver, silver halides, nitrate, and sulfate, silver–organic complexes and silver zeolite, silver oxide nanoparticles, and silver ions [4–6]. Silver nanoparticles

(AgNPs) cause damage to the bacterial membrane and subcellular structures, dependent on the shape, size, surface appearance, and chemical states, and aggregation of the AgNPs [7].

Chitosan is a chemical compound with specific antibacterial properties [2,8–10]. Its main medical applications include controlled drug delivery, wound healing, and tissue regeneration [11,12]. Multiple coatings have been developed to improve these biological properties. Chitosan–AgNP coatings showed an inhibitory effect on the growth of some pathogens and reduced biofilm formation with no observed cell cytotoxicity in one study [13]. In another study, chitosan-based films containing silver nanoparticles were shown to have wetting properties highly sensitive to the fraction of AgNPs [14]. Coatings composed of chitosan, silver, and hydroxyapatite exhibited antibacterial activity and were nontoxic to MC3T3-E1 cells [15]; chitosan coatings with silver-decorated calcium phosphate microspheres lowered bacterial viability up to 90% [16], and silver-doped  $\beta$ -tricalcium phosphate composite coatings exhibited antibacterial activity and no adverse cytotoxic effects towards the cell line MG-63 [17]. Chitosan–cellulose composite films with AgNPs demonstrated excellent antibacterial properties against *Escherichia coli* and *Staphylococcus aureus* [18]. Coatings comprising polyvinyl alcohol capped with silver nanoparticles and based on a chitosan matrix demonstrated bactericidal activity against *E. coli* and *S. aureus* [19]. Finally, chitosan–gelatin–nanosilver composite films also showed in vitro antibacterial activity against *E. coli* and *S. aureus* [20].

Similar antibacterial effectiveness was also exhibited by nanocomposites of chitosan and nanosilver, which demonstrated significant antimicrobial activity against Gram-negative *Salmonella* and a potent anticancer effect [21], reduced fungal growth and caused morphological and ultrastructural changes in the pathogen [22], and were effective against *S. aureus*, *Bacillus sp.*, *E. coli*, *Proteus sp.*, *Pseudomonas sp.*, *Serratia sp.*, and *Klebsiella sp.* and the fungal pathogens *Aspergillus niger*, *Aspergillus flavus*, *Aspergillus fumigatus*, and *Candida albicans* [23]. Such nanocomposites demonstrated minimum bactericidal concentration values of 39.1 and 312.5  $\mu\text{g/ml}$  for *E. coli* and *S. aureus*, respectively, and did not exhibit cytotoxicity to L-929 fibroblasts [24]. Chitosan hydrogels, reinforced with silver nanoparticles, revealed ultra-high mechanical and high antibacterial properties against *E. coli* and *S. aureus* and were used to accelerate wound healing [25].

The fundamental problem in the deposition of chitosan coatings is the perfect dispersion of nanosilver particles in such coatings. To introduce and maintain dispersion in an electrolyte, numerous surface dispersing agents are added to the bath, such as Tween 20, Tween 80, sodium dodecyl sulfate, trisodium citrate, and Span 20 [26–30]. Among these, polysorbate 20 (Tween 20) is often used for chitosan coatings because it provides a more stable, less aggregated suspension of metallic nanoparticles. Furthermore, it reduces the interfacial tension and improves the adhesion of the chitosan coating to the substrate [31,32].

All research conducted to date has clearly shown that chitosan–AgNP coatings demonstrate high antibacterial efficacy against a significant number of Gram-positive and Gram-negative strains, including fecal bacteria. However, the mechanical properties of such material systems, determined for thin layers mainly via phenomena occurring at titanium–chitosan/AgNPs interfaces, and the surface state have been much less investigated. In the present research, a nanotubular oxide layer was created and used to improve the adhesion of chitosan–AgNP coatings obtained by electrophoretic deposition (EPD), a technical solution often applied for different coatings, but seldom for the one investigated here. Adhesion was also determined by the chemistry of the metallic surface, and the presented research is likely the first study of this nature to apply the Ti13Zr13Nb alloy, the safest of all the titanium materials applied for load-bearing implants.

## 2. Materials and Methods

### 2.1. Preparation of Specimens

The Ti13Zr13Nb alloy (SeaBird Metal Materials Co., Baoji, China) used as a substrate had the composition shown in Table 1. Round samples, 4 mm thick, and with a 3.14  $\text{cm}^2$  area, were cut from rods of 40 mm diameter. The surface roughness was  $S_a = 0.15 \mu\text{m}$ , achieved by polishing with abrasive

sandpapers, with No. 2000 as the last. Subsequently, the specimens were rinsed in pure isopropanol and then in deionized water with an ultrasonic device (Sonic-3, POLSONIC, Warsaw, Poland) for 15 min. Finally, etching was performed for 10 min in 25% HNO<sub>3</sub> to remove the native oxide layers [33], after which the samples were once again rinsed with distilled water and air-dried.

**Table 1.** The chemical composition of the Ti13Zr13Nb alloy, wt.%.

Element	Nb	Zr	Fe	C	N	O	Ti
wt.%	13.0	13.0	0.05	0.04	0.019	0.11	remainder

### 2.2. Electrochemical Oxidation of Ti13Zr13Nb Alloy

Electrochemical oxidation was done in a test solution of 10 mL of 85% orthophosphoric acid (1M H<sub>3</sub>PO<sub>4</sub>) (Sigma Aldrich), 1.2 mL of 40% of hydrofluoric acid (HF) (both from Polskie Odczynniki Chemiczne, Gliwice, Poland), and 150 mL of deionized water. The tests were carried out in a standard electrical circuit comprising an electrochemical cell, a DC power source (MCP/SPN110-01C, Shanghai MCP Corp., Shanghai, China), a platinum polarising electrode as the cathode, and the tested alloy as the anode, placed at a distance of 10 mm. All tests were carried out at room temperature, at a constant voltage of 20 V, and a charging time of 20 min. After oxidation, the specimens were rinsed in distilled water and dried in air at ambient temperature for 24 h.

### 2.3. Electrophoretic Deposition of Chitosan—Nanosilver Coatings

The electrolytes were prepared by dispersing 1 g of high-weight chitosan (degree of deacetylation > 75%; Sigma Aldrich, St. Louis, MO, United States) and 0.05 g of silver nanopowder (Hongwu International Group Ltd, Guangzhou, China) with an average powder grain about 30 nm in 1 L of 1% acetic acid (Polskie Odczynniki Chemiczne, Gliwice, Poland). Two different electrolytes were used, without (Suspension 1, Specimen A) or with (Suspension 2, Specimens B and C) 1 ml of Tween 20 (Polysorbate 20) (Sigma Aldrich, St. Louis, MO, United States) diluted in 1 L of 1% (v/v) acetic acid. The electrolytes were then homogenized using a magnetic stirrer (at 250 rpm) for 24 h at room temperature. The suspensions were prepared 1 h before deposition. The Ti13Zr13Nb specimen was used as the cathode, and platinum was used as the anode. The electrodes were placed at a distance of 10 mm. A DC power source (MCP/SPN110-01C, Shanghai MCP Corp., Shanghai, China) was applied. The EPD was performed at 10 V (Specimens A and B) and 20 V (Specimen C) for 1 min at room temperature. Finally, the as-deposited composite coatings were rinsed with distilled water and air-dried at room temperature for 48 h. The test variables, their investigated combinations, and further notes are presented in Table 2.

**Table 2.** Test variables, their investigated combinations, and further notes.

Specimen	Properties of Electrophoretic Deposition				
	Chitosan Content (g)	Silver Nanoparticle Content (g)	Polysorbate 20 Content (ml)	Voltage of Deposition (V)	Time of Deposition (min)
	1 L of 1% (v/v) Acetic Acid				
A	1	0.05	-	10	1
B	1	0.05	1	10	1
C	1	0.05	1	20	1

### 2.4. Structure and Morphology of Composite TiO<sub>2</sub>—Chitosan—Nanosilver Coatings

The nanotubular TiO<sub>2</sub> layer and coating surface were examined for each specimen with a high-resolution scanning electron microscope (SEM JEOL JSM- 7800 F, JEOL Ltd., Tokyo, Japan), equipped with a LED detector, at 5 kV acceleration voltage. The chemical compositions of the obtained

coatings were determined using an X-ray energy dispersive spectrometer (EDS) (Edax Inc., Mahwah, NJ, U.S.A.). Specimens with chitosan coatings (A, B, and C) were sputtered with a 10 nm thick layer of gold using a table-top DC magnetron sputtering coater (EM SCD 500, Leica, Vienna, Austria) in pure Ar plasma condition (Argon, Air Products 99.9%) before SEM and EDS techniques were applied. The atomic force microscope (NaniteAFM, Nanosurf AGLiestal, Switzerland) was applied to examine the surface topography. The examinations were carried out in non-contact mode at a force set up at 55 mN. The roughness index Sa was calculated as the mean of several tests made over the area of  $50 \times 50 \mu\text{m}$ . The X-ray diffraction method (XRD) (Phillips X'Pert Pro, Almelo, Netherlands) was applied via a diffractometer (Cu  $K\alpha$ ,  $\lambda = 0.1554 \text{ nm}$ ) in the  $2\theta$  range of  $10\text{--}90^\circ$  at a 0.02 step and 2 s/point, at ambient temperature and under atmospheric pressure. The Fourier-transform infrared (FTIR) spectra were recorded with a spectrophotometer (Perkin Elmer Frontier, Poznań, Poland) at a resolution of  $2 \text{ cm}^{-1}$  in the range of  $400\text{--}4000 \text{ cm}^{-1}$ . For measurements in transmittance mode, the samples were mixed with KBr and pressed to obtain pellets.

### 2.5. Silver Release in Simulated Body Fluid (SBF) Solution

The contents of Ag ions were determined after immersion of specimens A, B, and C in simulated body fluid prepared according to PN-EN ISO 10993-15 by dissolving reagent grade chemicals:  $(\text{NH}_2)_2\text{CO}$  ( $0.13 \text{ gL}^{-1}$ ), NaCl ( $0.7 \text{ gL}^{-1}$ ),  $\text{NaHCO}_3$  ( $1.5 \text{ gL}^{-1}$ ),  $\text{Na}_2\text{HPO}_4$  ( $0.26 \text{ gL}^{-1}$ ),  $\text{K}_2\text{HPO}_4$  ( $0.2 \text{ gL}^{-1}$ ), KSCN ( $0.33 \text{ gL}^{-1}$ ), and KCl ( $1.2 \text{ gL}^{-1}$ ) in 1 L of deionized water. The immersion times were 1, 3, and 7 days at  $39^\circ\text{C}$ . The silver contents were determined using atomic absorption spectrometry (SensAA DUAL, GBC Scientific Equipment Pty Ltd, Australia). A dual-beam optical system with a deuterium lamp was applied for background correction, and a silver hollow cathode lamp (0.4 mA) was the radiation source. The wavelengths used for such analyses were 328.1 and 338.3 nm, and the slit width was 0.5 nm in both cases. To prepare the calibration curve, an Ag basic standard solution with a content of 1000 mg/L in 2%  $\text{HNO}_3$  (VWR Chemicals) was applied. The first standard solutions at a concentration of 10 mg/L were prepared by diluting 1000 mg/L stock solutions. Six subsequent standard solutions were prepared for the calibration curve, at 0.1, 0.3, 0.5, 1.0, 2.0, and 3.0 mg/L. The linear regression method was used to create the calibration curve. The  $R^2$  coefficient was equal to 0.998, which proved acceptable linearity.

### 2.6. Mechanical Studies—Nanoindentation and Nanoscratch Tests

Nanoindentation tests were performed with the NanoTest™ Vantage (NanoTest Vantage, Micro Materials, Wrexham, UK) equipment equipped with a Berkovich three-sided pyramidal diamond. Fifty ( $5 \times 10$ ) independent measurements of nanoindentation for the reference Ti13Zr13Nb sample, Ti13Zr13Nb–TiO<sub>2</sub>, and Ti13Zr13Nb–TiO<sub>2</sub>–chitosan–nanosilver tested specimens (A, B, and C) were carried out. The maximum applied force was 50 mN, the loading and unloading rates were set up at 20 s, and the dwell period at the maximum load was 10 s. The distances between the subsequent indents were 20  $\mu\text{m}$ . During the indent, the load-displacement curve was determined based on the Oliver and Pharr method. Afterward, surface hardness (H) and reduced Young's modulus ( $E_r$ ) were calculated using the integrated software. Estimating Young's modulus (E), Poisson's ratios of 0.33, 0.3, and 0.4 were assumed for the reference Ti13Zr13Nb, Ti13Zr13Nb–TiO<sub>2</sub>, and Ti13Zr13Nb–TiO<sub>2</sub>–chitosan–nanosilver specimens (A, B, and C, respectively).

Nanoscratch tests were made using the same device and the indenter for each specimen. The scratch tests were repeated 10 times while increasing the load from 0 mN to 200 mN at a loading rate of 1.3 mN/s at a distance of 500  $\mu\text{m}$ . The adhesion of the coating was assessed as the stress corresponding to an abrupt change in frictional force during the test.

### 2.7. Contact Angle Studies

The three water contact angle measurements of the reference Ti13Zr13Nb, Ti13Zr13Nb–TiO<sub>2</sub> and Ti13Zr13Nb–TiO<sub>2</sub>–chitosan–nanosilver specimens (A, B, and C) were taken with the contact angle

instrument (Goniometer, Attention Theta Life, Biolin Scientific, Espoo, Finland) at room temperature 10 s after the dropout.

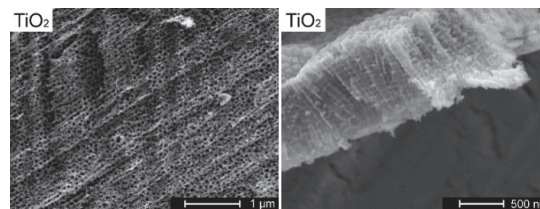
### 2.8. Statistical Analysis

Statistical analysis of the data was performed using a one-way ANOVA (analysis of variance). The Kolmogorov–Smirnov test was used to assess the normal distribution of the data. Statistical significance was set at  $p < 0.05$ . All of the results are presented as the mean  $\pm$  standard deviation (SD).

## 3. Results and Discussion

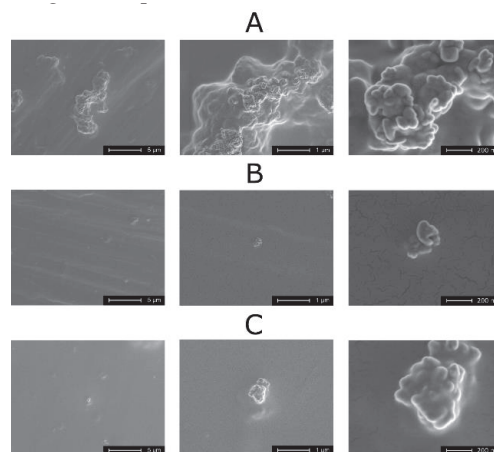
### 3.1. Structure and Morphology of Composite TiO<sub>2</sub>–Chitosan–Nanosilver Coatings

The morphology and cross-section of a nanotubular titanium dioxide layer are presented in Figure 1. The homogeneous layers possessed nanotubes, which were  $0.78 \pm 0.10 \mu\text{m}$  long, about 120 nm in inner diameter, and 25 nm of wall thickness. TiO<sub>2</sub> nanotubes were aligned vertically and densely packed. The TiO<sub>2</sub> nanotube layers were previously obtained on a titanium alloy using electrolytes with orthophosphoric acid and hydrofluoric acid [34,35]. Nanotubular titanium dioxide layers designed to ensure better adhesion between the substrate and coatings and for improved corrosion resistance of titanium alloy have also been investigated in the past [36,37].



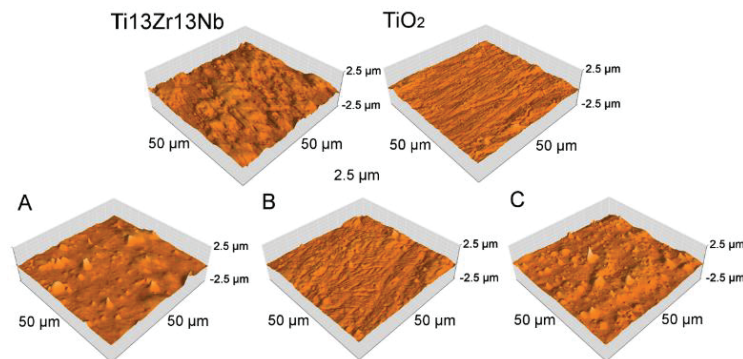
**Figure 1.** Nanotubular dioxide TiO<sub>2</sub> on the Ti13Zr13Nb alloy (topography—left, thickness—right), Magnifications 16,000  $\times$  (on left) and 32,000  $\times$  (on right).

Figure 2 shows homogenous chitosan coatings for three nanotubular titanium dioxide specimens produced (regardless of the EPD voltage or electrolyte) on the Ti13Zr13Nb alloy. The micrographs were prepared to examine the dispersion of Ag nanoparticles on chitosan coatings produced in a single process (EPD of chitosan with nanoparticles). For Specimen A (without dispersant in the electrolyte), large agglomerates of nanosilver were obtained (Figure 2A). The presence of dispersant in electrolytes used for the coating of Specimens B (Figure 2B) and C (Figure C) reduced the tendency of nanosilver agglomerates to form. The cracks visible at high magnifications were the result of gold sputtering on samples.



**Figure 2.** Chitosan coatings with nanosilver on the TiO<sub>2</sub> layer on the Ti13Zr13Nb alloy, Specimens A, B, and C. Magnifications 1000  $\times$  (on the left), 5000  $\times$  (at the center) and 25,000  $\times$  (on the right).

The surface morphology and area roughness of titanium alloy Ti13Zr13Nb, TiO<sub>2</sub> nanotube arrays, and the chitosan-based composite coating, characterized by AFM as 3D images, are shown in Figure 3. The roughness, determined by process parameters, is listed in Table 3.



**Figure 3.** Atomic force microscopy (AFM) topography of the Ti13Zr13Nb substrate, the substrate with the TiO<sub>2</sub> nanotubular layer, Specimens A, B, and C.

**Table 3.** Roughness parameters of the reference specimen, TiO<sub>2</sub> layer, and chitosan composite coatings.

Specimen	Properties	
	Sa Parameter (µm)	Thickness (µm); (mean ± SD; n = 10)
TiO <sub>2</sub> layer on Ti13Zr13Nb alloy	0.07	0.78 ± 0.10
A	0.10	0.78 ± 0.08
B	0.08	0.22 ± 0.04*
C	0.11	3.18 ± 0.18*
reference Ti13Zr13Nb alloy	0.15	-

\* significantly different from Specimen A (analysis of variance (ANOVA)  $p < 0.05$ )

A significant change in surface topography occurred following the anodization and electrophoretic deposition of the composite chitosan coatings. The addition of polysorbate 20 made the roughness lower because it is a compound that decreases surface tension and thus enhances the formation of the homogenous layer. An increase in voltage resulted in a small increase in the roughness and a 4-fold increase in coating thickness caused by the increasing amount of particles delivered to the surface in a time unit, always associated with a tendency to create thick and more porous layers. Moreover, the experiments confirmed that an increase of applied voltage caused the formation of more bubbles in chitosan coatings, which was the result of water hydrolysis during the EPD process and hydrogen evolution at the deposition electrode [38]. Higher voltage increases the intensity of this process, which results in more porous coatings [39]. The thickness of the composite coating was negatively influenced by the addition of polysorbate 20, which could be attributed to closer packing of particles (lower roughness). The presence of TiO<sub>2</sub> decreased the surface roughness due to the surface preparation before anodizing. Even on an unpolished surface with a high roughness parameter (0.15 µm), titanium dioxide was formed at the same rate across the entire surface, which thus created a homogenous layer and decreased the surface's roughness.

The thickness values of the chitosan composite layers are shown in Figure 4 and presented in Table 3. The thickness of the coatings correlated with the results shown in SEM images (Figure 2) and AFM topographies (Figure 3). The nanotubular titanium dioxide layer was distinctly observed under the thinnest chitosan coating by both SEM and AFM (Specimen B). The presence of polysorbate 20 for specimens obtained at 10 V decreased the thickness of the layer (Specimens A and B).

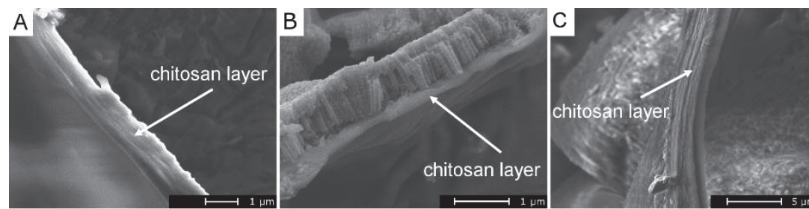


**Figure 4.** Chitosan composite coatings on TiO<sub>2</sub> on Ti13Zr13Nb. Three different parts of chitosan coating are shown in subfigures; arrows indicate one of the coating interfaces.

Figures 5 and 6 show the elemental distribution map and chemical composition of selected areas for Specimens A and B. The EDS map for Specimen A, shown in Figure 5, confirmed the occurrence of agglomerates of silver nanoparticles larger than those found in Specimen B. The EDS map for Specimen B, shown in Figure 6, proved an improved dispersion of silver nanoparticles following the use of dispersant (polysorbate 20) and, consequently, the appearance of a larger specific surface area with silver nanoparticles. For both specimens, A in Figure 5 and B in Figure 6, mapping Ti and O elements revealed a uniform distribution of nanotubular titanium dioxide on the Ti13Zr13Nb alloy.

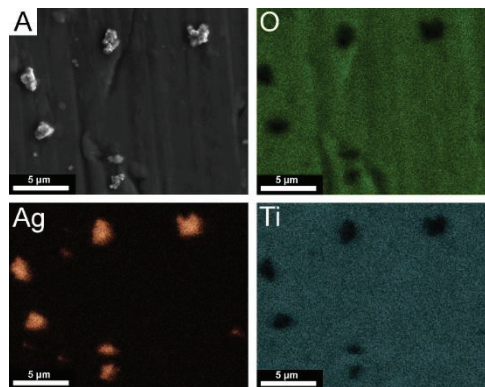


**Figure 5.** Elemental distribution map and chemical composition from a selected area, Specimen A.

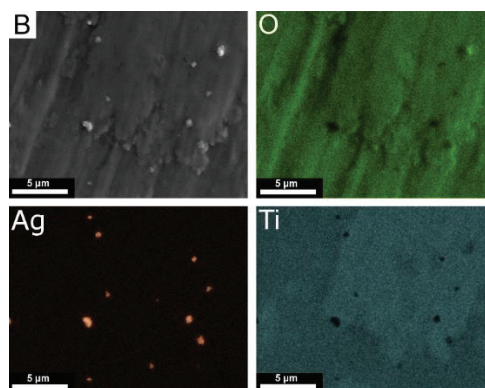


**Figure 6.** Elemental distribution map and chemical composition from a chosen region, Specimen B.

EDS mapping required collection of a stable image over about 30 min, which proved to be impossible for Specimen C. This was caused by the excessive thickness of the chitosan layer which, being an electrical insulator, resulted in image drift (a blurred image) during the EDS mapping, despite the sputtering of the gold layer. The highest content and more dispersed silver nanoparticles on Specimen B resulted in a more prolonged silver release to the surrounding implant tissue and, in consequence, a more effective bactericidal effect of these particles. The formation of agglomerates of silver nanoparticles has been previously reported [40,41]. The adverse impact of silver particles'

agglomeration on antimicrobial behavior has been explained as being due to decreasing contact between nanoparticles and bacterial cells. Silver nanoparticle agglomeration reduces their antibacterial effects and inhibits the release of silver ions, as the agglomerates have a lower surface-to-volume ratio and lower contact possibility with bacteria in comparison to nanoparticles. The problem of silver nanoparticle agglomeration may be solved by adding dispersing agents like polysorbate 20 to their suspension, which stabilizes Ag nanoparticles by enhancing the electrostatic repulsive forces between them.

The X-ray diffractograms of the tested specimens are depicted in Figure 7. In each of them, peaks can be observed that can be attributed to the Ti<sub>13</sub>Zr<sub>13</sub>Nb substrate (Figure 7) [42]. For the sample with the TiO<sub>2</sub> nanotubular layer, the difference in relative intensities of the primary phases (support) of peaks at the 2 $\theta$  range of 35–42° may have been linked to the formation of the layer visible in the SEM and AFM micrographs (Figures 1 and 3, respectively).

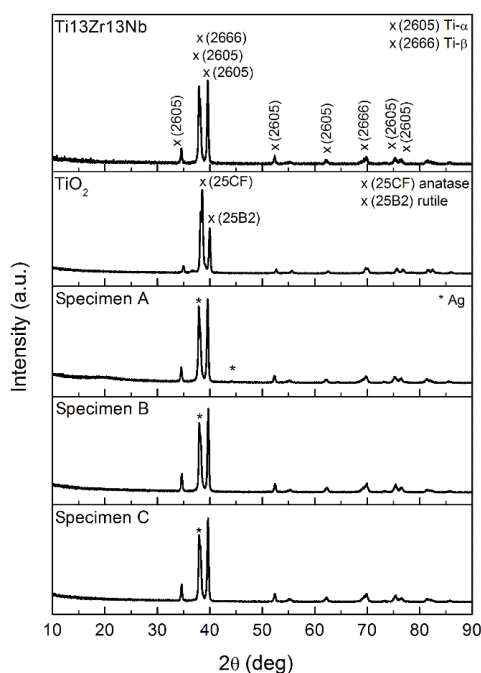


**Figure 7.** X-ray diffractogram of the Ti<sub>13</sub>Zr<sub>13</sub>Nb substrate, and the substrate with the TiO<sub>2</sub> nanotube layer, Specimens A, B, and C. The peak intensities are normalized.

Due to the overlapping of peaks, the crystalline structure of the titania nanotubes could not be determined. Similar results were reported previously for nanotube layers formed on pure titanium via anodization, where nanotube arrays of mixed-phase rutile and anatase were developed [43]. In the samples with the chitosan–nanosilver layer, the standard for amorphous chitosan broad maximum could be identified only for specimen A ( $2\theta = 15\text{--}25^\circ$ ); however, its relative (to main phase peaks) intensity was very low [44]. The visible peaks ( $2\theta = 38$  and  $44^\circ$ ) were attributed to the cubic crystalline structure of silver (ICDD 01-087-0717). Nevertheless, due to low concentration and nanocrystallinity, their intensity was very low. The main peak of the nanosilver phase overlapped with the support material peaks.

Figure 8 demonstrates the FTIR spectra of the investigated materials. A clear spectrum of chitosan was observed for Specimen C, with the most pronounced chitosan layer. The measured spectrum corresponded to other results on stand-alone and composite chitosan from the literature [45–49]. The main bands appearing in that spectrum were due to stretching vibrations of OH groups in the range from  $3750\text{ cm}^{-1}$  to  $3000\text{ cm}^{-1}$ , which overlapped with the stretching vibration of N–H and the C–H bond in  $-\text{CH}_2$  and  $-\text{CH}_3$  groups, respectively [45,50]. Bending vibrations of methylene and methyl groups were visible at  $1375\text{--}1430\text{ cm}^{-1}$  [51]. Absorption in the range of  $1680\text{--}1480\text{ cm}^{-1}$  was associated

with the vibrations of carbonyl bonds (C=O) of the amide groups [52], and absorption from 1160  $\text{cm}^{-1}$  to 1000  $\text{cm}^{-1}$  was associated with vibrations of CO [48]. The band located at around 1150  $\text{cm}^{-1}$  was related to asymmetrical vibrations of CO in the oxygen bridge resulting from the deacetylation of chitosan, and the bands near 1080–1025  $\text{cm}^{-1}$  were associated with C-O stretching [48]. The small peak at  $\sim 890 \text{ cm}^{-1}$  corresponded to the wagging of the saccharide structure of chitosan [46].

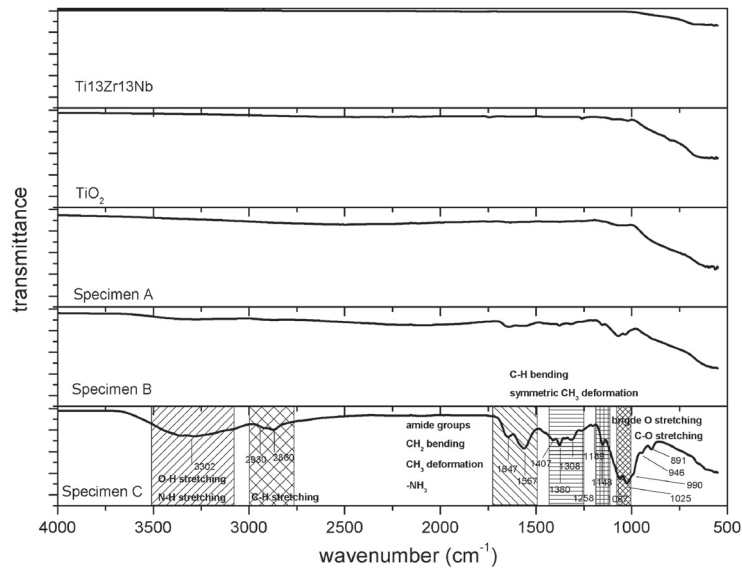


**Figure 8.** Fourier-transform infrared (FTIR) spectra of the Ti13Zr13Nb substrate and the substrate with the TiO<sub>2</sub> nanotube layers: Specimen A, Specimen B, and Specimen C.

### 3.2. Silver Release in Simulated Body Fluid (SBF) Solution

Ag total contents in solutions to which the specimens were exposed are presented in Figure 9. It was noted when the time of specimen exposure increased, the Ag concentration increased. Taking into account the calculated deviations of measured values, the increase in Ag content in solutions was 0.013–0.036 mg/L per day of exposure. The mean value of the increase of the Ag concentration can thus be expressed as an average of 0.025 mg/L per day of exposure, providing proof of the process of slow transport of Ag ions from tested materials to SBF.

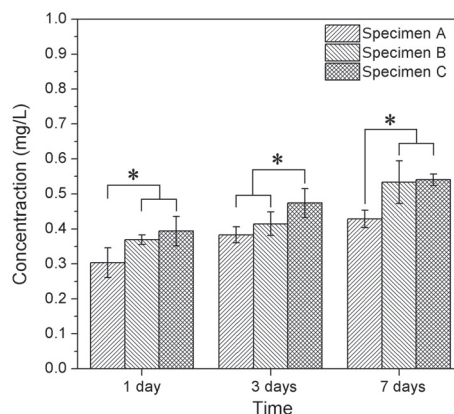


**Figure 9.** Cumulative concentrations of Ag ions released from chitosan composite coatings deposited on the nanotubular layer after 1, 3, and 7 days exposure in simulated body fluid (SBF) at 39 °C. Data are presented as the mean  $\pm$  SD ( $n = 4$ ). \*  $p < 0.05$ ; one-way ANOVA with Bonferroni post hoc correction.

Nowadays, postoperative infection is one of the main problems in orthopedic surgeries. The bactericidal properties of 35 ppb silver have been reported [53], and the most biofilm-forming

bacteria are found on the surface of implants [54]. Positive effects of released silver particles were observed for all tested specimens after 1 day when the risk of bacterial inflammation could be the highest. The slow release of silver nanoparticles into the SBF may have been caused by the presence of numerous hydroxyl and amine groups with a strong affinity to metallic elements such as silver [55]. A local increase in Ag content within the adjacent tissues in a human body will thus occur and prevent possible local inflammation states, which, consequently, will ensure long-term antibacterial protection. Moreover, the reference dose for allowable oral exposure of Ag, as defined by the US EPA (United States Environmental Protection Agency) is 0.005 mg of Ag/kg of body mass per day and, considering the maximum Ag release rate determined here, the maximum daily allowable consumption of Ag will not be exceeded in an average adult [56].

Bacterial inactivation may occur via two different actions: at the direct contact of bacteria with nanosilver at the interface or by the interaction of bacteria and the silver ions that appear during the dissolution of nanosilver [57–59]. The present results did not support either hypothesis, but the direct contact of silver ions and bacteria in solution seems more probable, as the antibacterial efficiency followed the silver release. Additionally, more bacteria could be present in solution than at the silver–solution interface, and more precisely at the surface of the nanosilver aggregates.

### 3.3. Mechanical Studies—Nanoindentation and Nanoscratch Tests

The results of the nanoindentation test are shown in Figure 10. Typical nanoindentation properties such as hardness, Young’s modulus, maximum depth, plastic and elastic work, and  $H^3/E^2$  factor were investigated. The remarkable standard deviations were characteristic of nanoindentation. For all of the Ti13Zr13Nb titanium surface modifications, decreasing nanohardness, Young’s modulus, and  $H^3/E^2$  factors were observed compared to the reference Ti13Zr13Nb alloy. The research proved a significant difference between Specimens A and B, and Specimens A and C for all studied nanoindentation properties.

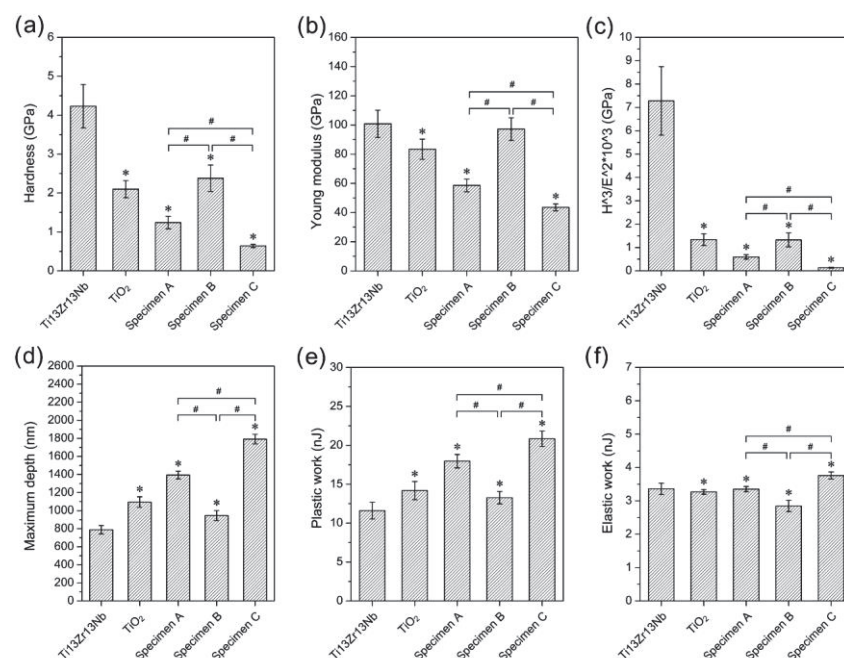


**Figure 10.** Nanomechanical properties: (a) hardness, (b) Young modulus, and (c)  $H^3/E^2$ ; nanoindentation properties: (d) maximum depth, (e) plastic work, and (f) elastic work for Ti13Zr13Nb substrate, substrate with the TiO<sub>2</sub> nanotube layer, Specimen A, Specimen B, and Specimen C. Data are presented as the mean  $\pm$  SD ( $n = 50$ ). A significant difference was observed between the Ti13Zr13Nb control specimen (ANOVA with Bonferroni post hoc correction  $*p < 0.05$ ) and Specimens A, B, and C (ANOVA with Bonferroni post hoc correction  $\#p < 0.05$ ).

The  $H^3/E^2$  factor was calculated using the results for the nanoindentation test. The  $H^3/E^2$  factor describes the resistance of a material to plastic deformation [60]. The deposition of composite coatings on the nanotubular layer caused a decrease in hardness and Young's modulus, except when a simultaneous deposition was made in the presence of a surface-active compound at a lower voltage value. This was assumed to be an effect of the close packing and high density of coatings obtained under such conditions. Mechanical properties such as hardness and Young's modulus are one of the most essential features for long-term and load-bearing implants. It has been proven that a significant difference between the properties of human bone and an implant can cause the "shielding effect" and, in consequence, a danger of loosening the implant [61]. The hardness and Young's modulus of Ti13Zr13Nb decreased after anodization, as reported previously by Chernozem et al. [60] and Crawford et al. [62]. A value of Young's modulus close to that of human bone (10–30 GPa) was obtained for Specimen C, characterized by the lowest nanohardness and  $E^3/H^2$  factor value [33]. It was expected that the specimens coated with chitosan (A, B, and C) would be characterized by lower nanomechanical properties than the Ti13Zr13Nb alloy and Ti13Zr13Nb after the anodization process, but, because of the small thickness of the chitosan coatings on Specimen B (about 0.22  $\mu\text{m}$ ), nanomechanical tests for this specimen probably involved to a significant extent the TiO<sub>2</sub> layer under the coating. This fact was confirmed by the lack of considerable difference between the nanohardness and Young's modulus values of the TiO<sub>2</sub> layer and Specimen B.

The results of the nanoscratch studies are shown in Table 4. The addition of the surface-active substance did not influence critical friction, but significantly decreased the load representative of the delamination force of the layers/coatings.

**Table 4.** Nanoscratch test properties of the TiO<sub>2</sub> layer and chitosan composite coatings (mean  $\pm$  SD;  $n = 10$ ).

Specimen	Nanoscratch Test Properties	
	Critical Friction (mN)	Critical Load (mN)
TiO <sub>2</sub> layer on Ti13Zr13Nb alloy	58.22 $\pm$ 20.43	85.95 $\pm$ 28.00
A	100.72 $\pm$ 9.31*	152.59 $\pm$ 13.93*
B	101.58 $\pm$ 41.76*	79.91 $\pm$ 25.44#
C	106.65 $\pm$ 28.97*	85.48 $\pm$ 30.34#

\* significantly different from TiO<sub>2</sub> layer on Ti13Zr13Nb alloy (ANOVA  $p < 0.05$ ). # significantly different from Specimen A (ANOVA  $p < 0.05$ ).

The highest adhesion to the bare surface was revealed for Specimen A. Values of the critical force were increased almost 2-fold for specimens with chitosan layers on TiO<sub>2</sub> compared with a single TiO<sub>2</sub> layer. Nowadays, the nanoscratch technique is preferred for determining the adhesion of thin layers and coatings [63–66]. The layers and coatings for implants should possess high adhesion to metallic substrates, in particular against shear stresses, and the nanoscratch test used here allows such expectations to be assessed. Unfortunately, to date, there has been almost no research conducted on the use of this technique on chitosan coatings. However, Tozar [67,68] determined only a friction coefficient in the nanoscratch sliding test as well as hardness and Young's modulus in the nanoindentation test for chitosan–hydroxyapatite–collagen coatings.

### 3.4. Measurements of the Contact Angle

The wettability of all specimens was in the range of values characteristic of high biocompatibility (Figure 11), which confirmed the hydrophilic character of the investigated surfaces ( $\theta < 90^\circ$ ). The wettability of a surface is crucial for cell attachment [38]. The recommended contact angle values needed for the best attachment to cells for bone replacement implants are 35–85°, and the optimal value is 55° [69]. All investigated surfaces fulfilled this criterion. Moreover, Specimens B and C are closest to the optimum contact angle value.

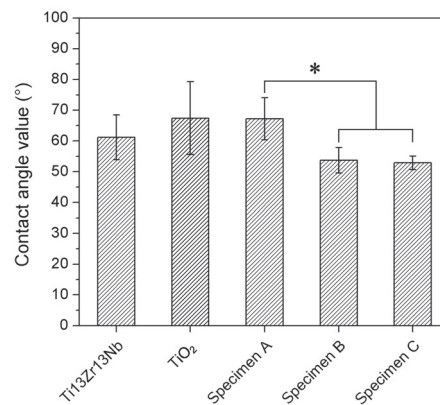


**Figure 11.** Water contact angle at room temperature for the reference non-coated specimen, TiO<sub>2</sub> layer, and chitosan composite coatings. Data are presented as the mean  $\pm$  SD ( $n = 3$ ). \*  $p < 0.05$ ; one-way ANOVA with Bonferroni post hoc correction.

The differences observed between uncoated and coated specimens, and for each coating, were tiny or fell within the standard deviations. The addition of the surface-active substance somewhat increased the wettability, but no explanation for this was found. The most likely reason is that the presence of polysorbate 20 in the chitosan coatings decreased the surface tension for Specimens B and C, as suggested by Ziani et al. [31], who applied Tween 20 as a surface-active substance. As a consequence, the decrease of the surface tension increased the water contact angle (Specimen B and C), which was a consequence of the presence of silver nanoparticles in specimens B and C provided that they were not agglomerated. Similar results have been previously reported [70]. Agglomeration of silver nanoparticles (as for Specimen A) resulted in an increase of hydrophobicity and contact angle in comparison to well-dispersed nanoparticles.

#### 4. Conclusions

Chitosan–nanosilver coatings were deposited on the nanotubular oxide layer of Ti13Zr13Nb alloy using the electrophoretic technique. The coatings were, at the applied solution and process parameters, homogeneous and well adjacent to the base, and demonstrated slow dissolution of nanosilver into the simulated body fluid.

The addition of a surface-active compound resulted in a small decrease in roughness, an increase in nanohardness, faster liberation of silver ions, and a reduction of critical load in a scratch test of tested composite coatings, which was attributed to a smoother and more packed (less porous) surface.

The increase in EPD voltage caused a high increase in coating thickness, a decrease in hardness, faster dissolution of nanosilver, and a small increase in the critical load and friction force of tested coatings.

The best process deposition parameters for the tested composite chitosan–nanosilver coating, the nanotubular oxide layer, and the Ti13Zr13Nb alloy as a substrate, used as an electrolyte 1 g/L of high-weight chitosan with a degree of deacetylation  $> 75\%$ , 0.05 g/L of nanosilver with an average particle size of about 30 nm, and 1 ml/L of Tween 20 (polysorbate 20) solution in 1% aqueous acetic acid; EPD voltage 10 V and time 1 min at room temperature.

**Author Contributions:** Conceptualization, M.B., and Ł.P.; methodology, M.B., Ł.P., A.M.-G., G.S., and B.C.; formal analysis, M.B., Ł.P., A.M.-G. and A.Z.; investigation, M.B., Ł.P., A.M.-G., G.S., and B.C.; writing—original draft preparation, M.B., and A.Z.; writing—review and editing, M.B. and A.Z.; supervision, M.B., and A.Z. All authors have read and agreed to the published version of the manuscript.

**Funding:** This research received no external funding.

**Conflicts of Interest:** The authors declare no conflict of interest.

## References

- Dinu, M.; Franchi, S.; Pruna, V.; Cotrut, C.M.; Secchi, V.; Santi, M.; Titorencu, I.; Battocchio, C.; Iucci, G.; Vladescu, A. Ti-Nb-Zr system and its surface biofunctionalization for biomedical applications. In *Titanium in Medical and Dental Applications*; Froes, F.H., Qian, M., Eds.; Woodhead Publishing Series in Biomaterials; Woodhead Publishing: Cambridge, UK, 2018; pp. 175–200. ISBN 978-0-12-812456-7.
- Ferraris, S.; Spriano, S. Antibacterial titanium surfaces for medical implants. *Mater. Sci. Eng. C* **2016**, *61*, 965–978. [CrossRef] [PubMed]
- Piałkowski, M.; Radwan-Pragłowska, J.; Janus, Ł.; Bogdał, D.; Matysek, D.; Cablik, V. Microwave-assisted synthesis and characterization of chitosan aerogels doped with Au-NPs for skin regeneration. *Polym. Test.* **2019**, *73*, 366–376. [CrossRef]
- Möhler, J.S.; Sim, W.; Blaskovich, M.A.T.; Cooper, M.A.; Ziora, Z.M. Silver bullets: A new lustre on an old antimicrobial agent. *Biotechnol. Adv.* **2018**, *36*, 1391–1411. [CrossRef] [PubMed]
- Wekwejt, M.; Moritz, N.; Świeczko-Żurek, B.; Pałubicka, A. Biomechanical testing of bioactive bone cements—A comparison of the impact of modifiers: Antibiotics and nanometals. *Polym. Test.* **2018**, *70*, 234–243. [CrossRef]
- Volova, T.G.; Shumilova, A.A.; Shidlovskiy, I.P.; Nikolaeva, E.D.; Sukovatiy, A.G.; Vasiliev, A.D.; Shishatskaya, E.I. Antibacterial properties of films of cellulose composites with silver nanoparticles and antibiotics. *Polym. Test.* **2018**, *65*, 54–68. [CrossRef]
- Zheng, K.; Setyawati, M.I.; Leong, D.T.; Xie, J. Antimicrobial silver nanomaterials. *Coord. Chem. Rev.* **2018**, *357*, 1–17. [CrossRef]
- Gilabert-Chirivella, E.; Pérez-Feito, R.; Ribeiro, C.; Ribeiro, S.; Correia, D.M.; González-Martín, M.L.; Manero, J.M.; Lanceros-Méndez, S.; Ferrer, G.G.; Gómez-Ribelles, J.L. Chitosan patterning on titanium implants. *Prog. Org. Coat.* **2017**, *111*, 23–28. [CrossRef]
- Sani, I.K.; Pirsá, S.; Tağı, Ş. Preparation of chitosan/zinc oxide/Melissa officinalis essential oil nano-composite film and evaluation of physical, mechanical and antimicrobial properties by response surface method. *Polym. Test.* **2019**, *79*, 106004. [CrossRef]
- Urbanek, O.; Sajkiewicz, P.; Pierini, F. The effect of polarity in the electrospinning process on PCL/chitosan nanofibres' structure, properties and efficiency of surface modification. *Polymer* **2017**, *124*, 168–175. [CrossRef]
- Muxika, A.; Etxabide, A.; Uranga, J.; Guerrero, P.; de la Caba, K. Chitosan as a bioactive polymer: Processing, properties and applications. *Int. J. Biol. Macromol.* **2017**, *105*, 1358–1368. [CrossRef]
- Olad, A.; Hagh, H.B.K. Graphene oxide and amin-modified graphene oxide incorporated chitosan-gelatin scaffolds as promising materials for tissue engineering. *Compos. Part B Eng.* **2019**, *162*, 692–702. [CrossRef]
- Divakar, D.D.; Jastaniyah, N.T.; Altamimi, H.G.; Alnakhli, Y.O.; Muzaheed; Alkheraif, A.A.; Haleem, S. Enhanced antimicrobial activity of naturally derived bioactive molecule chitosan conjugated silver nanoparticle against dental implant pathogens. *Int. J. Biol. Macromol.* **2018**, *108*, 790–797. [CrossRef] [PubMed]
- Praxedes, A.P.P.; Webler, G.D.; Souza, S.T.; Ribeiro, A.S.; Fonseca, E.J.S.; Oliveira, I.N. De Non-monotonic wetting behavior of chitosan films induced by silver nanoparticles. *Appl. Surf. Sci.* **2016**, *370*, 25–31. [CrossRef]
- Yan, Y.; Zhang, X.; Li, C.; Huang, Y.; Ding, Q.; Pang, X. Preparation and characterization of chitosan-silver/hydroxyapatite composite coatings on TiO<sub>2</sub> nanotube for biomedical applications. *Appl. Surf. Sci.* **2015**, *332*, 62–69. [CrossRef]
- Jennings, J.A.; Velasquez Pulgarin, D.A.; Kunwar, D.L.; Babu, J.; Mishra, S.; Bumgardner, J. Bacterial inhibition by chitosan coatings loaded with silver-decorated calcium phosphate microspheres. *Thin Solid Film.* **2015**, *596*, 83–86. [CrossRef]
- Kishore, R.; Awasthi, S.; Dhayalan, A.; Ferreira, J.M.F.; Kannan, S. Deposition, structure, physical and in-vitro characteristics of Ag-doped  $\beta$ -Ca<sub>3</sub>(PO<sub>4</sub>)<sub>2</sub>/chitosan hybrid composite coatings on Titanium metal. *Mater. Sci. Eng. C* **2016**, *62*, 692–701.
- Lin, S.; Chen, L.; Huang, L.; Cao, S.; Luo, X.; Liu, K. Novel antimicrobial chitosan-cellulose composite films bioconjugated with silver nanoparticles. *Ind. Crops Prod.* **2015**, *70*, 395–403. [CrossRef]
- Mishra, S.K.; Ferreira, J.M.F.; Kannan, S. Mechanically stable antimicrobial chitosan-PVA-silver nanocomposite coatings deposited on titanium implants. *Carbohydr. Polym.* **2015**, *121*, 37–48. [CrossRef]

20. Wang, Y.; Guo, X.; Pan, R.; Han, D.; Chen, T.; Geng, Z.; Xiong, Y.; Chen, Y. Electrodeposition of chitosan/gelatin/nanosilver: A new method for constructing biopolymer/nanoparticle composite films with conductivity and antibacterial activity. *Mater. Sci. Eng. C* **2015**, *53*, 222–228. [CrossRef]
21. Arjunan, N.; Kumari, H.L.J.; Singaravelu, C.M.; Kandasamy, R.; Kandasamy, J. Physicochemical investigations of biogenic chitosan-silver nanocomposite as antimicrobial and anticancer agent. *Int. J. Biol. Macromol.* **2016**, *92*, 77–87. [CrossRef]
22. Dananjaya, S.H.S.; Erandani, W.K.C.U.; Kim, C.H.; Nikapitiya, C.; Lee, J.; De Zoysa, M. Comparative study on antifungal activities of chitosan nanoparticles and chitosan silver nano composites against *Fusarium oxysporum* species complex. *Int. J. Biol. Macromol.* **2017**, *105*, 478–488. [CrossRef] [PubMed]
23. Kalaivani, R.; Maruthupandy, M.; Muneeswaran, T.; Hameedha Beevi, A.; Anand, M.; Ramakritinan, C.M.; Kumaraguru, A.K. Synthesis of chitosan mediated silver nanoparticles (Ag NPs) for potential antimicrobial applications. *Front. Lab. Med.* **2018**, *2*, 30–35. [CrossRef]
24. Wongpreecha, J.; Polpanich, D.; Suteewong, T.; Kaewsaneha, C. One-pot, large-scale green synthesis of silver nanoparticles-chitosan with enhanced antibacterial activity and low cytotoxicity. *Carbohydr. Polym.* **2018**, *199*, 641–648. [CrossRef] [PubMed]
25. Xie, Y.; Liao, X.; Zhang, J.; Yang, F.; Fan, Z. Novel chitosan hydrogels reinforced by silver nanoparticles with ultrahigh mechanical and high antibacterial properties for accelerating wound healing. *Int. J. Biol. Macromol.* **2018**, *119*, 402–412. [CrossRef]
26. Rinaldi, F.; Del Favero, E.; Moeller, J.; Hanieh, P.N.; Passeri, D.; Rossi, M.; Angeloni, L.; Venditti, I.; Marianecchi, C.; Carafa, M.; et al. Hydrophilic silver nanoparticles loaded into niosomes: Physical-chemical characterization in view of biological applications. *Nanomaterials* **2019**, *9*, 1177. [CrossRef]
27. Li, X.; Lenhart, J.J.; Walker, H.W. Aggregation kinetics and dissolution of coated silver nanoparticles. *Langmuir* **2012**, *28*, 1095–1104. [CrossRef]
28. Cavalieri, F.; Tortora, M.; Stringaro, A.; Colone, M.; Baldassarri, L. Nanomedicines for antimicrobial interventions. *J. Hosp. Infect.* **2014**, *88*, 183–190. [CrossRef]
29. Badawy, M.E.I.; Lotfy, T.M.R.; Shawir, S.M.S. Preparation and antibacterial activity of chitosan-silver nanoparticles for application in preservation of minced meat. *Bull. Natl. Res. Cent.* **2019**, *43*, 83. [CrossRef]
30. Chowdappa, P.; Shivakumar, G.; Chethana, C.S.; Madhur, S. Antifungal activity of chitosan-silver nanoparticle composite against *Colletotrichum gloeosporioides* associated with mango anthracnose. *Afr. J. Microbiol. Res.* **2014**, *8*, 1803–1812.
31. Ziani, K.; Oses, J.; Coma, V.; Maté, J.I. Effect of the presence of glycerol and Tween 20 on the chemical and physical properties of films based on chitosan with different degree of deacetylation. *LWT Food Sci. Technol.* **2008**, *41*, 2159–2165. [CrossRef]
32. Casariego, A.; Souza, B.W.S.; Vicente, A.A.; Teixeira, J.A.; Cruz, L.; Díaz, R. Chitosan coating surface properties as affected by plasticizer, surfactant and polymer concentrations in relation to the surface properties of tomato and carrot. *Food Hydrocoll.* **2008**, *22*, 1452–1459. [CrossRef]
33. Mohan, L.; Durgalakshmi, D.; Geetha, M.; Sankara Narayanan, T.S.N.; Asokamani, R. Electrophoretic deposition of nanocomposite (HAp + TiO<sub>2</sub>) on titanium alloy for biomedical applications. *Ceram. Int.* **2012**, *38*, 3435–3443. [CrossRef]
34. Kodama, A.; Bauer, S.; Komatsu, A.; Asoh, H.; Ono, S.; Schmuki, P. Bioactivation of titanium surfaces using coatings of TiO<sub>2</sub> nanotubes rapidly pre-loaded with synthetic hydroxyapatite. *Acta Biomater.* **2009**, *5*, 2322–2330. [CrossRef] [PubMed]
35. Ossowska, A.; Sobieszczyk, S.; Supernak, M.; Zielinski, A. Morphology and properties of nanotubular oxide layer on the “Ti-13Zr-13Nb” alloy. *Surf. Coat. Technol.* **2014**, *258*, 1239–1248. [CrossRef]
36. Zielinski, A.; Antoniuk, P.; Krzysztofowicz, K. Nanotubular oxide layers and hydroxyapatite coatings on “Ti-13Zr013Nb” alloy. *Surf. Sci.* **2014**, *30*, 643–649.
37. Chrzanowski, W.; Szewczenko, J.; Tyrlik-Held, J.; Marciniak, J.; Zak, J. Influence of the anodic oxidation on the physicochemical properties of the Ti6Al4V ELI alloy. *J. Mater. Process. Technol.* **2005**, *162–163*, 163–168. [CrossRef]
38. Gebhardt, F.; Seuss, S.; Turhan, M.C.; Hornberger, H.; Virtanen, S.; Boccaccini, A.R. Characterization of electrophoretic chitosan coatings on stainless steel. *Mater. Lett.* **2012**, *66*, 302–304. [CrossRef]
39. Pang, X.; Zhitomirsky, I. Electrophoretic deposition of composite hydroxyapatite-chitosan coatings. *Mater. Charact.* **2007**, *58*, 339–348. [CrossRef]

40. Guo, L.; Yuan, W.; Lu, Z.; Li, C.M. Polymer/nanosilver composite coatings for antibacterial applications. *Colloids Surf. A Physicochem. Eng. Asp.* **2013**, *439*, 69–83. [CrossRef]
41. Li, Y.; Zhang, W.; Niu, J.; Chen, Y. Surface-coating-dependent dissolution, aggregation, and reactive oxygen species (ROS) generation of silver nanoparticles under different irradiation conditions. *Environ. Sci. Technol.* **2013**, *47*, 10293–10301. [CrossRef]
42. Ozaltin, K.; Panigrahi, A.; Chrominski, W.; Bulutsuz, A.G.; Kulczyk, M.; Zehetbauer, M.J.; Lewandowska, M. Microstructure and Texture Evolutions of Biomedical Ti-13Nb-13Zr Alloy Processed by Hydrostatic Extrusion. *Metall. Mater. Trans. A Phys. Metall. Mater. Sci.* **2017**, *48*, 5747–5755. [CrossRef]
43. Goodarzi, S.; Moztarzadeh, F.; Nezafati, N.; Omidvar, H. Titanium dioxide nanotube arrays: A novel approach into periodontal tissue regeneration on the surface of titanium implants. *Adv. Mater. Lett.* **2016**, *7*, 209–215. [CrossRef]
44. Kumar, S.; Koh, J. Physicochemical and optical study of chitosan-terephthaldehyde derivative for biomedical applications. *Int. J. Biol. Macromol.* **2012**, *51*, 1167–1172. [CrossRef] [PubMed]
45. Rieppo, J.; Rieppo, L.; Saarakkala, S.; Jurvelin, J.S. Fourier Transform Infrared Imaging Spectroscopy in Biomedicine-Important Things to Consider When Planning a New Experiment. In *Fourier Transforms-New Analytical Approaches and FTIR Strategies*; Nikolic, G., Ed.; Intech Open: London, UK, 2011; pp. 1–14.
46. Paluszkiwicz, C.; Stodolak, E.; Hasik, M.; Blazewicz, M. FT-IR study of montmorillonite–chitosan nanocomposite materials. *Spectrochim. Acta Part A Mol. Biomol. Spectrosc.* **2011**, *79*, 784–788. [CrossRef] [PubMed]
47. Corazzari, I.; Nisticò, R.; Turci, F.; Faga, M.; Franzoso, F.; Tabasso, S.; Magnacca, G. Advanced physico-chemical characterization of chitosan by means of TGA coupled on-line with FTIR and GCMS: Thermal degradation and water adsorption capacity. *Polym. Degrad. Stab.* **2014**, *112*, 1–9. [CrossRef]
48. Dimzon, I.K.D.; Knepper, T.P. International Journal of Biological Macromolecules Degree of deacetylation of chitosan by infrared spectroscopy and partial least squares. *Int. J. Biol. Macromol.* **2015**, *72*, 939–945. [CrossRef]
49. Silva, S.M.L.; Braga, C.R.C.; Fook, M.V.L.; Raposo, C.M.O.; Carvalho, L.H.; Canedo, E.L. Application of Infrared Spectroscopy to Analysis of Chitosan/Clay Nanocomposites. In *Infrared Spectroscopy*; Theophanides, T., Ed.; IntechOpen: Rijeka, Croatia, 2012.
50. Fan, M.; Dai, D.; Huang, B. Fourier Transform Infrared Spectroscopy for Natural Fibres. In *Fourier Transform*; Salih, S.M., Ed.; IntechOpen: Rijeka, Croatia, 2012.
51. Mano, J.F.; Koniarova, D.; Reis, R.L. Thermal properties of thermoplastic starch/synthetic polymer blends with potential biomedical applicability. *J. Mater. Sci. Mater. Med.* **2003**, *14*, 127–135. [CrossRef]
52. Marchessault, R.H.; Ravenelle, F.; Zhu, X.X. (Eds.) *Polysaccharides for Drug Delivery and Pharmaceutical Applications*; ACS Symposium Series; American Chemical Society: Washington, DC, USA, 2006; Volume 934, ISBN 0-8412-3960-6.
53. Geng, Z.; Wang, R.; Zhuo, X.; Li, Z.; Huang, Y.; Ma, L.; Cui, Z.; Zhu, S.; Liang, Y.; Liu, Y.; et al. Incorporation of silver and strontium in hydroxyapatite coating on titanium surface for enhanced antibacterial and biological properties. *Mater. Sci. Eng. C* **2017**, *71*, 852–861. [CrossRef]
54. Jayaprakash, N.; Judith Vijaya, J.; John Kennedy, L.; Priadharsini, K.; Palani, P.; Louis, R.; Muthumary, J.; Silver, B.; Bright, P.; Dichlorotriazine, R. Antibacterial activity of silver nanoparticles synthesized from serine. *Mater. Sci. Eng. C* **2014**, *49*, 316–322. [CrossRef]
55. Sanpui, P.; Murugadoss, A.; Prasad, P.V.D.; Ghosh, S.S.; Chattopadhyay, A. The antibacterial properties of a novel chitosan-Ag-nanoparticle composite. *Int. J. Food Microbiol.* **2008**, *124*, 142–146. [CrossRef]
56. National Center for Environmental Assessment. *Integrated Risk Information System (IRIS) Chemical Assessment Summary: Silver*; CASRN 7440-22-4; National Center for Environmental Assessment: Oakbrook Terrace, IL, USA, 2003.
57. Rtimi, S.; Kiwi, J.; Karimi, A.; Sanjinés, R. Innovative Ti1–xNbxN–Ag Films Inducing Bacterial Disinfection by Visible Light/Thermal Treatment. *Acs Appl. Mater. Interfaces* **2018**, *10*, 12021–12030. [CrossRef] [PubMed]
58. Hajjaji, A.; Elabidi, M.; Trabelsi, K.; Assadi, A.A.; Bessais, B.; Rtimi, S. Bacterial adhesion and inactivation on Ag decorated TiO<sub>2</sub>-nanotubes under visible light: Effect of the nanotubes geometry on the photocatalytic activity. *Colloids Surf. B Biointerfaces* **2018**, *170*, 92–98. [CrossRef] [PubMed]

59. Rtimi, S.; Nadtochenko, V.; Khmel, I.; Bensimon, M.; Kiwi, J. First unambiguous evidence for distinct ionic and surface-contact effects during photocatalytic bacterial inactivation on Cu–Ag films: Kinetics, mechanism and energetics. *Mater. Today Chem.* **2017**, *6*, 62–74. [CrossRef]
60. Chernozem, R.V.; Surmeneva, M.A.; Krause, B.; Baumbach, T.; Ignatov, V.P.; Tyurin, A.I.; Loza, K.; Epple, M.; Surmenev, R.A. Hybrid biocomposites based on titania nanotubes and a hydroxyapatite coating deposited by RF-magnetron sputtering: Surface topography, structure, and mechanical properties. *Appl. Surf. Sci.* **2017**, *426*, 229–237. [CrossRef]
61. Niinomi, M.; Nakai, M.; Hieda, J. Development of new metallic alloys for biomedical applications. *Acta Biomater.* **2012**, *8*, 3888–3903. [CrossRef]
62. Crawford, G.A.; Chawla, N.; Das, K.; Bose, S.; Bandyopadhyay, A. Microstructure and deformation behavior of biocompatible TiO<sub>2</sub> nanotubes on titanium substrate. *Acta Biomater.* **2007**, *3*, 359–367. [CrossRef]
63. Manoj Kumar, R.; Kuntal, K.K.; Singh, S.; Gupta, P.; Bhushan, B.; Gopinath, P.; Lahiri, D. Electrophoretic deposition of hydroxyapatite coating on Mg-3Zn alloy for orthopaedic application. *Surf. Coat. Technol.* **2016**, *287*, 82–92. [CrossRef]
64. Hang, Y.; Liu, G.; Huang, K.; Jin, W. Mechanical properties and interfacial adhesion of composite membranes probed by in-situ nano-indentation/scratch technique. *J. Membr. Sci.* **2015**, *494*, 205–215. [CrossRef]
65. Mali, S.; Misra, R.D.K.; Somani, M.C.; Karjalainen, L.P. Biomimetic nanostructured coatings on nano-grained/ultrafine-grained substrate: Microstructure, surface adhesion strength, and biosolubility. *Mater. Sci. Eng. C* **2009**, *29*, 2417–2427. [CrossRef]
66. Bartmanski, M.; Cieslik, B.; Glodowska, J.; Kalka, P. Electrophoretic deposition (EPD) of nanohydroxyapatite—Nanosilver coatings on Ti<sub>13</sub>Zr<sub>13</sub>Nb alloy. *Ceram. Int.* **2017**, *43*, 11820–11829. [CrossRef]
67. Tozar, A.; Karahan, İ.H. A comparative study on the effect of collagen and h-BN reinforcement of hydroxyapatite/chitosan biocomposite coatings electrophoretically deposited on Ti-6Al-4V biomedical implants. *Surf. Coat. Technol.* **2018**, *340*, 167–176. [CrossRef]
68. Tozar, A.; Karahan, İ.H. A comprehensive study on electrophoretic deposition of a novel type of collagen and hexagonal boron nitride reinforced hydroxyapatite/chitosan biocomposite coating. *Appl. Surf. Sci.* **2018**, *452*, 322–336. [CrossRef]
69. Cordero-Arias, L.; Cabanas-Polo, S.; Gao, H.; Gilabert, J.; Sanchez, E.; Roether, J.A.; Schubert, D.W.; Virtanen, S.; Boccaccini, A.R. Electrophoretic deposition of nanostructured-TiO<sub>2</sub>/chitosan composite coatings on stainless steel. *RSC Adv.* **2013**, *3*, 11247–11254. [CrossRef]
70. Kasraei, S.; Azarsina, M. Addition of silver nanoparticles reduces the wettability of methacrylate and silorane-based composites. *Braz. Oral Res.* **2012**, *26*, 505–510. [CrossRef]



© 2020 by the authors. Licensee MDPI, Basel, Switzerland. This article is an open access article distributed under the terms and conditions of the Creative Commons Attribution (CC BY) license (<http://creativecommons.org/licenses/by/4.0/>).

Review

# Micro-Arc Oxidation in Titanium and Its Alloys: Development and Potential of Implants

Xinwei Ming<sup>1,2</sup>, Yan Wu<sup>3,\*</sup>, Ziyue Zhang<sup>1,2</sup> and Yan Li<sup>1,2,\*</sup>

<sup>1</sup> School of Materials Science and Engineering, Beihang University, Beijing 100191, China; zy2101140@buaa.edu.cn (X.M.); zhangziyuebk@163.com (Z.Z.)

<sup>2</sup> Zhongfa Aviation Institute, Beihang University, Hangzhou 311115, China

<sup>3</sup> Institute of Translational Medicine, Shanghai University, Shanghai 200444, China

\* Correspondence: wyone023@163.com (Y.W.); liyan@buaa.edu.cn (Y.L.)

**Abstract:** Titanium (Ti) and its alloys are widely recognized as preferred materials for bone implants due to their superior mechanical properties. However, their natural surface bio-inertness can hinder effective tissue integration. To address this challenge, micro-arc oxidation (MAO) has emerged as an innovative electrochemical surface modification technique. Its benefits range from operational simplicity and cost-effectiveness to environmental compatibility and scalability. Furthermore, the distinctive MAO process yields a porous topography that bestows versatile functionalities for biological applications, encompassing osteogenesis, antibacterial, and anti-inflammatory properties. In this review, we undertake an examination of the underlying mechanism governing the MAO process, scrutinize the multifaceted influence of various factors on coating performance, conduct an extensive analysis of the development of diverse biological functionalities conferred by MAO coatings, and discuss the practical application of MAO in implants. Finally, we provide insights into the limitations and potential pathways for further development of this technology in the field of bone implantation.

**Keywords:** titanium (Ti); micro-arc oxidation; surface modification; implants; biologic function

## 1. Introduction

The latest statistics show that by mid-century, the global population aged 65 or over is expected to more than double to a staggering 1.6 billion people [1]. An aging population means a larger population base of chronic diseases, and bone and joint diseases. In dentistry and orthopedics, implants, with titanium (Ti) and its alloys as the preferred choice among various materials, have become a common approach for treating conditions due to their exceptional biocompatibility and mechanical properties [2]. Despite the vast potential for Ti and its alloys, there are still limitations to surface bioactivity. They often exhibit biological inertness, limiting the close integration of implants with surrounding tissues. Furthermore, Ti alloys are susceptible to microorganisms, increasing the risk of postoperative infections, and threatening the prognosis of patients. To tackle these issues, apart from alloying [3–5], surface treatment proves to be an effective approach as well. Common methodologies encompass atmospheric plasma spraying [6], laser treatment [7], anodizing [8], micro-arc oxidation (MAO), and biomimetic deposition of apatite [9] or other biomaterials [10]. Among the various surface modifications available, MAO has garnered significant attention due to its simplicity of operation, cost-effectiveness, and applicability to complex devices. Through MAO, the surface of Ti-based implants can undergo alterations in microstructural features and chemical composition, rendering them more suitable for tissue adhesion and effectively reducing the risk of infections [11]. The specific impacts of MAO on the substrate surface can be found in Table 1.

**Table 1.** A comparison table with the improved properties of MAO coatings on titanium alloys and uncoated ones.

Performance	Uncoated Ti Alloy	Coated Ti Alloy	Reference
Topography	Smooth or machined	Rough and porous	[12,13]
Chemical composition	Ti alloy	Ceramics dominated by TiO <sub>2</sub>	[12,13]
Hardness	Relatively not hard	Relatively hard	[13,14]
Wear resistance	Relatively not wear-resistant	Relatively wear-resistant	[15,16]
Corrosion resistance	Corrosion-resistant	More corrosion-resistant	[12,14,17]
Bioactivity	Biological inert	Biological activity	[12,18]

In this review, we aim to provide an overview of MAO applied to the preparation of coatings on Ti and its alloys for biomedical applications over the past 5 years, especially orthopedic and dental implants. This review encompasses an analysis of the factors influencing the coating preparation process, and an examination of the biological functionalities of these coatings and their applications. Finally, we highlight the challenges and future directions for the application of MAO in metal implants and make a vision for the development of surface coatings for metal implants.

## 2. The Process of MAO

### 2.1. The Mechanism of MAO

MAO involves plasma discharge, but it differs from traditional plasma electrolytic discharge techniques like plasma cutting or welding. It is often confused with anodic oxidation (AO), but they do indeed represent different processes and technologies. MAO typically requires a higher voltage and shorter processing times, and the type of electrolyte used, as well as the characteristics of the resulting coating, are significantly different from AO [19].

At present, most researchers divide the MAO process into three, which are spark discharge, micro-arc discharge, and arc discharge. Some add the early short anodizing phase, for a total of four stages [11,20].

The formation mechanism of MAO coatings is essentially similar, regardless of the electrolyte or control mode used. Taking the constant current mode as an example, Figure 1 illustrates the changes during the MAO process. In the first stage, as the current increases, the voltage linearly increases, initiating the traditional anodic oxidation phase, involving only electrochemical reactions. At this stage, a porous insulating film with a columnar structure perpendicular to the substrate is formed on the metal substrate, accompanied by gas generation, serving as precursors for igniting plasma discharge [21].

With the increase in current, the voltage on the coating also rises, moving on to the second and third stages. Once the voltage exceeds the critical threshold, known as breakdown voltage, it leads to spark discharge. There are various areas of defects, stress concentrations, and uneven thickness on the coating, and these vulnerable areas are the first to break down. This is the micro-arc discharge stage. In the later stage, when the maximum thickness of the porous oxide film is approached, the oxide film grows slowly with the increase in time, which is the arc discharge stage [23].

The phenomenon of micro-arc discharge and arc discharge is very similar, with only a slight difference in energy level. Two models of arc discharge have been proposed: one involving dielectric breakdown of the oxide film [24], and the other involving gas breakdown within micro-pores [25]. Both models result in the generation of high-energy plasma, possibly coexisting. Optical Emission Spectroscopy (OES) and Intensified Charge Coupled Device (ICCD)-based spectral systems provide real-time imaging of the MAO discharge process (Figure 2). The bright spots in the figure represent sparks, and over time, the intensity and range of sparks increase, indicating a larger pore size formed on the surface of the oxide film [26].

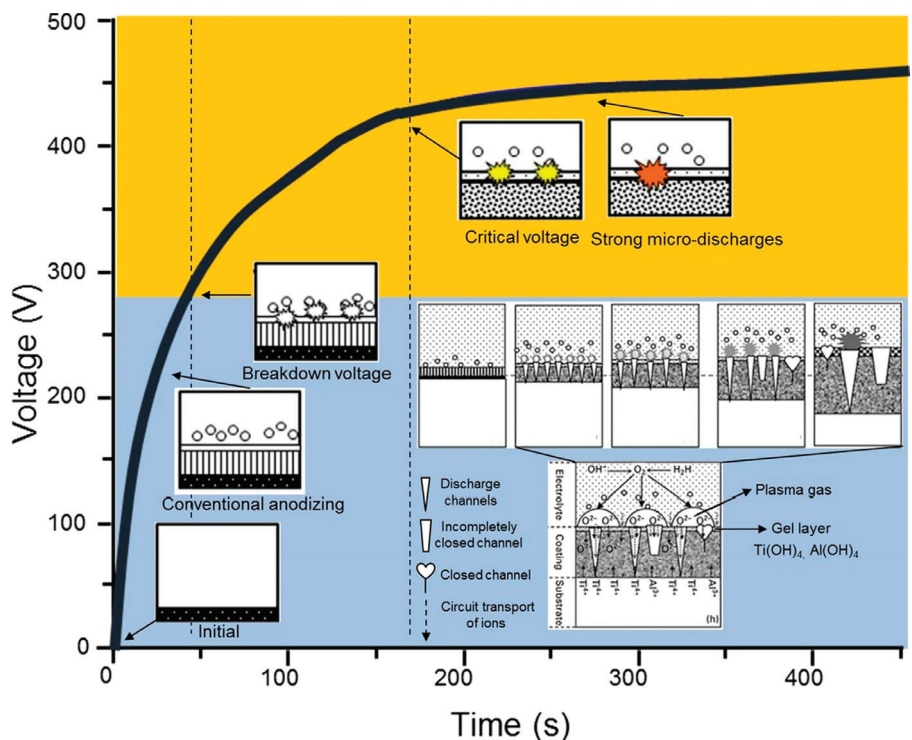


Figure 1. Voltage–time curve and various stages of the MAO process [22].

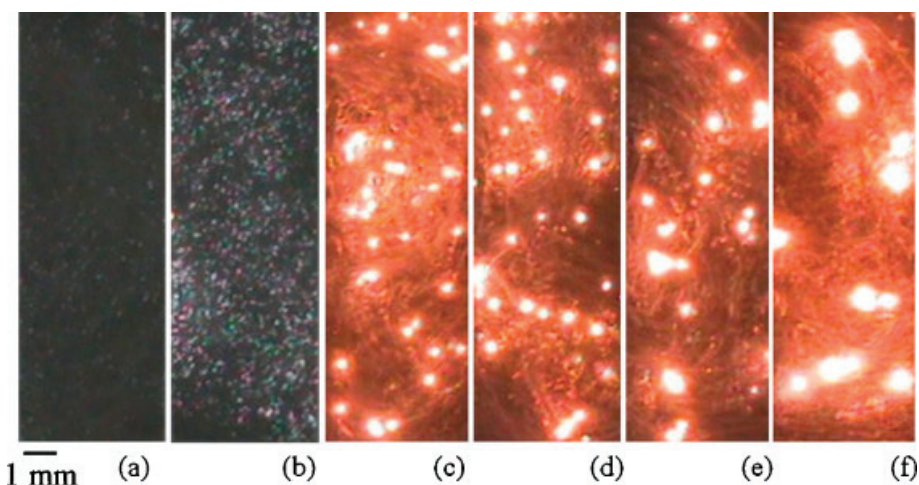


Figure 2. Micro-discharge phenomena at various stages of the MAO process on the same sample: (a) 15 s; (b) 30 s; (c) 150 s; (d) 300 s; (e) 600 s; (f) 1200 s [26].

Stojadinovic et al. [27] used OES-ICDD to record real-time discharges. Two types of plasma micro-discharge were observed during this process, with electron densities of  $N_e = 3.8 \times 10^{15} \text{ cm}^{-3}$  and  $N_e = 4.5 \times 10^{16} \text{ cm}^{-3}$ , and electron temperatures ranging from  $T_e = 3700 \pm 500 \text{ K}$ . Plasma discharge generates high temperatures, causing thermal decomposition of water molecules, producing more hydrogen and oxygen, further promoting plasma discharge. Oxides undergo melting ejections at high temperatures, encountering rapid solidification and recrystallization in contact with the cold electrolyte, depositing on the coating surface. A study [28] classified discharges into types a, b, and c, representing surface, internal, and intermediate discharges in coatings, leading to inward/outward growth of the coating. In this process, numerous white sparks scatter randomly and flicker on the workpiece surface [29]. As the discharge intensifies, the voltage increase rate slows down. With the melting and solidification of oxides, the thickness of coatings rapidly

increases, and gas release and breakdown discharge generate pores. The number of sparks decreases, and the color changes from white to yellow. This marks the transition to the micro-arc discharge stage, a crucial phase in coating growth. As the reaction continues, the voltage stabilizes, entering the strong arc discharge stage. The spark discharge diameter gradually increases, turning orange-red, accompanied by a sharp noise. Intense discharge can cause spattering of coating materials and localized severe ablation characteristics.

Stress-induced cracking cannot be avoided during the rapid solidification process in contact with the cold electrolyte [30]. The resulting coating usually consists of a thinner internal dense layer and a thicker external porous layer, with thickness ranging from 1 to 100  $\mu\text{m}$  [31]. To produce high-quality coatings, precise control of MAO process parameters is crucial, mainly including electrolytes, electrical parameters, and substrates.

## 2.2. Electrolyte

An electrolyte plays a pivotal role in the quality of MAO coatings. It directly influences the composition of coatings and exerts a significant impact on their growth mechanisms [31]. In the realm of MAO, electrolyte systems are traditionally classified by the anion type employed, including phosphate, silicate, borate, and aluminate. In recent years, organic phytic acid has gained recognition as an electrolyte for the MAO of biomedical alloys. Earlier practices involved acidic electrolytes [27], but recent mainstream electrolytes are typically alkaline with an ideal pH of around 13 [11]. The concentration, pH, electrical conductivity, additives, and temperature variations all influence coating formation.

In terms of electrolyte types, silicate and phosphate demonstrate better biocompatibility because Si and P elements promote osteogenesis [32]. When examining coating characteristics under similar conditions, it is observed that in the silicate electrolyte system, coatings grow more rapidly and to a greater thickness compared to other electrolyte systems. These coatings also exhibit increased roughness but relatively weaker adhesion to the metal substrates [33]. Consequently, such coatings often possess inferior wear resistance and corrosion resistance. The resulting bioceramic coatings primarily consist of rutile, anatase, and amorphous silica phases. In the phosphate electrolyte system, MAO coatings tend to be thinner but more compact, with lower roughness. They feature uniform, micrometer-sized pores, and exhibit strong adhesion to the substrate. These coatings consist primarily of anatase and rutile phases, providing excellent corrosion and wear resistance [30,34]. Silicate results in outward coating growth with poor adhesion due to oxide deposition, while phosphate promotes inward growth with strong adhesion linked to substrate oxidation. Combining silicate and phosphate achieves a balanced effect. The addition of calcium to the phosphate electrolyte can induce the formation of bone-like hydroxyapatite (HA), a biologically active material [32].

Due to the susceptibility of borates to hydrolysis, their solutions exhibit higher alkalinity and electrical conductivity. In the sodium tetraborate electrolyte, surfaces of Ti-based alloys undergo more intense discharges, resulting in the formation of a distinctive “channel-like” or “cortex-like” micro/nanostructure in the coatings (Figure 3). These coatings exhibit enhanced hydrophilicity and osseointegration. They are primarily composed of anatase, rutile  $\text{TiO}_2$ , and amorphous boron oxide [35]. Wang et al. [36] used sodium tetraborate to create a micro/nanoscale porous structure on the surface of a Ti-20Zr-10Nb-4Ta alloy. Results indicated that discharges in sodium tetraborate electrolytes lasted longer, compared to phosphate electrolytes, resulting in a larger pore size and higher porosity in the coatings.

When utilizing aluminate electrolytes, the coatings tend to precipitate aluminum oxide (or crystalline aluminum titanate,  $\text{TiAl}_2\text{O}_5$ ), which provides higher hardness and stability. Consequently, these coatings often display excellent resistance to wear and corrosion [37,38]. Jiang et al. [39] employed phosphate, silicate, and aluminate electrolytes to prepare MAO coatings. They found that coatings produced in aluminate electrolytes had the densest structure. It is imperative to acknowledge that aluminate, which exhibits relatively poor stability, is susceptible to hydrolysis, leading to the formation of aluminum

hydroxide. The presence of aluminum ions may potentially have detrimental effects on the human body. Consequently, the use of aluminate electrolytes in surface modification for biomedical metals has seen a gradual decline. In recent years, organic phytic acid has begun to find applications in the electrolytes of MAO [40,41]. It is an organic molecule rich in phosphorus elements, resulting in MAO films composed of anatase, rutile, and  $Ti_2O_7$ . It imparts outstanding biocompatibility to the coatings.

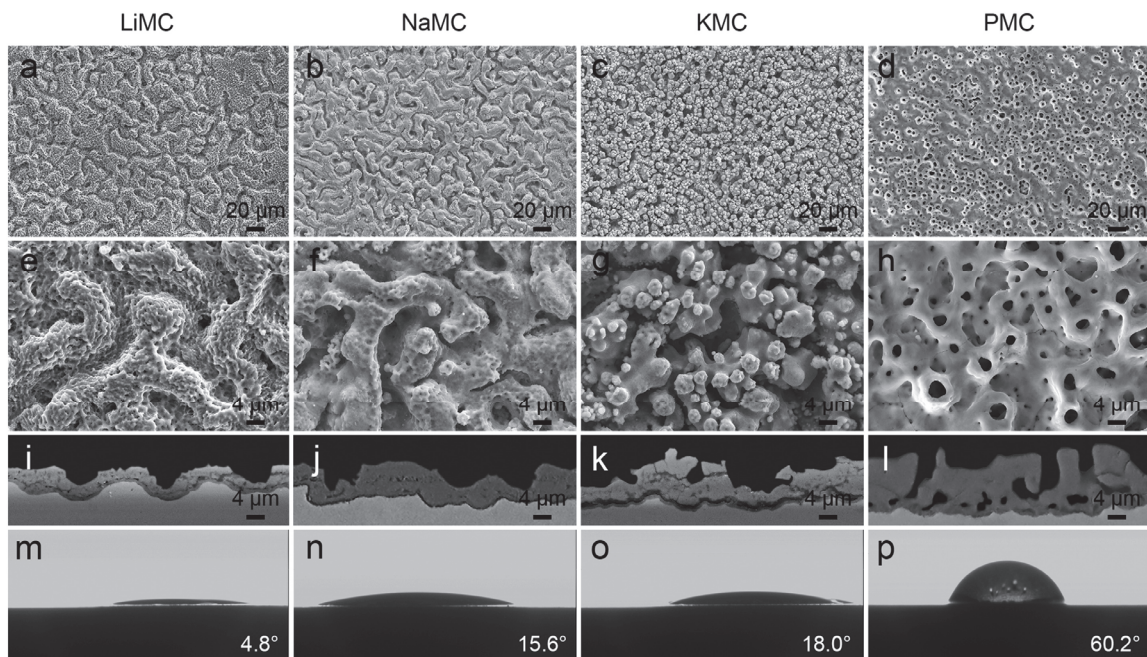


**Figure 3.** The electrolytes used on the surface SEM (a–d) are  $Li_2B_4O_7$ ,  $Na_2B_4O_7$ ,  $K_2B_4O_7$ , and  $Na_2HPO_4$ , respectively. From top to bottom are the corresponding enlarged view (e–h), the cross-sectional view (i–l), and the water contact angle (m–p). LiMC, NaMC, and KMC are “cortex-like”, and PMC is “volcanic crater-like” [35].

The anions in the electrolyte are involved in the discharge and coating formation processes, while cations typically influence the conductivity through concentration [42,43]. Conductivity is generally in the range of 5–100 mS/cm for the MAO electrolyte [41]. During the process, the conductivity of the electrolyte also changes, and the aging of the electrolyte is a noteworthy issue [44]. The conductivity is critical, influencing current and voltage within the narrow pores, thereby affecting the initiation of plasma discharge [27]. In the same anion electrolyte system, increasing conductivity leads to thicker coatings and reduced defects [45].

Currently, the incorporation of nano- and micro-particles into coatings is recognized as a primary approach for enhancing coating properties and expanding the scope of their chemical composition [46]. So far, various nanoparticles (NPs) (5–100 nm) and microparticles (0.18–44  $\mu\text{m}$ ) have been employed. These enhancements encompass a wide range of properties, including corrosion resistance, mechanical strength, tribological performance, and biocompatibility. For instance, the incorporation of graphene oxide (GO),  $TiO_2$ , and  $ZrO_2$  enhances the corrosion resistance and tribological characteristics of coatings, while the inclusion of HA improves the biocompatibility [47]. In terms of composition, some elements are beneficial for improving the biological activity of the material and further enhancing the osseointegration, such as P [48], Si [49], Ca [50], Zr [6], and Sr [32]. The addition of Ag, Cu, and Zn imparts antibacterial properties to the coatings [51]. Incorporating particles into coatings is complex due to their limited solubility in aqueous solutions. These particles may remain unchanged in size and shape or melt during micro-discharge, influencing the composition, microstructure, and other properties of coatings. Key factors

affecting these reactions at the solid–liquid interface include zeta potential, melting point, and particle size [22].

Zeta potential signifies the electrical charge at the particle–fluid interface, with high, negative zeta potential being favorable in electrolytes for stability, resisting agglomeration, and settling [15]. Adjusting the pH of the electrolyte can shift the zeta potential toward negativity. By measuring the zeta potential, Necula et al. [52] established optimal conditions for Ag incorporation in the Keronite electrolyte. Melting point and particle size are two other critical factors affecting incorporation, because of the elevated local temperatures during the MAO treatment ( $\sim 2700$  °C) [53]. Particles with high melting points, such as  $\text{CeO}_2$  and  $\text{SiC}$ , tend to remain inert or partially reactive regardless of their size. On the other hand, particles with lower melting points are more prone to reactive incorporation, resulting in mixed-oxide coatings within the discharge channels during the MAO process. As an example,  $\text{SiO}_2$  particles with a low melting point have been successfully incorporated into MAO coatings. Nanometric particles (around 12 nm) showed active integration, while micrometric particles (1–5  $\mu\text{m}$ ) remained inert [54]. To mitigate additive agglomeration, various strategies are available, including the utilization of chelating agents and organic acids, such as nitrilotriacetic acid ( $\text{C}_6\text{H}_9\text{NO}_6$ ), phosphoric acid ( $\text{H}_3\text{PO}_4$ ), phytic acid ( $\text{C}_6\text{H}_{18}\text{O}_{24}\text{P}_6$ ), and disodium EDTA ( $\text{Na}_2\text{EDAT}\cdot 2\text{H}_2\text{O}$ ). These approaches help create stable and chemically compatible solutions or suspensions [55].

Electrolyte temperature significantly impacts the discharge. There is a non-linear relationship between temperature and coating thickness. Initially, a higher temperature improves corrosion and wear resistance, peaking at 40 °C, but then it declines. Rapid temperature changes in the electrolyte pose challenges to process stability [56]. Electrolyte temperature fluctuations impact the properties of MAO coatings. Higher temperatures can lead to excessive discharging, causing uneven surface topography in the coating [11]. Coatings produced at 278 K have lower porosity than those at higher temperatures due to larger pores and increased pore density, resulting in reduced adhesion to substrates [57]. To obtain high-quality coatings, it is advisable to use a cooling system to keep the electrolyte temperature around 20 °C, with a maximum not exceeding 40 °C [58].

### 2.3. Electrical Parameters

In the MAO process, the performance of the coating is influenced not only by the electrolyte but also by various electrical parameters, including processing time, current mode, current density, and frequency.

In the standard power mode of the MAO process, different current modes can be employed, including direct current (DC) and alternating current (AC). Currently, the pulsed current is also widely used in MAO treatment, including both DC pulse power and AC pulse power, whether a unipolar or bipolar pulse [59]. The DC mode results in slower oxide growth and increased porosity, though it offers less control. Implementing pulsed DC may improve control over discharge duration and reduce energy consumption [60]. Compared to DC power, AC power can swiftly mitigate electrode polarization by intermittently interrupting the electric arc. It provides increased flexibility, improves process control efficiency, and enhances coating quality. Currently, the use of AC-pulsed bipolar MAO power sources is widespread due to their capacity to produce superior coatings. These coatings exhibit a greater thickness, higher micro-hardness, and enhanced adhesion to substrates [61]. This effectiveness is attributed to their ability to mitigate the impact of high-intensity plasma discharges and reduce the occurrence of high-temperature spikes [62]. In different power modes, constant current and constant voltage modes can be employed. A work [63] demonstrates that, when using the constant direct current mode, extending the duration at a low current density (2  $\text{A}/\text{dm}^2$ ) helps prolong the micro-arc phase and results in the formation of a porous layer with fewer internal defects. The compact internal structure enhances the hardness and corrosion resistance. Conversely, with higher current density, the discharge enters the large arc phase earlier, leading to an increase in internal defects and a decrease in adhesion. Seo et al. [64] treated the surfaces of CP-Ti and Ti-6Al-4V

ELI discs under pulsed DC with constant voltage conditions. Increasing voltage led to a larger grain size and surface pore size, and more rutile content, while anatase content decreased. A high voltage caused surface cracking. Both constant current and constant voltage modes have pros and cons. A constant current ensures uniform arc discharges but can generate excess heat, affecting coating uniformity. A constant voltage allows better control of arc discharges and reduces thermal effects, though it may slightly compromise coating uniformity.

Both unipolar and bipolar pulse modes introduce variable parameters like frequency, duty cycle, and anode-to-cathode current ratio, necessitating a deeper understanding of their impact on coatings. Previous research indicates that frequency plays a crucial role in coating performance. Lower frequencies result in rougher coatings with larger pores, making AC pulses more effective than DC pulses for coating formation. Higher frequencies lead to coatings with a higher density of finer pores [65]. Wang et al. [66] created Ca- and P-containing MAO films on Ti substrates at frequencies from 100 to 5000 Hz. Higher frequencies decrease crystallinity but increase Ca and P content. Films at higher frequencies have smaller pores on larger pore walls, improving film wettability.

Maintaining a constant voltage and frequency, an increased duty cycle lengthens the discharge period in a single-polarity pulse, resulting in thicker coatings, additional pores, and greater surface roughness [67,68]. However, excessively high duty cycles can damage the coating. Babaei et al. [69] prepared TiO<sub>2</sub>-ZrO<sub>2</sub> composite coatings on CP-Ti, finding that different micro-discharge states influence the performance of coatings prepared under varying duty cycles. Higher duty cycles lead to an increased coating thickness and greater surface roughness. Pavarini et al. [70] created Cu and Zn co-doped MAO coatings with antimicrobial and osteogenic properties using pulsed DC in a sodium tetraborate electrolyte system. Higher frequencies (800 Hz) produced thinner, less uniform, and less porous coatings with smaller pores. Similar effects occurred with lower duty cycles (10%). Increasing the duty cycle and reducing the frequency resulted in a higher proportion of rutile in the oxide composition.

Pulsed bipolar MAO power sources are currently widely used for increasing coating thickness and ensuring strong adhesion to substrates. If the cathodic pulse is increased, or the ratio of cathodic current to anodic current ( $I_c/I_a$ ) is increased [71], the residual discharge channels decrease, leading to higher coating density though the specific cathodic discharge mechanism remains to be elucidated [72]. Sun et al. [73] used  $\alpha$ -Al<sub>2</sub>O<sub>3</sub> to create a hard ceramic coating on a Ti-6Al-4V alloy. Lower  $I_c/I_a$  ratios led to thicker coatings, indicating higher anodic current density promotes growth. Conversely, higher  $I_c/I_a$  ratios resulted in thicker dense layers, reduced surface roughness, and increased coating hardness.

The duration of the MAO process is critical. In general, as the time is prolonged, the discharges become more intense, the number of micro-pores decreases, their size increases, and the coating thickness increases [29]. Wu et al. [74] found that as the processing time extended, the coating exhibited the mentioned phenomena, but some central pore sections closed and exhibited shrinkage. This is because the molten oxides flowing at the discharge locations sealed the pores.

MAO is an energy-intensive process, with actions like increasing current density, elevating voltage, reducing frequency, extending duty cycle, and prolonging processing time all equivalently increasing energy input over time [22]. Higher instant energy levels intensify discharges, resulting in more micro-pores in the coating, leading to increased roughness and a higher rutile phase content. Moderate energy increases create a complex porous structure, but excessive energy input may harm the coating. This can be addressed by raising the cathodic current, leading to the adoption of alternating current and pulse power sources. There is ongoing research into soft spark discharge states, which emit less heat, reducing excessive and damaging discharges [75]. This fosters uniform electrode reactions, lowers energy consumption, and promotes coatings rich in crystalline phases. However, soft spark discharge reduces surface porosity and roughness, and its potential benefits for enhancing bioactivity require further investigation [76].

The decision on when to use each mode or parameter requires a comprehensive evaluation of the desired coating characteristics, process control requirements, material and shape of the workpiece, energy efficiency, and application environment. The optimal choice often involves experimentation and optimization to meet specific project requirements.

#### 2.4. Substrate

The composition, topography, and properties of the coating are significantly influenced by the composition and structure of the metal substrate. Additionally, pre-treatments conducted before MAO can also impact the grain size and surface topography of the substrate, subsequently affecting the topography and quality of the MAO coatings. Currently, commonly used Ti and its alloys in clinical applications include CP-Ti, Ti-6Al-4V, and Ti-6Al-7Nb, which have been the focus of substantial surface modification research. However, the rise of  $\beta$ -Ti alloys for hard tissue implants, owing to their superior biocompatibility and reduced elastic modulus for reduced “stress shielding”, has led to an increasing emphasis [77].

Chen et al. [78] utilized  $\text{NaH}_2\text{PO}_4$  as an electrolyte for MAO treatment of a Ti-13Cr-3Al-1Fe alloy and found that the response to electrical parameters is akin to the trend observed in  $\alpha$  and  $\alpha + \beta$  alloys. Cimenoglu et al. [79] investigated MAO-treated Ti-6Al-4V and Ti-6Al-7Nb alloys using the same parameters. Both exhibited a similar thickness of approximately 10  $\mu\text{m}$ . However, the coating on Ti-6Al-4V contained HA precipitates, while the Ti-6Al-7Nb coating had granular oxides with calcium titanate. In the study by Wang [80], an MAO process was employed under identical conditions on pure Ti, Ti-6Al-4V, and Ti-35Nb-2Ta-3Zr substrates. The results revealed distinct topographies of coatings on the three different substrates (Figure 4). Notably, the Ti-35Nb-2Ta-3Zr surface exhibited a porous topography with increased crystalline anatase content, which effectively enhanced the deposition of HA. Additionally, corrosion resistance and hydrophilicity tests indicated superior performance for the coating.

Material pretreatment processes alter the surface topography and grain size, consequently affecting the properties of coatings. Physical methods like surface shot peening, severe plastic deformation (SPD), and laser surface remelting (LSR) treatments are primarily considered. High-energy shot peening (HESP) enhances the wettability and surface-free energy of MAO coatings, significantly improving bioactivity on Ti-based substrates [49]. Equal channel angular pressing (ECAP) on Ti surfaces results in ultrafine grains and increases the thickness and porosity of MAO coatings. Furthermore, the dense microstructure enhances the corrosion resistance of MAO coatings [14]. LSR pretreatment, in combination with MAO processing, modulates coating topography. Increasing the energy density of LSR pretreatment initially decreases surface roughness before subsequently increasing it. This enhances coating densification and bond strength with the substrate, thereby improving corrosion resistance [81]. In conclusion, appropriate pretreatment can enhance the performance of MAO coatings. Additionally, subjecting alloy substrates to solution treatment, quenching, and varying aging treatments before MAO results in changes in coating pore size, surface roughness, and porosity with increasing aging time. This is likely due to enhanced substrate electrical conductivity from the aging treatment, leading to higher current density during the MAO process [82]. The comprehensive effects of electrolytes, electrical parameters, and substrates can be found in Table 2.

At present, additive manufacturing, also known as 3D printing, is progressively emerging as the preferred method for custom orthopedic implants. It allows the production of complex structures that surpass the capabilities of traditional techniques, all while preserving the physical and chemical advantages inherent to Ti and its alloys. Implants produced through this method offer an elevated level of patient-specific adaptability. In the context of employing MAO to enhance the surface bioactivity of 3D-printing Ti alloy implants, more detailed comparisons are available in other comprehensive reviews [2,83].

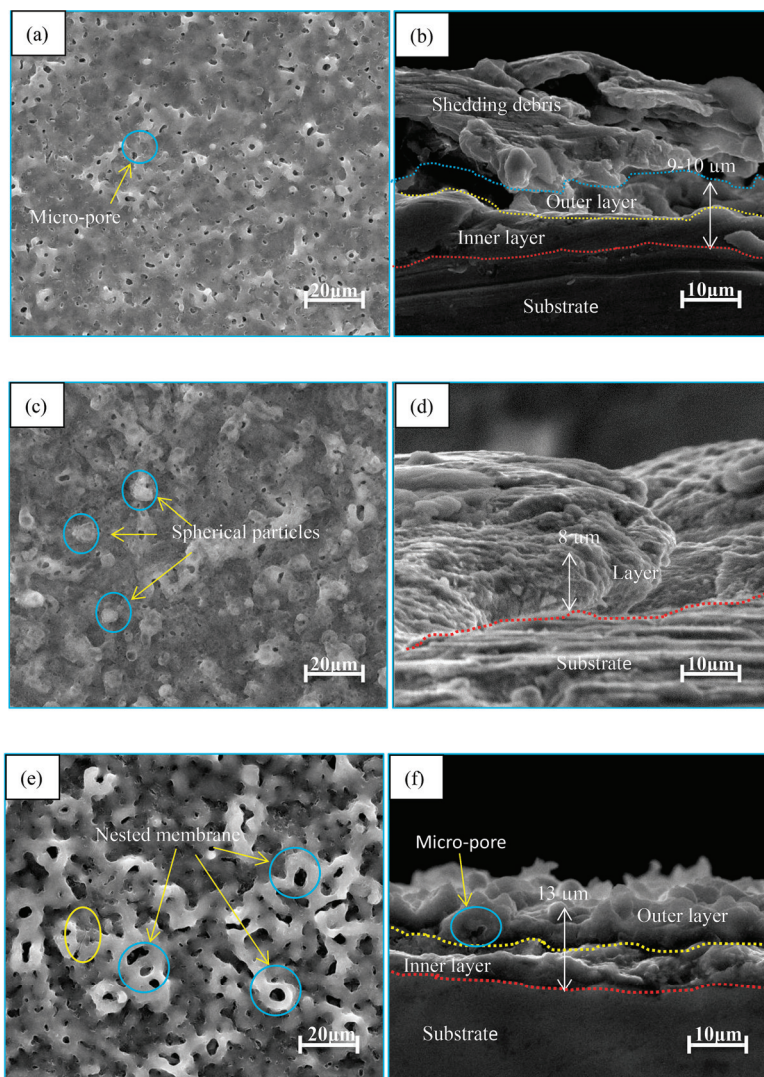


**Figure 4.** Surface and cross-sectional SEM of MAO coatings on three substrates (Ti: (a,b); Ti-6Al-4V: (c,d); Ti-35Nb-2Ta-3Zr: (e,f)) under the same conditions [80].

Obtaining the appropriate parameters requires multiple experiments. Researchers can start by choosing an experimentally suitable parameter range based on existing literature. They should then refine these parameters based on observed multifaceted effects of parameter changes on the coating. Due to the absence of a unified model, conducting multiple experiments is essential. The alteration of a single parameter in the MAO process can result in modifications across multiple coating properties, owing to the intricate interplay of various factors. Consequently, adjusting a specific parameter may necessitate the simultaneous coordination of other parameters to uphold the desired coating quality. This intricate balance poses a significant challenge in the production process of MAO coatings. Different applications of implants have varying requirements for the surface coating, leading to variations in the parameters used. Coating performances prepared under the same parameters with different devices may exhibit slight differences, making it challenging to define optimal parameters [22]. The parameters influencing the coatings are comprehensively addressed here to serve as a reference for subsequent researchers. After determining the parameters, real-time online monitoring systems can be introduced to track key parameters such as current, voltage, and electrolyte concentration. Through feedback control, maintaining parameters within a stable range ensures consistent and reproducible coating performance.

**Table 2.** Factors affecting coating performance.

Number	Substrate	Electrolyte	Electrical Regimes	Conclusion	Reference
1	Ti	Na <sub>3</sub> PO <sub>4</sub> , Na <sub>2</sub> SiO <sub>3</sub> , NaAlO <sub>2</sub> , composite electrolytes (Na <sub>3</sub> PO <sub>4</sub> + Na <sub>2</sub> SiO <sub>3</sub> + NaAlO <sub>2</sub> )	0.1–0.3 A/cm <sup>2</sup> current densities	The pores of coatings made in Na <sub>3</sub> PO <sub>4</sub> and composite electrolytes are smaller and more uniform than those in other electrolytes.	[39]
2	Ti	KH <sub>2</sub> PO <sub>4</sub> , Ca(OH) <sub>2</sub> or Ca(HCOO) <sub>2</sub> , Na <sub>2</sub> (EDTA)	Three different fixed set current densities: 50, 100, and 150 mA/cm <sup>2</sup>	Porous coating promotes apatite formation and resists corrosion.	[55]
3	Ti	(CH <sub>3</sub> COO) <sub>2</sub> Ca·H <sub>2</sub> O and NaH <sub>2</sub> PO <sub>4</sub> ·2H <sub>2</sub> O	Different voltages, currents, durations	HA-containing flower-like Structure Coatings have good biological activity.	[84]
4	Ti	Ca(OOCCH <sub>3</sub> ) <sub>2</sub> , Ca(H <sub>2</sub> PO <sub>4</sub> ) <sub>2</sub> , and Na <sub>2</sub> (EDTA)	Pulsed DC, duty cycle at 30%, 450 V, 5 min, 100–5000 Hz	Frequency affects the crystallinity, composition, topography, and wetting ability of the oxide film.	[66]
5	Ti	NaH <sub>2</sub> PO <sub>4</sub> , Na <sub>2</sub> ZrO <sub>3</sub> , and Na <sub>2</sub> SiO <sub>3</sub> of different concentrations	Pulsed DC, 500 V, 1000 Hz, different duty cycle	Concentration and duty cycle affect topography and photocatalytic activity.	[69]
6	Ti (high-energy shot peening, HESP)	C <sub>3</sub> H <sub>7</sub> Na <sub>2</sub> O <sub>6</sub> P·5H <sub>2</sub> O, Ca(CH <sub>3</sub> COO) <sub>2</sub> ·H <sub>2</sub> O, Na <sub>2</sub> SiO <sub>3</sub> ·9H <sub>2</sub> O, and Cu(CH <sub>3</sub> COO) <sub>2</sub> ·H <sub>2</sub> O	480 V, 5 min	Porous antimicrobial coatings are prepared.	[49]
7	Ti (equal channel angular pressing, ECAP)	NaH <sub>2</sub> PO <sub>2</sub> and (CH <sub>3</sub> COO) <sub>2</sub> Ca	350 mA/cm <sup>2</sup> , 8 min	Porous microcrack coatings are prepared.	[14]
8	Ti	K <sub>3</sub> PO <sub>4</sub> and KOH	Constant current density of 100 mA/cm <sup>2</sup> , frequency of 6 kHz, duty cycle at 50%, 6 min	Coating with pancake-like topography has corrosion resistance.	[46]
9	Ti	Different concentrations of KOH	160 V, 1 min	1 M KOH, Ca/P = 1.69. The higher the concentration of KOH, the stronger the corrosion resistance of the coating.	[42]
10	Ti	Na <sub>2</sub> B <sub>4</sub> O <sub>7</sub> ·10H <sub>2</sub> O, Na <sub>2</sub> O <sub>2</sub> SiO <sub>2</sub> ·2H <sub>2</sub> O, Cu(CH <sub>3</sub> COO) <sub>2</sub> , Zn(CH <sub>3</sub> COO) <sub>2</sub> , NaOH	AC, 300 V, different frequencies, and duty cycles	Duty cycle and frequency affect coating thickness, surface uniformity, and porosity.	[70]
11	Ti	Na <sub>2</sub> B <sub>4</sub> O <sub>7</sub> ·10H <sub>2</sub> O	Pulsed DC, 465 V, 600 Hz, and 9%	“Cortex-like” micro/nanostructured coating has improved biocompatibility.	[35]
12	Ti, Nb, Mg, Al, Zr, Ta	NaOH and Na <sub>2</sub> SiO <sub>3</sub>	Unipolar positive or bipolar working pulse	Soft sparks are more obvious on the surfaces of Mg, Al, Zr, and Ta, while Ti and Nb have only a small amount of spark softening.	[85]

Table 2. Cont.

Number	Substrate	Electrolyte	Electrical Regimes	Conclusion	Reference
13	Ti-6Al-4V	Ca(CH <sub>3</sub> COO) <sub>2</sub> , Ca(C <sub>3</sub> H <sub>7</sub> O <sub>6</sub> P), Mn(CH <sub>3</sub> COO) <sub>2</sub> ·4H <sub>2</sub> O, Mg(CH <sub>3</sub> COO) <sub>2</sub> ·4H <sub>2</sub> O, Sr(CH <sub>3</sub> COO) <sub>2</sub> ·0.5H <sub>2</sub> O, Zn(CH <sub>3</sub> COO) <sub>2</sub> , Na <sub>2</sub> SiO <sub>3</sub>	Pulsed DC, 280 V, 3 min	The coating surface is soaked in simulated body fluid (SBF) to generate bone-like apatite.	[32]
14	Ti-6Al-4V	Na <sub>3</sub> PO <sub>4</sub> , NaOH, Na <sub>2</sub> SiO <sub>3</sub>	Fixed DC voltage (270 V), 5 min	Coatings prepared in silicate-based electrolytes achieved the most uniform structure, with lower porosity.	[33]
15	Ti-6Al-4V	NaAlO <sub>2</sub> , NaF, KOH, CuSO <sub>4</sub> , Na <sub>2</sub> (EDTA)	Constant current of 2 A/cm <sup>2</sup>	It is porous at about 1 μm. The addition of Cu ions makes the coating uniform and reduces the roughness.	[38]
16	Ti-6Al-4V	Na <sub>2</sub> HPO <sub>4</sub> , HA microns, and NPs	Constant potential of 250 V and then pulse unipolar or pulse bipolar constant current of 300 mA/cm <sup>2</sup>	Micron and nanoscale HA have different effects on the microstructure of the coating, but both improve the scratch resistance and bioactivity of the coating.	[86]
17	Ti-6Al-4V	Na <sub>2</sub> AlO <sub>2</sub> , Na <sub>3</sub> PO <sub>4</sub>	Bipolar pulse	With an appropriate increase in cathodic pulses, the coating density increases.	[72]
18	Ti-6Al-4V	Na <sub>2</sub> AlO <sub>2</sub> , Na <sub>3</sub> PO <sub>4</sub>	Bipolar pulse	As the I <sub>c</sub> /I <sub>a</sub> ratio increases, the density and hardness of the coating increase, and the roughness decreases.	[73]
19	Ti-6Al-4V	Na <sub>2</sub> SiO <sub>3</sub> , NaH <sub>2</sub> PO <sub>2</sub> , Na <sub>2</sub> MoO <sub>4</sub>	520 V, 50 Hz, 10%, 30 min	Corrosion resistance is improved.	[81]
20	Ti-20Zr-10Nb-4Ta	Na <sub>2</sub> B <sub>4</sub> O <sub>7</sub> ·10H <sub>2</sub> O	DC power, 465 V, 600 Hz, and 9%	Hierarchical porous coatings have good biocompatibility.	[36]
21	Ti-15V-3Al-3Cr- 3Sn	Different electrolyte temperatures of 278–313 K, K <sub>2</sub> Al <sub>2</sub> O <sub>4</sub> , Na <sub>3</sub> PO <sub>4</sub> , NaOH	square waveform with 2.0 kA/m <sup>2</sup> and −1.0 kA/m <sup>2</sup> at 100 Hz	Wear resistance is improved at low temperatures.	[87]
22	Ti-13Cr-3Al-1Fe	NaH <sub>2</sub> PO <sub>4</sub> , pH = 9.2	Different voltages and durations	As the discharge voltage and treatment time increase, the oxide layer thickens, and the pore size and surface roughness increase.	[78]
23	Ti6Al4V and Ti6Al7Nb	(CH <sub>3</sub> COO) <sub>2</sub> Ca·H <sub>2</sub> O and Na <sub>3</sub> PO <sub>4</sub>	Bipolar power, +500 V and −83 V, 5 min	Two alloy coatings have different characteristics under the same conditions.	[79]
24	Ti-29Nb-13Ta- 4.6Zr (hot forge)	CaOH, Na <sub>3</sub> PO <sub>4</sub> ·12H <sub>2</sub> O, pH = 12.03, conductivity = 13.20 mS/cm	AC bipolar, different frequencies, and duty cycles	Frequency and duty cycle affect form and thickness, which in turn affects corrosion resistance.	[68]
25	Ti-25Ta-10Zr- 15Nb and Ti-25Ta- 20Zr30Nb	Ca(C <sub>2</sub> H <sub>3</sub> O <sub>2</sub> ) <sub>2</sub> , Mg(C <sub>2</sub> H <sub>3</sub> O <sub>2</sub> ) <sub>2</sub> , Glycerophosphate	300 V, 2.5 A, 1 min	Both alloys exhibit porous structures with different pore sizes.	[88]

Table 2. Cont.

Number	Substrate	Electrolyte	Electrical Regimes	Conclusion	Reference
26	Ti, Ti-6Al-4V, and Ti-15V-3Al-3Cr-3Sn	$K_2Al_2O_4$ , $Na_3PO_4$ , NaOH	Constant AC of $1.5 \text{ kA/m}^2$ up to a maximum peak voltage of 400 V	The coating has excellent wear resistance.	[57]
27	Ti, Ti-6Al-4V, Ti35Nb-2Ta-3Zr	$Na_2SiO_3 \cdot 9H_2O$ , $(HOCH_2CH_2)_3N$ , pH = 11.5	Voltage of +400 V, -50 V, duty cycle at +16%, -10%, 500 Hz	The coating of Ti-35Nb-2Ta-3Zr is durable and has good hydrophilicity.	[80]

### 3. Surface Biologic Function of MAO

#### 3.1. Osteointegration

When an implant is exposed to the internal environment, it selectively adsorbs various proteins, depending on the physical and chemical characteristics of its surface. Cells initiate their connection with the implant by interacting with these unique proteins [89]. Surface parameters of the implant, including surface topography, chemical composition, and charge, all contribute to regulating specific interactions between cells and biomaterials.

On smooth surfaces, BMSCs are more prone to differentiate into fibroblasts rather than osteoblasts (OBs). Additionally, fibroblasts also adhere more easily to smooth surfaces. On the other hand, bone cells tend to adhere, proliferate, and differentiate more readily on surfaces with rough nanoscale patterns (Figure 5). Surfaces with moderate roughness and porosity provide a larger bonding area and establish a strong mechanical interlock, promoting a more stable implant–bone integration. Osteoblasts cultured on such rough surfaces demonstrate increased collagen production and enhanced calcification processes [90,91].

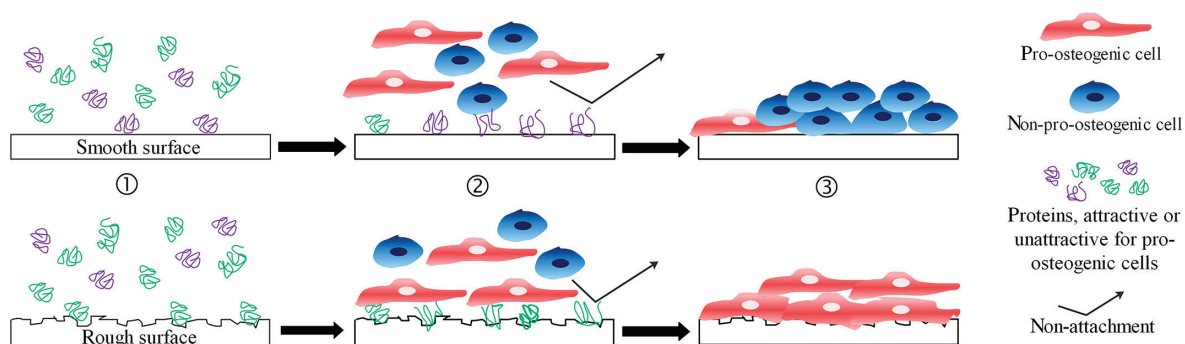


**Figure 5.** A diagram illustrates the interaction between cells and materials on smooth or textured surfaces; ① surface structure influences protein adsorption, ② proteins impact cell attraction, and attachment, and ③ proliferation, differentiation, and maturation [90].

The ideal implant surface should mimic natural bone, featuring mineralized large pores and nanoscale components. Hierarchical structure, from the nanoscale (collagen molecules and minerals) to microscale (bone units), guides cells' behavior [92]. Research suggests that multiscale topographical features on the implant surface are linked to increased osteoblast differentiation [93].

MAO can modify the surfaces of metal implants to give them specific characteristics. It can create various topological structures on the substrate, and incorporate substances for angiogenesis or osteointegration into the coatings.

It is widely acknowledged that a rough, porous surface contributes to improved osteogenic activity. Nevertheless, there is currently no consensus regarding the optimal specific values for roughness, pore size, and pore geometry [94]. Yamasaki et al. [95]

highlighted that the interconnected micropores in the range of 2–10  $\mu\text{m}$  can bestow osteoinductive properties upon the scaffold. Shalabi et al. [96] found that bone tissue bonded effectively to rough Ti surfaces within the 1 to 100  $\mu\text{m}$  range, with higher surface roughness providing a greater surface area. Currently, the surface topographies generated through MAO exhibit diversity, encompassing porous [38], hierarchical porous [97,98], and “cortex-like” (or “worm-like”) [35] structures. Li et al. [98] employed a two-step MAO process to create pores of different sizes. In the first step, large pores (100–300  $\mu\text{m}$ ) were generated using  $\text{NaNO}_3$  and  $\text{NaOH}$  electrolytes. Subsequently, a second MAO treatment was conducted using a  $\text{Na}_2\text{B}_4\text{O}_7$  electrolyte, resulting in the formation of micro-pores (3–10  $\mu\text{m}$ ) as well as sub-micron/nano-pores (80–200 nm). This innovative tri-level structure not only enhances hydrophilicity but also holds the potential to improve the adhesion of osteoblasts to the implant and enhance implant fixation. Moreover, they refined the electrolyte composition by introducing CaO and SrO into  $\text{Na}_2\text{B}_4\text{O}_7$  [46]. Following a one-step MAO treatment, both Ca and Sr were integrated into the  $\text{TiO}_2$  hierarchical porous coating. This hierarchical structure exhibits a high level of porosity and superhydrophilicity, and the incorporated Ca and Sr have shown superior efficacy in promoting the proliferation of human-bone-marrow-derived mesenchymal stem cells (hBMSCs). This highlights that, beyond surface topography, the chemical composition of MAO coatings plays a crucial role in influencing the biological activity of the coatings.

Currently, a highly researched area revolves around the development of biomimetic calcium phosphate (CaP) coatings on surfaces using electrolytes containing both Ca and P. Researchers are dedicated to optimizing the parameters that influence coating formation during the MAO process, with a specific emphasis on the composition of the electrolyte. They aim to achieve a Ca/P ratio that closely matches the natural bone value of 1.67 [48].

Typically, immersion in SBF is employed to assess the ability to form HA on its surface, thus quantifying its bioactivity. The general formula of HA is  $\text{Ca}_{10}(\text{PO}_4)_6(\text{OH})_2$ . Herein,  $\text{Ca}^{2+}$  can be completely or partially substituted by  $\text{Sr}^{2+}$ ,  $\text{Si}^{4+}$ ,  $\text{Mg}^{2+}$ ,  $\text{Mn}^{2+}$ , and  $\text{Zn}^{2+}$ , and  $\text{OH}^-$  can be replaced by halide ions  $\text{F}^-$ ,  $\text{Cl}^-$ , and  $\text{Br}^-$ . Therefore, in addition to Ca and P, adding Si, Sr, Mn, Zn, and other elements to the electrolyte may also improve the osteogenic activity of the surface. Plekhova et al. [18] assessed the morphological and functional status of bone-marrow-derived mesenchymal stem cells (BMSCs) cultured on Ti-CaP coatings formed by MAO. There were no cytotoxic effects observed on the cultured cells. Notably, the high expression of receptors (CD90, CD29, and CD106) along with enhanced synthesis of osteocalcin and osteopontin, as well as observable changes in the surface structure of BMSCs adhered to the samples, collectively confirmed the osteoinductive properties of the calcium phosphate MAO coating. Park et al. [99] utilized Ti-6Al-4V ELI discs and subjected them to treatment with pulsed DC power for 3 min at 280 V in electrolytes containing bioactive ions such as Si, Zn, Mg, Mn, Sr, Ca, and P. The energy-dispersive X-ray spectroscopy (EDS) results revealed that the  $(\text{Ca} + \text{Mg} + \text{Si} + \text{Mn} + \text{Zn} + \text{Sr})/\text{P}$  ratio was approximately 1.67. Some researchers have directly added HA to the electrolyte [100,101]. Zhou et al. [101] dispersed hydroxyapatite nanotubes (HNTs) in the MAO electrolyte and embedded HNTs into the Ti surface. When comparing three types of surfaces, Ti, MAO, and MAO-HNT, the HNT group outperformed the Ti and MAO groups in terms of angiogenesis, as evidenced by enhanced cell migration, tube formation, and vascular gene expression in HUVECs. Furthermore, concerning osteogenesis, the HNT group exhibited the highest levels of alkaline phosphatase (ALP) activity, collagen secretion, mineralized calcium nodules, and osteogenic gene expression in MC3T3-E1 cells, surpassing the other two groups. These findings suggest that HNT specimens can significantly promote angiogenesis and osteogenesis at both the cellular and molecular levels.

A good blood supply is essential for successful osseointegration. Studies have found that adulteration of appropriate amounts of Ca [101], Li [102], Se [103], Sr [104], Si [105], and Zn [106] elements can contribute to angiogenesis. Yu et al. [106] introduced zinc acetate

into the electrolyte to produce coatings enriched with zinc. Co-cultivation of HUVECs with these coatings demonstrated excellent biocompatibility. This study explores the inherent connection between angiogenesis and osteogenesis, presenting evidence that  $Zn^{2+}$  promotes both processes.

MAO is a versatile technique that enhances the hardness, corrosion resistance, wear resistance, and biocompatibility of metal surfaces. This versatility makes it ideal for integration with other technologies to fine-tune surface properties for diverse application needs. The joint application of MAO and other surface modification technologies can incorporate functional elements into the MAO coating, such as hydrothermal treatment (HT) [107,108], dip coating [109,110], radiofrequency magnetron sputtering (RF-MS) [111], etc. Many research groups are exploring post-processing techniques using inorganic compounds to mimic the Ca/P ratio in a natural bone structure for enhanced bioactivity [50].

For instance, Song et al. [107] applied HT in two different solutions after MAO treatment, resulting in the formation of HA with a higher Ca/P ratio than the MAO-treated sample, facilitating the migration of  $Ca^{2+}$  and  $PO_4^{3-}$  ions to the surface. MAO and HT treatments provide binding sites for other functional factors like osteogenic growth factors, and antibacterial and anti-inflammatory substances [112]. In a study [113], MAO was initially used to create a hierarchical micro/nano-topography on a substrate, followed by electrochemical reduction in an alkaline solution. The results demonstrated improved BMSC adhesion, proliferation, and up-regulation of osteogenesis-related gene expression, indicating the potential to enhance osteogenic processes.

Magnetron sputtering, when combined with MAO, deposits metal particles onto coatings, enhancing osteogenesis. Park et al. [114] used RF-MS to create a Mn coating on the MAO-treated Ti-29Nb-xHf alloy, highlighting the potential for introducing metal coatings to boost surface osteogenic properties.

The combination of multiple surface modification techniques offers a broader selection of surface ingredients, including growth factors, hormones, and proteins. Bone morphogenic proteins (BMPs), such as BMP-2 and BMP-7, are pivotal for bone cell proliferation, differentiation, and matrix synthesis. Fibroblast growth factors (FGFs) like FGF-2 and FGF-7 influence bone cell proliferation and differentiation, while insulin-like growth factors (IGFs) like IGF-I and IGF-II promote cell growth and protein synthesis, crucial for bone tissue growth and repair. Vascular Endothelial Growth Factor (VEGF), as a key growth factor, directly stimulates new blood vessel formation. These biological factors are typically incorporated onto material surfaces through gentle methods, such as the dip-coating method [115,116], immersion [110], and chemical deposition [109], to ensure the preservation of their activity.

Teng [117] employed a method combining MAO and Ca, P layers with BMP co-precipitation to treat 3D-printed porous Ti alloy implants, named MAO-CaP-BMP2. The porosity facilitates bone tissue and blood vessel ingrowth. The microporous dioxide layer, created by MAO treatment, serves as nucleation sites for concurrent deposition of the CaP layer and BMP-2. This microstructural arrangement allows the extended, controlled release of BMP-2 over 35 days. The modification of Ti alloy implants with MAO-CaP-BMP2 enhances their osteoinductive and osteoconductive properties, leading to superior osteogenic and angiogenic outcomes.

### 3.2. Antibacterial

Among common orthopedic infections, osteomyelitis stands out, often stemming from pathogens like *Staphylococcus aureus* (*S. aureus*), *Escherichia coli* (*E. coli*), and *Pseudomonas aeruginosa* (*P. aeruginosa*). Symptoms encompass a range of discomforts such as pain, swelling, pus formation, the presence of fistulas and/or sinus tracts, and wound reopening. The approach to treatment depends on various factors including the severity of infection, the responsible pathogen, and the overall health of patients. Treatment varies based on infection severity, pathogen, and patient health, typically involving debridement to remove infected bone tissue and implanted devices. Debridement surgery is complex and requires

an extended recovery period. Dental-implant-associated microbial colonization may give rise to peri-implant mucositis or even peri-implantitis. Key pathogens involved include *Porphyromonas gingivalis* (*P. gingivalis*), *Streptococcus sanguinis* (*S. sanguinis*), *Aggregatibacter actinomycetemcomitans* (*A. actinomycetemcomitans*), etc. Peri-implantitis has a lower incidence compared to peri-implant issues in orthopedic implants, but it still demands attention as it could directly contribute to implant failure [118].

Microbial cells adhering to surfaces can come together to form highly structured microbial communities commonly known as “biofilms”. These biofilms often display drug resistance, complicating infection treatment. The process of biofilm formation involves various stages, including the adsorption of proteins, microbial adhesion, aggregation, biofilm maturation, and the diffusion of biofilm (Figure 6). Proteins adhere to surfaces, facilitating microbial attachment through electrostatic interactions and protein receptor recognition. As attachment progresses, biofilm formation occurs as microorganisms aggregate. Once established, biofilms involve intercellular communication and extracellular polymeric substance (EPS) secretion, transforming into a three-dimensional structure [119].

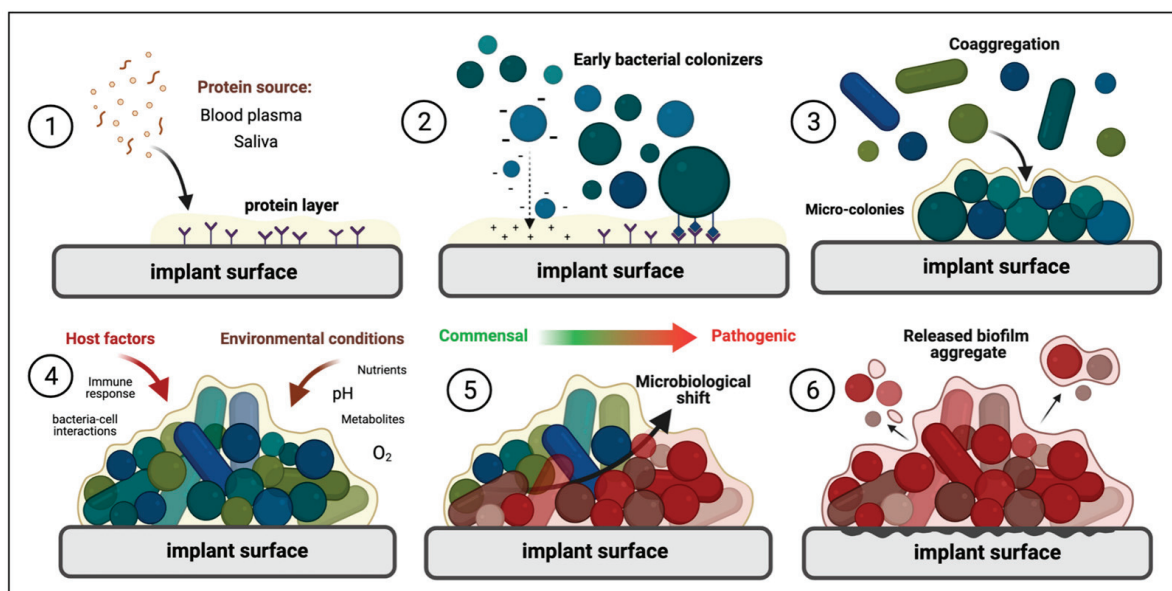


**Figure 6.** Microbial biofilm formation on implant surfaces comprises five key stages: ① Protein adsorption, ② Microbial adhesion, ③ Coaggregation, ④ Mature biofilm, ⑤ and ⑥ Dispersal. This complex process can result in infection, tissue damage, and implant surface degradation [119].

Antimicrobial implant materials must inhibit biofilm formation, particularly in the initial stages. Researchers and clinicians continue to seek effective prevention and treatment of implant-associated infections. In recent years, the development of surface antibacterial methods using MAO has been a research hotspot in preventing and managing biofilm growth on Ti-based implants [120].

Some researchers suggest that MAO-generated anatase TiO<sub>2</sub> structures can reduce bacterial adhesion or confer antibacterial properties. For instance, Alipal et al. [121] found that circular TiO<sub>2</sub> structures on MAO coatings exhibit improved biocompatibility and antibacterial properties compared to needle-like TiO<sub>2</sub>. Similarly, Jia et al. [122] proposed that the structure of TiO<sub>2</sub> layers created by MAO can trap and kill bacteria on implant surfaces. However, conflicting views exist in the literature, with some researchers arguing that rough, porous MAO coatings increase microbial adhesion [123,124], while others contend there is no significant difference compared to untreated Ti [125]. Current research on MAO-based antibacterial coatings mainly focuses on incorporating antibacterial additives to alter surface chemistry and enhance functionality.

The main mechanisms to promote the killing of bacteria on the surface of antimicrobial implants are (i) the contact reaction of bacteria with the surface, causing the destruction of bacterial membranes or inhibiting the synthesis of their membranes; (ii) the gradual release of ions from the coating, resulting in electron transfer and cell membrane destruction; (iii) antimicrobial ions enter microbial cells, interrupt protein synthesis, block Adenosine Triphosphate (ATP) synthesis and deoxyribonucleic acid (DNA) replication, and promote apoptosis; and (iv) generation of ROS, which also induces apoptosis by denaturing proteins and damaging DNA [126]. Costa et al. [119] categorized antimicrobial agents into four primary groups: organic (biopolymers and bioactive agents), inorganic (metallic and semi-metallic elements), drugs (substances with pharmacological action), and biological (growth factors, peptides, and extracellular matrix proteins). Among these additives, people are more interested in inorganic elements, due to their stability and cost-effectiveness. The specific effects of elements on the biological function of the coating are shown in Table 3.

Since 2009, one-step MAO has been employed to create antimicrobial Ti surfaces by binding Ag, Cu, and Zn elements, as summarized in 35 articles by Shimabukuro up to 2020 [51]. The half-maximal inhibitory concentrations (IC<sub>50</sub>) of Ag<sup>+</sup>, Cu<sup>2+</sup>, and Zn<sup>2+</sup> on MC3T3-E1 cells are 2.77, 15.9, and 90.0 μM, respectively [127]. Ag exhibits high toxicity, but controlled dosages do not negatively affect osteoblast activity. Researchers are increasingly interested in incorporating diverse elements (Ag + Cu [23], Ag + Zn [128–131], Cu + Zn [132,133]) into coatings through one- or two-step MAO processes to enhance antimicrobial effects or/and extend the duration of antimicrobial activity. Shimabukuro et al. [134,135] simulated the biodegradation behavior of Ti doped with Ag, Cu, and Zn by MAO soaked in physiological saline for 28 days to study the changes in surface composition and antibacterial effect. After 28 days, the antibacterial effect of the Ag-incorporated samples weakened, the antibacterial effect of Cu was maintained, and the antibacterial effect of Zn enhanced in the later period (Figure 7). In another study, Tsutsumi [136] employed a two-step MAO process to tailor surface coatings with Ag, with or without Zn, to assess the binding and ion release behavior of Ag and Zn in the resulting oxide layer. Over a 6-month immersion period, the release of Ag<sup>+</sup> from the oxide layer indicated early antibacterial performance, while the release of Zn<sup>2+</sup> signified later antibacterial effectiveness.

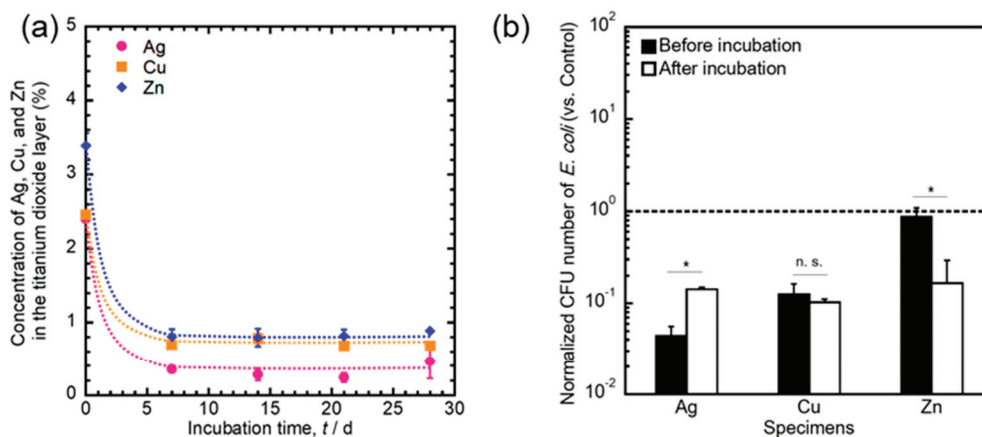


**Figure 7.** The changes in the concentrations of Ag, Cu, and Zn in the oxide layer (a) and their antimicrobial effectiveness (b) after 28 days of cultivation in a saline solution. \*: Significant difference between specimens ( $p < 0.05$ ), n.s.: No significant difference [51].

Research involving Mn on the surface of Ti-based implants shows promise, as it enhances osteoblast activity while also inhibiting the proliferation of Gram-negative *E. coli* and *P. aeruginosa*. Zhao et al. [137] employed MAO to create a Mn-TiO<sub>2</sub> micro-porous coating. Their results revealed that the coating induced *E. coli* cell wall perforation, effectively inhibiting bacterial proliferation. Additionally, Bi compounds have shown

efficacy in treating mucosal and dermal infections and are recognized as antimicrobial additives for calcium phosphate bone cement. Lin et al. [138] used MAO to develop a TiO<sub>2</sub> coating containing the bismuth (Bi) element. The coating with 6.2% Bi displayed good biocompatibility with MG63 cells and demonstrated 1.5 times higher antibacterial efficacy against *A. actinomycetemcomitans* and 1.9 times higher efficacy against methicillin-resistant *Staphylococcus aureus* (MRSA) compared to the control group. MAO technology can also incorporate other non-metallic antibacterial ingredients into the coating, such as Ce [139], Se [103], I [140,141], B [142,143], and F [144–146].

MAO combined with other techniques can produce antimicrobial coatings that enhance effectiveness and minimize cytotoxicity. Arun et al. [111] employed a combination of MAO and RF-MS processes to create dual-phase coatings on Ti-6Al-4V. They conducted MAO in Ca/P electrolytes with varying Ag NP concentrations and applied an HA top layer using the RF-MS process. This approach generated a passivation layer with robust barrier properties. Ag contributed to antibacterial activity, while HA promoted cell proliferation and mitigated the minor adverse effect of Ag on cell viability. To enhance cell compatibility with antibacterial coatings or extend antibacterial substance release, polydopamine [147,148] and polylactic acid [149] can be loaded on the coating surface through secondary surface treatment.

Graphene and its derivatives (e.g., graphene oxide (GO) and redox graphene (rGO)) can be integrated into MAO coatings either directly through electrolytes or in combination with techniques like electrophoretic deposition (EPD), sol-gel, and dropping coating. This incorporation imparts favorable antibacterial and tribological properties [150]. For instance, Mazinani et al. [151] combined MAO and EPD to deposit GO sheets onto the MAO coating, resulting in significant antimicrobial properties against *E. coli* and *S. aureus*. Moreover, San et al. [152] created a suspension of rGO and Ag NPs, added it to the MAO electrolyte, and achieved a more effective coating against MRSA due to the generation of ROS and the “Nanoknife” structure of rGO.

Chitosan (CS) interacts with the anionic components on the microbial cell wall, resulting in cell wall damage and the killing of microorganisms, due to its cationic nature and polyamine structure. CS can be fixed on the MAO coating by dip coating [153]. For example, BMP-2-encapsulated CS gives the coating good osteogenic and antibacterial properties [115].

Incorporating drugs, such as antibiotics, is an effective means of rapid sterilization during early implantation stages. For example, Zhou et al. [154] used ciprofloxacin-loaded CS hydrogel to modify the coating, effectively sterilizing the sample with the bacteriostatic zone. Xu et al. [155] covalently grafted vancomycin to the MAO coating, creating Ti@MV with significant antibacterial properties and enhanced osteogenic differentiation of BMSCs. In another study [156], octenidine (OCT) was loaded onto MAO-prepared coatings via electrophoresis, resulting in improved early antibacterial efficiency without compromising cell compatibility. This early-stage (4–6 h) intervention is crucial for preventing long-term bacterial infections. Octenidine, vancomycin, and heparin were among the early attempts at drug loading on polyethylene glycol MAO-treated surfaces. However, their initial release is too large, and it is easy for bacteria to develop drug resistance. Therefore, the use of antibiotics in implant surface modification is gradually decreasing [157]. In terms of biological compounds, antimicrobial peptides (AMPs) have become the main substances for functionalization in Ti surfaces through a multi-step process on MAO surfaces [147,158]. However, the main challenge with these antimicrobial surfaces is that cross-linking of peptides on the surfaces is difficult, resulting in less stable coatings, limited duration of antimicrobial activity, and higher manufacturing costs [159].

Phototherapy, including photothermal and photodynamic therapy, offers safe and controllable methods. Photothermal therapy employs agents that generate high temperatures under near-infrared light, effectively disrupting bacterial structures. In contrast, photodynamic therapy relies on photosensitizers absorbing specific light wavelengths to create reactive oxygen species (ROS), which disrupt bacterial DNA, proteins, and

biomembranes. Hydrothermal treatment or sol-gel can be used to combine photothermal agents or photosensitizers into the coating [160]. Chai et al. [161] successfully prepared a  $\text{TiO}_2/\text{MoO}_2$ /chitosan coating on Ti surfaces using a composite process involving MAO, HT, and electrospinning. The  $\text{MoO}_2$  significantly improved the phototherapy performance. Both in vitro and in vivo experiments demonstrated excellent antibacterial capabilities against *Streptococcus mutans* (*S. mutans*) after 15 min of irradiation with near  $-808$  nm wavelength infrared light, facilitated by the synergistic effects of a high temperature and ROS. Moreover, Li et al. [108] used MAO and HT techniques to form a  $\beta\text{-FeOOH}/\text{Fe TiO}_2$  heterojunction, which can also generate ROS under irradiation. In addition, ultraviolet rays can remove surface carbon contaminants and increase the negative charge density on the surface of crystal  $\text{TiO}_2$ , thereby reducing bacteria through electrostatic repulsion [125]. However, because UV rays have carcinogenic effects, they can be used as a pretreatment before implant placement.

### 3.3. Anti-Inflammatory

The biological properties of materials are initially evaluated through in vitro studies on osteoblast activity. In some cases, differences between in vivo and in vitro research results may stem from immune cell responses. Bone immunology emphasizes the role of immune cells in osteointegration, which involves the inflammatory response in the early and late stages after implantation [162].

The implantation of biomaterials is intricately tied to a continuous biological process (Figure 8). Shortly after implantation, proteins from the vascular system and interstitial fluid adhere to the surface of the biomaterial within minutes. Subsequently, various cells, including platelets, monocytes, and macrophages, infiltrate and adhere to the biomaterial. Within 1 to 5 days post-implantation, immune cells release cytokines on the biomaterial surface, initiating a pro-inflammatory response while recruiting bone repair cells (e.g., BMSCs and OBs) from distant sites to the inflammatory site [163]. This early-stage inflammation is crucial. The fate of the bone biomaterial, whether it becomes encapsulated by a fibrous capsule (indicating failure) or undergoes long-term replacement by new bone (the desired outcome), is determined by bone repair cell interactions with the inflammatory microenvironment and biomaterial properties in the following days. Acute inflammation typically subsides in less than 1 week, while a duration exceeding 3 weeks may lead to implant failure. The emerging field of bone immunology and immune modulation has shifted our expectations for bone biomaterials, emphasizing their role in bone immune modulation rather than just reducing inflammatory responses [164].

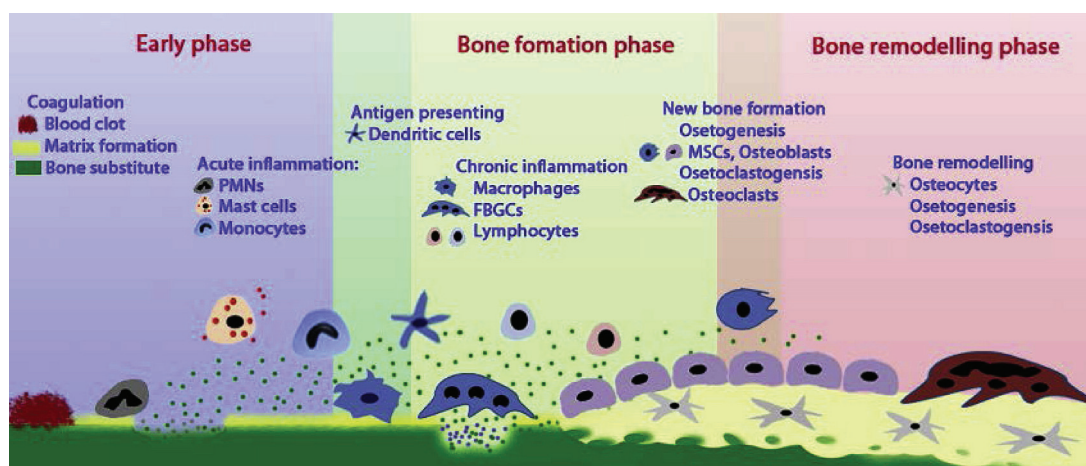


**Figure 8.** Three key stages involve interactions between host immune cells, bone cells, and biomaterials in bone regeneration: early stage (thrombosis and acute inflammation), bone formation (chronic inflammation and new bone initiation), and bone remodeling [162].

Recent advancements in Ti surface engineering focus on managing host and inflammatory responses. This approach leverages the benefits of physiological inflammation, such as cellular debris removal and infection prevention, while also mitigating the risks associated with severe inflammatory reactions. These risks include implant rejection, early or late failures, and impacts on implant functionality.

To modulate the inflammatory response of biomaterials, these strategies can be followed [164]:

1. Adsorption of specific proteins: control the adsorption of plasma proteins on the implant surface to influence inflammatory responses.
2. Macrophage polarization: M1 (pro-inflammatory) and M2 (anti-inflammatory) phenotypes can be induced. M1 macrophages clear debris and potential pathogens in the early stages of implantation, while M2 macrophages support inflammation resolution and tissue healing. The M1 phenotype is produced by M0 macrophages activated by the lipopolysaccharide (LPS) or interferon- $\gamma$  (INF- $\gamma$ ). It secretes inflammatory mediators, including Interleukin-1 $\beta$  (IL-1 $\beta$ ), IL-6, IL-12, IL-23, ROS, and Tumor Necrosis Factor- $\alpha$  (TNF- $\alpha$ ). However, the M2 phenotype is induced by stimulation with IL-4, IL-10, and IL-1 $\beta$ . M2 macrophages release anti-inflammatory cytokines and growth factors, such as IL-10 and transforming growth factor- $\beta$  (TGF- $\beta$ ).
3. Surface topography: Surface roughness and texture can affect macrophage phenotype. Rough surfaces may favor M1 activation, while nano- or micron-scale directional textures promote an M2-like response. Hydrophilic surfaces can reduce pro-inflammatory cytokines.
4. Biomimetic coating: modify the implant surface with biomimetic coatings like collagen, transmembrane molecular markers, mesenchymal stem cells, or biological peptides to reduce macrophage activation and pro-inflammatory factors.
5. Local drug delivery: implement local drug delivery systems on the implant surface to create a localized anti-inflammatory environment with high drug concentration and minimal systemic side effects.

Local inflammatory reactions can result from debris accumulation caused by wear during implantation or long-term friction between the implant and surrounding bone tissue [165,166]. Furthermore, the corrosion of metals in the complex environment of the body can release metal ions, potentially triggering inflammation. MAO coatings offer excellent tribological properties and corrosion resistance. They can be modified to regulate host and inflammatory responses by adjusting the surface topography and composition of the implant. Li et al. [163] examined the in vitro immune response to Ca- and Si-doped MAO coatings. They found that the macrophage interaction with MAO-Ti favored the M1 phenotype, but collagen synthesis and matrix mineralization for osteocyte-like cell growth on the coating were favorable. This suggests that MAO-modified implant–bone interfaces support osteogenesis both before and after osteoblast recruitment to the biomaterial surface. Furthermore, Ti-Ta metal–metal composites with bioceramic coatings containing Ca and Si also demonstrate osteogenic, anti-inflammatory, and bone immunoregulatory properties [167].

Some metallic elements, such as Cu [168], Zn [169], Mg [170], Li [102], and Co [171], have been shown to modulate the immune environment at the implant surface. They can regulate macrophage polarization phenotypes, thus promoting either early pro-inflammatory and antimicrobial effects or long-term anti-inflammatory and pro-osteogenic effects of the implant. For instance, Li et al. [168] utilized MAO to create Cu-containing ceramic coatings on Ti surfaces (Cu-MAO). Macrophages on Cu-MAO displayed polarization toward the M1 phenotype, exhibiting high levels of inducible nitric oxide synthase (iNOS) expression, low arginase-1 (Arg1) expression, enhanced release of IL-6, and inhibited release of IL-4 and IL-10. This promoted a favorable inflammatory microenvironment for osteoblast-like cell differentiation and enhanced bactericidal abilities of the surface. Sun et al. [169] took a similar approach by developing Zn-doped MAO coatings on Ti surfaces, which exhibited excellent biocompatibility and osteogenic differentiation perfor-

mance with BMSCs. In addition, evaluation of RAW264.7 cells' survival on the surface and related pro-inflammatory markers revealed that this coating downregulated the expression of pro-inflammatory genes. Peng et al. [102] incorporated Lithium (Li) into Ti surface coatings via MAO. Low-dose Li was slowly released as ions, enhancing the recruitment of BMDMs while favoring M2 polarization and limiting M1 polarization. In vivo, implantation mimicking aseptic loosening revealed the ability of Li to mitigate inflammatory responses. Additionally, Li-doped MAO coatings supported healthy growth of both mouse embryonic cell lines (C3H10T1/2) and HUVECs in a macrophage-conditioned medium, highlighting their potential for osteogenic differentiation and angiogenesis. The molecular mechanism involved the regulation of cascade molecules in the PI3K/AKT signaling pathway for bone immunomodulation. Similarly, Yang et al. [171] prepared Co-doped MAO coatings on Ti implants with varying Co content. Their results showed that, in comparison to pure Ti samples, cobalt-loaded Ti exhibited immunomodulatory functions on macrophages, upregulating the expression of M1 genes and downregulating the expression of M2 genes. Notably, higher cobalt levels induced the polarization of macrophages into the M2 type.

Similar to antimicrobial properties, other surface modification techniques can incorporate a greater amount of anti-inflammatory components onto the surface of the MAO coating. Bai et al. [172] investigated the effects of MAO and steam heat treatment (SHT) on the preparation of nano-HA coatings on porous Ti surfaces. They found that Ti surfaces coated with HA NPs exhibited adjustable inflammatory responses, while HA nanorods negatively affected osteo-/angiogenesis and osteoimmunomodulation. Additionally, they [100] annealed the MAO-HA surfaces and observed that annealing temperature influenced surface topography, wettability, and chemical properties. In vitro experiments demonstrated that MAO coatings annealed at 650 °C promoted the proliferation and differentiation of osteoblasts and endothelial cells, while inhibiting the inflammatory response of macrophages.

Schmidlin et al. [173] found that ZrO<sub>2</sub> particles induced lower expression of inflammatory factors compared to TiO<sub>2</sub> particles at an equivalent dose. Zhu et al. [174] combined the MAO and sol-gel methods to fabricate a multifunctional composite coating on the surface of Ti, composed of SiO<sub>2</sub> particles and zirconium hydrogen phosphate (ZrP). The ZrP coating exhibited superhydrophilicity and significantly reduced the release of pro-inflammatory cytokines (TNF- $\alpha$ , IL-6, and IL-1 $\beta$ ). This coating also enhanced corrosion resistance and friction, resulting in reduced Ti ion/fragment release and minimized inflammatory responses. Wang et al. [175] prepared Sr-doped nanostructures on the Ti surface through MAO and electrochemical deposition, and subsequently incorporated silk fibroin protein-based nanocomposites (Ti-MAO/Sr/LBL/WNP) through a layer-by-layer self-assembly technique (LBL). This coating exhibited sustained release of wogonin and Sr ions for over 7 days, promoted the expression of anti-inflammatory factors (TGF- $\beta$ 1 and Arg-1) in M2 macrophages, and facilitated cell proliferation and osteogenic differentiation. Moreover, MAO coatings can be utilized to locally load bioactive substances and drugs, such as peptides that recruit immune-modulating cells (T cells, monocytes, mast cells, and neutrophils) [158].

MAO provides biofunctional coatings that interact with tissues over an extended period, involving multiple biological and biochemical processes [90]. This interaction is determined by the implant characteristics and the implantation environment. Evaluating the biocompatibility and long-term performance of the coatings is a task that requires various factors and methods. Biocompatibility testing includes both in vitro and in vivo assessments [109,113]. In vitro experiments can detect the effects of the coating on cell adhesion, proliferation, and differentiation. In vivo experiments assess the biocompatibility, tissue response, and implant stability within live animals. Assessing engineering parameters in the surrounding tissues, such as vascularization, bone formation, and healing, provides information on the coating impact on tissue reconstruction. Monitoring implant position and stability through imaging techniques such as X-rays, CT scans, and

MRI is crucial for detecting issues like coating delamination, implant loosening, or displacement. Animal experiments observe the morphology, structure, chemical composition, and mechanical properties of the coating after a certain period of implantation, offering insights into the long-term stability of coatings in vivo. Evaluating long-term performance also involves considering inflammation and immune reactions around the implant, monitoring through tissue slices, inflammation levels, biomarker detection, and immune cell activity [168,172,175–177] (refer to the literature listed in Table 3). Integrating these assessments provides a more comprehensive understanding of the performance of MAO coatings during long-term use and their interaction with surrounding tissues. This multidisciplinary task typically requires collaboration among professionals in medicine, biomedical engineering, and materials science. Moreover, dental implants and hip stems featuring MAO coatings have been introduced as products and subjected to market testing over the long term, yet relevant literature reports are scarce [178,179].

**Table 3.** Coatings contain different components with different biological functions and are validated in vitro and in vivo.

Number	Biologic Function	Adding Substances	Technique	In Vitro		In Vivo	Conclusion/Remark	Reference
				Cell	Bacterium	Animal Parts		
1	Osteogenesis	Ca, Sr	MAO	hBMSCs			Simultaneously incorporating Ca and Sr demonstrated superior promotion of hBMSC proliferation.	[97]
2	Osteogenesis/Angiogenesis	Zn	MAO	HUVECs and BMSCs			In the Zn <sup>2+</sup> environment, angiogenesis and osteogenesis mutually promote each other.	[106]
3	Osteogenesis/Angiogenesis	Hydroxyapatite nanotubes (HNTs)	MAO	HUVECs and MC3T3-E1 cells			HNT specimens promote both angiogenesis and osteogenesis on cellular and molecular levels.	[101]
4	Osteogenesis	B	MAO, hydrothermal treatment, and heat treatment	SaOS-2 cells			Nanorods inhibit SaOS-2 cell activity, whereas nanoparticles promote it.	[143]
5	Osteogenesis	Hierarchical coatings	MAO, electrochemical reduction	BMSCs		Beagle dogs, the shaft of the canine femur	The hierarchical coatings show higher osteogenesis rates compared to the ordinary MAO group.	[113]
6	Osteogenesis	HA, BMP-2	MAO, dip coating	MC3T3-E1 cells		Beagle femur	The interface bonding strength between HA/BMP-2 coating and surrounding new bone tissue is higher than that of Ca/PMAO coating.	[109]
7	Osteogenesis/Angiogenesis	Ca, P, BMP-2	3D printing, sandblasting etching, MAO, electrochemical deposition	BMSCs		New Zealand White Rabbit Skull	MAO-CaP-BMP-2 is superior to the MAO and MAO-CaP groups in new bone formation.	[117]
8	Osteogenesis/Antibacterial	Ca, P	MAO	hFOBs	<i>E. coli</i> and <i>S. aureus</i>		Volcanic-crater-like and needle-like CaP structures form at 350 V and 450 V, respectively. The former exhibits superior antibacterial performance and biocompatibility.	[121]

Table 3. Cont.

Number	Biologic Function	Adding Substances	Technique	In Vitro		In Vivo	Conclusion/Remark	Reference
				Cell	Bacterium	Animal Parts		
9	Bioactivity/ Antibacterial	Ca, P	MAO, UV catalysis	HGFs	<i>S. sanguinis</i>		Photofunctionalization reduces hydrocarbons and enhances surface protein adsorption.	[125]
10	Osteogenesis/ Antibacterial	Zn	MAO	MC3T3-E1 cells	<i>E. coli</i>		Incubation with salt solution converts Zn ions into zinc oxide, which helps with long-lasting antibacterial activity.	[134]
11	Antibacterial/ Osteogenesis/ Angiogenesis	Sr, Zn	MAO	HUVECs, BMSC	MRSA and <i>P. gingivalis</i>	Rat femoral model	The surface osteogenesis of samples doped with Sr and Zn is superior to other groups. (No in vivo antibacterial test conducted.)	[104]
12	Antibacterial	Ag, Cu NPs	MAO	MC3T3-E1 cells	MRSA	Mouse femur ex vivo experiment	Ag and Cu ions synergistically kill bacteria, allowing a 10-fold reduction in Ag ion concentration with consistent antibacterial efficacy.	[124]
13	Osteogenesis/ Antibacterial	Ag, Zn	3D printing, MAO	MC3T3-E1 cells	MRSA	Mouse femur ex vivo experiment	The synergistic effect of Ag and Zn reduces the concentration of Ag <sup>+</sup> by 120 times.	[128]
14	Osteogenesis/ Antibacterial	Ag, Zn	MAO	MC3T3-E1 cells	<i>S. aureus</i>		Ag and ZnO synergy enhances antibacterial performance and promotes CaP phase formation.	[129]
15	Osteogenesis/ Antibacterial	Ag, Zn	MAO	MC3T3-E1 cells	<i>S. aureus</i>		Ag and Zn ion release is above the antibacterial threshold yet well below cytotoxic levels.	[130]
16	Osteogenesis/ Antibacterial	Ag, Zn	MAO		<i>S. aureus</i>		Ag and Zn have good synergistic antibacterial effects.	[131]
17	Osteogenesis, Antibacterial	Cu, Zn	MAO	MG63	<i>E. coli</i> , <i>S. aureus</i> , and MRSA		Orthogonal experiments explore electrolyte effects on coatings, with phytic acid supplying the P element.	[132]
18	Skin- integration/ Antibacterial	Cu, Zn	MAO	Fibroblasts (L-929)	<i>S. aureus</i>		The synergistic effect of Cu and Zn facilitates skin integration and antibacterial activity.	[133]
19	Osteogenesis, Anti-tumor/ Antibacterial	Se	MAO	BMSCs, cancerous osteoblasts	<i>S. aureus</i> and <i>E. coli</i>		Se doping enhances osteogenic, anti-tumor, and antibacterial properties.	[103]
20	Osteogenesis/ Antibacterial	Mn	MAO	MC3T3-E1 cells	<i>E. coli</i>	Rabbit femur	The coating induces osteogenesis and promotes osseointegration.	[137]
21	Antibacterial	Bi	MAO	MG63 cells	<i>A. actino- mycetemcomi- tans</i> , MRSA		Bismuth nitrate has excellent antibacterial activity compared to bismuth acetate, bismuth gallate, and silver nitrate.	[138]
22	Osteogenesis/ Antibacterial	Ce	MAO	BMSCs	<i>P. gingivalis</i> , <i>S. aureus</i>	Osteoporotic rat hind legs	Ce-TiO <sub>2</sub> coating has excellent antibacterial and anti-inflammatory properties.	[139]

Table 3. Cont.

Number	Biologic Function	Adding Substances	Technique	In Vitro		In Vivo	Conclusion/Remark	Reference
				Cell	Bacterium	Animal Parts		
23	Antibacterial	I	MAO, HT, photocatalysis	BMSCs	<i>S. aureus</i>	Tibial Intra-medullary Infection Model of Rats	Under NIR, the coating has good antibacterial and osteogenic properties.	[140]
24	Antibacterial	I	MAO, electrophoresis	BMSCs	<i>S. aureus</i> and <i>E. coli</i>	The rat osteomyelitis in-tramedullary nail model	Thirty days after implantation, excellent antimicrobial ability was verified.	[141]
25	Bioactivity/ Antibacterial	B	MAO	ADSCs	<i>S. aureus</i> and <i>P. aeruginosa</i>		Add a small amount of sodium tetraborate to the Ca, P electrolyte system.	[142]
26	Osteogenesis/ Antibacterial	F	MAO	BMSCs	<i>S. aureus</i> and <i>E. coli</i>	Rabbit femur	Coatings with high F addition showed improved antibacterial and osteogenic abilities.	[144]
27	Antibacterial/ Osteogenesis/ Angiogenesis	Sr, Co, and F	MAO	BMSCs	<i>S. aureus</i> and <i>E. coli</i>	Rabbit femur	Sr, Co, and F co-doped coatings induce osteogenesis.	[145]
28	Osteogenesis/ Antibacterial	Mn, F	MAO	BMSCs	<i>S. aureus</i>		Mn and F co-doped coatings show excellent wear and corrosion resistance, along with strong antibacterial properties.	[146]
29	Osteogenesis/ Antibacterial	Cu, BMP-2	MAO, dip coating	MC3T3-E1 cells	<i>E. coli</i> , MRSA, <i>Neurospora crassa</i> , and <i>Candida albicans</i>	Mouse craniotomy model	The coating significantly promotes osseointegration.	[110]
30	Osteogenesis/ Antibacterial	Ag, HA	MAO, RF-MS	MC3T3-E1 cells	<i>E. coli</i>		This coating exhibits strong biological activity and antibacterial properties.	[111]
31	Bioactivity/ Antibacterial	Ag NPs, polylactic acid (PLA)	MAO, electro-spinning	MC3T3-E1 cells	<i>S. aureus</i>		PLA ultrafine fibers produced by electrospinning can control the release of silver ions.	[149]
32	Osteogenesis/ Antibacterial	AgNPs, polydopamine	MAO, dip coating	MG63 cells	<i>S. aureus</i>	New Zealand rabbit subdermal implantation	This coating exhibits strong biological activity and antibacterial properties.	[122]
33	Osteogenesis/ Antibacterial	Polydopamine, cationic antimicrobial peptide LL-3, phospholipid	MAO, dip coating	BMSCs and OBs	<i>S. aureus</i> and <i>E. coli</i>		The coating exhibits good osteogenesis and antibacterial properties.	[147]
34	Antibacterial	GO	MAO, EPD		<i>S. aureus</i> and <i>E. coli</i>		Achieves ~80% antibacterial activity against <i>E. coli</i> and 100% against <i>S. aureus</i> .	[151]
35	Antibacterial	rGO, Ag NPs	MAO	MC3T3-E1 cells	MRSA		The coating exhibits good osseogenesis and antibacterial properties.	[152]
36	Osteogenesis/ Antibacterial	HA, chitosan (CS)	MAO, dip coating	MC3T3-E1 cells	<i>E. coli</i>		Higher usage of CS results in decreased biological performance but improved antimicrobial performance.	[153]
37	Osteogenesis/ Antibacterial	HA, CS hydrogel containing ciprofloxacin	MAO, HT, chemical grafting	hBMSCs	<i>S. aureus</i> and <i>E. coli</i>		The coating exhibits good osseogenesis and antibacterial properties.	[154]

Table 3. Cont.

Number	Biologic Function	Adding Substances	Technique	In Vitro		In Vivo	Conclusion/Remark	Reference
				Cell	Bacterium	Animal Parts		
38	Osteogenesis/ Antibacterial	BMP-2/CS/HA	MAO, dip coating	MC3T3-E1 cells	<i>E. coli</i>		CS encapsulation sustains BMP-2 release with added antibacterial properties.	[115]
39	Antibacterial	Vancomycin	MAO, dip coating			The rabbit osteomyelitis model (infection with MRSA)	In vivo studies demonstrate the potential of this coating to prevent MRSA infection.	[148]
40	Osteogenesis/ Antibacterial	Vancomycin	MAO, dip coating, chemical grafting	BMSCs	<i>S. aureus</i>	Rat femur	Functional coatings prevent prosthesis infection and promote bone integration at the interface.	[155]
41	Antibacterial	Mesoporous silica NPs (MSNs), octenidine (OCT)	Electrophoretic-enhanced MAO	OBs	<i>S. aureus</i> and <i>E. coli</i>		The coating exhibits good osseogenesis and antibacterial properties.	[156]
42	Bioactivity/ Antibacterial	N, Bi	MAO, photocatalysis	HGFs	<i>Streptococcus sanguinis</i> and <i>Actinomyces nasseri</i>		The coating has bactericidal properties under visible light.	[123]
43	Osteogenesis/ Antibacterial	MoSe <sub>2</sub> , CS	MAO, electrospinning, photocatalysis	MC3T3-E1 cells	<i>S. mutans</i>	Rat tibia	Adding MoSe <sub>2</sub> significantly enhances TiO <sub>2</sub> coating photothermal and photodynamic capabilities.	[161]
44	Skin-integration/ Antibacterial	$\beta$ -FeOOH, Fe-TiO <sub>2</sub>	MAO, HT, photocatalysis	Mouse fibroblasts (L-929)	<i>S. aureus</i>	Mouse skin infection model	The $\beta$ -FeOOH/FeTiO <sub>2</sub> heterojunction prevents bacterial infection under light irradiation.	[108]
45	Osteogenesis/ Anti-inflammatory	Ca, Si	MAO	SaOS-2 cells			The coating inhibits inflammation and induces M2 macrophage polarization.	[167]
46	Antibacterial/ Immunoregulation	Cu	MAO	RAW 264.7 macrophages, SaOS-2 cells	<i>S. aureus</i>		Cu boosts macrophage-driven osteogenesis and antibacterial activity in biomaterials.	[168]
47	Osteogenesis/ Anti-inflammatory	Zn	MAO	RAW264.7 macrophages, BMSCs			The coating shows good osteogenic and anti-inflammatory properties.	[169]
48	Osteogenesis/ Anti-inflammatory	Mg	MAO	RAW 264.7 macrophages			Mg acts as an anti-inflammatory agent, inhibiting inflammation and promoting osteogenesis.	[170]
49	Anti-inflammatory	Co	MAO	RAW 264.7 macrophages		Mouse air chamber model	Cobalt-loaded Ti exhibits immune-regulatory effects on macrophages.	[171]
50	Osteogenesis/ Angiogenesis/ Anti-inflammatory	Li	MAO	BMDMs, mouse embryonic cell line (C3H10T1/2), HUVEC		Mouse air-pouch model	Low Li doses effectively regulate immunity, and promote osteogenesis.	[102]
51	Osteogenesis/ Angiogenesis/ Anti-inflammatory	HA	MAO, SHT	MC3T3-E1 cells, human umbilical vein fusion cells, RAW 264.7 cells		Rabbit femur	This coating promotes osteogenesis and angiogenesis, and induces M2 macrophage phenotype.	[172]

Table 3. Cont.

Number	Biologic Function	Adding Substances	Technique	In Vitro		In Vivo	Conclusion/Remark	Reference
				Cell	Bacterium	Animal Parts		
52	Osteogenesis/ Anti-inflammatory	HA	MAO, SHT	MC3T3-E1 cells, endothelial cells, RAW 264.7 cells		Rabbit femur	Nanoparticle-shaped HA is beneficial for osteogenesis, angiogenesis, and immune regulation, whereas nanorod-shaped HA is the opposite.	[173]
53	Osteogenesis/ Anti-inflammatory	SiO <sub>2</sub> , ZnPs	MAO, sol-gel	MC3T3-E1 cells			The coating shows good osteogenic and anti-inflammatory properties.	[175]
54	Osteogenesis/ Anti-inflammatory	Sr, silk fibroin-based wogonin NPs	MAO, electro-chemical deposition, LBL	RAW 264.7 cells, OBs		Osteoporotic rat femur	The coating shows good osteogenic and anti-inflammatory properties.	[176]

## 4. Applications and Challenges of MAO in Implants

### 4.1. Applications

MAO coatings, particularly with specific functional additives, possess remarkable biological functionalities including bone promotion, antimicrobial properties, and anti-inflammatory effects. Though clinical applications of Ti-based implants with MAO-modified functional coatings are limited, animal experiments have validated several implants with such coatings (Table 3). Presently, surface modification techniques like sandblasting, acid etching, and anodization, along with the introduction of bioactive materials such as calcium phosphate, hydroxyapatite, and calcium nanoparticles, are widely employed to optimize implant surface microstructure and topography. These modifications primarily aim to enhance biocompatibility and promote osseointegration. For example, MAO techniques have been utilized to create rough and porous surfaces on dental implants and femoral stems, facilitating improved tissue bonding [119].

TiUnite and TiUltra surfaces (Nobel Biocare, Zurich, Switzerland), along with the Ospol implant (OspolAB, Malmö, Sweden) and the M implant (Shinhung, Seoul, Republic of Korea), are all manufactured using the MAO process and are commercially available. The TiUnite surface series by Nobel Biocare<sup>TM</sup>, introduced in the early 2000s, has undergone continuous refinement and gained worldwide acceptance. These implants, containing 7% phosphorus in the form of titanium phosphate chemical bonds, are fabricated using an electrolyte mixture with phosphorus. A comprehensive review [178] encompassing prospective studies spanning from 2000 to 2016 on the clinical performance of implants featuring the TiUnite surface affirms the high survival rates and favorable maintenance of marginal bone associated with such implants. Incidences of peri-implantitis are notably lower for implants employing the TiUnite surface. Notably, implants with this surface consistently exhibit predictable treatment outcomes across diverse indications. In 2019, Nobel Biocare<sup>TM</sup> introduced the TiUltra surface series (Figure 9), which features a progressively rough and porous surface texture extending from the implant collar to its tip, exhibiting excellent hydrophilic properties [180]. Moreover, the M implants of Shinhung<sup>TM</sup> are produced using the MAO method with an electrolyte mixture containing magnesium, resulting in a TiO<sub>2</sub> surface containing magnesium ( $\leq 9.3\%$ ) and phosphorus ( $\leq 3\%$ ) [181]. Similarly, Ospol<sup>TM</sup> implants are created using the MAO method with an electrolyte mixture containing Ca, leading to the incorporation of calcium ions (less than 11%) within the TiO<sub>2</sub> in the form of calcium titanium oxide bonds [182].

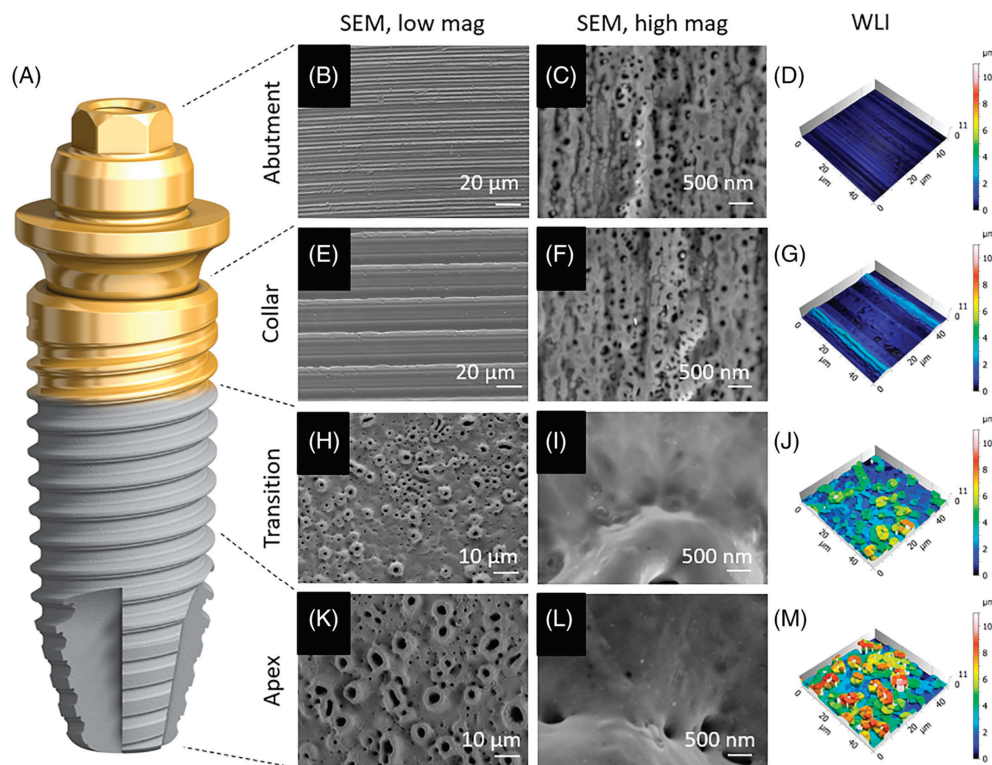


**Figure 9.** Implants with TiUltra surfaces [180]. (A) Microscopic analysis of the implant system's four regions: abutment (B–D), implant collar (E–G), transition zone (H–J), and apex (K–M). This includes an overview (B,E,H,K), high-magnification scanning electron micrographs of each region (C,F,I,L), and 3D surface profile reconstructions using white-light interferometry (D,G,J,M).

Femoral shafts treated with sandblasting and MAO coating are commercially available. For example, the Korean Bencox™ hip system (Corentec, Seoul, Republic of Korea) has cementless sandblasted femoral stems with MAO coating on the surface (Figure 10). Made from Ti-6Al-4V alloy, it is a double-wedge straight tapered stem with a rectangular cross-section. The coating method of MAO coating is as follows: After Ti plating, the sample is electrochemically oxidized using the MAO process. The sample is subjected to MAO treatment with a DC pulse power supply in an aqueous electrolyte containing Ca and P.

In a study by Lim et al. [179], in a follow-up period of at least 5 years, the MAO-coated sandblasted surface did not demonstrate superiority over primary total hip arthroplasty (THA) with the same femoral component design. While MAO is theoretically known to promote bone growth through calcium and phosphorus binding to the titanium alloy surface, forming thick oxides and nano-porous coatings, its clinical utility has not been confirmed. In a study with 10 years of follow up [183], 309 cases of THA (involving 256 patients) were performed using the non-cemented Bencox™ hip joint system. A Kaplan–Meier survival analysis indicated a 10-year survival rate of 97.4% when using revision for any reason as the endpoint, and a survival rate of 98.7% when using aseptic loosening revision as the endpoint. While there was a decrease in the proportion of cases with bone resorption in the follow up, the absence of a control group precludes concluding the ability of MAO coatings to resist bone resorption, despite various studies suggesting their potential for preventing bone resorption. In summary, after a follow-up period of at least 10 years, the outcomes of non-cemented sandblasted and MAO-coated THA tapered wedge stems are satisfactory.



**Figure 10.** The Bencox™ stem is a collarless cementless bi-tapered rectangular Ti stem with an MAO-coated sandblasted surface [183].

The MAO coating cannot only promote bone integration but also improve the wear and corrosion resistance of implants. Khanna et al. [184] performed cold spraying to deposit an Al metal layer onto a Ti-6Al-4V alloy substrate, followed by heat treatment to enhance adhesion. They then conducted MAO treatment to form a dense  $\alpha\text{-Al}_2\text{O}_3$  layer on the substrate surface, with a Vickers hardness matching that of sintered alumina used for femoral heads (Figure 11).

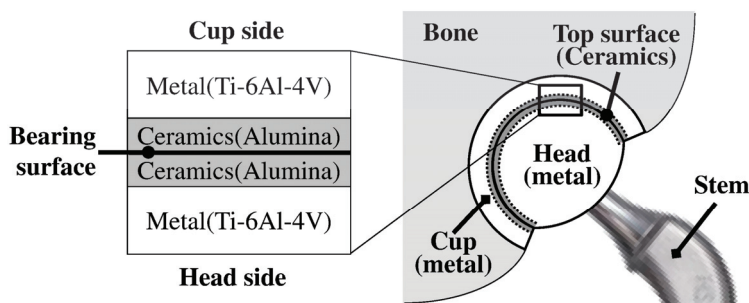


**Figure 11.** Ceramic/metal hybrid artificial hip joint cross-sectional design schematic, with alumina layers formed on Ti alloy for both the cup and head components [184].

#### 4.2. Challenges

Although MAO coatings have undergone extensive research and led to the emergence of related products, there are still challenges and limitations in the production and application:

1. Despite considerable progress in studying the discharge process of MAO, some micro-scale mechanisms remain unclear, such as cathodic discharge and soft spark discharge. This uncertainty affects the control of the microstructure of MAO coatings [22].
2. In the coating manufacturing process, establishing the electrolyte composition and electrical parameters still necessitates multiple experiments. Defining the optimal parameters remains challenging. Minor losses of electrolytes during usage and the settling of particulate or colloidal electrolytes can also impact coating performance [44,54].
3. The impact of coating morphology on cell bioactivity remains inconclusive. While some studies suggest that moderate roughness aids in cell adhesion and proliferation,

and porous surfaces facilitate cell osteogenic differentiation, there is still debate about the optimal pore size. Different cell types may have varied requirements for morphology [90,91]. Additionally, due to cracks and interconnected pores, their durability and wear resistance require attention [20].

4. Coatings with added functionalities, such as antimicrobial and anti-inflammatory components, may exhibit toxic effects on normal cells, especially with high concentrations of antibiotics or antimicrobial agents [119,164].
5. There is a substantial amount of research on biologically functional coatings; the availability of implants in the market is relatively limited. Successfully translating these technologies into commercial products may face greater challenges [119].

## 5. Conclusions and Prospects

### 5.1. Conclusions

The main focus of this paper revolves around a series of factors influencing the performance of MAO coatings and the biological functions of these coatings under various treatment conditions. As a result, the following conclusions are drawn:

1. The discharge process is pivotal, influenced by the electrolyte, electrical parameters, and substrate. The electrolyte affects the composition and structure of coatings. Electrical parameters impact coating performance by altering discharge energy. Additionally, the substrate and pre-treatment also contribute.
2. MAO transforms implant surfaces, creating varied topologies and infusing substances for osteointegration. It provides multiple strategies to combat surface infections by adding antibacterial agents. Recent surface engineering maximizes inflammation benefits while minimizing risks, with MAO coatings showing considerable potential. The biocompatibility and long-term stability of coatings require more attention.
3. Presently, MAO is being clinically applied to promote bone integration, especially in the field of dentistry. Despite some progress in the MAO bioactive coatings on Ti and its alloys, challenges still exist in the production and application of coatings.

### 5.2. Prospects

The progress and challenges of MAO coatings suggest considerable research and application potential for implant surfaces. The following outlines prospects:

1. Certain micro-mechanisms in the MAO process need more study. Collaborative efforts across disciplines will enhance the understanding of discharge, electrolyte behavior, and coating growth complexities. Real-time detection, high-resolution characterization, and numerical simulation may unveil the link between microstructures and performance, paving the way for tailored and controllable coatings.
2. Developments in electrolytes will prioritize optimizing formulations, extending lifespan, and emphasizing sustainability by using renewable or recyclable components. Equipment improvements will focus on enhancing power supply design for increased efficiency and stability. Orthogonal experiments can be used to validate new formulations and equipment designs under various conditions. Standardized and automated manufacturing will enhance production efficiency and reduce waste, contributing to the sustainability and cost-effectiveness of MAO technology.
3. The integration of biology, materials science, and engineering will be employed to design a controllable coating. Comprehensive experiments are imperative to unveil the influence of morphology on cellular behavior. Incorporating nanoparticles into the electrolyte or using other techniques to repair defects in MAO coatings could potentially enhance wear resistance and durability.
4. Optimizing antimicrobial and anti-inflammatory components in coatings is crucial. Researchers need to delve into understanding mechanisms of action to reduce concentrations while maintaining efficiency and minimizing adverse effects. Avoiding overuse aims to slow bacterial resistance. When designing coatings, selecting friendly

components and comprehensive biocompatibility testing will ensure coatings do not trigger allergic or inflammatory responses.

- MAO coatings have vast market opportunities. However, successful market entry requires meeting strict approval and regulatory standards. Key factors include in-depth research on biocompatibility, drug release kinetics, and rigorous safety testing. The evaluation methods and standards for coatings also need to be further developed. Collaboration, innovation, and a continued focus on product safety will drive the successful commercialization of coatings in the future.

**Author Contributions:** X.M. formulated the work plan, wrote the paper, and designed the manuscript layout. Y.W. adjusted the framework and revised the paper. Z.Z. provided important information and made some additions. Y.L. provided critical comments and revised further. All authors have read and agreed to the published version of the manuscript.

**Funding:** This work was supported by the National Key Research and Development Program of China (No. 2018YFC1106600).

**Data Availability Statement:** No new data were created or analyzed in this study. Data sharing is not applicable to this article.

**Conflicts of Interest:** The authors declare no conflict of interest.

## References

- Vereinte, N. (Ed.) *Leaving No One Behind in an Ageing World*; World social report; United Nations: New York, NY, USA, 2023; ISBN 978-92-1-130458-9.
- Jing, Z.; Zhang, T.; Xiu, P.; Cai, H.; Wei, Q.; Fan, D.; Lin, X.; Song, C.; Liu, Z. Functionalization of 3D-printed titanium alloy orthopedic implants: A literature review. *Biomed. Mater.* **2020**, *15*, 052003. [CrossRef]
- Jimenez-Marcos, C.; Mirza-Rosca, J.C.; Baltatu, M.S.; Vizureanu, P. Experimental Research on New Developed Titanium Alloys for Biomedical Applications. *Bioengineering* **2022**, *9*, 686. [CrossRef] [PubMed]
- Zhang, Z.; He, D.; Zheng, Y.; Wu, Y.; Li, Q.; Gong, H.; Ma, X.; Li, Y. Microstructure and mechanical properties of hot-extruded Mg-2Zn-xGa (x = 1, 3, 5 and 7 wt.%) alloys. *Mater. Sci. Eng. A* **2022**, *859*, 144208. [CrossRef]
- Li, Q.; Ma, X.; Xiong, C.; Qu, W.; Li, Y. Effects of annealing temperature on microstructures and shape memory effect of Ti-19Zr-11Nb-2Ta alloy sheets. *J. Alloys Compd.* **2022**, *897*, 162728. [CrossRef]
- Istrate, B.; Mareci, D.; Munteanu, C.; Stanciu, S.; Luca, D.; Crimu, C.I.; Kamel, E. In vitro electrochemical properties of biodegradable ZrO<sub>2</sub>-CaO coated MgCa alloy using atmospheric plasma spraying. *J. Optoelectron. Adv. Mater.* **2015**, *17*, 1186–1192.
- Xue, X.; Ma, C.; An, H.; Li, Y.; Guan, Y. Corrosion resistance and cytocompatibility of Ti-20Zr-10Nb-4Ta alloy surface modified by a focused fiber laser. *Sci. China Mater.* **2018**, *61*, 516–524. [CrossRef]
- Wu, Y.; Li, Q.; Xu, B.; Fu, H.; Li, Y. Nano-hydroxyapatite coated TiO<sub>2</sub> nanotubes on Ti-19Zr-10Nb-1Fe alloy promotes osteogenesis in vitro. *Colloids Surf. B Biointerfaces* **2021**, *207*, 112019. [CrossRef] [PubMed]
- Di Pompo, G.; Liguori, A.; Carlini, M.; Avnet, S.; Boi, M.; Baldini, N.; Focarete, M.L.; Bianchi, M.; Gualandi, C.; Graziani, G. Electrospun fibers coated with nanostructured biomimetic hydroxyapatite: A new platform for regeneration at the bone interfaces. *Biomater. Adv.* **2023**, *144*, 213231. [CrossRef]
- Nijhuis, A.W.G.; Nejadnik, M.R.; Nudelman, F.; Walboomers, X.F.; Te Riet, J.; Habibovic, P.; Tahmasebi Birgani, Z.; Li, Y.; Bomans, P.H.H.; Jansen, J.A.; et al. Enzymatic pH control for biomimetic deposition of calcium phosphate coatings. *Acta Biomater.* **2014**, *10*, 931–939. [CrossRef]
- Li, G.; Ma, F.; Liu, P.; Qi, S.; Li, W.; Zhang, K.; Chen, X. Review of micro-arc oxidation of titanium alloys: Mechanism, properties and applications. *J. Alloys Compd.* **2023**, *948*, 169773. [CrossRef]
- Yu, S.; Yu, Z.; Wang, G.; Han, J.; Ma, X.; Dargusch, M.S. Biocompatibility and osteoconduction of active porous calcium-phosphate films on a novel Ti-3Zr-2Sn-3Mo-25Nb biomedical alloy. *Colloids Surf. B Biointerfaces* **2011**, *85*, 103–115. [CrossRef] [PubMed]
- De Lima, G.G.; De Souza, G.B.; Lepienski, C.M.; Kuromoto, N.K. Mechanical properties of anodic titanium films containing ions of Ca and P submitted to heat and hydrothermal treatment. *J. Mech. Behav. Biomed. Mater.* **2016**, *64*, 18–30. [CrossRef] [PubMed]
- Reshadi, F.; Faraji, G.; Baniassadi, M.; Tajeddini, M. Surface modification of severe plastically deformed ultrafine grained pure titanium by plasma electrolytic oxidation. *Surf. Coat. Technol.* **2017**, *316*, 113–121. [CrossRef]
- Chen, L.; Wei, K.; Qu, Y.; Li, T.; Chang, B.; Liao, B.; Xue, W. Characterization of plasma electrolytic oxidation film on biomedical high niobium-containing  $\beta$ -titanium alloy. *Surf. Coat. Technol.* **2018**, *352*, 295–301. [CrossRef]
- Lederer, S.; Arat, S.; Fuerbeth, W. Influence of Process Parameters on the Tribological Behavior of PEO Coatings on CP-Titanium 4+ Alloys for Biomedical Applications. *Materials* **2021**, *14*, 5364. [CrossRef] [PubMed]
- Lederer, S.; Sankaran, S.; Smith, T.; Fürbeth, W. Formation of bioactive hydroxyapatite-containing titania coatings on CP-Ti 4+ alloy generated by plasma electrolytic oxidation. *Surf. Coat. Technol.* **2019**, *363*, 66–74. [CrossRef]

18. Plekhova, N.G.; Lyapun, I.N.; Drobot, E.I.; Shevchuk, D.V.; Sinebryukhov, S.L.; Mashtalyar, D.V.; Gnednikov, S.V. Functional State of Mesenchymal Stem Cells upon Exposure to Bioactive Coatings on Titanium Alloys. *Bull. Exp. Biol. Med.* **2020**, *169*, 147–156. [CrossRef]
19. Makurat-Kasprolewicz, B.; Ossowska, A. Recent advances in electrochemically surface treated titanium and its alloys for biomedical applications: A review of anodic and plasma electrolytic oxidation methods. *Mater. Today Commun.* **2023**, *34*, 105425. [CrossRef]
20. Aliofkhaezrai, M.; Macdonald, D.D.; Matykina, E.; Parfenov, E.V.; Egorin, V.S.; Curran, J.A.; Troughton, S.C.; Sinebryukhov, S.L.; Gnednikov, S.V.; Lampke, T.; et al. Review of plasma electrolytic oxidation of titanium substrates: Mechanism, properties, applications and limitations. *Appl. Surf. Sci. Adv.* **2021**, *5*, 100121. [CrossRef]
21. Jiang, B.L.; Wang, Y.M. Plasma electrolytic oxidation treatment of aluminium and titanium alloys. In *Surface Engineering of Light Alloys*; Elsevier: Amsterdam, The Netherlands, 2010; pp. 110–154. ISBN 978-1-84569-537-8.
22. Kaseem, M.; Fatimah, S.; Nashrah, N.; Ko, Y.G. Recent progress in surface modification of metals coated by plasma electrolytic oxidation: Principle, structure, and performance. *Progress Mater. Sci.* **2021**, *117*, 100735. [CrossRef]
23. Gao, A.; Hang, R.; Bai, L.; Tang, B.; Chu, P.K. Electrochemical surface engineering of titanium-based alloys for biomedical application. *Electrochim. Acta* **2018**, *271*, 699–718. [CrossRef]
24. Albella, J.M.; Montero, I.; Martinez-Duart, J.M. A theory of avalanche breakdown during anodic oxidation. *Electrochim. Acta* **1987**, *32*, 255–258. [CrossRef]
25. Yerokhin, A.L.; Snizhko, L.O.; Gurevina, N.L.; Leyland, A.; Pilkington, A.; Matthews, A. Discharge characterization in plasma electrolytic oxidation of aluminium. *J. Phys. D Appl. Phys.* **2003**, *36*, 2110–2120. [CrossRef]
26. Stojadinović, S.; Vasilić, R.; Petković, M.; Kasalica, B.; Belča, I.; Žekić, A.; Zeković, L. Characterization of the plasma electrolytic oxidation of titanium in sodium metasilicate. *Appl. Surf. Sci.* **2013**, *265*, 226–233. [CrossRef]
27. Stojadinović, S.; Vasilić, R.; Petković, M.; Zeković, L. Plasma electrolytic oxidation of titanium in heteropolytungstate acids. *Surf. Coat. Technol.* **2011**, *206*, 575–581. [CrossRef]
28. Hussein, R.O.; Northwood, D.O.; Nie, X. Processing-Microstructure Relationships in the Plasma Electrolytic Oxidation (PEO) Coating of a Magnesium Alloy. *Mater. Sci. Appl.* **2014**, *5*, 124–139. [CrossRef]
29. Wang, Y.; Yu, H.; Chen, C.; Zhao, Z. Review of the biocompatibility of micro-arc oxidation coated titanium alloys. *Mater. Des.* **2015**, *85*, 640–652. [CrossRef]
30. Wang, J.; Pan, Y.; Feng, R.; Cui, H.; Gong, B.; Zhang, L.; Gao, Z.; Cui, X.; Zhang, H.; Jia, Z. Effect of electrolyte composition on the microstructure and bio-corrosion behavior of micro-arc oxidized coatings on biomedical Ti6Al4V alloy. *J. Mater. Res. Technol.* **2020**, *9*, 1477–1490. [CrossRef]
31. Liu, W.; Liu, S.; Wang, L. Surface Modification of Biomedical Titanium Alloy: Micromorphology, Microstructure Evolution and Biomedical Applications. *Coatings* **2019**, *9*, 249. [CrossRef]
32. Lim, B.-S.; Lim, S.-G.; Choe, H.-C. Precipitation of bone-like apatite on plasma electrolytic oxidized Ti-6Al-4V alloy. *Thin Solid. Film.* **2022**, *746*, 139136. [CrossRef]
33. Rakhadilov, B.; Baizhan, D. Creation of Bioceramic Coatings on the Surface of Ti-6Al-4V Alloy by Plasma Electrolytic Oxidation Followed by Gas Detonation Spraying. *Coatings* **2021**, *11*, 1433. [CrossRef]
34. Li, Q.; Yang, W.; Liu, C.; Wang, D.; Liang, J. Correlations between the growth mechanism and properties of micro-arc oxidation coatings on titanium alloy: Effects of electrolytes. *Surf. Coat. Technol.* **2017**, *316*, 162–170. [CrossRef]
35. Li, Y. Formation and in vitro/in vivo performance of “cortex-like” micro/nano-structured TiO<sub>2</sub> coatings on titanium by micro-arc oxidation. *Mater. Sci.* **2018**, *14*, 90–103.
36. Wang, W.; Zheng, X.; Yu, F.; Li, Y.; Xue, X.; Qi, M.; Li, Y. Formation and cytocompatibility of a hierarchical porous coating on Ti-20Zr-10Nb-4Ta alloy by micro-arc oxidation. *Surf. Coat. Technol.* **2020**, *404*, 126471. [CrossRef]
37. Wu, T.; Blawert, C.; Serdechnova, M.; Karlova, P.; Dovzhenko, G.; Florian Wieland, D.C.; Stojadinovic, S.; Vasilić, R.; Mojsilovic, K.; Zheludkevich, M.L. Formation of plasma electrolytic oxidation coatings on pure niobium in different electrolytes. *Appl. Surf. Sci.* **2022**, *573*, 151629. [CrossRef]
38. Yu, S.-R.; Yao, Q.; Chu, H.-C. Morphology and phase composition of MAO ceramic coating containing Cu on Ti6Al4V alloy. *Rare Met.* **2017**, *36*, 671–675. [CrossRef]
39. Jiang, H.; Shao, Z.; Benqin, J. Effect of Electrolyte Composition on Photocatalytic Activity and Corrosion Resistance of Micro-Arc Oxidation Coating on Pure Titanium. *Procedia Earth Planet. Sci.* **2011**, *2*, 156–161. [CrossRef]
40. Zhang, R.; Zhong, S.; Zeng, L.; Li, H.; Zhao, R.; Zhang, S.; Duan, X.; Huang, J.; Zhao, Y. Novel Mg-Incorporated Micro-Arc Oxidation Coatings for Orthopedic Implants Application. *Materials* **2021**, *14*, 5710. [CrossRef] [PubMed]
41. Li, G.; Wang, Y.; Qiao, L.; Zhao, R.; Zhang, S.; Zhang, R.; Chen, C.; Li, X.; Zhao, Y. Preparation and formation mechanism of copper incorporated micro-arc oxidation coatings developed on Ti-6Al-4V alloys. *Surf. Coat. Technol.* **2019**, *375*, 74–85. [CrossRef]
42. Tkachuk, O.V.; Pohrelyuk, I.M.; Proskurnyak, R.V.; Danyliak, M.-O.M.; Vynar, V.A. Influence of Concentration of Potassium Hydroxide in Electrolyte on Formation of Hydroxyapatite Coatings on Titanium. *JOM* **2023**, *75*, 5088–5095. [CrossRef]
43. Lakrat, M.; Mejdoubi, E.M.; Ozdemir, F.; Santos, C. Effect of sodium silicate concentration on the physico-chemical properties of dual-setting bone-like apatite cements. *Mater. Today Commun.* **2022**, *31*, 103421. [CrossRef]
44. Martin, J.; Leone, P.; Nominé, A.; Veys-Renaux, D.; Henrion, G.; Belmonte, T. Influence of electrolyte ageing on the Plasma Electrolytic Oxidation of aluminium. *Surf. Coat. Technol.* **2015**, *269*, 36–46. [CrossRef]

45. Simchen, F.; Sieber, M.; Lampke, T. Electrolyte influence on ignition of plasma electrolytic oxidation processes on light metals. *Surf. Coat. Technol.* **2017**, *315*, 205–213. [CrossRef]
46. Bordbar-Khiabani, A.; Ebrahimi, S.; Yarmand, B. Highly corrosion protection properties of plasma electrolytic oxidized titanium using rGO nanosheets. *Appl. Surf. Sci.* **2019**, *486*, 153–165. [CrossRef]
47. Fattah-alhosseini, A.; Molaei, M.; Babaei, K. The effects of nano- and micro-particles on properties of plasma electrolytic oxidation (PEO) coatings applied on titanium substrates: A review. *Surf. Interfaces* **2020**, *21*, 100659. [CrossRef]
48. Su, Y.; Cockerill, I.; Zheng, Y.; Tang, L.; Qin, Y.-X.; Zhu, D. Biofunctionalization of metallic implants by calcium phosphate coatings. *Bioact. Mater.* **2019**, *4*, 196–206. [CrossRef] [PubMed]
49. Shen, X.; Hu, W.; Ping, L.; Liu, C.; Yao, L.; Deng, Z.; Wu, G. Antibacterial and Osteogenic Functionalization of Titanium with Silicon/Copper-Doped High-Energy Shot Peening-Assisted Micro-Arc Oxidation Technique. *Front. Bioeng. Biotechnol.* **2020**, *8*, 573464. [CrossRef]
50. Qadir, M.; Li, Y.; Munir, K.; Wen, C. Calcium Phosphate-Based Composite Coating by Micro-Arc Oxidation (MAO) for Biomedical Application: A Review. *Crit. Rev. Solid. State Mater. Sci.* **2018**, *43*, 392–416. [CrossRef]
51. Shimabukuro, M. Antibacterial Property and Biocompatibility of Silver, Copper, and Zinc in Titanium Dioxide Layers Incorporated by One-Step Micro-Arc Oxidation: A Review. *Antibiotics* **2020**, *9*, 716. [CrossRef]
52. Nacula, B.S.; Fratila-Apachitei, L.E.; Berkani, A.; Apachitei, I.; Duszczuk, J. Enrichment of anodic MgO layers with Ag nanoparticles for biomedical applications. *J. Mater. Sci. Mater. Med.* **2009**, *20*, 339–345. [CrossRef]
53. Yerokhin, A.L.; Nie, X.; Leyland, A.; Matthews, A.; Dowey, S.J. Plasma electrolysis for surface engineering. *Surf. Coat. Technol.* **1999**, *122*, 73–93. [CrossRef]
54. Lu, X.; Blawert, C.; Zheludkevich, M.L.; Kainer, K.U. Insights into plasma electrolytic oxidation treatment with particle addition. *Corros. Sci.* **2015**, *101*, 201–207. [CrossRef]
55. Kyrylenko, S.; Warchoń, F.; Oleshko, O.; Husak, Y.; Kazek-Kęsik, A.; Korniienko, V.; Deineka, V.; Sowa, M.; Maciej, A.; Michalska, J.; et al. Effects of the sources of calcium and phosphorus on the structural and functional properties of ceramic coatings on titanium dental implants produced by plasma electrolytic oxidation. *Mater. Sci. Eng. C* **2021**, *119*, 111607. [CrossRef] [PubMed]
56. Wang, J.; Lu, H.; Sun, Z.; Xu, G.; Bai, Z.; Peng, Z. Effect of ultra accurate control of electrolyte temperature on the performance of micro arc oxidation ceramic coatings. *Ceram. Int.* **2023**, *49*, 33236–33246. [CrossRef]
57. Nakajima, M.; Miura, Y.; Fushimi, K.; Habazaki, H. Spark anodizing behaviour of titanium and its alloys in alkaline aluminate electrolyte. *Corros. Sci.* **2009**, *51*, 1534–1539. [CrossRef]
58. O'Hara, M.; Troughton, S.C.; Francis, R.; Clyne, T.W. The incorporation of particles suspended in the electrolyte into plasma electrolytic oxidation coatings on Ti and Al substrates. *Surf. Coat. Technol.* **2020**, *385*, 125354. [CrossRef]
59. Sikdar, S.; Menezes, P.V.; Maccione, R.; Jacob, T.; Menezes, P.L. Plasma Electrolytic Oxidation (PEO) Process—Processing, Properties, and Applications. *Nanomaterials* **2021**, *11*, 1375. [CrossRef]
60. Famiyeh, L.; Huang, X. Plasma Electrolytic Oxidation Coatings on Aluminum Alloys: Microstructures, Properties, and Applications. *Mod. Concepts Mater. Sci.* **2019**, *2*, 526. [CrossRef]
61. Pesode, P. Surface modification of titanium and titanium alloy by plasma electrolytic oxidation process for biomedical applications: A review. *Mater. Today* **2021**, *46*, 594–602. [CrossRef]
62. Hussein, R.O.; Zhang, P.; Nie, X.; Xia, Y.; Northwood, D.O. The effect of current mode and discharge type on the corrosion resistance of plasma electrolytic oxidation (PEO) coated magnesium alloy AJ62. *Surf. Coat. Technol.* **2011**, *206*, 1990–1997. [CrossRef]
63. Zhao, Z.; Pan, Q.; Yan, J.; Ye, J.; Liu, Y. Direct current micro-arc oxidation coatings on Al-Zn-Mg-Mn-Zr extruded alloy with tunable structures and properties templated by discharge stages. *Vacuum* **2018**, *150*, 155–165. [CrossRef]
64. Seo, C.-S.; Lee, S.-R.; Choe, H.-C. Phenomena of nano-particle formation in the plasma electrolytic oxidation process according to applied potentials. *Appl. Nanosci.* **2022**, *12*, 3337–3342. [CrossRef]
65. Lv, G.-H.; Chen, H.; Gu, W.-C.; Li, L.; Niu, E.-W.; Zhang, X.-H.; Yang, S.-Z. Effects of current frequency on the structural characteristics and corrosion property of ceramic coatings formed on magnesium alloy by PEO technology. *J. Mater. Process. Technol.* **2008**, *208*, 9–13. [CrossRef]
66. Wang, Y.; Wang, L.; Zheng, H.; Du, C.; Ning, C.; Shi, Z.; Xu, C. Effect of frequency on the structure and cell response of Ca- and P-containing MAO films. *Appl. Surf. Sci.* **2010**, *256*, 2018–2024. [CrossRef]
67. Dehnavi, V.; Luan, B.L.; Shoosmith, D.W.; Liu, X.Y.; Rohani, S. Effect of duty cycle and applied current frequency on plasma electrolytic oxidation (PEO) coating growth behavior. *Surf. Coat. Technol.* **2013**, *226*, 100–107. [CrossRef]
68. Songur, F.; Dikici, B.; Niinomi, M.; Arslan, E. The plasma electrolytic oxidation (PEO) coatings to enhance in-vitro corrosion resistance of Ti-29Nb-13Ta-4.6Zr alloys: The combined effect of duty cycle and the deposition frequency. *Surf. Coat. Technol.* **2019**, *374*, 345–354. [CrossRef]
69. Babaei, M.; Dehghanian, C.; Taheri, P.; Babaei, M. Effect of duty cycle and electrolyte additive on photocatalytic performance of TiO<sub>2</sub>-ZrO<sub>2</sub> composite layers prepared on CP Ti by micro arc oxidation method. *Surf. Coat. Technol.* **2016**, *307*, 554–564. [CrossRef]
70. Pavarini, M.; Moscatelli, M.; Candiani, G.; Tarsini, P.; Cochis, A.; Rimondini, L.; Najmi, Z.; Rocchetti, V.; De Giglio, E.; Cometa, S.; et al. Influence of frequency and duty cycle on the properties of antibacterial borate-based PEO coatings on titanium for bone-contact applications. *Appl. Surf. Sci.* **2021**, *567*, 150811. [CrossRef]

71. Sun, X.; Jiang, Z.; Yao, Z.; Zhang, X. The effects of anodic and cathodic processes on the characteristics of ceramic coatings formed on titanium alloy through the MAO coating technology. *Appl. Surf. Sci.* **2005**, *252*, 441–447. [CrossRef]
72. Yao, Z.; Liu, Y.; Xu, Y.; Jiang, Z.; Wang, F. Effects of cathode pulse at high frequency on structure and composition of Al<sub>2</sub>TiO<sub>5</sub> ceramic coatings on Ti alloy by plasma electrolytic oxidation. *Mater. Chem. Phys.* **2011**, *126*, 227–231. [CrossRef]
73. Sun, X.; Jiang, Z.; Xin, S.; Yao, Z. Composition and mechanical properties of hard ceramic coating containing  $\alpha$ -Al<sub>2</sub>O<sub>3</sub> produced by microarc oxidation on Ti–6Al–4V alloy. *Thin Solid. Film.* **2005**, *471*, 194–199. [CrossRef]
74. Wu, Y.; Yang, Z.; Wang, R.; Wu, G.; Chen, D.; Wang, D.; Liu, X.; Li, D.; Guo, C.; Yu, S.; et al. An investigation of microstructure evolution for plasma electrolytic oxidation (PEO) coated Al in an alkaline silicate electrolyte. *Surf. Coat. Technol.* **2018**, *351*, 136–152. [CrossRef]
75. Tang, Q.; Qiu, T.; Ni, P.; Zhai, D.; Shen, J. Soft Sparking Discharge Mechanism of Micro-Arc Oxidation Occurring on Titanium Alloys in Different Electrolytes. *Coatings* **2022**, *15*, 1191. [CrossRef]
76. Zhai, D.; Tang, Q.; Ni, P.; Li, X.; Shen, J. Growth pattern of soft-spark micro-arc oxide coating on titanium alloy in silicon anion electrolyte. *Surf. Coat. Technol.* **2023**, *473*, 130030. [CrossRef]
77. Xue, X.; Lu, L.; He, D.; Guan, Y.; Li, Y. Antibacterial properties and cytocompatibility of Ti-20Zr-10Nb-4Ta alloy surface with Ag microparticles by laser treatment. *Surf. Coat. Technol.* **2021**, *425*, 127716. [CrossRef]
78. Chen, H.-T.; Hsiao, C.-H.; Long, H.-Y.; Chung, C.-J.; Tang, C.-H.; Chen, K.-C.; He, J.-L. Micro-arc oxidation of  $\beta$ -titanium alloy: Structural characterization and osteoblast compatibility. *Surf. Coat. Technol.* **2009**, *204*, 1126–1131. [CrossRef]
79. Cimenoglu, H.; Gunyuz, M.; Kose, G.T.; Baydogan, M.; Uğurlu, F.; Sener, C. Micro-arc oxidation of Ti6Al4V and Ti6Al7Nb alloys for biomedical applications. *Mater. Charact.* **2011**, *62*, 304–311. [CrossRef]
80. Wang, C.; Ma, F.; Liu, P.; Chen, J.; Liu, X.; Zhang, K.; Li, W.; Han, Q. The influence of alloy elements in Ti6Al4V and Ti35Nb2Ta3Zr on the structure, morphology and properties of MAO coatings. *Vacuum* **2018**, *157*, 229–236. [CrossRef]
81. Gu, Y.; Chen, L.; Yue, W.; Chen, P.; Chen, F.; Ning, C. Corrosion behavior and mechanism of MAO coated Ti6Al4V with a grain-fined surface layer. *J. Alloys Compd.* **2016**, *664*, 770–776. [CrossRef]
82. Qi, X.; Jiang, B.; Song, R. Effects of ageing treatment on corrosion behavior of 7075 aluminum alloy coated by micro arc oxidation (MAO). *Corros. Sci.* **2022**, *199*, 110164. [CrossRef]
83. Bose, S.; Robertson, S.F.; Bandyopadhyay, A. Surface modification of biomaterials and biomedical devices using additive manufacturing. *Acta Biomater.* **2018**, *66*, 6–22. [CrossRef] [PubMed]
84. Chen, K.-T.; Huang, J.-W.; Lin, W.-T.; Kuo, T.-Y.; Chien, C.-S.; Chang, C.-P.; Lin, Y.-D. Effects of Micro-Arc Oxidation Discharge Parameters on Formation and Biomedical Properties of Hydroxyapatite-Containing Flower-like Structure Coatings. *Materials* **2023**, *16*, 57. [CrossRef] [PubMed]
85. Rogov, A.B.; Huang, Y.; Shore, D.; Matthews, A.; Yerokhin, A. Toward rational design of ceramic coatings generated on valve metals by plasma electrolytic oxidation: The role of cathodic polarisation. *Ceram. Int.* **2021**, *47*, 34137–34158. [CrossRef]
86. Yeung, W.K.; Sukhorukova, I.V.; Shtansky, D.V.; Levashov, E.A.; Zhitnyak, I.Y.; Gloushankova, N.A.; Kiryukhantsev-Korneev, P.V.; Petrzhik, M.I.; Matthews, A.; Yerokhin, A. Characteristics and in vitro response of thin hydroxyapatite–titania films produced by plasma electrolytic oxidation of Ti alloys in electrolytes with particle additions. *RSC Adv.* **2016**, *6*, 12688–12698. [CrossRef] [PubMed]
87. Habazaki, H.; Tsunekawa, S.; Tsuji, E.; Nakayama, T. Formation and characterization of wear-resistant PEO coatings formed on  $\beta$ -titanium alloy at different electrolyte temperatures. *Appl. Surf. Sci.* **2012**, *259*, 711–718. [CrossRef]
88. Kuroda, P.A.B.; Grandini, C.R.; Afonso, C.R.M. Surface Characterization of New  $\beta$  Ti-25Ta-Zr-Nb Alloys Modified by Micro-Arc Oxidation. *Materials* **2023**, *16*, 2352. [CrossRef] [PubMed]
89. Kim, Y.; Meade, S.M.; Chen, K.; Feng, H.; Rayyan, J.; Hess-Dunning, A.; Ereifej, E.S. Nano-Architectural Approaches for Improved Intracortical Interface Technologies. *Front. Neurosci.* **2018**, *12*, 456. [CrossRef]
90. Stich, T.; Alagboso, F.; Křenek, T.; Kovářik, T.; Alt, V.; Docheva, D. Implant-bone-interface: Reviewing the impact of titanium surface modifications on osteogenic processes in vitro and in vivo. *Bioeng. Transl. Med.* **2022**, *7*, e10239. [CrossRef]
91. Balshe, A.A.; Assad, D.A.; Eckert, S.E.; Koka, S.; Weaver, A.L. A Retrospective Study of the Survival of Smooth- and Rough-Surface Dental Implants. *Int. J. Oral Maxillofac. Implant* **2009**, *24*, 1113–1118.
92. Shah, F.A.; Thomsen, P.; Palmquist, A. Osseointegration and current interpretations of the bone-implant interface. *Acta Biomater.* **2019**, *84*, 1–15. [CrossRef]
93. Hanawa, T. Titanium–Tissue Interface Reaction and Its Control with Surface Treatment. *Front. Bioeng. Biotechnol.* **2019**, *7*, 170. [CrossRef]
94. Perez, R.A.; Mestres, G. Role of pore size and morphology in musculo-skeletal tissue regeneration. *Mater. Sci. Eng. C* **2016**, *61*, 922–939. [CrossRef]
95. Yamasaki, H.; Sakai, H. Osteogenic response to porous hydroxyapatite ceramics under the skin of dogs. *Biomaterials* **1992**, *13*, 308–312. [CrossRef] [PubMed]
96. Shalabi, M.M.; Gortemaker, A.; Hof, M.A.V.; Jansen, J.A.; Creugers, N.H.J. Implant Surface Roughness and Bone Healing: A Systematic Review. *J. Dent. Res.* **2006**, *85*, 496–500. [CrossRef] [PubMed]
97. Li, Y.; Wang, W.; Yu, F.; Wang, D.; Guan, S.; Li, Y.; Qi, M. Characterization and cytocompatibility of hierarchical porous TiO<sub>2</sub> coatings incorporated with calcium and strontium by one-step micro-arc oxidation. *Mater. Sci. Eng. C* **2020**, *109*, 110610. [CrossRef] [PubMed]

98. Li, Y.; Wang, W.; Duan, J.; Qi, M. A super-hydrophilic coating with a macro/micro/nano triple hierarchical structure on titanium by two-step micro-arc oxidation treatment for biomedical applications. *Surf. Coat. Technol.* **2017**, *311*, 1–9. [CrossRef]
99. Park, M.-G.; Choe, H.-C. Corrosion behaviors of bioactive element coatings on PEO-treated Ti-6Al-4V alloys. *Surf. Coat. Technol.* **2019**, *376*, 44–51. [CrossRef]
100. Bai, L.; Du, Z.; Du, J.; Yao, W.; Zhang, J.; Weng, Z.; Liu, S.; Zhao, Y.; Liu, Y.; Zhang, X.; et al. A multifaceted coating on titanium dictates osteoimmunomodulation and osteo/angio-genesis towards ameliorative osseointegration. *Biomaterials* **2018**, *162*, 154–169. [CrossRef]
101. Zhou, Z.; Cai, K.; Shen, J.; Cai, L.; Dai, B.; Wang, Z.; Ma, P.; Liu, J.; Shen, X. Fabrication and biological assessment of halloysite-doped micro/nano structures on titanium surface. *Ceram. Int.* **2023**, *49*, 8886–8896. [CrossRef]
102. Peng, F.; Qiu, L.; Yao, M.; Liu, L.; Zheng, Y.; Wu, S.; Ruan, Q.; Liu, X.; Zhang, Y.; Li, M.; et al. A lithium-doped surface inspires immunomodulatory functions for enhanced osseointegration through PI3K/AKT signaling axis regulation. *Biomater. Sci.* **2021**, *9*, 8202–8220. [CrossRef]
103. Zhou, J.; Wang, X. The osteogenic, anti-oncogenic and antibacterial activities of selenium-doped titanium dioxide coatings on titanium. *Surf. Coat. Technol.* **2020**, *403*, 126408. [CrossRef]
104. Yan, R.; Li, J.; Wu, Q.; Zhang, X.; Hu, L.; Deng, Y.; Jiang, R.; Wen, J.; Jiang, X. Trace Element-Augmented Titanium Implant with Targeted Angiogenesis and Enhanced Osseointegration in Osteoporotic Rats. *Front. Chem.* **2022**, *10*, 839062. [CrossRef] [PubMed]
105. Lin, K.; Wang, X.; Zhang, N.; Shen, Y. Strontium (Sr) strengthens the silicon (Si) upon osteoblast proliferation, osteogenic differentiation and angiogenic factor expression. *J. Mater. Chem. B* **2016**, *4*, 3632–3638. [CrossRef] [PubMed]
106. Yu, L.; Yin, Y.; Guo, Z.; Fei, Y.; Wen, X.; Wang, J.; Sun, H.; Hu, J.; Jin, S. A functional study of zinc–titanium coatings and exploration of the intrinsic correlation between angiogenesis and osteogenesis. *J. Mater. Chem. B* **2023**, *11*, 3236–3251. [CrossRef] [PubMed]
107. Song, H.-J.; Shin, K.-H.; Kook, M.-S.; Oh, H.-K.; Park, Y.-J. Effects of the electric conditions of AC-type microarc oxidation and hydrothermal treatment solution on the characteristics of hydroxyapatite formed on titanium. *Surf. Coat. Technol.* **2010**, *204*, 2273–2278. [CrossRef]
108. Li, K.; Xue, Y.; Zhang, L.; Han, Y.  $\beta$ -FeOOH/Fe-TiO<sub>2</sub> heterojunctions on Ti for bacteria inactivation under light irradiation and biosealing. *Biomater. Sci.* **2020**, *8*, 6004–6016. [CrossRef]
109. Yu, S.; Yu, Z.; Guo, D.; Zhu, H.; Zhang, M.; Han, J.; Yu, Z.; Cao, Y.; Wang, G. Enhanced bioactivity and interfacial bonding strength of Ti<sub>3</sub>Zr<sub>2</sub>Sn<sub>3</sub>Mo<sub>2</sub>Nb alloy through graded porosity and surface bioactivation. *J. Mater. Sci. Technol.* **2022**, *100*, 137–149. [CrossRef]
110. Popova, A.D.; Sheveyko, A.N.; Kuptsov, K.A.; Advakhova, D.Y.; Karyagina, A.S.; Gromov, A.V.; Krivozubov, M.S.; Orlova, P.A.; Volkov, A.V.; Slukin, P.V.; et al. Osteoconductive, Osteogenic, and Antipathogenic Plasma Electrolytic Oxidation Coatings on Titanium Implants with BMP-2. *ACS Appl. Mater. Interfaces* **2023**, *15*, 37274–37289. [CrossRef]
111. Arun, S.; Ahn, S.-G.; Choe, H.-C. Surface characteristics of HA-coated and PEO-treated Ti-6Al-4V alloy in solution containing Ag nanoparticles. *Surf. Interfaces* **2023**, *39*, 102932. [CrossRef]
112. Liu, F.; Wang, F.; Shimizu, T.; Igarashi, K.; Zhao, L. Formation of hydroxyapatite on Ti-6Al-4V alloy by microarc oxidation and hydrothermal treatment. *Surf. Coat. Technol.* **2005**, *199*, 220–224. [CrossRef]
113. Li, G.; Cao, H.; Zhang, W.; Ding, X.; Yang, G.; Qiao, Y.; Liu, X.; Jiang, X. Enhanced Osseointegration of Hierarchical Micro/Nanotopographic Titanium Fabricated by Microarc Oxidation and Electrochemical Treatment. *ACS Appl. Mater. Interfaces* **2016**, *8*, 3840–3852. [CrossRef] [PubMed]
114. Park, S.-Y.; Choe, H.-C. Mn-coatings on the micro-pore formed Ti-29Nb-xHf alloys by RF-magnetron sputtering for dental applications. *Appl. Surf. Sci.* **2018**, *432*, 278–284. [CrossRef]
115. Wang, X.; Li, B.; Liu, S.; Zhang, C.; Hao, J. Antibacterial and Biological Properties of a Micro-structured BMP-2/Chitosan/Hydroxyapatite Hybrid Coating on Ti Surface. *J. Hard Tissue Biol.* **2019**, *28*, 303–314. [CrossRef]
116. Wang, X.; Li, B.; Zhang, C. Preparation of BMP-2/chitosan/hydroxyapatite antibacterial bio-composite coatings on titanium surfaces for bone tissue engineering. *Biomed. Microdevices* **2019**, *21*, 89. [CrossRef] [PubMed]
117. Teng, F.-Y.; Tai, I.-C.; Ho, M.-L.; Wang, J.-W.; Weng, L.W.; Wang, Y.J.; Wang, M.-W.; Tseng, C.-C. Controlled release of BMP-2 from titanium with electrodeposition modification enhancing critical size bone formation. *Mater. Sci. Eng. C* **2019**, *105*, 109879. [CrossRef] [PubMed]
118. Belibasakis, G.N.; Manoil, D. Microbial Community-Driven Etiopathogenesis of Peri-Implantitis. *J. Dent. Res.* **2021**, *100*, 21–28. [CrossRef] [PubMed]
119. Costa, R.C.; Nagay, B.E.; Dini, C.; Borges, M.H.R.; Miranda, L.F.B.; Cordeiro, J.M.; Souza, J.G.S.; Sukotjo, C.; Cruz, N.C.; Barão, V.A.R. The race for the optimal antimicrobial surface: Perspectives and challenges related to plasma electrolytic oxidation coating for titanium-based implants. *Adv. Colloid Interface Sci.* **2023**, *311*, 102805. [CrossRef] [PubMed]
120. Wu, Y.; Deng, Z.; Wang, X.; Chen, A.; Li, Y. Synergistic antibacterial photocatalytic and photothermal properties over bowl-shaped TiO<sub>2</sub> nanostructures on Ti-19Zr-10Nb-1Fe alloy. *Regen. Biomater.* **2022**, *9*, rbac025. [CrossRef]
121. Alipal, J.; Saidin, S.; Lo, A.Z.K.; Koshy, P.; Abdullah, H.Z.; Idris, M.I.; Lee, T.C. In vitro surface efficacy of CaP-based anodised titanium for bone implants. *Surf. Interfaces* **2023**, *39*, 102872. [CrossRef]

122. Jia, Z.; Xiu, P.; Li, M.; Xu, X.; Shi, Y.; Cheng, Y.; Wei, S.; Zheng, Y.; Xi, T.; Cai, H.; et al. Bioinspired anchoring AgNPs onto micro-nanoporous TiO<sub>2</sub> orthopedic coatings: Trap-killing of bacteria, surface-regulated osteoblast functions and host responses. *Biomaterials* **2016**, *75*, 203–222. [CrossRef]
123. Nagay, B.E.; Dini, C.; Cordeiro, J.M.; Ricomini-Filho, A.P.; de Avila, E.D.; Rangel, E.C.; da Cruz, N.C.; Barão, V.A.R. Visible-Light-Induced Photocatalytic and Antibacterial Activity of TiO<sub>2</sub> Codoped with Nitrogen and Bismuth: New Perspectives to Control Implant-Biofilm-Related Diseases. *ACS Appl. Mater. Interfaces* **2019**, *11*, 18186–18202. [CrossRef] [PubMed]
124. van Hengel, I.A.J.; Tierolf, M.W.A.M.; Valerio, V.P.M.; Minneboo, M.; Fluit, A.C.; Fratila-Apachitei, L.E.; Apachitei, I.; Zadpoor, A.A. Self-defending additively manufactured bone implants bearing silver and copper nanoparticles. *J. Mater. Chem. B* **2020**, *8*, 1589–1602. [CrossRef] [PubMed]
125. Dini, C.; Nagay, B.E.; Cordeiro, J.M.; da Cruz, N.C.; Rangel, E.C.; Ricomini-Filho, A.P.; de Avila, E.D.; Barão, V.A.R. UV-photofunctionalization of a biomimetic coating for dental implants application. *Mater. Sci. Eng. C* **2020**, *110*, 110657. [CrossRef] [PubMed]
126. Rizwan, M.; Alias, R.; Zaidi, U.Z.; Mahmoodian, R.; Hamdi, M. Surface modification of valve metals using plasma electrolytic oxidation for antibacterial applications: A review. *J. Biomed. Mater. Res. Part. A* **2018**, *106*, 590–605. [CrossRef] [PubMed]
127. Yamamoto, A.; Honma, R.; Sumita, M. Cytotoxicity evaluation of 43 metal salts using murine fibroblasts and osteoblastic cells. *J. Biomed. Mater. Res.* **1998**, *39*, 331–340. [CrossRef]
128. van Hengel, I.A.J.; Putra, N.E.; Tierolf, M.W.A.M.; Minneboo, M.; Fluit, A.C.; Fratila-Apachitei, L.E.; Apachitei, I.; Zadpoor, A.A. Biofunctionalization of selective laser melted porous titanium using silver and zinc nanoparticles to prevent infections by antibiotic-resistant bacteria. *Acta Biomater.* **2020**, *107*, 325–337. [CrossRef] [PubMed]
129. Lv, Y.; Zhang, T.; Zhang, X.; Fu, S.; Yang, L.; Dong, Z.; Ma, Y.; Zhang, E. The synergistic effect of Ag and ZnO on the microstructure, corrosion resistance and in vitro biological performance of titania coating. *Surf. Coat. Technol.* **2021**, *426*, 127798. [CrossRef]
130. Zhang, L.; Gao, Q.; Han, Y. Zn and Ag Co-doped Anti-microbial TiO<sub>2</sub> Coatings on Ti by Micro-arc Oxidation. *J. Mater. Sci. Technol.* **2016**, *32*, 919–924. [CrossRef]
131. Lv, Y.; Cai, G.; Zhang, X.; Fu, S.; Zhang, E.; Yang, L.; Xiao, J.; Dong, Z. Microstructural characterization and in vitro biological performances of Ag, Zn co-incorporated TiO<sub>2</sub> coating. *Ceram. Int.* **2020**, *46*, 29160–29172. [CrossRef]
132. Wang, Y.; Zhao, S.; Li, G.; Zhang, S.; Zhao, R.; Dong, A.; Zhang, R. Preparation and in vitro antibacterial properties of anodic coatings co-doped with Cu, Zn, and P on a Ti-6Al-4V alloy. *Mater. Chem. Phys.* **2020**, *241*, 122360. [CrossRef]
133. Zhang, L.; Guo, J.; Yan, T.; Han, Y. Fibroblast responses and antibacterial activity of Cu and Zn co-doped TiO<sub>2</sub> for percutaneous implants. *Appl. Surf. Sci.* **2018**, *434*, 633–642. [CrossRef]
134. Shimabukuro, M.; Tsutsumi, Y.; Nozaki, K.; Chen, P.; Yamada, R.; Ashida, M.; Doi, H.; Nagai, A.; Hanawa, T. Chemical and Biological Roles of Zinc in a Porous Titanium Dioxide Layer Formed by Micro-Arc Oxidation. *Coatings* **2019**, *9*, 705. [CrossRef]
135. Shimabukuro, M.; Hiji, A.; Manaka, T.; Nozaki, K.; Chen, P.; Ashida, M.; Tsutsumi, Y.; Nagai, A.; Hanawa, T. Time-Transient Effects of Silver and Copper in the Porous Titanium Dioxide Layer on Antibacterial Properties. *J. Funct. Biomater.* **2020**, *11*, 44. [CrossRef] [PubMed]
136. Tsutsumi, H.; Tsutsumi, Y.; Shimabukuro, M.; Manaka, T.; Chen, P.; Ashida, M.; Ishikawa, K.; Katayama, H.; Hanawa, T. Investigation of the Long-Term Antibacterial Properties of Titanium by Two-Step Micro-Arc Oxidation Treatment. *Coatings* **2021**, *11*, 798. [CrossRef]
137. Zhao, Q.-M.; Sun, Y.-Y.; Wu, C.-S.; Yang, J.; Bao, G.-F.; Cui, Z.-M. Enhanced osteogenic activity and antibacterial ability of manganese-titanium dioxide microporous coating on titanium surfaces. *Nanotoxicology* **2020**, *14*, 289–309. [CrossRef] [PubMed]
138. Lin, D.-J.; Tsai, M.-T.; Shieh, T.-M.; Huang, H.-L.; Hsu, J.-T.; Ko, Y.-C.; Fuh, L.-J. In vitro antibacterial activity and cytocompatibility of bismuth doped micro-arc oxidized titanium. *J. Biomater. Appl.* **2013**, *27*, 553–563. [CrossRef] [PubMed]
139. Qi, S.; Kang, B.; Yao, C.; Lan, D.; Chen, X.; Ma, F.; Liu, P.; Liu, Y. Cerium doped TiO<sub>2</sub> coating with superior antibacterial property and biocompatibility prepared by micro-arc oxidation. *Mater. Des.* **2023**, *234*, 112312. [CrossRef]
140. Teng, W.; Zhang, Z.; Wang, Y.; Ye, Y.; Yinwang, E.; Liu, A.; Zhou, X.; Xu, J.; Zhou, C.; Sun, H.; et al. Iodine Immobilized Metal–Organic Framework for NIR-Triggered Antibacterial Therapy on Orthopedic Implants. *Small* **2021**, *17*, 2102315. [CrossRef] [PubMed]
141. Wang, Y.; Teng, W.; Zhang, Z.; Ma, S.; Jin, Z.; Zhou, X.; Ye, Y.; Zhang, C.; Gou, Z.; Yu, X.; et al. Remote Eradication of Bacteria on Orthopedic Implants via Delayed Delivery of Polycaprolactone Stabilized Polyvinylpyrrolidone Iodine. *JFB* **2022**, *13*, 195. [CrossRef]
142. Sopchenski, L.; Cogo, S.; Dias-Ntipanyj, M.F.; Elifio-Espósito, S.; Popat, K.C.; Soares, P. Bioactive and antibacterial boron doped TiO<sub>2</sub> coating obtained by PEO. *Appl. Surf. Sci.* **2018**, *458*, 49–58. [CrossRef]
143. Ying, D.; Ouyang, Z.; Liu, T.; Liu, X.; Huang, Q. Boron-containing micro/nano-structured TiO<sub>2</sub>/bioceramics coatings with modulatory effects on SaOS-2 cell response. *Mater. Lett.* **2018**, *228*, 29–32. [CrossRef]
144. Zhou, J.; Li, B.; Han, Y. F-doped TiO<sub>2</sub> microporous coating on titanium with enhanced antibacterial and osteogenic activities. *Sci. Rep.* **2018**, *8*, 17858. [CrossRef]
145. Zhou, J.; Zhao, L. Multifunction Sr, Co and F co-doped microporous coating on titanium of antibacterial, angiogenic and osteogenic activities. *Sci. Rep.* **2016**, *6*, 29069. [CrossRef] [PubMed]
146. Zhao, Q.; Wu, J.; Zhang, S.; Ni, X.; Wang, B.; Lu, K.; Zhang, P.; Xu, R. Preparation and properties of composite manganese/fluorine coatings on metallic titanium. *RSC Adv.* **2023**, *13*, 14863–14877. [CrossRef] [PubMed]

147. He, Y.; Zhang, Y.; Shen, X.; Tao, B.; Liu, J.; Yuan, Z.; Cai, K. The fabrication and in vitro properties of antibacterial polydopamine-LL-37-POPC coatings on micro-arc oxidized titanium. *Colloids Surf. B Biointerfaces* **2018**, *170*, 54–63. [CrossRef]
148. Zhang, H.; Wang, G.; Liu, P.; Tong, D.; Ding, C.; Zhang, Z.; Xie, Y.; Tang, H.; Ji, F. Vancomycin-loaded titanium coatings with an interconnected micro-patterned structure for prophylaxis of infections: An in vivo study. *RSC Adv.* **2018**, *8*, 9223–9231. [CrossRef]
149. Zaniolo, K.; Biaggio, S.; Cirelli, J.; Cominotte, M.; Bocchi, N.; Rocha-Filho, R.; De Souza, C. Production and Characterization of Bioactive and Antimicrobial Titanium Oxide Surfaces with Silver Nanoparticles and a Poly (lactic Acid) Microfiber Coating. *J. Braz. Chem. Soc.* **2023**, e-20230134. [CrossRef]
150. Fattah-alhosseini, A.; Molaei, M.; Nouri, M.; Babaei, K. Review of the role of graphene and its derivatives in enhancing the performance of plasma electrolytic oxidation coatings on titanium and its alloys. *Appl. Surf. Sci. Adv.* **2021**, *6*, 100140. [CrossRef]
151. Mazinani, A.; Nine, M.J.; Chiesa, R.; Candiani, G.; Tarsini, P.; Tung, T.T.; Losic, D. Graphene oxide (GO) decorated on multi-structured porous titania fabricated by plasma electrolytic oxidation (PEO) for enhanced antibacterial performance. *Mater. Des.* **2021**, *200*, 109443. [CrossRef]
152. San, H.; Paresoglou, M.; Minneboo, M.; van Hengel, I.A.J.; Yilmaz, A.; Gonzalez-Garcia, Y.; Fluit, A.C.; Hagedoorn, P.-L.; Fratila-Apachitei, L.E.; Apachitei, I.; et al. Fighting Antibiotic-Resistant Bacterial Infections by Surface Biofunctionalization of 3D-Printed Porous Titanium Implants with Reduced Graphene Oxide and Silver Nanoparticles. *Int. J. Mol. Sci.* **2022**, *23*, 9204. [CrossRef]
153. Li, B.; Xia, X.; Guo, M.; Jiang, Y.; Li, Y.; Zhang, Z.; Liu, S.; Li, H.; Liang, C.; Wang, H. Biological and antibacterial properties of the micro-nanostructured hydroxyapatite/chitosan coating on titanium. *Sci. Rep.* **2019**, *9*, 14052. [CrossRef] [PubMed]
154. Zhou, R.; Zhou, Y.; Cheng, J.; Cao, J.; Li, M.; Yu, H.; Wei, D.; Li, B.; Wang, Y.; Zhou, Y. Surface configuration of microarc oxidized Ti with regionally loaded chitosan hydrogel containing ciprofloxacin for improving biological performance. *Mater. Today Bio* **2022**, *16*, 100380. [CrossRef]
155. Xu, X.; Xu, H.; Chai, Q.; Li, Z.; Man, Z.; Li, W. Novel functionalized Ti6Al4V scaffold for preventing infection and promoting rapid osseointegration. *Mater. Des.* **2023**, *226*, 111612. [CrossRef]
156. Xu, G.; Shen, X.; Dai, L.; Ran, Q.; Ma, P.; Cai, K. Reduced bacteria adhesion on octenidine loaded mesoporous silica nanoparticles coating on titanium substrates. *Mater. Sci. Eng. C* **2017**, *70*, 386–395. [CrossRef]
157. Souza, J.G.S.; Bertolini, M.M.; Costa, R.C.; Nagay, B.E.; Dongari-Bagtzoglou, A.; Barão, V.A.R. Targeting implant-associated infections: Titanium surface loaded with antimicrobial. *iScience* **2021**, *24*, 102008. [CrossRef]
158. Pinto, I.B.; Dos Santos Machado, L.; Meneguetti, B.T.; Nogueira, M.L.; Espínola Carvalho, C.M.; Roel, A.R.; Franco, O.L. Utilization of antimicrobial peptides, analogues and mimics in creating antimicrobial surfaces and bio-materials. *Biochem. Eng. J.* **2019**, *150*, 107237. [CrossRef]
159. Costa, R.C.; Nagay, B.E.; Bertolini, M.; Costa-Oliveira, B.E.; Sampaio, A.A.; Retamal-Valdes, B.; Shibli, J.A.; Feres, M.; Barão, V.A.R.; Souza, J.G.S. Fitting pieces into the puzzle: The impact of titanium-based dental implant surface modifications on bacterial accumulation and polymicrobial infections. *Adv. Colloid Interface Sci.* **2021**, *298*, 102551. [CrossRef]
160. Li, T.; Zhao, Y.; Chen, M. Study on Enhancing the Corrosion Resistance and Photo-Thermal Antibacterial Properties of the Micro-Arc Oxidation Coating Fabricated on Medical Magnesium Alloy. *Int. J. Mol. Sci.* **2022**, *23*, 10708. [CrossRef] [PubMed]
161. Chai, M.; An, M.; Zhang, X. Construction of a TiO<sub>2</sub>/MoSe<sub>2</sub>/CHI coating on dental implants for combating Streptococcus mutans infection. *Mater. Sci. Eng. C* **2021**, *129*, 112416. [CrossRef] [PubMed]
162. Chen, Z.; Yuen, J.; Crawford, R.; Chang, J.; Wu, C.; Xiao, Y. The effect of osteoimmunomodulation on the osteogenic effects of cobalt incorporated β-tricalcium phosphate. *Biomaterials* **2015**, *61*, 126–138. [CrossRef] [PubMed]
163. Li, X.; Huang, Q.; Hu, X.; Wu, D.; Li, N.; Liu, Y.; Li, Q.; Wu, H. Evaluating the osteoimmunomodulatory properties of micro-arc oxidized titanium surface at two different biological stages using an optimized in vitro cell culture strategy. *Mater. Sci. Eng. C* **2020**, *110*, 110722. [CrossRef] [PubMed]
164. Spriano, S.; Yamaguchi, S.; Baino, F.; Ferraris, S. A critical review of multifunctional titanium surfaces: New frontiers for improving osseointegration and host response, avoiding bacteria contamination. *Acta Biomater.* **2018**, *79*, 1–22. [CrossRef]
165. Mokarram, N.; Bellamkonda, R.V. A Perspective on Immunomodulation and Tissue Repair. *Ann. Biomed. Eng.* **2014**, *42*, 338–351. [CrossRef]
166. Li, H.-F.; Huang, J.-Y.; Lin, G.-C.; Wang, P.-Y. Recent advances in tribological and wear properties of biomedical metallic materials. *Rare Met.* **2021**, *40*, 3091–3106. [CrossRef]
167. Huang, Q.; Li, X.; Elkhooley, T.A.; Xu, S.; Liu, X.; Feng, Q.; Wu, H.; Liu, Y. The osteogenic, inflammatory and osteoimmunomodulatory performances of biomedical Ti-Ta metal-metal composite with Ca- and Si-containing bioceramic coatings. *Colloids Surf. B Biointerfaces* **2018**, *169*, 49–59. [CrossRef]
168. Huang, Q.; Li, X.; Elkhooley, T.A.; Liu, X.; Zhang, R.; Wu, H.; Feng, Q.; Liu, Y. The Cu-containing TiO<sub>2</sub> coatings with modulatory effects on macrophage polarization and bactericidal capacity prepared by micro-arc oxidation on titanium substrates. *Colloids Surf. B Biointerfaces* **2018**, *170*, 242–250. [CrossRef]
169. Sun, H.; Yang, Y.; Yu, L.; Liu, K.; Fei, Y.; Guo, C.; Zhou, Y.; Hu, J.; Shi, L.; Ji, H. Inhibition of Inflammatory Response and Promotion of Osteogenic Activity of Zinc-Doped Micro-Arc Titanium Oxide Coatings. *ACS Omega* **2022**, *7*, 14920–14932. [CrossRef] [PubMed]
170. Li, X.; Huang, Q.; Liu, L.; Zhu, W.; Elkhooley, T.A.; Liu, Y.; Feng, Q.; Li, Q.; Zhou, S.; Liu, Y.; et al. Reduced inflammatory response by incorporating magnesium into porous TiO<sub>2</sub> coating on titanium substrate. *Colloids Surf. B Biointerfaces* **2018**, *171*, 276–284. [CrossRef]

171. Yang, X.; Zhang, C.; Zhang, T.; Xiao, J. Cobalt-doped Ti surface promotes immunomodulation. *Biomed. Mater.* **2022**, *17*, 025003. [CrossRef] [PubMed]
172. Bai, L.; Liu, Y.; Du, Z.; Weng, Z.; Yao, W.; Zhang, X.; Huang, X.; Yao, X.; Crawford, R.; Hang, R.; et al. Differential effect of hydroxyapatite nano-particle versus nano-rod decorated titanium micro-surface on osseointegration. *Acta Biomater.* **2018**, *76*, 344–358. [CrossRef] [PubMed]
173. Ramenzoni, L.L.; Flückiger, L.B.; Attin, T.; Schmidlin, P.R. Effect of Titanium and Zirconium Oxide Microparticles on Pro-Inflammatory Response in Human Macrophages under Induced Sterile Inflammation: An In Vitro Study. *Materials* **2021**, *14*, 4166. [CrossRef] [PubMed]
174. Zhu, Y.; Shen, Y.; Xiang, Y.; Fang, K.; Xu, K.; Ma, P.; Cai, C.; Ma, J.; Shen, X. Combined application of silica particles and zirconium hydrogen phosphate coating to improve the friction resistance and osteogenic/anti-inflammatory properties of micro-arc oxidation-treated titanium. *Surf. Coat. Technol.* **2022**, *451*, 129037. [CrossRef]
175. Wang, D.; Chen, M.-W.; Wei, Y.-J.; Geng, W.-B.; Hu, Y.; Luo, Z.; Cai, K.-Y. Construction of Wogonin Nanoparticle-Containing Strontium-Doped Nanoporous Structure on Titanium Surface to Promote Osteoporosis Fracture Repair. *Adv. Healthc. Mater.* **2022**, *11*, 2201405. [CrossRef] [PubMed]
176. Wang, X.; Mei, L.; Jiang, X.; Jin, M.; Xu, Y.; Li, J.; Li, X.; Meng, Z.; Zhu, J.; Wu, F. Hydroxyapatite-Coated Titanium by Micro-Arc Oxidation and Steam-Hydrothermal Treatment Promotes Osseointegration. *Front. Bioeng. Biotechnol.* **2021**, *9*, 625877. [CrossRef] [PubMed]
177. Trindade, R.; Albrektsson, T.; Tengvall, P.; Wennerberg, A. Foreign Body Reaction to Biomaterials: On Mechanisms for Buildup and Breakdown of Osseointegration. *Clin. Implant Dent. Relat. Res.* **2016**, *18*, 192–203. [CrossRef] [PubMed]
178. Karl, M.; Albrektsson, T. Clinical Performance of Dental Implants with a Moderately Rough (TiUnite) Surface: A Meta-Analysis of Prospective Clinical Studies. *Int. J. Oral. Maxillofac. Implants* **2017**, *32*, 717–734. [CrossRef] [PubMed]
179. Lim, Y.W.; Kwon, S.Y.; Sun, D.H.; Kim, Y.S. The Otto Aufranc Award: Enhanced Biocompatibility of Stainless Steel Implants by Titanium Coating and Microarc Oxidation. *Clin. Orthop. Relat. Res.* **2011**, *469*, 330–338. [CrossRef]
180. Milleret, V.; Lienemann, P.S.; Gasser, A.; Bauer, S.; Ehrbar, M.; Wennerberg, A. Rational design and in vitro characterization of novel dental implant and abutment surfaces for balancing clinical and biological needs. *Clin. Implant Dent. Relat. Res.* **2019**, *21*, 15–24. [CrossRef]
181. Pang, K.-M.; Lee, J.-W.; Lee, J.-Y.; Lee, J.-B.; Kim, S.-M.; Kim, M.-J.; Lee, J.-H. Clinical outcomes of magnesium-incorporated oxidised implants: A randomised double-blind clinical trial. *Clin. Oral. Implants Res.* **2014**, *25*, 616–621. [CrossRef]
182. Kang, B.-S. *On the Bone Tissue Response to Surface Chemistry Modifications of Titanium Implants*; Department of Biomaterials, Institute of Clinical Sciences, Sahlgrenska Academy at University of Gothenburg: Göteborg, Sweden, 2011; ISBN 978-91-628-8325-6.
183. Lim, Y.-W.; Song, J.-H.; Kwon, S.-Y.; Kim, Y.-S.; Byun, Y.-S.; Lee, S.-W. Minimum 10-year follow-up of micro-arc oxidation coating on a cementless grit-blasted tapered-wedge stem of total hip arthroplasty: A multicentre study. *HIP Int.* **2022**, *32*, 501–509. [CrossRef]
184. Khanna, R.; Kokubo, T.; Matsushita, T.; Takadama, H. Fabrication of dense  $\alpha$ -alumina layer on Ti-6Al-4V alloy hybrid for bearing surfaces of artificial hip joint. *Mater. Sci. Eng. C* **2016**, *69*, 1229–1239. [CrossRef] [PubMed]

**Disclaimer/Publisher’s Note:** The statements, opinions and data contained in all publications are solely those of the individual author(s) and contributor(s) and not of MDPI and/or the editor(s). MDPI and/or the editor(s) disclaim responsibility for any injury to people or property resulting from any ideas, methods, instructions or products referred to in the content.

MDPI AG  
Grosspeteranlage 5  
4052 Basel  
Switzerland  
Tel.: +41 61 683 77 34

*Coatings* Editorial Office  
E-mail: [coatings@mdpi.com](mailto:coatings@mdpi.com)  
[www.mdpi.com/journal/coatings](http://www.mdpi.com/journal/coatings)



Disclaimer/Publisher's Note: The title and front matter of this reprint are at the discretion of the Guest Editor. The publisher is not responsible for their content or any associated concerns. The statements, opinions and data contained in all individual articles are solely those of the individual Editor and contributors and not of MDPI. MDPI disclaims responsibility for any injury to people or property resulting from any ideas, methods, instructions or products referred to in the content.





Academic Open  
Access Publishing

[mdpi.com](http://mdpi.com)

ISBN 978-3-7258-4632-0